UNIVERSITY OF OKLAHOMA GRADUATE COLLEGE

ON THE DESIGN OF UNMANNED AERIAL WEATHER MEASUREMENT SYSTEMS FOR WINTRY PRECIPITATION OBSERVATIONS

A DISSERTATION

SUBMITTED TO THE GRADUATE FACULTY

in partial fulfillment of the requirements for the

Degree of

DOCTOR OF PHILOSOPHY

By GUSTAVO BRITTO HUPSEL DE AZEVEDO
Norman, Oklahoma
2024

Downloaded from SHAREOK. Persistent Handle URL: https://hdl.handle.net/11244/341268

ON THE DESIGN OF

UNMANNED AERIAL WEATHER MEASUREMENT SYSTEMS

FOR WINTRY PRECIPITATION OBSERVATIONS

A DISSERTATION APPROVED FOR THE
SCHOOL OF ELECTRICAL AND COMPUTER ENGINEERING

BY THE COMMITTEE CONSISTING OF

Dr. David Schvartzman, Chair

Dr. Tian-You Yu

Dr. Robert D. Palmer

Dr. Petra Klein

Dr. Jamey D. Jacob

©Copyright by GUSTAVO BRITTO HUPSEL DE AZEVEDO 2024
All Rights Reserved.

DEDICATION

to

My wife

Renata

For

Encouraging me to pursue my passion

for engineering.

My parents

Yara and Carlos

For

Fostering curiosity

My siblings

Livia, Marta, Julia and Bernardo

For

Inspiring me to better

Acknowledgements

First, I wish to express my gratitude to my advisor, Dr. Schvartzman, who believed in my potential, guided me, and helped me become a better scientist and communicator.

I also wish to thank my committee members, Drs. Palmer, Yu, Klein, and Jacob, who, besides serving on this committee, each had a critical role in affording me the opportunity to be a part of and complete this degree.

I also would like to express my deepest gratitude to my friends and collaborators, Bill Doyle and Dr. Avery, who, without this research, would not have been possible.

I also thank David Grimsley and Dr. Chris Fiebrich from the Oklahoma Mesonet for their guidance in my journey of becoming an atmospheric measurements specialist and their indispensable support during the laboratory and field experiments.

I also wish to express my gratitude to Matt Fronzak, who welcomed me to the aviation weather community and enabled me to access critical experts in this research.

I also thank Stephanie DiVito, Dr. Landolt, Ben Bernstein, Brian Filipiak, and Daniel Tripp for their role as consultants and subject matter experts in winter weather precipitation.

I would be remiss if I did not thank and mention the critical role played by my peers and the staff at the Advanced Radar Research Center, particularly Jorge Alva, Rosalind Agasti, Dr. Salazar-Aquino, Danny Feland, Dale Sexton, Kerri Raper, and Mark David.

Finally, I wish to thank my friends and family. In particular, Kyle Sandidge and my brothers and sisters in Christ from Providence Road Church for showing us God's love and making Renata and me feel at home away from home.

Contents

Abstract **xvi**

1 Introduction **1**
1.1 Background . . . 3
1.2 Motivation . . . 5
1.3 Contribution . . . 11
1.4 Broader Impact . . . 13
1.5 Outline . . . 15

2 Literature Review **17**
2.1 Key-Term Definitions . . . 18
2.2 Atmospheric Measurement Systems . . . 21
2.2.1 Design Challenges . . . 23
2.2.2 Integration of New Observations Into Forecast and Decision-Making Workflows . . . 28
2.2.3 Integration of WxUAS Data Into Forecast and Decision-Making Workflows . . . 30
2.3 WxUAS Design Challenges . . . 32
2.3.1 System Operation . . . 32
2.3.2 Sensor Integration . . . 34

3 In-Situ Measurement Design **41**
3.1 Sensor Shield . . . 43
3.2 Sensors and Sampling Techniques . . . 46
3.3 Flight Control Integration . . . 52
3.4 Validation . . . 58
3.4.1 Laboratory Experiment . . . 59
3.4.2 Field Experiment - OKMesonet . . . 60
3.4.3 Field Experiment - Marshall . . . 63

4 Remote Measurement Design **69**
4.1 Radar System . . . 70
4.2 Initial Experiments . . . 71
4.3 Integration and Deployment Strategy . . . 76
4.4 WxUAS Radar Post-Processing Algorithm . . . 80

4.4.1 Aircraft Motion Compensation . . . 82
4.4.2 Synthetic Long Exposure . . . 84
4.4.3 Context-Dependent Noise Reduction . . . 90

5 Unmanned Aerial Vehicle Design 96
5.1 Platform-base Selection . . . 98
5.2 Winter Weather Requirements . . . 100
5.3 Aircraft Design . . . 103
5.3.1 Measurement Quality Features . . . 107
5.3.2 Safety and Operational Features . . . 110
5.4 Performance Metrics . . . 114

6 Data Processing and Fusion 117
6.1 Measurement, Information, and Insight . . . 118
6.1.1 Spatiotemporal Maps . . . 120
6.1.2 Time Series . . . 123
6.1.3 Considerations on Data Use . . . 125
6.2 Multi-modal Fusion and Algorithmic Weather Inference . . . 126

7 Field Deployment 134
7.1 Multi Atmospheric Instrument Intercomparison Study . . . 135
7.1.1 WxUAS Data and Sampling Strategy . . . 138
7.1.2 Deployment 1 . . . 139
7.1.3 Deployment 2 . . . 150
7.1.4 Deployments 3 and 4 . . . 156
7.2 Final MAI^{2}S Considerations . . . 162

8 Conclusion 164
8.1 Discussion . . . 169
8.2 Future Work . . . 173
8.3 Final Considerations . . . 174

A OK Mesonet Chamber Experiment 176

B OK Mesonet Flight Comparison Experiment 178

C Radar Configuration Parameters 182

D Pitch Angle Compensation Experiment 184

E Aircraft CAD 187

F Field Campaign Supporting Weather Data 192

List of Figures

1.1 Illustration of precipitation phase change with altitude and coverage by radar and surface observations. The first case shows frozen precipitation melting gradually with the decrease in height. The second case shows a shallow freezing layer producing mixed-phased precipitation below the radar and above the ASOS coverage. The final case shows a melting and a freezing layer creating a mix of frozen and liquid precipitation. 10
1.2 Overlap within this research's primary motivation and its broader impact areas. 15

2.1 Example of environmental interference, a frozen cup anemometer at the Kingfisher Oklahoma Mesonet tower after the ice storm of January 28-30, 2002. Photo by Chris Fiebrich. 25
2.2 Examples of physical sensor integration into UAS: (A) Omnidirectional shielded integration with propeller-based passive aspiration [54]; (B) No shielding with partial propeller-based, passive ventilation [66]; (C) Fixed-wing two-layer shielding with passive ventilation through vehicle motion [8]; (D) Multi-direction with partial shielding and propeller-based ventilation [46]; (E) Comparison of directional shield with active aspiration with partial shielding and propeller-based ventilation [37]. 39

3.1 Lateral cross-section of the two-layer custom sensor shield designed to prevent contact with freezing precipitation while allowing for direct atmospheric observation. 44
3.2 Frontal cross-section view of the two-layer custom sensor shield designed to prevent contact with freezing precipitation while allowing for direct atmospheric observation. 45
3.3 Lateral cross-section view of the two-layer custom sensor shield design highlighting construction dimensions that enhance flow characteristics, where "d" is the diameter of the inner shield. 46
3.4 Sensors for in-situ measurements: (A) The OPC-N3 for particle size distribution, (B) the PT-100 bead thermistor and ADS1115 ADC for fast temperature; (C) the HYT 271 for slow temperature and relative humidity; and (D) the MS5611 for fast pressure measurements. 47
3.5 Concentric sensor ring with redundancy for increased accuracy. The right panel illustrates 60° segmentation strategy, and the left panel illustrates its implementation. 48

3.6 Example of enhanced neighboring sensor analysis showing temperature values for sensors across four stages of a profile to 200 m above ground level. 50
3.7 Diagram depicting the ArduPilot open-source vehicle control software framework with this dissertation's weather sensor integration library. This architectural solution enables the seamless and standardized cross-platform use of the proposed in-situ sensor design. 54
3.8 Diagram depicting the weather sensor library's use of the framework's service loop as a mitigation strategy for the risks associated with the direct integration method. 55
3.9 Diagram depicting the weather sensor library producing inputs to the control loop under the safety of the framework's navigation library. 57
3.10 Examples of cross-platform use of the proposed WxUAS in-situ sensor hardware and software. 58
3.11 In-situ inner shield calibration at the Oklahoma Mesonet's Calibration Laboratory. The left panel shows the Thunder Scientific 2500 benchtop humidity generator, and the right panel details the experimental setup inside the chamber's test section. 60
3.12 Experimental setup for the system's performance evaluation under operational conditions. Two identical WxUAS were flown next to the reference Oklahoma Mesonet 10 m tower for colocated measurements. 61
3.13 Results for the second temperature and relative humidity ground-based intercomparison experiment. The small mean absolute errors are below both manufacturers' reported accuracies. 64
3.14 Results for particle size distribution (left) and power and Doppler velocity (right) during the second ground-based experiment. For the vertically pointing radar, negative Doppler velocities indicate particles falling towards the radar. 65
3.15 Ceilometer data (above) indicating the cloud base and the profiles of the particle size distribution (below) for each of the four flights to 120 m. The orange-shaded columns in the ceilometer's scatter plot represent the time intervals for the four flights 67

4.1 Experimental setup for initial evaluation of the TI AWR2243: (A) the setup for precipitation perpendicular to the radar beam, (B) the parallel setup. (C) The perpendicular "Mist" experiment. (D) The improvised radome to emulate a vertically pointing radar in parallel experiments. (E) The ice shavings used to mimic frozen precipitation. 72
4.2 range-Doppler map for the large water drops and ice shavings falling vertically toward the radar (i.e., parallel setup). 74
4.3 range-Doppler map for the mist generated by the handheld spray floating in front of the radar (i.e., perpendicular setup). 75
4.4 Illustration of the multiple angles scanned by the TI AWR2243 PAR, which can be leveraged to compensate aircraft motion in pitch. 77

4.5 Illustration of cross-platform application of this chapter's proposed remote measurement solution. Images on the top detail the integration into Oklahoma State University's Skateboard, and the bottom image depicts a conceptual design for fixed-wing deployment. 78
4.6 Illustration of the 3D-printed radar enclosure lid with a slope to remove precipitation accumulation from the radome. 80
4.7 Illustration of the effectiveness of the slopped, edgeless design used in the lightweight radar enclosure. 81
4.8 Illustration of the TPU-based suspended raft used to decouple the TI AWR2243 from motor-induced vibrations commonly found in multi-rotor UAVs. 82
4.9 Range-Doppler map for the four frames of an atmospheric profile during a drizzle event at the MAI^{2}S field campaign. The data presented here includes the aircraft compensation algorithm. 87
4.10 Range-Doppler map for an atmospheric profile during a drizzle event at the MAI^{2}S field campaign. The data presented here includes the aircraft compensation and the SLE partial algorithms. 88
4.11 Range-Doppler map for the same drizzle event presented in Fig. 4.10 after the use of the motion correction, partial SLE, and a 5 dB threshold. 89
4.12 Example of the noise-induced challenge for programmatic calculations of relevant statistics, using the data displayed in Fig. 4.11. 89
4.13 Example of Context-Dependent Noise Reduction Algorithm in a simplified context. The left panel presents the binary 20 by 20-pixel matrix with the word "HELLO", and the center panel presents the original and added noise. The right panel presents the noise-reduced recovery results. The red circle indicates a noise pixel that was not cleaned. 92
4.14 Illustration of the final range-Doppler map and velocity and distribution profiles using the motion compensation, SLE, and Context-Dependent Noise Reduction algorithms for the same drizzle event presented in Figs. 4.10 and 4.11. 94
4.15 Illustration of the range-Doppler map and velocity and distribution profiles using the motion compensation, SLE, and Context-Dependent Noise Reduction algorithms for a new rain event. 95

5.1 Isometric view of the 3-dimensional computer-aided design for this dissertation's WxUAS technology demonstration platform with the remote (left) and in-situ (right) measurement solutions integrated as its topmost component. . 105
5.2 Exploded orthographic front view of the main components in the 3-dimensional computer-aided design for this dissertation's WxUAS technology demonstration platform. 106
5.3 3-Dimensional computer-aided design for this dissertation's in-situ and remote measurement solutions with the critical obstruction zones for each measurement. (A) Orthographic top view, with elliptical shading over the radar's field of view and arrow indicating the predominant direction for the incoming wind for in-situ samples. (B) Orthographic front view with the same obstruction regions. 108

5.4 3-Dimensional computer-aided design illustrating how the aircraft arm length can be defined based on propeller size to allow an unimpeded path to the sensors. (A) The aircraft's orthographic top view with the red shaded areas representing the propeller discs and the blue shaded area representing the 1.5-propeller diameter clearance from above. (B) Orthographic front view with the same highlighted regions. 109
5.5 Diagonal cross-section view of the aircraft's 3-dimensional computer-aided design illustrating the seal-less water resistance design techniques. 111
5.6 Horizontal cross-section of the aircraft's orthographic top view highlighting the two water escaping points within the motor arm. 112
5.7 X-Frame co-axial quadcopter implementation of a partial version of this design for increased resiliency against icing. 114
5.8 Two units of the StormTrooper winter precipitation WxUAS built for the MAI^{2}S field campaign. This configuration represents the baseline for this dissertation's proposed WxUAS aircraft design. 115
5.9 Performance metrics for the StormTrooper winter precipitation WxUAS in its baseline configuration. 116

6.1 Illustration of the graphical summaries for a profile gathered by this dissertation's WxUAS. Variations with height for: (A) particle size distribution, (B) micro-range Water content, (C) temperature, and (D) relative humidity. Along with one of the many similar snapshots produced by the radar during a profile with (E) Doppler-range map, (F) Doppler velocity distributions, and (G) mean velocity. 120
6.2 Illustration of the steps to produce the time-height maps that graphically summarize the WxUAS spatiotemporal datasets. 122
6.3 Relative humidity time-height map for the last WxUAS data collection in the MAI^{2}S field campaign. 123
6.4 Temporal evolution of approximate hydrometeor fall velocity during a rain/drizzle event. 124
6.5 Overlay of the results for the automated cloud detection algorithm. 130
6.6 Distribution of the reported lowest cloud bases by a colocated ceilometer. . . 131

7.1 Multi Atmospheric Instrument Intercomparison Study (MAI^{2}S) location at the University of Connecticut's Campus (red dot) shown here with an MRMS reflectivity overlay for the 500 m level. 136
7.2 MAI^{2}S instruments. 137
7.3 Spatiotemporal temperature map for the WxUAS profiles on March 9, 2024. 140
7.4 Radar-derived precipitation variables used for type and intensity classification. The dynamic classification thresholds for liquid precipitation are shown as a reference. 141
7.5 WxUAS cloud-sized particle distribution profiles compared to the colocated ceilometer. (A) ceilometer reports for the lowest cloud base. (B) WxUAS cloud-sized particle distribution profiles. (C) Box and whisker plot for the ceilometer lowest cloud base for the interval of the four WxUAS profiles. . . 143

7.6 Height-time map for precipitation reflectivity from the colocated Micro-rain radars (MRRs). 144
7.7 Relative humidity map for the WxUAS profiles on March 9, 2024. 145
7.8 Frames from the WxUAS's onboard camera at 160, 185, 210, and 240 m indicating the start of the cloud transition layer and base of the cloud layer during the profile at 22:55. 146
7.9 Complementary weather data from mesoscale networks. The top two rows present the relative humidity profiles from the KOKX and KALB sounding stations, and the bottom row presents the MRMS composite reflectivity at the same time steps. 149
7.10 Temperature and relative humidity maps for the WxUAS profiles on March 11th, 2024. 151
7.11 Radar-derived precipitation variables used for type and intensity classification for March 11th, 2024. 152
7.12 MRMS composite reflectivity for the snow band sampled on March 11th, 2024: (left) 05:30, (center) 06:00, and (right) 06:30. 153
7.13 Wet bulb Temperature spatiotemporal map from the WxUAS profiles for March 11th, 2024. 154
7.14 Height-time map for precipitation reflectivity from the colocated MRRs. . . . 155
7.15 Height-time map for the Ceilometer's cloud-based reports during the passage of the snow band on the backside of the low-pressure system. 156
7.16 Temperature and relative humidity spatiotemporal maps for the WxUAS profiles on March 23rd, 2024. 157
7.17 Height-time map for precipitation reflectivity from the colocated MRRs. . . . 159
7.18 Temperature and relative humidity spatiotemporal maps for the WxUAS profiles on March 23rd, 2024. 160
7.19 MRMS composite reflectivity for March 24th, 2024 at 01:00. 162

8.1 This dissertation's in-situ measurements solution deployed as a calibration reference for 36 WxUAS from various manufacturers and research groups. . . 165
8.2 Diagram illustrating the framework, its modules, and how its implementation leads to novel atmospheric information. 168
8.3 Illustration of weather passing through the WxUAS profile path and inducing unexpected measurement values (e.g., sharp increase and decrease in relative humidity). 172

A.1 Time series for the temperature and relative humidity experiment at the Oklahoma Mesonet's Calibration Laboratory. The black series represents the chamber reference values, and the colored series represents the calibrated individual sensors. 177

B.1 Time series for the tower and two aircraft data highlighting the comparison interval. Mean and maximum absolut errors are found in Table 3.4. 179
B.2 Temperature time series for the tower data (1.5 and 9 m) with both aircraft data, including data before and after take-off. 180

B.3 Relative humidity time series for the tower data (1.5 m) with both aircraft data, including data before and after take-off. 181

C.1 Chirp illustration from Texas Instrument's user guide showing each chirp parameter. Source: TI mmwaveSDKUserGuide. 182

D.1 Experiment setup, a metal pole at broadside and a 60-degree angle. Both at approximately 10 m. 185
D.2 Experiment results for the pitch angle compensation via beamforming in post-processing. Metal pole at broadside on the left and 60 degrees on the right. . 186

E.1 3-dimensional computer-aided design for this dissertation's WxUAS aircraft designs. (A) Orthographic top view and (B) orthographic front view. 188
E.2 3-dimensional computer-aided design for this dissertation's WxUAS aircraft designs in a vertical cross-section cut of the orthographic back view illustrating the internal components and the overlapping layer technique for seal-less water-resistance. 189
E.3 Evolutionary desing steps that led to the StormTrooper's final design. The top left corner shows the initial waterproofing test. The top right corner shows the initial test of the landing gear integration for modular co-axial design. The bottom image shows the final baseline configuration as used in the MAI^{2}S field campaign. 190
E.4 Two units of this dissertation's WxUAS aircraft design in the baseline configuration. These two units were purpose-built for the MAI^{2}S field campaign. . 191

F.1 MRMS composite reflectivity product for the northeastern United States from March 9$^{\text{th}}$, 06Z (top left) until the 11$^{\text{th}}$ at 06Z (bottom right). 193
F.2 Weather Prediction Center's surface observation maps for the NE U.S. The time stamps for the data are (top left) March 9$^{\text{th}}$ 15Z, (top right) 18Z, (bottom left) March 10$^{\text{th}}$ 0Z, and (bottom right) 3Z. 194
F.3 MRMS composite reflectivity product for the northeastern United States from March 22$^{\text{th}}$, 18Z (top left) until the 24$^{\text{th}}$ at 0130Z (bottom right). The initial two rows advance in a 6-hour step, while the final row advances in a 30-minute step to highlight the missed rain event at Storrs (CT). 195
F.4 Soundings from Albany (left), and Long Island (right) for March 24$^{\text{th}}$ 0Z. . . 196

List of Acronyms

AGL	above ground-level	3
AAM	Advanced Air Mobility	3
AIO	all-in-one weather stations	138
CIP/FIP	Current and Forecasted Icing Potential	8
FZDZ	Freezing drizzle	2
FZFG	Freezing fog	30
FZRA	Freezing rain	2
GAIL	NASA GPM Atmospheric Instrumentation Laboratory	138
IMPACTS	Investigation of Microphysics and Precipitation for Atlantic Coast-Threatening Snowstorms	135
ISARRA	International Society for Atmospheric Research using Remotely-piloted Aircraft	165
LW-PLA	Lightweight Polylactic Acid	104
LiPo	Lithium-Polymer	102
LLJ	Low Level Jet	101
mmWave	millimeter wave	2
MAI²S	Multi Atmospheric Instrument Intercomparison Study	xi
mPING	Meteorological Phenomena Identification Near the Ground	156
MRRs	Micro-rain radars	xii
MRMS	Multi-Radar Multi-Sensor System	28
NOAA	National Oceanic and Atmospheric Administration	2
NSF	National Science Foundation	96
PAR	Phased Array Radar	76
PBL	Planetary Boundary Layer	29
PIPs	Precipitation Imaging Packages	138
PID	Proportional–Integral–Derivative	100
PLA-CF	Carbon-fiber reinforced Polylactic Acid	104

RAM Regional Air Mobility 4
SN Snow 30
SLD Supercooled Liquid Droplets 24
SLW Supercooled Liquid Water 6
STL Stereolithography Computer-Aided Design 106
SWaP Size, Weight, and Power 13
SCALES Small-UAS Coordination for Atmospheric Low-Level Environmental Sampling 165
TAIWIN Terminal Area Icing Weather Information for NextGen 4
TPU Thermoplastic Polyurethane 104
UAM Urban Air Mobility 4
UAMDAR Unmanned Aircraft Meteorological Data Reporting Network 14
UAVs Unmanned Aerial Vehicles 4
VTOL Vertical Take Off and Land 98
WMO World Meteorological Organization 30
WxUAS Unmanned Aerial Weather Measurement Systems 2

Abstract

Weakly forced winter weather precipitation events within the atmospheric boundary layer can lead to considerable negative economic impacts. Due to their proximity to the ground and varying range of particle sizes, some of these precipitation phenomena are not well captured by current observation systems (e.g., radiosondes, ground and space-based radars, and automated surface observations). In aerial transportation, undetected low-altitude freezing rain and drizzle can produce almost invisible hazards with potentially catastrophic consequences for aircraft within low altitudes (e.g., the terminal area). However, the lack of direct observations of the low-altitude freezing precipitation environment creates a challenge for forecasters, flight crews, dispatchers, and air traffic controllers. This challenge is further exacerbated by the integration of autonomous aircraft (i.e., sUAS and AAM) into the national airspace system, which will necessitate the availability of this currently missing information at higher spatial and temporal resolutions. To address this need, this dissertation endeavors to develop a novel unmanned aerial weather measurement system (WxUAS) to complement the current observation systems and provide insight into the mechanisms that govern low-altitude wintry precipitation. Such insight is achieved through a multi-modal data fusion algorithm that leverages novel WxUAS-base techniques for in-situ measurements in active precipitation and airborne radar measurements to produce an automated present weather inference aimed at detecting and locating freezing and melting layers, cloud and cloud-transition layers, as well as precipitation type and intensity. Validation for these novel techniques is presented through an intercomparison study with NASA instruments.

Chapter 1

Introduction

"Without measurements, we cannot gain any cognition on the exact state of our environment (...) Taking measurements is thus one of the most basic and elementary exercises in each science. This very fact justifies a monograph on meteorological measurement techniques and methods."

Stefan Emeis

Winter weather events can lead to power grid failures, damaged crops, loss of livestock, transportation disruptions, and other negative economic impacts. In addition, a considerable portion of these negative impacts is produced by shallow (lowest 1 to 1.5 km of the atmosphere), weakly forced events [1]. Due to the proximity to the ground and varying range of particle sizes, some of these precipitation phenomena are not well captured by current observation systems. For example, due to their fast ascent rate through the atmosphere's first 1.5 km, radiosondes do not capture enough vertical samples to characterize low-altitude atmospheric structural features [2]; In particular, structural features that lead to a precipitation phase change (e.g., melting and freezing layers) [1]. The poor observation-based characterization of the lower atmosphere impacts the parametrization of numerical models

and leads to the underrepresentation of specific precipitation types in the final forecast products. For example, in some instances, ice pellets, Freezing rain (FZRA), and Freezing drizzle (FZDZ) can produce low radar reflectivity and have their observed values fall below the assimilation thresholds for the National Oceanic and Atmospheric Administration (NOAA) High-Resolution Rapid Refresh (HRRR) forecast model [3].

In the case of aerial transportation, FZRA and FZDZ can produce nearly invisible hazards with potentially catastrophic consequences. For this reason, the Federal Aviation Administration (FAA) is implementing new standards that restrict flights into and out of commercial airports during freezing precipitation events to prevent icing-related accidents [3, 4, 5]. Therefore, precisely determining precipitation type in the lower atmosphere is required to implement such standards successfully. However, limitations in the current observation systems prevent the classification of mixed-phased precipitation in the lower atmosphere for certain scenarios [3, 6, 7].

This dissertation demonstrates how Unmanned Aerial Vehicles (UAVs) can be designed and instrumented to create Unmanned Aerial Weather Measurement Systems (WxUAS) capable of sampling the low-altitude wintry precipitation environment, including mix-phased and freezing precipitation. The proposed WxUAS provides in-situ samples of pressure, temperature, relative humidity, and particle size count. Additionally, it provides remote samples of reflectivity and velocity from an onboard, vertically pointing millimeter wave (mmWave) radar. Leveraging the mobility of UAVs, the proposed WxUAS creates a spatial distribution of the measured atmospheric parameters. Via repetition of the flight pattern at regular intervals, the proposed WxUAS captures the temporal evolution of the measured parameters' spatial distribution. Together, the spatiotemporal aspects of the WxUAS measurements can help bridge the measurements of the current observation systems, aid researchers in new studies, and assist forecasters in validating new algorithms and models. Hopefully, the insight into currently under-observed low-altitude freezing precipitation will increase flight operations safety.

1.1 Background

The term low altitude does not have an official definition. So, in this dissertation, we will consider low altitude to indicate the region between the surface and 1.5 km above ground-level (AGL). The 1.5 km relative altitude is selected for multiple reasons. First, it is a well-accepted value to represent the depth of a generalized atmospheric boundary layer, in spite of regionality and seasonality [2, 8, 9]. Second, this altitude represents the level at which ground-based radar coverage may start to deteriorate [6, 10], and radiosonde sampling is still vertically sparsed [8]. Finally, this altitude is selected because it encompasses the flight envelope of the most vulnerable flight operations (e.g., small helicopters and general aviation aircraft, larger aircraft in holding patterns, and the next-generation autonomous aircraft).

Low-altitude freezing precipitation is a concern across all categories of flight operations. Ice build-up can increase weight and drag while reducing lift, resulting in increased stall speed and a deterioration of aircraft performance [11, 12]. Even large commercial aircraft are affected by these issues because FZRA and FZDZ can produce ice accretion beyond the location of traditional icing mitigation mechanisms (e.g., wing boots) [13]. Although large commercial aircraft only encounter low-altitude freezing precipitation during take-off and landing, traffic delays caused by icy runways can prolong their flight time in low altitudes. This is particularly concerning given that 12 mm of accumulation can reduce lifting power by 50% in some aircraft, and over 20 mm of ice can accumulate on an airframe in less than 5 minutes, under certain conditions [11]. Moreover, a recent study indicates that within 30 NM from an airport, an aircraft spends up to 60% of its flight time below 1.5 km [14].

Low-flying aircraft (e.g., Helicopters and general aviation airplanes) are also severely impacted by low-altitude freezing precipitation. Their lower altitude flight envelopes create more prolonged exposure, and their size and weight limitations reduce the availability of icing mitigation mechanisms. Several aircraft in this category are not certified to fly in these conditions. They are required by the FAA to avoid and evade these conditions when inadvertently encountered [15]. The same is true for most aircraft in the Advanced Air

Mobility (AAM), which encompasses Regional Air Mobility (RAM), Urban Air Mobility (UAM), and delivery Unmanned Aerial Vehicles (UAVs). However, without a human aboard the aircraft to avoid and evade icing conditions, AAM aircraft will need to rely on weather-aware path planning and sensors to detect unforeseen icing conditions.

The concerns with low-altitude freezing precipitation that motivated the FAA to enact the 2015 rule change [4] also provoked changes in the Meteorological Aerodrome Reports (METAR) and the aviation-weather products generated by the FAA and the National Weather Service (NWS). In the case of METARs, an observation field was created to report ice accretion, even when freezing precipitation is not reported [16]. Within the NWS, the Helicopter Emergency Medical Services (HEMS) tool was created to provide a gridded view of critical weather parameters for low-flying aircraft (up to 1.5 km). Within the FAA, the Terminal Area Icing Weather Information for NextGen (TAIWIN) is currently under development to support operations in a 30 NM radius (from the airport center) and up to 3.5 km.

Even though the changes and advances mentioned above indicate a positive trend toward operational safety, systems like HEMS and TAIWIN still depend on the current forecast models and observation infrastructure. Both systems integrate data streams from multiple radars, surface and upper air observations, satellites, and forecast models. However, the coverage and resolution of the available systems and models do not accurately characterize low-altitude wintry precipitation in the atmosphere's first 1.5 km, in particular, FZDZ and FZRA [1, 3, 6, 7, 10, 17]. Often, the detection of low-altitude icing conditions is still reliant on human observations (e.g., pilot reports and augmented station reports). Therefore, there is a need for observations of mixed-phased and freezing precipitation to inform and train low-altitude forecasting tools.

1.2 Motivation

Providing an accurate forecast of wintry precipitation is a challenging task. First, observations from soundings, radar, and automated surface stations need to accurately describe the current state of the atmosphere. Then, after assimilating this initial atmospheric state as parametrization, an NWP model must accurately determine what kind of precipitation will be formed (i.e., precipitation generation layer). At this point, general forecast products can be generated. However, within aviation weather, low-altitude forecast systems (e.g., HEMS, TAIWIN, Forecast Icing Potential, FIP) continue this workflow to generate a detailed view of precipitation hazards for each flight level. To generate this detailed hazard prediction for the coming hours (up to 18 hours), low-altitude forecast systems need to take into account potential variations in atmospheric conditions with height and microphysical information to determine what possible phase changes may occur. After that, a low-altitude forecast system can generate a detailed view of precipitation hazards for each flight level. Once this work is done for one location, it must be repeated to cover the entire National Airspace System (NAS). However, scaling this process to the NAS creates a trade-off between spatial resolution, coverage, and operational feasibility. Traditional NWPs generate outputs for large areas with resolution in the tens of kilometers. Low-altitude forecast systems can improve these results to produce information with one to three-kilometer resolution, but only for smaller volumes (e.g., the terminal area) [6, 14]. Nonetheless, with new FAA requirements and the introduction of AAM aircraft into the NAS, the current spatial resolution requirements will increase (i.e., hundreds of meters), and the tolerance for forecasting errors will decrease. Furthermore, the increase in aerial commercial operation will also increase the temporal resolution requirements.

Given the number and complexity of the steps required to forecast wintry precipitation in the lower atmosphere, the errors found in forecasting tools can also be induced by the errors present in each previous step. Even though each step's exact contribution is unknown, some studies examine the carryover impacts from one stage to the next [1, 3, 7, 18, 19].

Considering the importance of observations on the forecast workflow and their real-time impact on operations, this dissertation focuses on this first step and proposes a new unmanned aerial weather measurement system to complement the current observation systems. Within the currently available systems, the most commonly assimilated into forecast workflows for aviation weather are radar, radiosondes, Automated Surface Observing Stations (ASOS), Automated Weather Observing Systems (AWOS), Significant Meteorological Information (SIGMETs), Meteorological Aerodrome Reports (METARs), and human-observed reports (e.g., Pilot Weather Reports, PIREPs). The current operational networks using these systems span the conterminous U.S. (CONUS) and provide weather observations at regular intervals. For example, the Weather Surveillance Radar - 1988 Doppler (WSR-88D) network has 159 sites, providing a 460 km coverage radius, scanning up to 15 different elevation angles every 5 minutes, generating a radar image of each elevation. Radiosondes are launched twice a day from 92 stations in the CONUS and Pacific region. AWOS and ASOS are deployed in 2000 and 900 locations and provide automatic updates on local weather every minute. Together, these observation networks compose a mosaic of atmospheric data, providing invaluable insight into several phenomena (e.g., guidance for hail, tornado, and lightning hazards [20]). However, given their operational characteristics and observational focus, these networks present some limitations regarding the observations of the low-altitude freezing precipitation environment [1, 6, 7, 18, 19, 21]. Some examples are given next.

Although radiosondes provide atmospheric profiles of pressure, temperature, humidity, wind speed, and direction from the ground to 30 km, they are only able to capture 10 to 15 measurements in the atmosphere's first 1.5 km at irregular spacing [2]. When measuring in freezing environments, radiosondes can present a warm bias upon contact with Supercooled Liquid Water (SLW) droplets [22]. Another drawback of radiosondes is their cost and availability. Soundings are launched twice a day, making their temporal resolution inadequate for nowcasting and short-term forecasting (e.g., HEMS 6-hour and FIP 18-hour outlooks). In the case of AWOS sites, pressure, wind speed and direction, temperature, and dew point ob-

servations are available every minute of the day. However, AWOS measurements are limited to the ground level, and inferences drawn from visibility measurements are only available at select sites. ASOS sites expand the AWOS observations with cloud base height and precipitation measurements at every site. Although ASOS can detect rain, snow, and freezing rain, it reports unknown precipitation (UP) for cases of mixed-phase hydrometeors [7]. It also reports "clear" for some cases of light-intensity precipitation (e.g., freezing or regular drizzle, or light snow). For this reason, 130 of the 900 ASOS locations in the CONUS still rely on human observers to correct observation errors, particularly the errors associated with their limitation to discern between freezing rain, ice pellets, and freezing drizzle. These 130 locations are at airports where high-quality weather data is critical for operations [7].

In the case of weather radars, the smallest droplet sizes of SLW are beyond the current operational radar network's direct measurement scope [12]. Nonetheless, these SLW droplets can freeze on contact with aircraft, causing the icing issues mentioned in Section 1.1. In near 0 °C environments, radar reflectivity distributions of rain, snow, freezing rain, ice pellets, drizzle, and freezing drizzle can span a 30 dB range and produce an overlap across scenarios of light, moderate, and heavy precipitation [3]. This occurs because reflectivity is a function of the number and size of hydrometeors. Therefore, a large number of small particles can produce the same reflectivity as a small number of large particles. Since low-altitude freezing precipitation events can simultaneously present any combination of hydrometeor amounts, sizes, and phases, radar-based hydrometeor classification becomes challenging. Advances in radar technology (e.g., dual-polarization) and the incorporation of radiosonde (or even NWP generated) soundings into radar-based hydrometeor classification algorithms have helped mitigate these issues [12, 19]. However, the lack of in-situ validation of radar data and the complexity of the low-altitude freezing precipitation can still cause freezing precipitation to be misclassified or under-represented in forecasts [3].

Given the abovementioned limitations, human-observed weather reports became the unofficial standard for low-altitude freezing precipitation and icing observations. These reports

can come from professional weather observers, pilots, and air traffic controllers and are available via PIREPs, SIGMETs, and METARs. Two examples of this unofficial standard are the NOAA/NWS Aviation Weather Center's (AWC) HEMS tool and the Current and Forecasted Icing Potential (CIP/FIP). These products warn their users about the uncertainty within the product and recommend use with caution.

> "NOTE: CIP/FIP are intended for flight planning purposes and should always be used in combination with icing information from all available sources including AIRMETs, SIGMETs, and PIREPs" [NOAA/NWS/AWC].[1]

This uncertainty and lack of trust are also reflected in the literature. Some studies limit their datasets to use only human-augmented observations from the current automated systems [3, 6, 7, 21]. However, human-observed weather reports are not uniform, regular, or continuously available. Controllers are only allowed to submit reports on the downtime of their primary duties, pilot reports are often submitted after the aircraft has safely landed, and only a few airports have 24-hour professional observers [7].

Another challenge found in the observations of the low-altitude freezing precipitation environment is the limitation in coverage. As mentioned above, ASOS and AWOS have good temporal coverage but limited spatial coverage. Radiosondes have a large vertical coverage but poor temporal and low-altitude spatial coverages. Even radars in the WSR-88D network, that cover large volumes within minutes, have limited coverage below 1.5 km for distances greater than 100 km due to the earth's curvature [10]. Indeed, considering the size of the NAS, these limitations are understandable. However, even if we restrict our focus to the terminal area airspace (TAS[2]), we find that most commercial airports in the CONUS have limited-to-no radar coverage within their TAS [3]. The quality of radar in a TAS is a function of three variables, the airport-to-radar distance (A2R), the Volume Coverage Pattern (VCP) mode, and terrain effects [3]. The terrain effects can be well characterized,

[1] Source: AWC FIP website - https://www.aviationweather.gov/icing/fip

[2] The terminal area airspace does not have an official definition. The definition adopted here is the one given by the FAA's TAWIN project team: 55.56 km radius (from airport center) and up to 3.5 km.

and its relevant impacts are limited to specific locations. However, varying degrees of beam broadening or overshooting create conditions that prevent radar-inferred icing from being useful across several commercial airports [3, 6]. For example, hazardous low-altitude freezing precipitation events may not be captured unless the airport is near a radar site. This occurs because the lowest elevation beams rise to the point of potentially overshooting the precipitation generation layer. This problem can be noted in relatively weak clouds and worsens with increasing distance from the radar. The introduction of the Terminal Doppler Weather Radar (TDWR) network mitigates these issues, but the TDWRs are only available at 47 out of 513 commercial airports in the CONUS. VCP mode can also cause coverage issues. Near the radar, the lack of sampling at very high beam elevation angles can cause precipitation overhead to be missed [23]. Antenna beam broadening and distance to the radar make classifying hydrometeor type harder, particularly in mixed-phase precipitation cases. Although these issues can be partially mitigated if classification algorithms account for the melting layer depth and height, as well as the size of the sampling volume, classification algorithms still rely on modeled thermodynamic information to complete this task [12, 19].

Even though the multi-sensor approach used in the low-altitude wintry precipitation forecasting systems mitigates some of the issues highlighted above, there are some scenarios where the sensors can produce conflicting results or not detect hazardous freezing precipitation conditions. For example, mixed-phased precipitation aloft can produce an ambiguous radar-based classification, while surface observations produce only one type of precipitation (see Fig. 1.1, case 1). In this case, it may be challenging to determine if a classification algorithm error occurred or if actual mixed-phased precipitation occurred. A more hazardous example is shown in Fig. 1.1, case 2. In this case, the weather radar may detect rain aloft, but a low-altitude freezing layer (below the radar coverage) produces freezing rain (FZRA) on the surface. In this scenario, a counterintuitive icing environment may be encountered by pilots in which the proper evasive maneuver is to climb. This example is comparable to the atmospheric conditions that caused the American Eagle 4184 accident in Roselawn (IN)

in 1994, which claimed 68 lives [13].

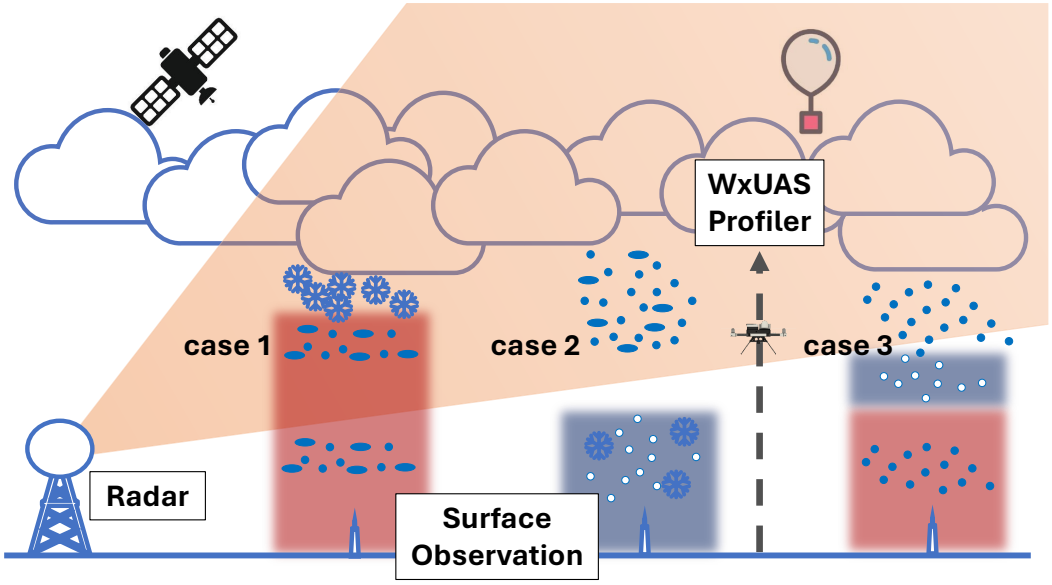


Figure 1.1: Illustration of precipitation phase change with altitude and coverage by radar and surface observations. The first case shows frozen precipitation melting gradually with the decrease in height. The second case shows a shallow freezing layer producing mixed-phased precipitation below the radar and above the ASOS coverage. The final case shows a melting and a freezing layer creating a mix of frozen and liquid precipitation.

Finally, other scenarios (see Fig. 1.1, case 3) with complete or partial melting and refreezing present a more complex detection and forecasting challenge. This scenario also presents more hazardous flight conditions. Therefore, to mitigate these risks, meet the requirements of the abovementioned 2015 FAA rule change, and expand these requirements for the safe introduction of AAM aircraft into the NAS, the products from the current observation systems need to be improved. For this reason, a new unmanned aerial weather measurement system capable of sampling the low-altitude wintry precipitation environment is proposed in this dissertation. The proposed WxUAS provides in-situ samples of pressure, temperature, relative humidity, and particle size count. It also offers remote samples of reflectivity and Doppler velocity from an onboard, vertically pointing mmWave radar. With this sensor payload, the proposed WxUAS will characterize the thermodynamic structure of the lower atmosphere while coupling it with its microphysical properties. Leveraging the mobility of UAVs, the

proposed WxUAS creates a spatial distribution of the measured atmospheric parameters. Via repetition of the flight pattern at regular intervals, the proposed WxUAS captures the temporal evolution of the measured parameters' spatial distribution. These new spatiotemporal measurements within the atmosphere's first 1.5 km can be used for local studies of the low-altitude freezing precipitation environment, provide local validation for new models and classification algorithms, and eventually be scaled to bridge the measurements of the current observation systems, increasing flight operations safety.

1.3 Contribution

This dissertation's primary aim is to develop and validate a novel unmanned aerial weather measurement system capable of sampling the low-altitude wintry precipitation environment, providing insight into atmospheric mechanisms that govern it, and improving the detection and forecast of hazards it may harbor for manned and unmanned aerial vehicles. This new WxUAS provides direct observations of atmospheric structures previously inferred or unobserved. These new observations allow researchers to investigate the micro-scale changes near the low-altitude precipitation generation layer and the interactions between hydrometeors and the planetary boundary layer as they fall to the surface.

The complexity and harshness of the low-altitude wintry precipitation environment imply the need for a considerable number of mission-specific subsystems to conceive a measurement tool that reliably retrieves atmospheric profiles in these operational conditions. For example, the development of a rotary-wing UAV to serve as the base for the proposed WxUAS. Although there are several commercially available UAVs, they do not offer the openness to modifications necessary for weather sensor integration, nor are they designed to minimize atmospheric disturbance near the weather sensors, nor would they meet the necessary flight performance requirements, fly up to 1.5 km AGL, even in harsh conditions with heavy or freezing precipitation and wind speeds exceeding $15\,\mathrm{m\,s^{-1}}$, while carrying a 2 kg scientific

payload.

The mission-specific subsystems, methods, and algorithms conceived in the process of developing the WxUAS for low-altitude wintry precipitation measurements will be described throughout this document. Nonetheless, it is important to highlight here the contributions that are most impactful to the low-altitude wintry precipitation research field. They are detailed below.

- **Multi-modal sensor data-fusion method for autonomous present weather reporting.** This dissertation demonstrates a method for combining temperature, relative humidity, and micron-range particle size measurements with hydrometeor reflectivity and Doppler velocity to report the presence of precipitation and infer its type, indicate visibility ceiling, and determine flight-level hazards for small UAVs. This novel solution provides a much higher resolution alternative to ground-based present weather stations at a lower cost, advancing the impact of future UAS-based weather observation networks (e.g., the 3D Mesonet).

- **A new measurement technique for in-situ sampling of temperature, relative humidity, and particle size for airborne instruments in active precipitation environments.** Leveraging gravity and an innovative air-intake design, this technique segregates freezing precipitation droplets from the air allowing for the atmosphere's temperature, relative humidity, and particles (between 1 to 40 µm) to be measured without exposing the sensor to the elements, thus reducing bias from contact with supercooled liquid water and other error sources (e.g., sunlight). Sensor redundancy and a concentric sensor placement strategy produce flow homogeneity, enabling enhanced accuracy and automated sensor failure detection. This design efficacy is underscored by temperature measurements exhibiting a mean absolute error of 0.051 °C and a maximum absolute error of 0.17 °C. These design attributes enable the WxUAS detailed in this dissertation to accurately capture atmospheric gradients of $0.22\,^{\circ}\mathrm{C\,m^{-1}}$. These findings hold particular importance in mixed-phase wintry precipitation environments,

where even minor disturbances of 0.5 °C can have notable implications on hydrometeor phase.

- **UAV-based mmWave radar precipitation measurements.** As one of the initial studies in this domain, this dissertation provides insights into the complexities associated with integrating a weather radar system into the Size, Weight, and Power (SWaP) constrained environment of UAV platforms. Moreover, this dissertation presents findings regarding the feasibility of employing a vertically-pointing UAV-based mmWave phased array radar for hydrometeor reflectivity and velocity observations and demonstrates how this measurement can supplement the current observation network for specific locations.

1.4 Broader Impact

Although this dissertation's primary motivation is to support low-altitude wintry precipitation research, the developed measurement tool and its subsystems may extend their impact beyond this specific domain. Notably, in its potential role to support aviation's weather-based operations, regulation development, and aircraft certification procedures. This potential benefit becomes more evident when considering the challenges within the three above-mentioned categories for the safe introduction of AAM aircraft into the NAS.

Given the wide range of AAM aircraft and their diverse SWaP limitations, the FAA is considering a plan to categorize AAM aircraft into a tiered safety and permission system, akin to the structure used in manned aviation. Under this system, autonomous vehicles are categorized into three tiers:

Tier 1 - Weather Dependent Flight Planning: Aircraft do not have any weather mitigation/awareness systems, and their operations are limited to areas with known weather conditions.

Tier 2 - Weather Detection and Avoidance: Aircraft have minimum weather awareness systems to identify conditions outside their flight envelope and perform autonomous evasive procedures.

Tier 3 - Weather Detection and Autonomous Monitoring: Aircraft possess a comprehensive weather awareness system and must exhibit capabilities similar to those of a pilot in the cockpit, actively identifying and monitoring hazardous weather conditions. Autonomous aircraft in this tier are required to navigate away from hazardous conditions only if those conditions approach the limits defined by the aircraft's rating.

Nevertheless, the implementation of this tiered system faces notable challenges. For example, the spatial resolution of existing weather observation systems, such as the WSR-88D radar network and the ASOS/AWOS network, is insufficient for weather-oriented path planning (below 1 km AGL) in most of the NAS. The lack of a method and standard to integrate weather sensors and perform atmospheric measurements from AAM aircraft presents a challenge for minimum onboard weather awareness. Furthermore, the absence of a low-altitude reference observation system poses a significant obstacle to aircraft certification procedures.

Given the modularity and cross-platform characteristics of the pressure, temperature, and relative humidity sensing package developed for this dissertation, it can be used as a standardized open-source format for minimum weather awareness in commercial AAM aircraft in tier 2. Upon reaching a critical level of adoption, such a sensing package can be leveraged to establish an Unmanned Aircraft Meteorological Data Reporting Network (UAMDAR). Such a network can be used to fill the local weather data gap and enable weather-based path planning for aircraft in tier 1. Finally, the full system developed in this dissertation can be used to provide insight into the low-altitude environmental conditions for icing certification of commercial AAM aircraft in tier 3. Finally, as a low-altitude freezing precipitation measurement system, it can provide targeted observations at some airports when low-altitude icing conditions from ground-based systems produce ambiguous results.

For these reasons, the technologies developed within this dissertation have an elevated potential to enhance aviation's weather-based operations, regulation development, and aircraft certification procedures, particularly with regard to the new AAM aircraft.

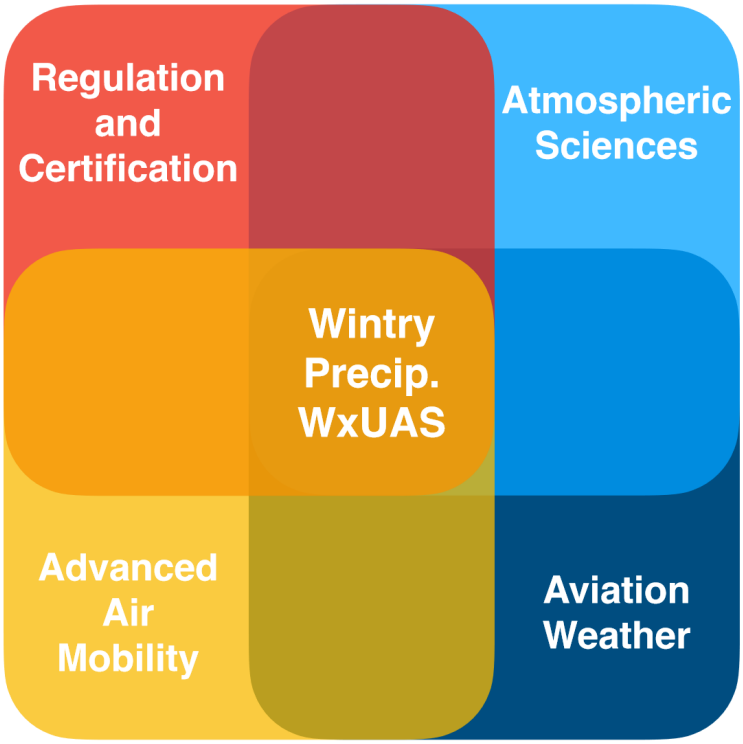


Figure 1.2: Overlap within this research's primary motivation and its broader impact areas.

1.5 Outline

To attain its objective, this dissertation is structured as follows: Chapter 2 presents an overview of the development process of atmospheric measurement systems, common design and deployment challenges, and their impact on measurement comparability. It also provides a discussion on measurement challenges faced by unmanned aerial weather measurement systems and their implications for UAS-based wintry precipitation measurements; Chapter 3 introduces a novel technique for in-situ sampling of temperature, relative humidity, and cloud-sized particles for airborne instruments in freezing precipitation environments; Chap-

ter 4 details the experimentation and feasibility evaluation efforts to adapt an automotive mmWave phased-array radar for airborne precipitation measurements onboard a UAS; Chapter 5 outlines the design details for a new multirotor UAV tailored to withstand the harsh conditions of the freezing precipitation environment; Chapter 6 presents the data processing and multi-modal data fusion techniques used to produce meaningful weather data products that enable insight. It also presents a proof of concept for an automated present weather inference algorithm; Chapter 7 highlights the system's performance during the four deployments of an exploratory field experiment in Storrs, CT. This experiment includes validation against NASA's Global Precipitation Mission instruments; Chapter 8 offers final remarks regarding this dissertation's atmospheric measurement system development cycle and insights drawn from the field deployment results, concluding with considerations regarding future research.

Chapter 2

Literature Review

"Good students (...) peek over the fences of their own discipline - and once you have done that, you cannot go back and do what everyone else is doing, even if you now must deal with heterogenous ideas that come without a manual on how they might fit together."

Sönke Ahrens

Considering the inherent multidisciplinarity in the development of an Unmanned Aerial Weather Measurement System (WxUAS) for low-altitude observations of wintry precipitation, a literature review for this research topic is inevitably broad, traversing multiple research domains. Consequently, this chapter aims to delineate a focused theme that not only refines the scope of inquiry but also positions it as a valuable contribution for future researchers in the field. This dissertation's focus naturally directs this review towards the atmospheric measurement systems literature. Although this literature segment has been extensively covered in existing textbooks and review articles [24, 25, 26, 27, 28], this chapter revisits it with a focus on the atmospheric measurement challenges that impact system

design.

This theme selection is pertinent because the challenges faced in developing a WxUAS for the wintry precipitation environment are often analogous to those found in other atmospheric sampling methodologies. Examples of these challenges include characterizing the interplay between system time-response, vehicle motion, and atmospheric feature spatiotemporal resolution, balancing the trade-off between system resiliency and accuracy, mitigating the system's interference in the sampled environment, and determining the limitations of inferences from multimodal measurements.

To accomplish this task, this chapter is structured as follows: Section 2.1 provides a list of definitions to clarify some of the ambiguity found in the atmospheric and unmanned aerial weather measurement systems literatures; Section 2.2 presents an overview of the development process of atmospheric measurement systems, common design and deployment challenges, and their impact on data assimilation; Section 2.3 closes the chapter with a review focused on measurement challenges faced by Unmanned Aerial Weather Measurement Systems.

2.1 Key-Term Definitions

Considering this dissertation's broad range of stakeholders (i.e., engineers, meteorologists, government regulators, air traffic managers, and pilots), it is important to define a few terms that will be heavily used throughout this dissertation but have ambiguous use in the literature. They are as follows:

- **Sensing element:** Is the material used to detect and quantify the changes in the atmospheric variable of interest. For example, in a PT-100 bead thermistor, the platinum filament is the sensing element that changes its resistance in response to changes in the surrounding air temperature. The physicochemical characteristics of the sensing element determine the measurement inversion function that allows the conversion of

physicochemical changes into a measurement. In some cases, the sensing element is mistakenly referred to as a sensor.

- **Sensor:** Is the combination of a sensing element with an inversion function translator that is capable of receiving an input signal (e.g., a change in air temperature) and producing a quantified output (e.g., a temperature measurement in degrees). Other common elements found in contemporary sensors are amplifiers and analog to digital converters.

- **Measurement system:** Can be referred to as an observation system, measurement instrument, or observation instrument. It is the deployed tool that produces a collection of measurements over time. It comprises a measurement platform hosting one or more sensors of a single or multiple types. The measurements collected by its sensor(s) are stored in a local data logger or transmitted to a remote data storage unit. It often employs some level of sample conditioning to mitigate environmental influences on the measurements (e.g., solar radiation shielding and aspiration fans). Because the measurement system includes the measurement platform, it requires a characterization of its own that accounts for any interferences introduced by the platform. For example, in airborne measurement systems, the system time-response may be longer than the sensor time-response.

- **UAV – Unmanned Aerial Vehicle:** Although the terms UAV, UAS, and drone are often used interchangeably, clarity is crucial, especially in the realm of atmospheric measurements. Therefore, for the purpose of this dissertation, UAV refers explicitly to the aerial vehicle itself and its associated flight systems, including a flight controller computer, a radio control receiver, a GPS, and a flight telemetry radio. While it may transport scientific payloads, its primary function is flight from one point to another without undertaking additional tasks beyond this scope.

- **UAS – Unmanned Aerial System:** Denotes a comprehensive system comprising

a UAV and additional subsystems integrated to execute a predetermined category of tasks. In a UAS setup, the sensors and subsystems are not merely appended as payloads but are integrated into the vehicle, transforming it into a distinct third system. For example, a UAV carrying a camera makes a UAV-based camera. A UAV with a camera integration into the flight controller becomes a new airborne imaging system that can use the imaging data to make decisions about its task. Such a system is herein defined as an imaging UAS.

- **WxUAS – Weather UAS:** Is an unmanned aerial weather measurement system. It comprises weather sensors integrated into a UAV and is characterized as a complete measurement system, accounting for the interactions between the sensors, the aircraft, and the measurement environment. As explained in the UAS definition, the integration of the sensors is a critical distinction of the WxUAS. Besides mitigating the impact of the vehicle on the measurement, this integration allows the system to autonomously adapt to the sampling environment, optimizing the data collection.

- **Atmospheric profile:** Sometimes called vertical profile, it is a sequence of vertical measurements directly above a specific point on the surface that produces a representation of the changes in atmospheric condition with height. Although any system sampling the atmosphere from the ground to a pre-determined height incurs a travel time, atmospheric profiles are often interpreted as instantaneous given the difference in time scales between travel time (order of minutes) and mesoscale atmospheric changes (order of tens of minutes to hours). In radiosondes, horizontal drift is often ignored, and their measurements are interpreted as perfectly vertical. The same applies to spiral ascent flight patterns in fixed-wing WxUAS and manned aircraft.

- **Atmospheric transect:** Sometimes called a horizontal transect, is a sequence of horizontal atmospheric measurements taken at a fixed height above the ground. Similarly to atmospheric profiles, they are also interpreted as instantaneous snapshots. Tran-

sects are less common than profiles due to the lack of algorithms for the assimilation of their data into weather models. Nonetheless, they produce valuable insight into horizontally moving features such as dry lines and fronts.

2.2 Atmospheric Measurement Systems

Given their potentially life-threatening impacts, weather phenomena have perennially concerned humanity, as evidenced by their depiction in rudimentary paintings, chronicles, and later in our first writings. However, it was not until the late 16^{th} century that instruments for quantifiable and repeatable atmospheric measurement were developed [29]. While the initial impetus for developing these instruments was rooted in scientific inquiry, their rapid evolution, particularly in the last 100 years, was increasingly driven by the societal benefits derived from enhanced meteorological understanding [28].

Indeed, the relationship between increases in meteorological understanding and economic development can be described as a cycle. Observations enhance our scientific comprehension of the Earth's system and its changing climate. This heightened understanding contributes to the refinement of predictive models, thereby bolstering forecast accuracy and predictability. These advancements, in turn, yield tangible societal benefits, such as enhanced agricultural planning and safer aviation operations [30, 31]. The perception of these benefits and the suge of unforeseen weather data applications create the need for more observation systems and the willingness to fund their development.

Aviation stands as a prime illustration of this cyclical progression, where enhanced wind observations near airports have virtually eradicated wind-shear-related airline accidents. This safety milestone furthered the airline industry's growth. Consequently, the additional number of commercial aircraft in the skies enabled the creation of the Aircraft Meteorological Data Relay (AMDAR) network, a weather observation network using airliners as measurement platforms [28]. A similar cycle seems to be occurring within unmanned aviation. As

the momentum intensifies toward leveraging advanced air mobility for economic growth, the need for low-altitude observation drives instrument development [32]. Subsequently, an increased presence of AAM vehicles at low altitudes will enable their use as measurement platforms, creating an analogous unmanned aircraft meteorological data delay network.

This prediction based on the cyclical development pattern of atmospheric observing systems is substantiated in shared conclusions found in the American Meteorological Society's and the National Research Council's evaluation of the state of the art in atmospheric measurements. Both documents point to the need for increased small-scale observations of localized weather events in mountains, coastlines, and cities. Small-scale phenomena in these environments are largely undersampled yet negatively impact life and property. A key component presented in both works is the need for increased coverage in the vertical dimension for these phenomena [28, 33].

New atmospheric observing systems undergo a maturing process that may take several years. This process often starts with initial feasibility studies, which may involve laboratory and field testing. This stage aims to quickly rule out concepts and principles that may prevent the technology from coming to fruition. These initial tests are commonly followed by exploratory research in a small-scale investigative field campaign alongside well-established systems. This stage provides an initial assessment of the system's potential to provide insight into relevant atmospheric properties. If successful, the system is further improved and hardened for operational use in a specific societal need (e.g., forecasting). This extended improvement and hardening phase is mostly done in testbeds where the tool's capabilities can be evaluated by decision-makers in a semi-controlled environment. Besides reducing the complexity of the operational environment, testbeds also allow stakeholders to provide early feedback and influence the final developmental stages [25, 26, 27, 28].

This lengthy maturing process is costly and may diminish the new system's impact due to partial technology obsolescence. Nonetheless, it is unavoidable because errors associated with exposure, static, and dynamic properties are not present in most laboratory settings.

Therefore, system characterization and error mitigation require long testbed deployment periods to allow these types of errors to manifest themselves [25, 26]. Nevertheless, this maturing process is imperfect; operational systems still require quality assurance and control methods. These and other atmospheric measurement system design challenges are discussed in the following subsection.

2.2.1 Design Challenges

In approximately 400 years, atmospheric measurement instruments have evolved from Torricelli's barometer, Galilei's thermometer, and Saussure's hair hygrometer to advanced capacitive, sonic, and optical devices. While contemporary instruments boast enhanced accuracy and precision, they remain dependent on the physical properties of their sensing elements to describe atmospheric conditions through indirect observations. For example, through temperature-induced changes in resistance in certain metals and humidity-induced variations in capacitance in microfilms. Thus, despite improvements, the foundational principles of sensing remain the same [25, 26, 29].

All indirect observations create the need for inversion functions that map the relationship between the atmospheric variable of interest, the desired measurand (e.g., temperature), and the effectively measured variable (e.g., resistance). This inevitable characteristic fosters two types of error sources. The first type is associated with the sensing element's physical properties (e.g., time-response), and the second relates the physical properties to the inversion function's performance. For instance, sensing elements may not exhibit consistent behavior across their entire measurement range, particularly near the edges of their operational limits. Therefore, sensors may require multiple functions to map the relationship accurately or specify different errors across the range as an operational limitation.

This inherent sensing element characteristic is commonly treated as a sensor operational limit and is sometimes reported as part of the final system's specifications. Fortunately, system design techniques such as redundant sensors, sample conditioning, integrative sampling,

and multi-modal sensing can mitigate the impact of some of these issues [7, 34]. Nonetheless, the adoption of these techniques must be done with care as they may introduce other errors. For this reason, it is critical to highlight that the same sensing element and sensor characterization procedures must be extended to the final measurement system.

Within the atmospheric measurement system literature, system-level characterization is also motivated by exposure errors [24, 25, 26, 27]. As mentioned in the previous section, some errors do not occur in laboratory settings. Additionally, some of these errors associated with exposure stem from complex interactions between the system and the environment and between multivariable changes in the environment. For this reason, in this dissertation, the errors caused by environmental interactions, commonly labeled exposure errors, are reclassified as environmental interference errors. Given the wide variety of environmental interference sources and the extent of their impact on different categories of atmospheric measurement systems, this new category can be further divided into external and internal environmental interference errors.

The principal motivation for this distinction is that, in practice, even well-designed systems sometimes encounter conditions in which they fail despite the designers' best efforts. A great visual representation of this concept is the external environmental interference example shown in Fig. 2.1. In this case, the mesonet tower system employs a cup anemometer sensor that complies with the World Meteorological Organization's exposure recommendations [35], and had its reported wind speeds slowed and then stopped by severe ice accretion during an ice storm from January 28 to 30, 2002. Other less obvious examples of external environmental interference include cases where Supercooled Liquid Droplets (SLD) come in contact with radiosonde sensors mid-profile [36], and angle-dependent solar radiation heating affects WxUAS temperature sensors [37].

Internal environmental interference poses a considerable challenge for atmospheric observations because it may stem from multiple causes, some of which may be unknown. For example, an optical carbon dioxide sensor may yield erroneous readings in a high-humidity



Figure 2.1: Example of environmental interference, a frozen cup anemometer at the Kingfisher Oklahoma Mesonet tower after the ice storm of January 28-30, 2002. Photo by Chris Fiebrich.

environment due to the spectral similarities of water vapor and carbon dioxide. The same sensor may also produce inaccurate measurements in low-pressure environments as a result of inadequate sample volume compensation for the new gas density. To address this type of error, new systems need to be evaluated in their operational environments, and system units must also undergo a field calibration in their specific deployment conditions [34].

As the category name implies, both types of interferences are naturally occurring, and system deployment conditions mostly determine the extent of their impact. In some cases, environmental interference errors can be mitigated by effectively designed sensor shielding, sample conditioning, and algorithmic compensation [8, 34]. However, in other cases, environmental interference must be considered an operational limitation, and atmospheric observations must be deemed invalid when the system cannot perform within 95% of its

specified characteristics [26].

Given the complexity of environmental interference errors, design-based mitigation strategies may introduce new interference sources. For example, relative humidity sensors deployed in ground-based systems (e.g., weather stations and towers) often employ a microporous filter to prevent dust accumulation on its sensing element, an external environmental interference source. However, laboratory results indicate that, although moisture can permeate these filters quickly through advection, temperature changes inside the filter occur at a slower rate through conduction. This difference in the rate of change between the two variables creates a micro-climate inside the filter that no longer represents the surrounding atmosphere. Consequently, this departure from accurate representation leads to errors in relative humidity measurements [38]. This example illustrates how a mitigation strategy for an external environmental interference error can result in an inadvertent internal environmental interference error.

The previous example also underscores how system application determines the extent of the impact of certain errors. For instance, in climatological studies, sampling rates are usually ingested on hourly or daily scales. In these cases, microporous-induced relative humidity errors can be diminished by downsampling the data via averaging (e.g., taking 1-minute to 1-hour data by averaging sixty 1-minute samples). This technique is also known as integrative sampling [26]. This example further highlights the reciprocal relationship between system design and its application, wherein certain design features may constrain operational capabilities while application-driven requirements influence design considerations.

Based on the aforementioned discussions, it is evident that designing atmospheric measurement systems presents complex and challenging tasks. This process is intricately guided by the physical properties of the desired measurand and sensing elements, technology availability, funding, target data application, and operational conditions. This complexity further motivates the need for system-wide characterization and calibration during development and the employment of data quality throughout the system's lifecycle.

Reliable measurements require consistent procedures for quality assurance and control. Quality assurance starts before the first measurements. It begins with the definition of range, spatiotemporal resolution, and accuracy of the desired data. The system is then tested and calibrated in controlled environments before field deployment. In the case of a network, the systems deployed at distinct locations should be tested simultaneously in a representative location. This ensures that differing results can be later interpreted as spatial differences and gradients. Finally, the quality assurance concludes or repeats itself at the end of the field deployment or during cyclical maintenance periods. This allows for drift errors to be detected [26].

Quality control procedures consist of proactive measures during the data collection period. Some examples of quality control techniques include but are not limited to the detection of instrument/sensor failure, internal consistency of colocated sensors, and expected result checks based on the bounds of physical laws. For example, the absolute moisture content cannot exceed a certain temperature-dependent saturation level [26]. Thankfully, well-designed systems can have quality control procedures through automated tests.

In the American Meteorological Society's review of the past 100 years of atmospheric observations, the authors note that the integration of new observations into official forecast and decision-making systems is often slow. According to the authors, new atmospheric measurement systems are sometimes to blame. Often, new systems are developed in the silo of their driving application and do not employ the same rigor seen in data collection to their data distribution practices [28]. This lack of concern with data distribution during the system design phase produces a dampening effect in the broader measurement system development cycle because non-standardized, unvetted data sources can't be immediately inserted into forecasters' workflows. Therefore, as new observations overwhelm users, the societal drive for system development diminishes. Once assimilation middleware is developed and data becomes integrated, its societal benefit becomes evident again.

A notable example of this phenomenon is illustrated by the contrast between the conclu-

sions of the 1958 and 1998 National Research Council's reports. The former presents concerns with the excess push for new observations, citing the limited capability to use them. The latter concludes with concerns regarding the lack of measurement capabilities [28]. Therefore, novel systems should push boundaries and solve societal needs while producing data that is comparable with current and legacy systems and adhering to data distribution formats and standards. This is critical for the continuous advancement of atmospheric knowledge.

2.2.2 Integration of New Observations Into Forecast and Decision-Making Workflows

The segmented evolution of atmospheric measurement systems and networks presented a substantial hurdle in the distribution and assimilation of their data. However, in the past 30 years, a considerable effort has been made to drive the atmospheric sciences community toward standardized data formats, open solutions, shared workflows, and data aggregation practices [39, 40, 41, 42]. These efforts are crucial because weather data is critical for decision-making across several societal areas. Moreover, economic growth and geographical expansion drive weather data needs toward extended coverage and higher resolution.

One example of this need is the integration of AAM aircraft into the NAS. Given the absence of a human to evaluate hazardous conditions on board, these operations will simultaneously require data with spatial coverage scales similar to traditional aviation (i.e., CONUS-wide) and high spatiotemporal resolution similar to local networks (i.e., minutes and hundreds of meters). Therefore, support for these operations will likely come from weather data aggregation systems such as the Multi-Radar Multi-Sensor System (MRMS), CIP/FIP, and TAIWIN. Besides aggregating weather information from multiple sources, these systems blend observations, inferences, and forecasts into an actionable product and offer invaluable support to weather-based decision-making.

Although the abovementioned efforts have steered the community in a fruitful direction, the integration of new observation systems and networks into forecast and decision-making

workflows is still slow [28]. Part of the reason for this slow integration process is the high entry barrier for third-party weather data providers into the workflow of federal agencies (e.g., NWS and FAA). This high entry barrier is understandable, considering these agencies' roles in decision-making and public safety. However, the other reason is the systemic ambiguity in weather data. This ambiguity is attributable to several factors, including the inherent complexity of atmospheric structures, the decentralization of weather management amongst governmental agencies, and the wide variety of measurement technologies in use.

The complexity of atmospheric structures creates a need to divide their study into more accessible areas (e.g., hydrology, cloud physics, and atmospheric chemistry). However, the natural overlap of these areas of study can create ambiguity in the characterization of atmospheric structures. This occurs because each area of study attempts to characterize shared atmospheric features through the observations of different atmospheric parameters. For example, a field experiment studying potential temperature and aerosol dispersion in Tarong, Queensland (AU) demonstrated how these two parameters produced differing results for the depth of the planetary boundary layer [43].

A similar example is found in a study comparing the results of different Large Eddy Simulation (LES) implementations. In this study, the authors show that while variables such as mean virtual potential temperature, resolved temperature variance, and vertical kinematic heat flux show agreement between each LES implementation, the characterization of the Planetary Boundary Layer (PBL) depth given by each variable shows considerable disagreement in all models [44]. Both examples illustrate how atmospheric feature characterization is highly dependent on the observed parameter. Consequently, the observed parameters can greatly influence decision-making based on the intensity and extent of a weather event or atmospheric feature.

Understanding the abovementioned relationship between observed parameters, feature characterization, and decision-making is important because when different governmental agencies fund, implement, and manage atmospheric observation networks, their application

bias directly impacts how features and phenomena are reported. A study investigating Snow (SN) mixed with Freezing fog (FZFG) events reported in ASOS-based METARs provides a quintessential example of this issue. This study shows that two ASOS, 6.5 miles apart, operated by two agencies, produced differing FZFG METARs 99.5% of the time over a 22-year interval. Upon further investigation, it was found that the over-reporting ASOS was wrong more than 90% of the time [45]. However, these errors were not observation errors. They were caused by the managing agency's rules for FZFG inference. This reporting distinction severely impacts commercial aviation operations because it informs decisions regarding the amounts and compositions of fluids used in ground de-icing operations. Consequently, impacting holdover times and operational safety.

Although standardized data formats facilitate data-sharing across measurement systems and networks, the wide variety of measurement technologies in use creates ambiguity within this standard. This occurs because the observation context is critical for data interpretation [25, 26]. For this reason, the World Meteorological Organization (WMO) stresses the importance of sharing metadata and is working on a standard for key observations [35]. This is critical for the integration of new observations into forecast and decision-making workflows because standards help eliminate or minimize measurement differences between measurement methods, exposure, and other factors, allowing for data comparison and phenomenon tracking across different measurement sites [27].

2.2.3 Integration of WxUAS Data Into Forecast and Decision-Making Workflows

When new measurement systems are introduced, it is essential that their data is evaluated in comparison to data from established systems. If a new system replaces an existing system, additional comparability steps are required to ensure time series continuity. This process should not result in the degradation of good measurements generated by the improved systems in order to make them compatible with the poorer measurements of an existing system

[35]. As a new entrant in the low-altitude weather observation field, WxUAS have been thoroughly compared to existing systems [2, 37, 46]. However, the spatiotemporal resolution of WxUAS data and its flexibility in sampling patterns are unique, and data assimilation requires new methods. For this reason, several studies are evaluating how this new measurement tool can support forecast and decision-making workflows [47, 48, 49, 50]. Nonetheless, the integration of WxUAS data faces similar challenges as the ones discussed in Section 2.2.2.

Similarly to other atmospheric measurement systems, WxUAS development has also been historically linked to societal needs and applications. The diverse requirements of these different weather applications produced many interesting technological advancements in the field. However, this diversity has also created low cohesion of measurement outputs between systems, as shown by the large intercomparison study in support of the LAPSE-RATE field campaign [51]. The bias towards specific applications in WxUAS development appears to exacerbate this issue. Even when focusing on the same atmospheric variables, choices in system design have led to significant divergence in outcomes [37, 46].

WxUAS's supporting role in the safe introduction of AAM aircraft into the NAS has motivated the creation of standardization groups, such as the ASTM F38. This group is developing performance-based standards for low-altitude observation for Supplemental Data Service Providers (SDSPs). SDSPs' weather data is intended to extend coverage and increase the resolution in support of weather-based path planning for Unmanned Traffic Management (UTM). Although standardization efforts such as these could help bring cohesion to WxUAS, this effort's very clear application can bring with it some of the application bias issues previously discussed. Nonetheless, to implement this standard, new WxUAS must overcome three critical design factors: sensor integration, vehicle interference, and system operation. The following section details these and other WxUAS design considerations.

2.3 WxUAS Design Challenges

As previously discussed, designing atmospheric measurement systems is a complex and challenging task. Designing systems for airborne in-situ atmospheric measurement adds another layer of difficulty to this challenge due to the motion of the measurement platform, its interaction with the sampling environment, and the increased exposure to environmental interference errors (see Section 2.2.1 for details). This section presents a review of how these challenges impact WxUAS design and limit its operations.

2.3.1 System Operation

The diverse requirements of different weather applications directly influenced WxUAS design, producing a wide variety of system sizes, shapes, and flight capabilities. Nonetheless, these can still generally be described as fixed— and rotary-wing WxUAS, which reasonably indicates their expected sampling patterns. Although both types can perform either transects or profiles (see Section 2.1), their operational limitations may influence how their observations can be interpreted. For this reason, incorporating the system's operational limitations into a well-designed flight plan is a critical step within WxUAS measurements.

For instance, in some applications, the flight speeds required to maintain the assumption of an "instantaneous" representation of a rapidly evolving phenomenon may degrade the accuracy of the observations [52]. Simulations have shown that observation errors of atmospheric features with strong gradients scale with flight speed and the system's time response [53]. Although post-processing algorithms are capable of correcting some time response errors, they only work within the speed limit that allows the system to detect these strong gradients [54].

The abovementioned simulation study indicates that in WxUAS-based profiles, the maximum errors for temperature measurements are less than the typically reported sensor accuracy (i.e., $\pm 0.5\,^{\circ}\mathrm{C}$), as long as ascent rates are less than $10\,\mathrm{m\,s^{-1}}$ and the system's time

response is less than 5 s. For transects, the study has shown maximum errors smaller than or equal to $\pm 0.5\,^{\circ}\mathrm{C}$ for flight speeds less than $10\,\mathrm{m\,s^{-1}}$ and system time response less than 1.5 s [53]. Field experiments and statistical analysis corroborate these simulated results and further detail the recommendations for vertical sampling.

For temperature measurements, the recommended ascent rates are $5\,\mathrm{m\,s^{-1}}$, prior to atmospheric mixing, and $3\,\mathrm{m\,s^{-1}}$ once mixing has occurred. For humidity measurements, due to typically slower response sensors, the recommended ascent rate is $2\,\mathrm{m\,s^{-1}}$ [2, 37, 46, 55, 56]. When following the above recommendations, systems with time responses of 1 s (for temperature) and 4 s (for humidity) have shown to be capable of capturing mesoscale and microscale boundary-layer phenomena such as convective thermals, well-mixed boundary layers, and airmass boundaries [52].

Other WxUAS challenges associated with the system's operations are more nuanced. For example, ground-influenced heating (between flights) can be "transported" to the lower layers of the atmosphere because the system's time response from motors-off to full-flight may be greater than its average full-flight time response. This potential source of error may require the aircraft to be flown near the ground to allow the aircraft to reach its full-flight equilibrium with the atmosphere before the profiling commences [57].

Additionally, flight speed, system hysteresis, and sensor integration choices directly restrict the orientation a feature should be sampled. For example, when attempting to characterize the depth and height of atmospheric layers, the abovementioned variables may produce a smearing effect on the sampling data. When the sampling is performed during the system's ascent to the profile top, this smearing effect tends to position the sampled layers further from the ground. When performed during decent, this smearing effect tends to report the layer heights closer to the ground [57, 58].

For these reasons, considerations regarding WxUAS deployment methods and operational conditions must have a greater weight in WxUAS design than in the design of traditional ground-based atmospheric measurement systems. Therefore, WxUAS design, particularly

sensor integration, must consider all the challenges discussed in Section 2.2.1 in conjunction with its specific challenges and operational limitations, to produce meaningful measurements that lead to insight into low-altitude atmospheric phenomena.

2.3.2 Sensor Integration

As defined in Section 2.1, an unmanned aerial weather measurement system (Fig. 2.2 A, C-E) is not the same as a UAV that carries a weather sampling payload (Fig. 2.2 B). By definition, the critical difference between the two is the integration aspect of weather sensors into a WxUAS. Two principles guide this integration process: the software integration that allows the WxUAS to adjust its task execution based on sensing the environment and the physical integration that maximizes sensor exposure while minimizing environmental interference sources (see Section 2.2.1) and platform interference.

2.3.2.1 Software Integration

Within WxUAS, software integration of weather sensors is still in its infancy, with very few academic papers describing this type of effort [8, 34, 59, 60]. This is, in part, explained by the evolutionary process of WxUAS. This research field started with exploratory experiments using remotely piloted aircraft as a platform to transport sensors through the atmospheric boundary layer [61]. Once initial exploration demonstrated the value of these observations, UAV-based weather measurement development was mostly focused on mitigating physical integration issues and evaluating measurement performance against well-established measurement systems (e.g., radiosondes) [1, 2, 51].

Through this period, most of the weather data collection was performed with the assistance of secondary single-board computers or even microcontroller development boards (e.g., Arduinos) [57, 58, 62]. These secondary data recording mechanisms created additional issues when merging measurement files with aircraft flight logs to create the spatiotemporal distribution of the atmospheric measurands. In addition to data post-processing issues,

secondary data recording mechanisms hinder UAV performance due to the increased weight and power requirements. For this reason, the initial software integration efforts were mostly focused on weight reduction and real-time data transmission to ground-station computers and data-cloud services [8, 34, 59].

With the advent of software integration into the flight controller and considerable physical integration characterization, UAV-based atmospheric measurements were transformed into unmanned aerial weather measurement systems. With the advent of WxUAS, adaptive sampling and new operational strategies became possible. However, given the necessity to compare WxUAS measurements to well-established systems, the initial weather-based adaptations to task executions were limited to minor adjustments to preprogrammed paths. For example, facing the vehicle or sensor payload towards the incoming wind to increase accuracy while doing a profile or transect (i.e., Wind-vaning) [59].

Additionally, efforts in flight control software development for weather applications also unlocked the ability to transform a vehicle frame into a weather sensor. Leveraging the aircraft's GPS and Inertial Measurement Unit (IMU), new flight control subroutines can be used to measure wind speed, direction, and, in some multi-vehicle applications, turbulence [60, 63].

As WxUAS matures as an alternative for high-resolution sampling in the lower atmosphere and its data gains broader adoption, new observational needs drive WxUAS capability development, many of them enabled by software integration. In Chapter 5, we offer an example of how weather sensing can be used for autonomous trajectory decisions, allowing WxUAS to trace hydrometeor fall paths and correct potential erroneous assumptions in processing radiosonde data.

2.3.2.2 Physical Integration

In addition to the ability to adjust its task execution based on environmental cues, the measurement quality aspect of sensor integration is another defining characteristic of WxUAS.

This assertion stems from the inherent disruption any in-situ measurement platform introduces to its environment [26]. Thus, physical integration techniques serve as the means to maximize sensor exposure while minimizing environmental interference sources and platform interference.

Many of the sampling challenges found in WxUAS have been present for years in manned aircraft and balloon-based measurements. This occurs because all three platforms share common sensors, and their data can be assimilated under similar spatiotemporal assumptions [37, 64, 65]. These similarities allow the adoption of some successful error mitigation strategies developed for other airborne platforms in WxUAS research. However, WxUAS's unique flight characteristics and reduced SWaP create WxUAS-specific challenges.

An ideal WxUAS would not interfere with its measurement environment, and its sensing payload would be considered decoupled, allowing it to be characterized independently from the vehicle. However, even the best system designs still present some degree of interference caused by the aerial vehicle. Therefore, the most important elements of physical sensor integration are contaminant shielding, airflow, and placement. For this reason, this section discusses physical integration issues from the perspective of the complete system and its operational conditions (i.e., vehicle, sensors, shields, sample conditioning techniques, flight pattern, and sampling environment).

As with any atmospheric measurement system, the sensors on a WxUAS require maximum exposure to ensure they truly measure the environment. However, the WxUAS's dynamic flight characteristics introduce additional sources of external environmental interference. One significant challenge lies in designing solar radiation shielding that effectively eliminates direct exposure from a multitude of angles without inadvertently introducing internal environmental interference errors (as seen in Section 2.2.1). In some cases, solar radiation can heat the shielding material and generate errors up to 1 °C in temperature measurements [37, 46]. To mitigate this problem, external shields can be designed with two layers, where solar radiation only affects the outer shield, and the inner shield is isolated via

natural airflow [8].

Other solutions are internal shields, integrated inside the main fuselage [37], and external shields built with low thermal mass material and reflective paint [54]. Sensor shield designs must also consider precipitation, as accumulated droplets may produce artificial wet-bulbing [54]. This concern is more common for winter weather research applications but should also be accounted for in any technology used for year-round nationwide mesoscale measurements. In contrast, the intermittent nature of WxUAS sampling allows the reduction of exposure to solar heating, precipitation cooling, and other external environmental interference sources by removing the system from the sampling environment between flights [32].

Another important aspect to consider during sensor shield design is self-contamination. This is particularly true for temperature and relative humidity measurements because a UAV generates considerable heat in its motors, propeller tips (frictional and compressional heating from turbulent fluctuations), LiPO batteries, and the thermal mass of the airframe [2, 37, 46, 53, 54, 61, 66, 67, 68]. Besides an effective shield design, it is also imperative to choose an appropriate position relative to the heat sources on the aircraft to place the sensor payload [37, 46, 54, 66]. For improved chances of success, it is recommended to use computational fluid dynamics during the design phase [59] and later validate the built design using thermal imaging [66].

Sensor shielding is also important to protect the sensors from other external interference sources. Since WxUAS can be operated at any location, adverse take-off and landing conditions can expose the system to dust, dew, and deposited precipitation. Therefore, WxUAS design decisions must favor either system resilience (i.e., reduced sensor exposure) or system accuracy (i.e., increased sensor exposure). A compromise solution often adopted in WxUAS with active aspiration or flow-related sampling conditioning techniques involves halting airflow to sensors during take-off and landing. However, this approach requires discarding samples acquired within the first one or two meters off the ground [34, 59].

This exposure during takeoff and landing generally influences sensor physical integration

toward placement above the vehicle. However, this influence introduces an imbalance in sensor exposure to flows coming from above compared to airflow from below. In most cases, this introduces a system-level bias that can limit the system's operation to data acquisition only during the ascent portion of the flight. Without this limitation, top-mounted sensors can often produce ambiguous characterization of atmospheric features [57, 58].

Besides measurement errors induced by external heat sources, some sensors used in WxUAS also suffer from self-heating. On thermistors, for example, the electrical current through the sensitive element can produce readings of $0.5\,^{\circ}\mathrm{C}$ above the background temperature [46]. The most common way to mitigate this problem is to promote additional airflow over the sensors [2, 37, 46, 53, 54, 57, 66, 67]. Although empirical results have demonstrated acceptable accuracy with airflow over sensors of $3\,\mathrm{m\,s^{-1}}$, temperature sensor manufacturers still recommend airflow of at least $5\,\mathrm{m\,s^{-1}}$.

To achieve the desired flow rates, WxUAS can use active and passive techniques for aspiration or ventilation. Passive flow depends on the system's motion or the airflow produced by the system's propellers. In this method, airflow over the sensors varies with flight speed. Active airflow methods use a dedicated fan or pump that produces constant flow independent of flight speed. The distinction between aspirated and ventilated systems is given by the relative position of the flow generation mechanism. In aspirated systems, the fan, pump, or propeller is behind the sensors. Air flows through the sensors before reaching the aspiration source.

The various flow control methods, sensor shielding designs, and airframes produced a wide variety of WxUAS designs. Each of them exhibits a set of design choices based on their application-specific optimum point in the resiliency and accuracy trade-off scale. Figure 2.2 illustrates a few of them. Nonetheless, for all of them, it is recommended to ensure the sensing payload always faces the incoming wind because the heat sources on the aircraft will alter the air immediately near it [37, 46, 54, 66].

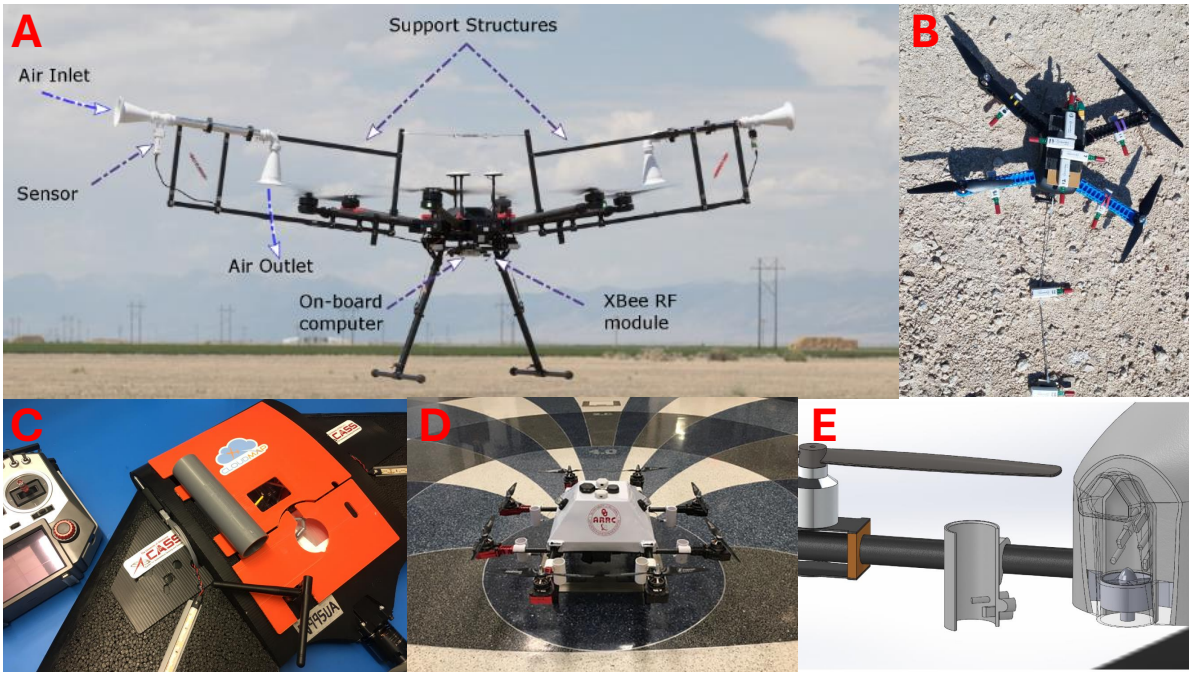


Figure 2.2: Examples of physical sensor integration into UAS: (A) Omnidirectional shielded integration with propeller-based passive aspiration [54]; (B) No shielding with partial propeller-based, passive ventilation [66]; (C) Fixed-wing two-layer shielding with passive ventilation through vehicle motion [8]; (D) Multi-direction with partial shielding and propeller-based ventilation [46]; (E) Comparison of directional shield with active aspiration with partial shielding and propeller-based ventilation [37].

As mentioned before, some designs use the airflow produced by the aircraft propellers (e.g., Fig. 2.2 A, B, D, and E). However, this strategy must be used with caution, as proximity to the motor or the propeller tips can induce errors. For this reason, sensor shields using rotor-wash passive ventilation (under the propeller, Fig. 2.2 B, D, and E) must be placed at a third of the distance between the propeller tip and the motor [46]. Rotor-wash passive aspiration (above the propeller, Fig. 2.2 A) is less sensitive to placement because it utilizes the pressure deficit to promote flow from the shield to the propellers [54].

Proponents of propeller-based passive aspiration argue this method reduces the aircraft's weight and optimizes battery usage. However, recent experiments showed that active aspiration (via a dedicated fan inside the sensor shield, Fig. 2.2 E - center) did not hinder the aircraft's endurance. Direct aspiration proponents raise concerns regarding the potential

negative impact of varying aspiration rates present in rotor-wash passive aspiration [37].

The numerous possibilities of platform interference on in-situ sUAS-based measurements make designing a platform-decoupled sensor package unrealistic. Recent experiments have shown that sensor characterization techniques, such as oil bath step functions, are not enough to correct time response errors in sUAS-based measurements [54]. Consequently, there is growing support in the literature for system-level characterizations of accuracy, time response, and other parameters [52, 53, 54, 56, 58, 62, 65, 67, 68].

Among all characterization parameters, time response may be the one where system-level characterization is the most important. This assertion stems from delays that may be introduced by flow control systems in sensor shields and the recirculation induced by propeller wash, which can create a system time response that is larger than the sensor's. Systems with inadequate time response are incapable of resolving fine-scale changes and cause undesirable spatial "smoothing" of atmospheric structural parameters [52, 54, 65]. One example of "smoothing", sometimes called gradient dampening, is the misrepresentation of the height of the PBL [57]. This misrepresentation can negatively impact convection inhibition studies and consequently severe storm research [69].

The sensor integration issues discussed in the section represent a concise overview of the challenges that impact WxUAS design. Many other issues in application-specific contexts may also hinder WxUAS design and measurements. However, they are not the focus of this chapter. Chapter 3 will discuss the specific issues faced when designing an unmanned aerial weather measurement system capable of sampling the low-altitude wintry precipitation environment, including mix-phased and freezing precipitation.

Chapter 3

In-Situ Measurement Design

"Automated instrumentation is used to make measurements that humans cannot, for reasons of safety, cost, or performance (speed or accuracy for example), and the instrumentation must deliver data to the user. Therefore, all measurement systems must be viewed as extensions of the human who wishes to use the data."

Fred V. Brock and Scott J. Richardson

In near 0 °C environments, radar reflectivity distributions of rain, snow, freezing rain, ice pellets, drizzle, and freezing drizzle can span a 30 dB range and produce overlapping results across light, moderate, and heavy precipitation scenarios [3]. Therefore, information regarding the atmosphere's thermodynamic profile is critical for hydrometeor classification and hazard assessments [14, 21]. The current operational observation system for this information is the radiosonde network. However, radiosonde soundings are only available twice daily, resulting in a temporal observation gap larger than the temporal scales of many wintry precipitation events.

In addition to the low temporal resolution, radiosondes have a sensor exposure issue that

hinders their use in wintry precipitation studies. Due to weight considerations and their disposable nature, radiosondes deploy fully exposed sensors and leverage airflow induced by the system's motion through the air. This design produces satisfactory measurements in most environmental conditions. However, during freezing precipitation events, sensors can be struck by supercooled drops, resulting in encapsulation in ice. This encapsulation produces errors in portions of radiosonde-based atmospheric profiles [1, 36]. The low temporal resolution and potential freezing bias of the radiosonde network lead developers of radar-based hydrometeor classification models to rely on numerically generated soundings and radar data inferences [3, 12].

In light of the aforementioned considerations, this dissertation endeavors to develop and validate an innovative WxUAS in-situ sampling technique for measurements in the low-altitude wintry precipitation environment as part of a broader WxUAS solution to provide insight into atmospheric mechanisms that govern it. However, as expounded upon in Chapter 2, designing WxUAS measurements is challenging because it can introduce layer mixing (particularly in multirotors) and heat from motors, batteries, and other sources. Given that precipitation phase can be affected by temperature variations as small as 0.5 °C, meticulous attention to sensor shielding, placement, and sample conditioning are critical for measurement accuracy [34, 46, 52, 53].

To account for all these requirements, a WxUAS sensor shield design must be able to expose the sensors to atmospheric conditions (e.g., temperature, moisture, and cloud size particles) without exposing them to large precipitation droplets. Although designs in other atmospheric measurement systems account for precipitation, they do not account for the previously discussed WxUAS-specific challenges (e.g., varying tilt angles and relative position). Therefore, this dissertation presents a design proposal that leverages gravity to mechanically separate large precipitation droplets from the air while accounting for other WxUAS-specific challenges (Figs. 3.1 and 3.2).

3.1 Sensor Shield

As previously stated, this dissertation aims to provide insight into atmospheric mechanisms that govern the low-altitude wintry precipitation environment, particularly in mixed-phased precipitation events that lead to ambiguity and uncertainty in forecast and hazard assessment products. To attain this goal, the proposed WxUAS focuses on temperature, relative humidity, cloud size particle distribution, precipitation reflectivity, and Doppler velocity. These variables were selected because they can directly reduce ambiguity in other remote measurements, provide understating of a large body of weather phenomena, and have SWaP characteristics in accordance with UAS limitations. This chapter focuses on the in-situ temperature, relative humidity, and cloud-sized particle distribution measurements.

In the wintry precipitation environment, temperature measurements allow for understanding how temperature changes with height impact precipitation as it falls. More specifically, temperature profiles allow the height and depth of freezing and melting layers to be determined, resolving the precipitation phase observed at the surface. Relative humidity profiles indicate the amount of moisture the atmosphere can absorb before becoming saturated. Additionally, repeated relative humidity profiles allow the understanding of how certain atmospheric transport mechanisms change the atmospheric structure over time. Finally, the amounts and sizes (i.e., distribution) of low-altitude cloud particles can inform about precipitation generation layers that form below radar coverage and operation visibility for low-level flights. The combined spatiotemporal evolution of these parameters helps elucidate the hazards produced by certain winter storms and their expected impacts on the surface.

The sensors for these measurements are extremely sensitive to external environmental interferences (see Chapter 2) and require careful sample conditioning for accurate and precise measurements. To reduce the impact of measurement interference sources, the proposed sensor shield employs a cylindrical two-layer solution that optimizes flow conditions over the sensors (Figs. 3.1 and 3.2). It shelters three bead thermistors, two capacitive hygrometers,

and one optical particle counter. Leveraging the concentric cylindrical solution, the sensors are symmetrically placed around the inner shield's perimeter, equidistantly from the center point of a constant flow (greater than $5\,\mathrm{m\,s^{-1}}$). This constant flow is produced by a dedicated aspiration fan. The sensor ring is strategically placed at 2-diameter lengths from the aspiration fan and the inner shield's intake (see Fig. 3.3).

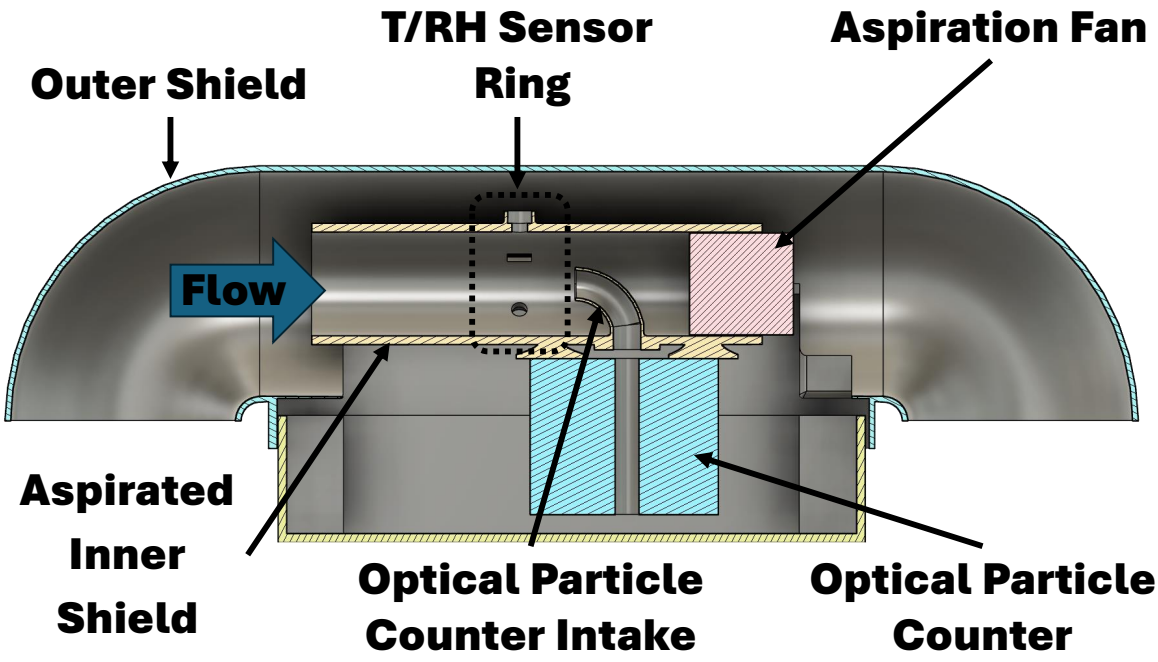


Figure 3.1: Lateral cross-section of the two-layer custom sensor shield designed to prevent contact with freezing precipitation while allowing for direct atmospheric observation.

The outer shield is a passive protection layer that guards the inner shield from direct contact with precipitation and sunlight, even through the many angle variations that occur during a WxUAS flight. This is possible because the outer shield's intake extends over the inner shield's intake and curves downward, prolonging in this new direction. As mentioned, only the inner shield is aspirated. This design feature lessens the degree of turbulent heating in the outer shield. Additionally, the outer shield's diameter is twice as large as the inner shield's diameter. The resultant air gap insulates the sensor ring from radiative and sensible heat fluxes and impinging water and snow.

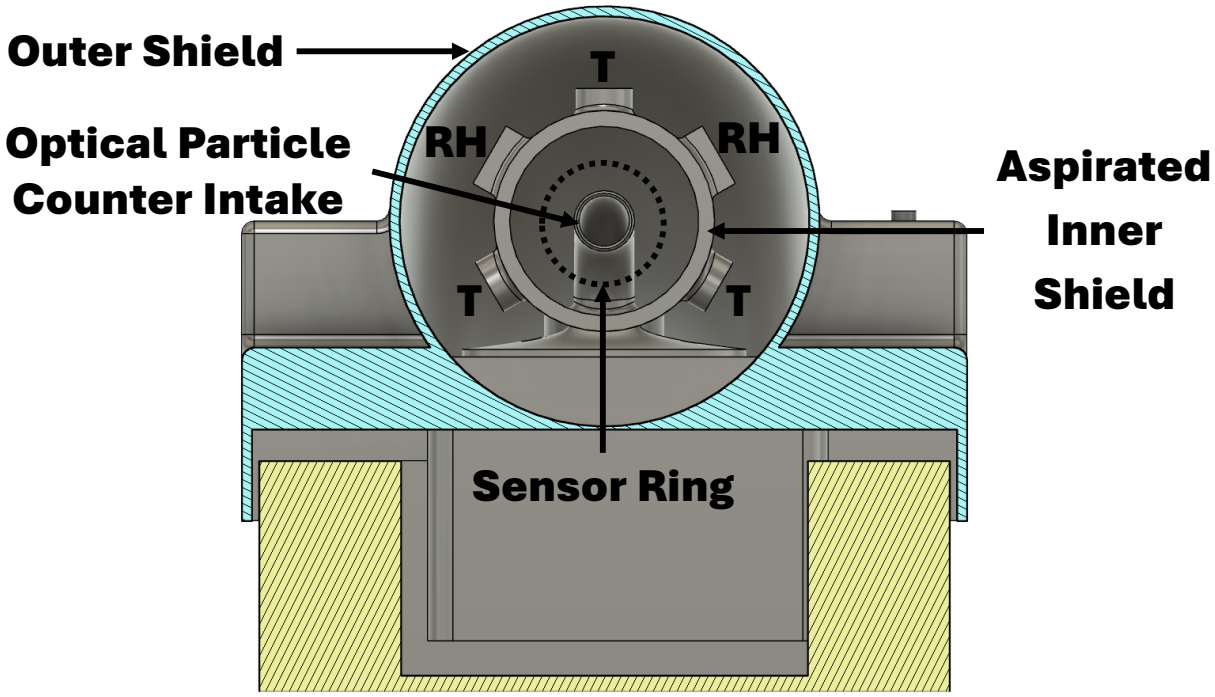


Figure 3.2: Frontal cross-section view of the two-layer custom sensor shield designed to prevent contact with freezing precipitation while allowing for direct atmospheric observation.

Due to its shape, this design can leverage gravity to mechanically separate large precipitation drops from the air. This separation occurs because larger droplets will be dominated by their inertia while small droplets will follow the streamlines on the intake system according to Stokes flow. This flow characteristic allows the system to sample the atmospheric conditions without exposure to harmful freezing precipitation and other external interference sources.

The aspiration rate and interior sensor shield's diameter produce a flow with an approximate Reynolds number of 10,000. This Reynolds number and the two-diameter distance between the sensor ring and the inner shield's intake ensure the sensors have a consistent flow profile due to a well-mixed flow that is sampled beyond the entrance length (see Fig. 3.3). The Weber numbers for the objective particles at the flow rate range from 3 to 7. These low spectrum numbers denote the minimal presence of droplets smearing and separating within the inner shield.

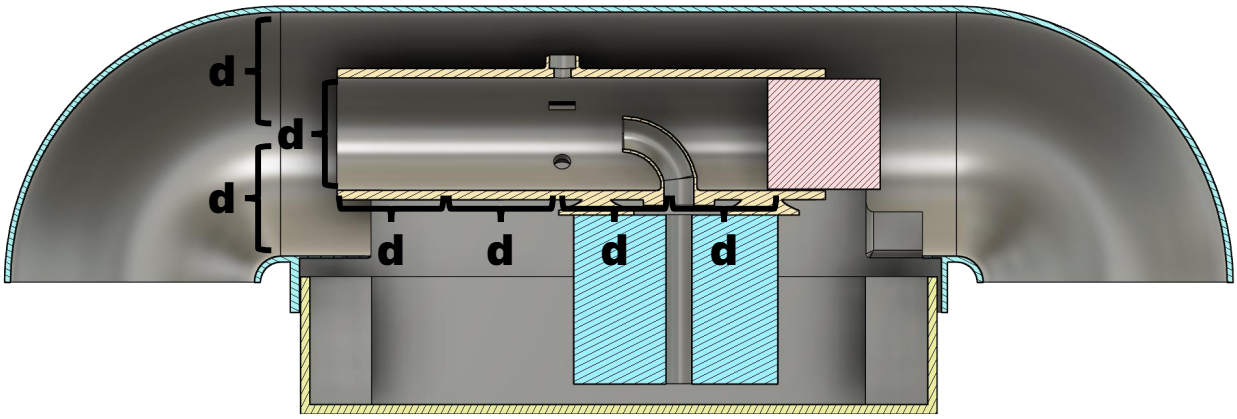


Figure 3.3: Lateral cross-section view of the two-layer custom sensor shield design highlighting construction dimensions that enhance flow characteristics, where "d" is the diameter of the inner shield.

The abovementioned flow characteristics assume a shield placement on the vehicle's topside, away from vehicle-generated interference sources. At this point, vehicle-specific characterization will not be discussed because this is a cross-platform solution. This solution's portability is possible because the two-layered solution covers various flight angles and relative intake flows, and the sensors are directly integrated into a multiplatform flight control software framework. The details of this software integration are among the topics covered in the following section.

3.2 Sensors and Sampling Techniques

As depicted in Fig. 3.2, the proposed sensor shield houses one optical particle counter (OPC) and three temperature and two relative humidity sensors. The OPC is the AlphaSense N3 model. The temperature sensors are Platinum-based bead thermistors with a 100 Ω resis-

tance at 0 °C (PT-100), combined with a 16-bit ADS1115 ADC, manufactured by Texas Instruments. The bead thermistor and ADC are combined and sold as a temperature sensor by InterMet Systems (iMet). The relative humidity sensors are HYT 271 modules manufactured by Innovative Sensing Technologies. In addition to these sensors, the WxUAS's flight controller has a built-in MS5611 digital barometer from TE Connectivity's Measurement Specialties Sensors. An illustration and the sensor specifications are given by Fig. 3.4 and Table 3.1.

These sensors were selected based on their quality, resiliency, and low SWaP characteristics. Additionally, the pressure, temperature, and relative humidity sensors are widely adopted across the WxUAS research community and are present in a considerable number of commercial radiosonde solutions. The ubiquity of these sensors is important because it creates a baseline for measurement comparability between different WxUAS and radiosondes, allowing the study of WxUAS design and measurement quality.

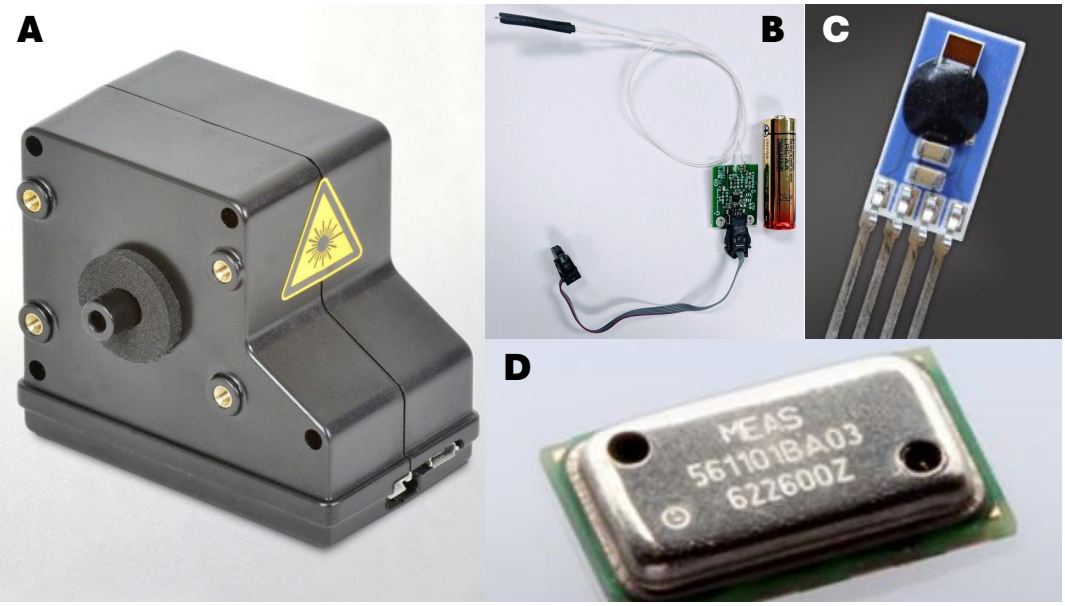


Figure 3.4: Sensors for in-situ measurements: (A) The OPC-N3 for particle size distribution, (B) the PT-100 bead thermistor and ADS1115 ADC for fast temperature; (C) the HYT 271 for slow temperature and relative humidity; and (D) the MS5611 for fast pressure measurements.

Sensor	Range	Accuracy	Time Resp. (t_{63})	Current [µA]	Dimension [mm]
MS5611	1 to 120 kPa	±1.5 kPa	1.7 ms	1	5 x 3 x 1
PT-100	−90 to 50 °C	±0.3 °C	1 s	150	30 x 15 x 3
HYT 271	0 to 100 %RH	±1.8 %RH	1 s	850	10.2 x 5.1 x 1.8
	−40 to 125 °C	±0.2 °C	5 s		
OPC-N3	0.35 to 40 µm	–	1 s	180 mA	75 x 64 x 60

Table 3.1: In-situ sensor specifications.

Leveraging the sensor shield's cylindrical design (Fig. 3.2) and a sensor redundancy strategy, a concentric sensor ring was created to increase the system's accuracy. As illustrated in Fig. 3.5, the inner shield's 360° is divided into six 60° slices. The five temperature and relative humidity sensors occupy the upper slices, and the OPC intake fills the lower slice. Moreover, this innovative concentric design ensures all sensors are under the same airflow conditions, which enables the evaluation of flow quality metrics and the implementation of measurement-quality-control and failure-and-recovery algorithms.

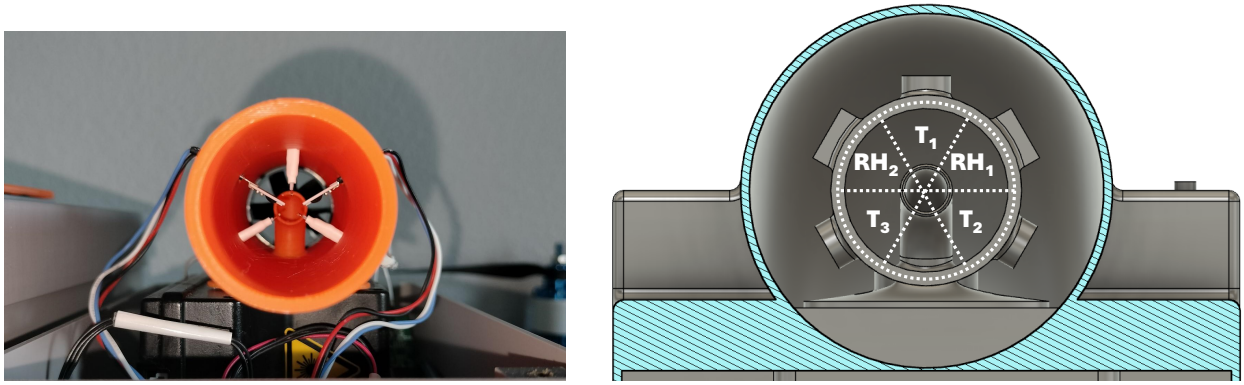


Figure 3.5: Concentric sensor ring with redundancy for increased accuracy. The right panel illustrates 60° segmentation strategy, and the left panel illustrates its implementation.

The temperature and relative humidity sensors inside the inner shield sample the atmosphere at 10 Hz, while the optical particle counter produces a distribution every second. The higher sampling rate of each thermistor and hygrometer allows for intra-sensor averaging,

where every ten samples within a second are averaged to produce higher quality samples at 1 Hz. This technique adds one digit of precision for each sensor, reducing noise and the effects of analog to digital quantization. A similar process is already implemented by the manufacturer on the OPC measurements to produce its 1 Hz data.

Following the intra-sensor averaging process, the temperature measurements from the individual sensors are combined to produce a single temperature measurement for the system. A similar multi-sensor averaging procedure is applied to the relative humidity sensors. However, before these system measurements are produced, the sensors' spatial distribution inside the inner shield is leveraged to evaluate sensor health and intake airflow quality. Each sensor is assessed individually and in comparison to neighboring sensors.

This approach facilitates the identification and removal of occasional sampling errors from the final multi-sensor system measurement. Additionally, persistent temporal bias in any individual sensor (e.g., drift) can also be identified, prompting a recalibration or replacement procedure. The neighboring sensor analysis validates the uniform flow assumptions that enable the multi-sensor average. Persistent regional bias detected through this analysis also triggers maintenance procedures. Supplementary system health investigations can be performed using the auxiliary temperature measurements available from the relative humidity sensors. This auxiliary method uses all five upper 60° portions of the inner shield, forming a higher resolution neighboring sensor analysis.

As an example of this enhanced neighboring sensor analysis, let's consider a profile flight to 200 m above ground level (AGL). In this flight, the ascent rate was $2.5\,\mathrm{m\,s^{-1}}$, which produces at least 80 measurements after the 1 Hz intra-sensor averaging. For the sake of conciseness, let's consider four instants to represent varied flight conditions that can produce airflow disturbances: take-off acceleration (at 2 m), developed flight 1 (at 70 m), developed flight 2 (at 130 m), and profile top deceleration (at 192 m). The choice to represent two developed flight stages accounts for potential wind gusts that can disturb the constant ascent assumptions and produce sharp aircraft angle changes.

Figure 3.6 graphically summarizes this example, illustrating the 1 Hz intra-sensor averaged temperatures at each flight stage for all temperature sensors (PT-100) and the auxiliary temperatures measured by the two relative humidity sensors (HYT 271). The temperature values are organized in the same 60° spatial orientation as depicted in Fig. 3.5 to clearly indicate the adjacent sensors (i.e., neighbors). The colors in each plot are part of an undepicted scale that allows for quick visual evaluation of the entire flight through an animation of the 80 (or more) measurement heights.

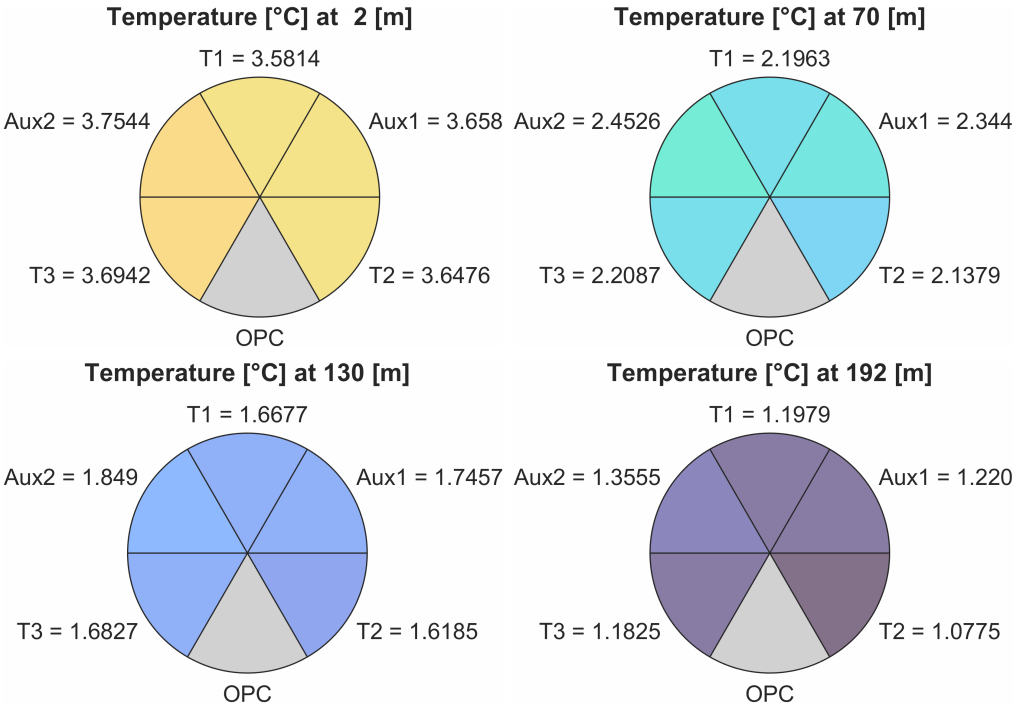


Figure 3.6: Example of enhanced neighboring sensor analysis showing temperature values for sensors across four stages of a profile to 200 m above ground level.

In this example profile, temperatures range from approximately 3.6 °C at the surface to 1.2 °C near 200 m AGL, providing an adequate amount of variation to perform this analysis. The first step in this analysis is to determine if the difference between maximum and minimum temperatures observed for each flight stage is below 0.5 °C, which is the minimum temperature difference for precipitation phase change. In this example, the differences are

0.173, 0.3147, 0.2305, and 0.278 °C. In this case, all flight stages show acceptable differences, indicating airflow through the sensors was consistent, and the sensors are healthy.

For the sake of continuing the analysis, let's assume a 0.3 °C threshold (the manufacturer's reported accuracy) and evaluate the 0.3147 °C difference seen in the "developed flight 1" stage (i.e., 70 m) as an example of a flagged discrepancy. This Max/Min temperature difference is given by a PT-100 temperature sensor (T_2) and a HYT 271 auxiliary temperature measurement (Aux_2). As a reminder, the HYT 271 auxiliary temperature measurements are not part of the system's final reported temperature. Evaluating only the three temperature sensors used for the system's reported value (T_1, T_2, and T_3), the Max/Min difference is reduced to 0.0708 °C, well bellow the acceptance threshold.

Considering that T_2 and Aux_2 are not adjacent, this discrepancy could indicate a regional airflow imbalance. However, this discrepancy only occurs in one out of the four flight stages, and the sensors involved are of different types. Therefore, this difference is more likely caused by the slower time response of the auxiliary temperature measurements, 5 Hz instead of 1 Hz (see Table 3.1). This conclusion is further corroborated by comparing the temperature difference in Aux_1 and Aux_2, 0.1086 °C, which are also not adjacent.

In addition, correlation coefficients are calculated for sensor pairs based on location (adjacent) and type. These coefficients, shown in Table 3.2, are calculated based on the data for the entire profile. Within a sensor type, coefficients are above 0.998, and within adjacent sensors (mixing types), coefficients are still above 0.98. These high correlations indicate overall sensor health and airflow consistency, enabling measurement assumptions that allow the multi-sensor average and increase the system's accuracy.

Although similar analyses can be manually performed in other atmospheric observation systems, this design's unique features give the analyses presented here an algorithmic characteristic that allows for their automation. The implementation of automated measurement-quality-control and failure-and-recovery algorithms allows these analyses to be performed on large bodies of data (e.g., for all flights in a multiday field campaign).

Sensors	T1	Aux1	T2	T3	Aux2
T1					
Aux1	0.9848				
T2	0.9983	0.9834			
T3	0.9979		0.9989		
Aux2	0.9870	0.9984		0.9809	

Table 3.2: Correlation coefficients for the five sensors in the manual neighboring sensor analysis.

The scalability of these automated measurement-quality-control and failure-and-recovery procedures, which are promoted by this innovative design, is a critical feature for any WxUAS with aspirations of broad adoption in operational workflows. Therefore, the design presented here is a meaningful contribution to atmospheric observations, serving as a roadmap for future implementations. More examples that further validate this design and the quality of its measurements are provided in Section 3.4.

3.3 Flight Control Integration

As discussed in Chapter 2, WxUAS comprises weather sensors integrated into a UAV specifically designed for measurement operations, which is characterized as a complete measurement system, accounting for the interactions between the sensors, the aircraft, and the measurement environment. In the same chapter, the UAS definition explains that sensor integration is a critical distinction between a vehicle payload and a new measurement system. Besides mitigating the vehicle's impact on the measurement, this integration allows the system to autonomously adapt to the sampling environment, optimizing the data collection.

Flight control integration can take two forms: an external computer managing the flight controller or via direct wiring and programming into the flight controller's microcontroller unit (MCU). Both methods have advantages and disadvantages. This section presents their distinctions as means to justify the implementation design choices in the proposed unmanned aerial weather measurement system for the low-altitude wintry precipitation environment.

An external processing unit has the advantage of higher computational power. In certain cases, the additional computational capability is a requirement to implement the desired autonomous adaptive behavior, such as vision-based navigation in GPS-denied environments. In this integration method, sensors are wired to the external computer, where their data is stored and processed. In most cases, the external computer is integrated into the flight controller via half-duplex serial communication. Through this communication line, the external processor can receive flight data (e.g., position, attitude, airspeed) and send back simple or complex flight commands. Examples of simple commands are "accelerate", "climb", and "yaw 30°". An example of a complex command is: "go to the next waypoint" (defining coordinates, altitude, and travel speed).

Although the additional computational power allows fast processing of complex algorithms onboard, the half-duplex serial communication can become a limiting factor in the system's reactiveness. The complementary hardware necessary for this integration method adds to the total system weight and power consumption, impacting flight endurance and resiliency. Some cases of poor integration via external computation also create separate navigation and sensor data files requiring post-flight reconciliation, which can lead to errors in the spatiotemporal results provided by the system.

Given the low computational requirements for the aforementioned sensors, the harshness of the low-altitude wintry precipitation environment, and the abovementioned integration drawbacks, the WxUAS solution proposed in this dissertation used the direct flight controller integration method. In this method, sensors must be directly wired to the available communication buses, and their processing, storage, and communication relay software codes must be compiled and flashed directly to the flight controller's MCU.

Although the direct integration method has the benefit of weight, power, and cost reduction, it requires a very steep learning curve for MCU programming. This method also has the added risk of total system failure due to poor programming causing slow processing loops and segmentation faults. To mitigate these issues and enable cross-platform bene-

fits, the proposed WxUAS adopted an open-source vehicle control software framework. The ArduPilot vehicle control framework was created in 2007 and is maintained by nearly 500 developers across the globe. Its source code repository[1] has over 41,000 commits.

As an autonomous vehicle control framework, ArduPilot encompasses a large variety of vehicles, ranging from aircraft to submarines. Figure 3.7 illustrates this architectural solution, highlighting how shared features are inherited by each vehicle class and how specific vehicles can be developed as implementations of classes. Through this software architecture, developers can expand the range of vehicle implementations via class extension and create minor vehicle modifications via parametrization of existing vehicles. ArduPilot is freely available to be downloaded and extended with a GPL3.0 license.

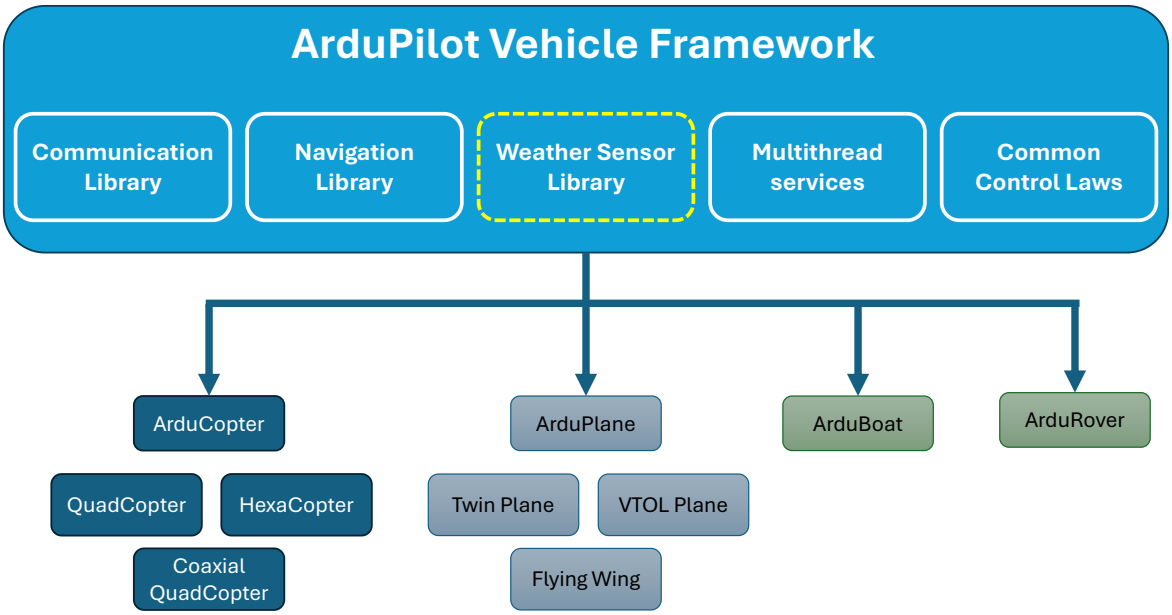


Figure 3.7: Diagram depicting the ArduPilot open-source vehicle control software framework with this dissertation's weather sensor integration library. This architectural solution enables the seamless and standardized cross-platform use of the proposed in-situ sensor design.

With the explicit intention of addressing the WxUAS standardization needs discussed in Chapter 2 and leveraging the framework's multi-thread infrastructure separating control

[1]https://github.com/ArduPilot/ardupilot

and service loops, this dissertation's direct sensor integration solution was implemented as a native library inside the ArduPilot autonomous vehicle framework. As highlighted by the dashed yellow line in Fig. 3.7, each vehicle class also inherits the autonomous vehicle weather sensor library, allowing for seamless and standardized cross-platform use of the in-situ sensor package design proposed in this chapter.

As part of the framework, the weather sensor library has direct access to all other framework libraries and services (e.g., navigation, communication, and multithreading). Access to the multithreading services enables the development of software strategies to mitigate the abovementioned direct integration risks. For example, as illustrated by Fig. 3.8, the weather sensor library can use the framework's service loop to communicate with the sensors, acquire new data, log the data to the onboard SD card, and stream live data to the ground station computer. Because these tasks are in a separate and lower-priority computational loop, errors and run-time exceptions within these tasks can not hinder the vehicle's control and operation.

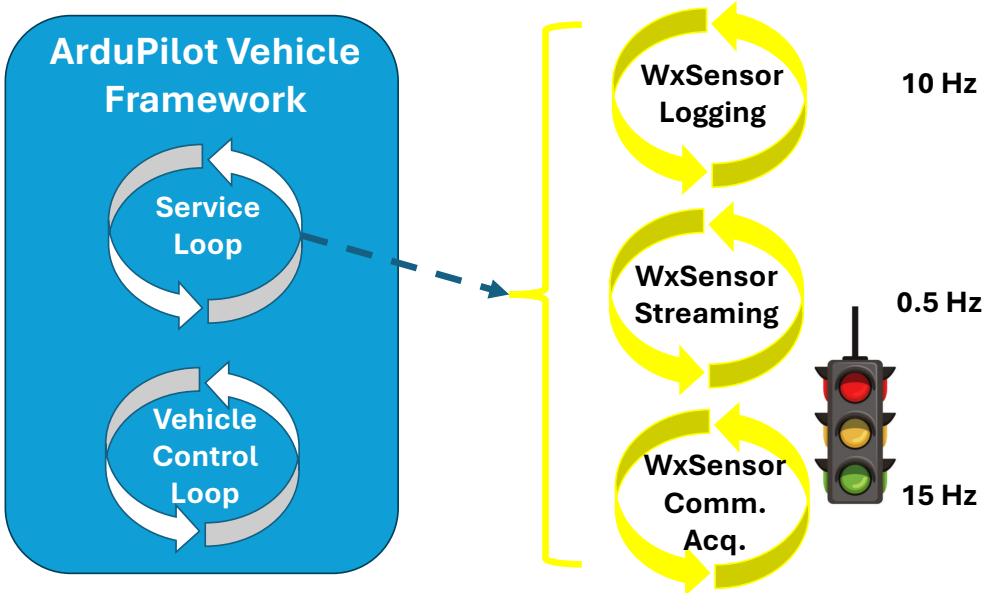


Figure 3.8: Diagram depicting the weather sensor library's use of the framework's service loop as a mitigation strategy for the risks associated with the direct integration method.

As also illustrated by Fig. 3.8, each of the tasks mentioned above is performed in asyn-

chronous sub-loops at different rates. This strategy ensures the sensor information is always updated while avoiding costly I/O routines and overwhelming the telemetry radio link. Additionally, this strategy divides the failure risks, creating opportunities for data recovery. To implement this strategy, the library submodule responsible for sensor communication and data acquisition uses the SPI and I^2C buses to request and collect data from the sensors. At a separate time, the logging submodule uses the framework's I/O library to save measurements into flight data SD card. Because each entry in the flight data SD card is associated with a time, position, and attitude, the sensor data in the SD card is automatically logged in a spatiotemporal representation. Finally, at a reduced rate, real-time data is transmitted to the ground station computer to provide system users with indications of atmospheric conditions during the flight.

Although the adopted sensors have 1 and 5 s time responses, sensor data is acquired at 15 Hz and logged at 10 Hz. The sensors' faster oversampling and slightly slower measurement logging (still one order of magnitude faster than the sensors' time response) ensure that any sensor step change is always captured. Repeated samples are naturally eliminated through the 1 s intra-sensor average mentioned in Section 3.2. To avoid errors associated with racing conditions, a semaphore is used in the sensor data acquisition submodule. To ensure data integrity, only the sensor data acquisition submodule has access to write on the sensor measurement variables. The remaining submodules have read-only access to the sensor measurements.

Besides eliminating redundant hardware (e.g., the external computer and sensor data streaming link), the direct integration method also enables adaptive sampling and other sensor-based autonomous decisions. To implement these features in alignment with the previously discussed direct integration risk mitigation strategies, the weather sensor library leverages its native state in the vehicle framework to safely provide inputs to the vehicle control loop through the framework's navigation library. This layered implementation through the framework's architecture separates sensor communication and processing from adjust-

ments to the flight and sampling patterns, ensuring minimum risk to the control loop and providing a safe development environment. Figure 3.9 illustrates this concept.

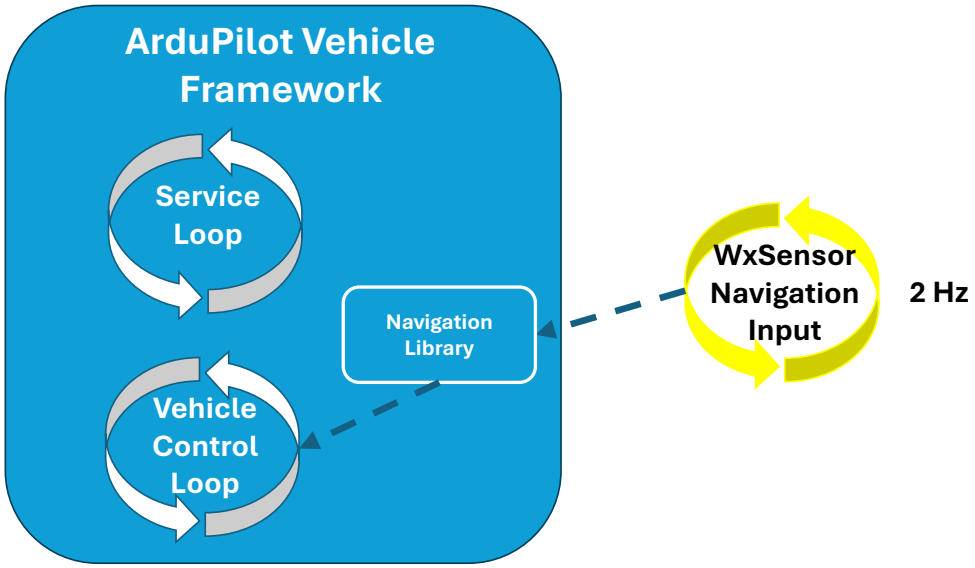


Figure 3.9: Diagram depicting the weather sensor library producing inputs to the control loop under the safety of the framework's navigation library.

The direct integration of weather sensors into the flight controller through an open-source vehicle control framework as a native library enables the seamless and standardized cross-platform use of the in-situ measurement design outlined in this chapter. Figure 3.10 presents a few examples of WxUAS in which the proposed design was deployed during this dissertation's research phase. These examples include a fixed-wing vehicle utilizing the weather sensor library via the ArduPlane class, as well as three rotary-wing vehicles incorporating the proposed in-situ hardware and software designs. The rotary-wing examples comprise a coaxial quadcopter with eight motors and two different sizes of conventional quadcopters.



Figure 3.10: Examples of cross-platform use of the proposed WxUAS in-situ sensor hardware and software.

3.4 Validation

As detailed in Chapter 2, new atmospheric measurement systems must undergo a maturing process that starts with laboratory testing, followed by exploratory research in small-scale investigative field campaigns alongside well-established systems, concluding with an extended improvement and hardening phase in a realistic testbed. This lengthy maturing process is necessary because errors associated with exposure, static, and dynamic properties are not present in most laboratory settings. Therefore, operational system characterization requires several years.

Within this dissertation's scope, the first two phases of this maturing process were accomplished through a series of controlled experiments at the Oklahoma Mesonet's calibration laboratory and field deployments at the Kessler Atmospheric Environmental Field Station

(KAEFS), Research Applications Laboratoy's field station (Marshall), and during MAI^{2}S. The complete details on these field deployments are given in Chapter 7; nonetheless, part of their results are presented in this section to validate the in-situ measurement design outlined in this chapter.

3.4.1 Laboratory Experiment

Initial calibrations at the Oklahoma Mesonet's Calibration Laboratory used the Thunder Scientific 2500 benchtop humidity generator (left panel in Fig. 3.11). This chamber produces controlled temperature and relative humidity conditions following NIST's two-pressure method. Within this controlled environment, the design's inner shield was taken through three 3-hour ramps where temperatures varied from 5 to 15 °C and relative humidity varied from 65 through 95 %RH. These ranges were selected to reflect the system's operational environment within wintry precipitation.

After determining the calibration coefficients for each sensor, the intra- and inter-sensor averaging procedures (described in Section 3.2) were applied, and the system's temperature and relative humidity were performed. Plots illustrating one of the three experiments are provided in Fig. A.1. For this example, the mean and maximum absolute errors (MAE and MxAE) for temperature and relative humidity are presented in Table 3.3.

Temperature		Relative Humidity	
MAE	MxAE	MAE	MxAE
0.0537 °C	0.4856 °C	0.1458 %RH	1.3073 %RH

Table 3.3: Mean and maximum absolute errors during the experiment at the Oklahoma Mesonet's Calibration Laboratory.

Although a calibration procedure such as this is expected to improve static errors, the small mean error found indicates the proposed in-situ inner shield design also has a predictable dynamic behavior across different combinations of individual and simultaneous variations in temperature and relative humidity (see Fig. A.1). This finding is further corrobo-

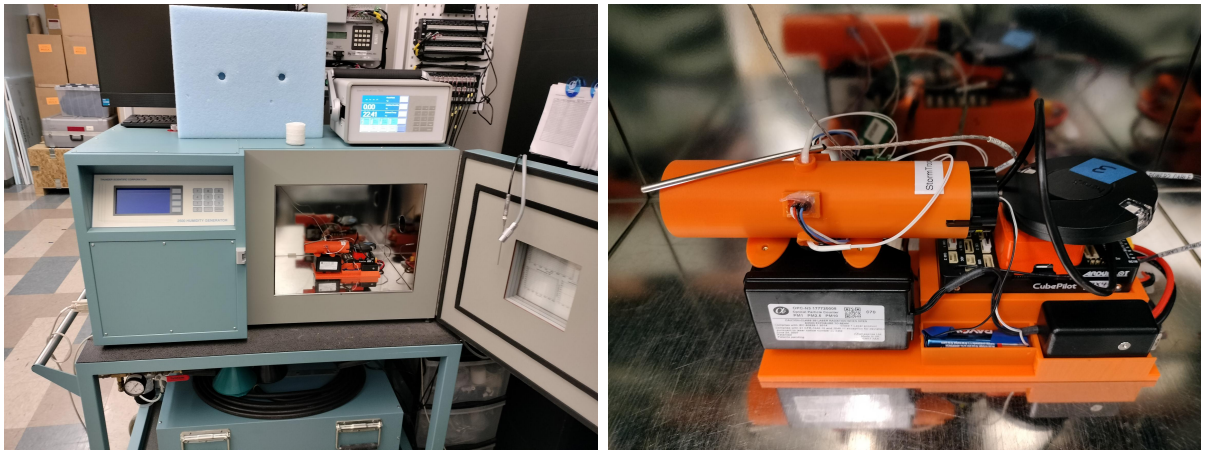


Figure 3.11: In-situ inner shield calibration at the Oklahoma Mesonet's Calibration Laboratory. The left panel shows the Thunder Scientific 2500 benchtop humidity generator, and the right panel details the experimental setup inside the chamber's test section.

rated by the maximum errors below our self-imposed accuracy standards of 0.5 °C and 2.5 %RH (a larger discussion on WxUAS accuracy standards is presented in Chapter 7). This result is very meaningful because it indicates that in 3 hours, that is, in 10,800 samples, not one sample crossed the accuracy threshold expected for the mean.

3.4.2 Field Experiment - OKMesonet

To evaluate performance under operational conditions, the system was deployed near an Oklahoma Mesonet tower for collocated measurements. Each Mesonet station has a collection of instruments placed at heights that range from 60 cm below to 10 m above the surface. This experiment leveraged the temperature sensors at 1.5 and 9 m and the relative humidity sensor at 1.5 m. Figure 3.12 offers an illustration of the tower's sensor placements along with a depiction of the experimental setup.

In this comparison experiment, two identical rotary-wing WxUAS, with the proposed in-situ measurement design solution, were placed on the ground next to the tower (one on each side). After a period of baseline measurements without any effects introduced by the aircraft's flight characteristics, both aircraft took off and hovered next to the tower at 9 m

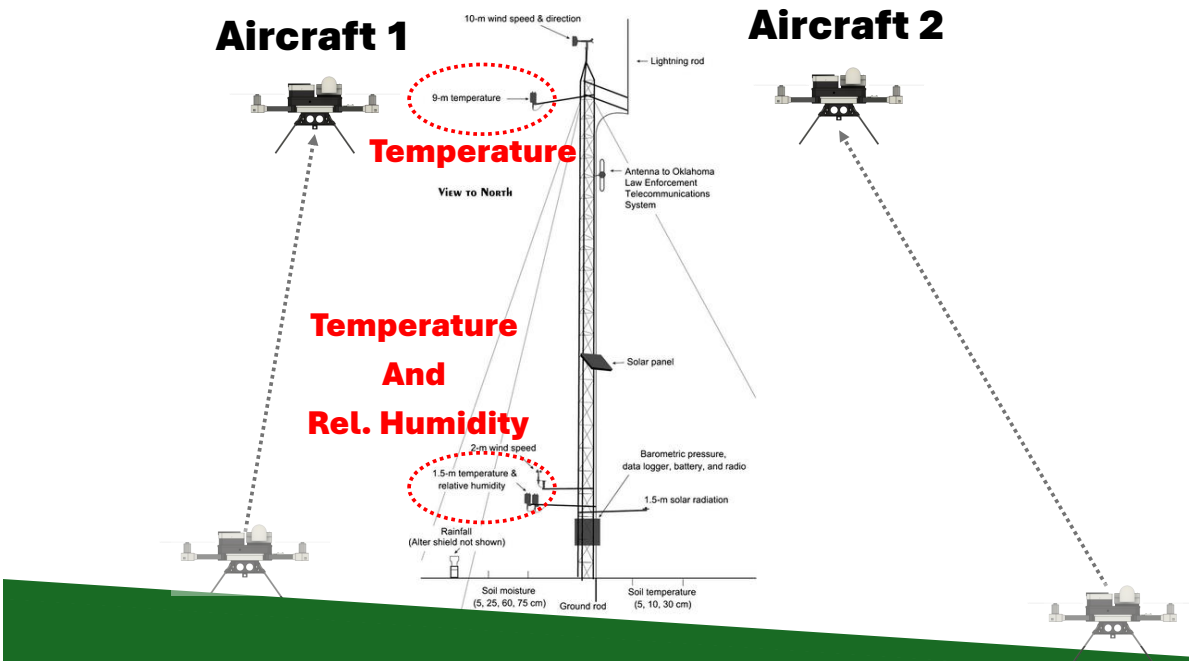


Figure 3.12: Experimental setup for the system's performance evaluation under operational conditions. Two identical WxUAS were flown next to the reference Oklahoma Mesonet 10 m tower for colocated measurements.

above the ground (height of the temperature sensor). This hover height was selected to eliminate any potential recirculation produced by aircraft ground effects, which could bias the experiment and interfere with the time series of this operational Mesonet station. For similar reasons, each aircraft flanked the tower on opposing sides, facing the mild incoming breeze.

Table 3.4 presents the mean and maximum absolute errors for each aircraft. The temperature errors presented similar values to the ones obtained in the laboratory experiments, with mean errors lower than the abovementioned 0.5 °C standard by an order of magnitude and maximum errors of 0.2 degrees below the sensor manufacturer's reported accuracy. Unfortunately, the same can not be said about the relative humidity results, which presented mean errors between 6 and 7 %RH and maximum errors above 7.5 %RH. Thankfully, this divergence can be explained by the experimental setup and conditions and does not indicate poor performance or a design flaw.

	Temperature		Relative Humidity	
	MAE	MxAE	MAE	MxAE
Aircraft 1	0.0361 °C	0.116 °C	6.1565 %RH	7.093 %RH
Aircraft 2	0.0808 °C	0.1856 °C	6.9813 %RH	7.6312 %RH

Table 3.4: Mean and maximum absolute errors during the Oklahoma Mesonet's Flight Comparison experiment.

As previously discussed, the tower only offers relative humidity measurements at 1.5 m, and the data collection height was set at 9 m to avoid interference from rotor wash recirculation. In many atmospheric conditions, this experimental limitation is deemed acceptable because %RH values at 9 m are assumed to be the same as at 1.5 m, as long as temperatures at both levels are the same. Given the limited availability of relative humidity measurements above 2 m, this comparison limitation is well known and documented in the scientific literature [37, 51, 59].

To increase the experiment's representativity for winter weather, the data collection occurred at night when the temperatures were below 6 °C, mimicking the chamber experiment's condition. Unfortunately, during most of the few data collection opportunities in Oklahoma's 2024 winter[2], the atmospheric conditions available produced considerable vertical temperature gradients. As presented in Fig. B.2, the reported mesonet temperatures during the experiment fluctuated around 4.08 and 5.67 °C at 1.5 and 9 m, producing a 0.21 °C m^{-1} gradient.

The 0.21 °C m^{-1} gradient found in the experiment's data invalidates the humidity homogeneity assumption between 1.5 and 9 m. This is indicated by the mean relative humidity errors between 6 and 7 %RH. Nonetheless, further analyzing the experiment's results reveals a few positive insights into the system's performance for relative humidity measurements in operational conditions. Appendix B provides extended experimental details, and Figs. B.1 to B.3 depict the resulting data's time series.

[2]Average monthly temperatures at the selected Mesonet tower during JAN-MAR 2024 were, 1.5, 10.1, and 13.2 °C.

The tower data time series in Fig. B.3 reveals the tower experienced relative humidity fluctuations larger than 10 %RH before and after the experiment, with a fairly stable period during the data collection. These same behaviors can be seen in the data for both aircraft, indicating the differences in absolute values are likely due to the differences in temperatures between 1.5 and 9 m. Additionally, during the stable data collection period, the maximum difference between both aircraft measurements was less than 1 %RH, indicating similar conditions experienced by both systems at 9 m and measurement consistency. Finally, considering the reasonable agreement between both aircraft and the tower in the short period before take-off and after landing, coupled with small errors in temperature measurements, it is reasonable to assume %RH measurements would also have acceptable errors.

Analyzed as a whole, the minor chamber errors for temperature and relative humidity, the minor temperature errors during flight, the relative humidity agreement between aircraft, and their agreement with the tower from the ground indicate the proposed two-layer in-situ measurement design does not hinder the sensor's ability to describe atmospheric conditions accurately. This conclusion will be further corroborated in Chapter 7 with more details on field deployments at the Research Applications Laboratoy's field station and during the Multi Atmospheric Instrument Intercomparison Study (MAI^{2}S).

3.4.3 Field Experiment - Marshall

To validate the proposed design's ability to effectively shield the sensors from wintry precipitation while accurately sampling the atmosphere, results from the field deployment at the Applications Laboratoy's field station (Marshall Field) for the National Center for Atmospheric Research (NCAR) are partially presented here. Particularly a ground comparison experiment during a snow event and flights in the presence of low-level clouds and drizzle. In the two ground comparison experiments, the mean absolute errors were 0.2155 °C and 1.1653 %RH (not shown), and 0.1439 °C and 1.0778 %RH (Fig. 3.13). Both results are below the sensors' accuracies specified by their manufacturers, which are 0.3 °C and 1.8 %RH.

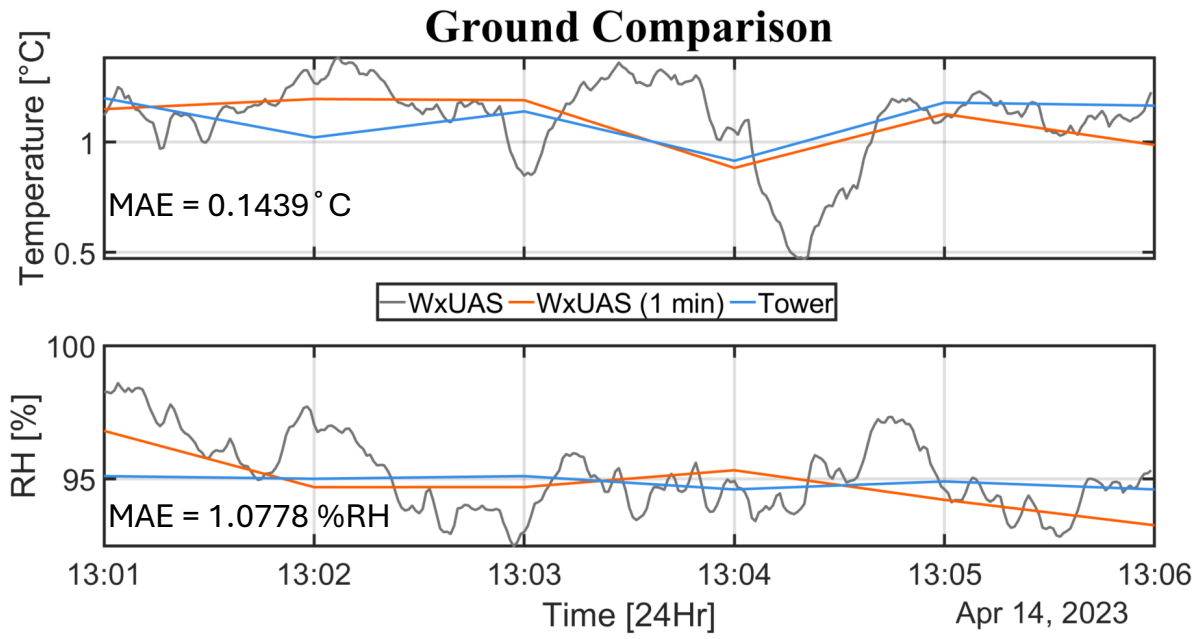


Figure 3.13: Results for the second temperature and relative humidity ground-based intercomparison experiment. The small mean absolute errors are below both manufacturers' reported accuracies.

During these ground-based experiments, the Marshall Field distrometer reported snow with total counts increasing from 0 to 400 particles per minute. During this same period, the 77 GHz vertically pointing radar, part of this dissertation's proposed design discussed in Chapter 4, detected a 15 to 25 dB increase in power with Doppler velocities of -2 and $-4\,\mathrm{m\,s^{-1}}$. Also, in this period, the optical particle counter inside the two-layer in-situ sensor shield did not report any change in particle size distribution.

These results are shown in Fig. 3.14, where the left panel presents the temporal evolution of the particle size distribution's mode, and the right panel presents three range-Doppler plots. In the particle size plot, the x-axis is the total particle count per second, the y-axis is time, and the color expresses the size of the particle associated with the distribution's mode. In each range-Doppler map, the y-axis represents altitude above the radar, and the x-axis indicates the Doppler velocity, where negative velocities indicate hydrometeors falling towards the radar. Evaluating the particle size distribution's mode, it is possible to note the

distribution's bin with the highest count remained between 0 and 2 µm with a total count between 50 to 100 particles per second. These rates and distribution modes are consistent with the sensor's background readings.

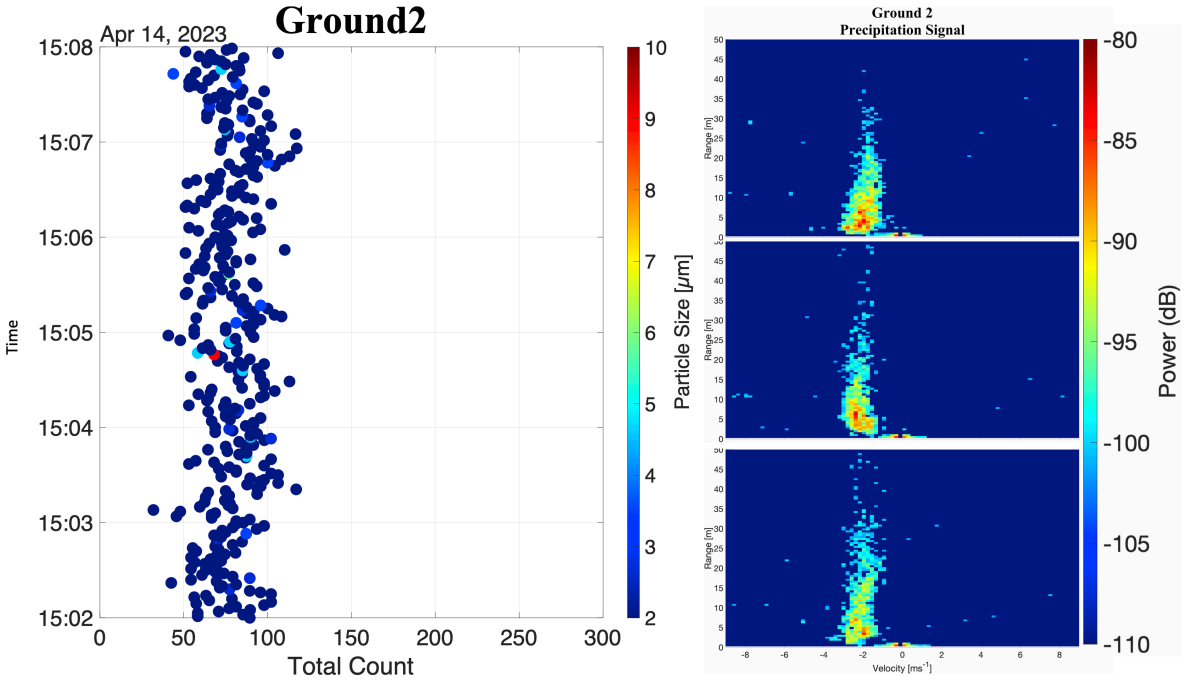


Figure 3.14: Results for particle size distribution (left) and power and Doppler velocity (right) during the second ground-based experiment. For the vertically pointing radar, negative Doppler velocities indicate particles falling towards the radar.

The results from these ground experiments reveal that, during active precipitation, the proposed in-situ measurement design effectively utilized gravity to mechanically separate large precipitation from the air, avoiding impinging the system's sensing elements. Additionally, the small mean absolute errors in temperature and relative humidity indicate the design strategy does not introduce any bias or artifacts. Combined, these results help validate the proposed design and confirm our expectations regarding the mechanical separation of large precipitation drops from the air while eliminating the impact of radiative and sensible heat fluxes.

3.4.3.1 Particle Size Distribution

Given the novelty of WxUAS cloud-size particle profiles, methods for validating the proposed design are not yet well established. Additionally, considering the physical complexity of clouds, controlled chambers with artificially generated clouds are not abundantly available. Therefore, the initial tests for the proposed WxUAS in-situ measurements of particle size distribution in the 2 to 40 µm range were executed at the Marshall Field Station using naturally occurring conditions.

Upon conclusion of the abovementioned ground-based experiments, four vertical profiles from the ground to 120 m were performed to evaluate the WxUAS's ability to characterize the atmosphere's thermodynamic structure and its microphysical properties in near-freezing conditions. Although the WxUAS was designed to perform profiles up to 1500 m, flight ceilings were limited for compliance with the FAA's Part 107 rules. This limitation was unfortunate as it could have hindered the system's ability to observe any meaningful structural change with height. However, given the field station's proximity to the mountains and elevation (1627 m, ASL) and the intensity of the weather event, the four profiles were performed in scientifically relevant conditions and permitted gauging the WxUAS's potential.

Although all in-situ and remote sensors were in use, we highlight only the particle size distribution results here, leaving the other results to be discussed in Chapter 7. Hence, Fig. 3.15 displays the particle size distribution profiles (bottom panels) against the ground-based ceilometer data (top panels). In all plots, the y-axis signifies altitude, and the x-axis corresponds to the variable of interest. For the particle size distribution profiles, the data represents the distribution's mode – the particle size bin with the highest count. The color in these profiles denotes the mode's particle size, while the x-axis portrays the distribution's total count for that second. For the ceilometer scatter plot, the orange shaded columns represent the time intervals for the four flights.

The first profile occurred immediately after an intense snow event had subsided, while the ceilometer reported a low-altitude cloud base near 95 m AGL (Fig. 3.15). The snow, freshly

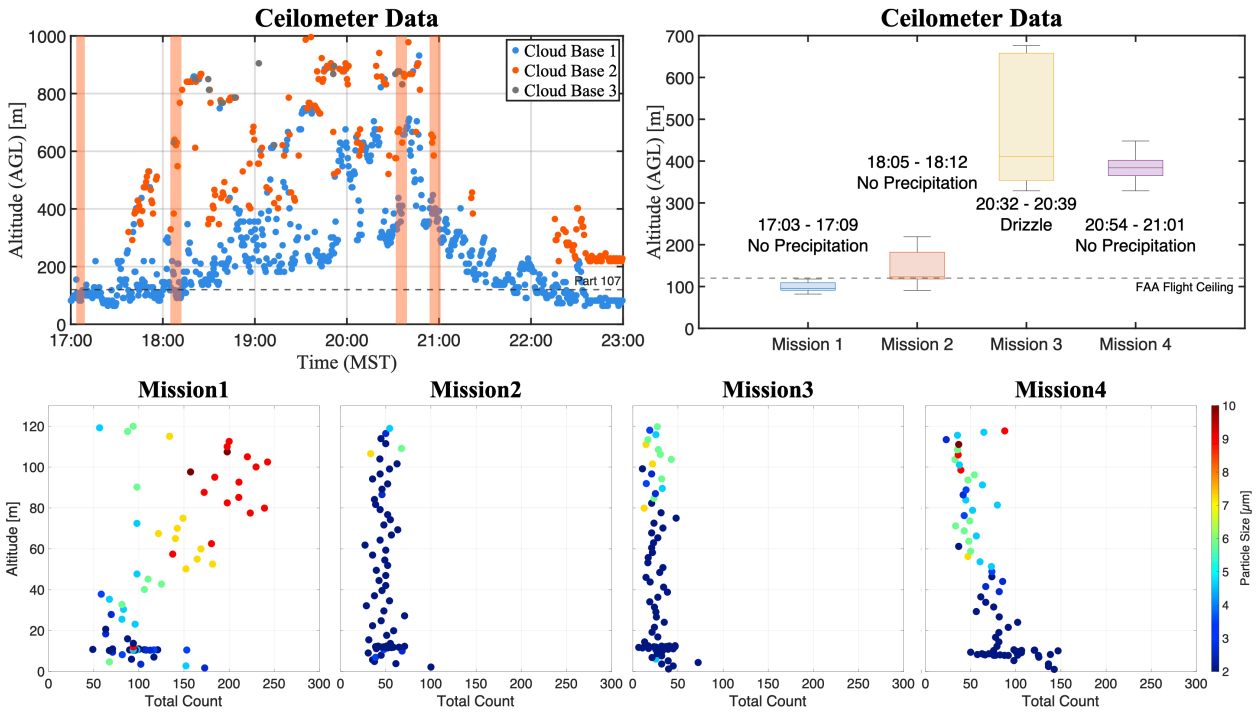


Figure 3.15: Ceilometer data (above) indicating the cloud base and the profiles of the particle size distribution (below) for each of the four flights to 120 m. The orange-shaded columns in the ceilometer's scatter plot represent the time intervals for the four flights

deposited on the ground, produced lower temperatures and intense moisture on the surface layer, as reported by the tower instruments. These conditions were also reflected in the WxUAS measurements. Most notably in the particle counter data that showed distribution modes with total counts above 150 particles per second on the surface, falling to 100 between 10 and 50 m AGL and rising to 200 between 80 to 110 m (Fig. 3.15: 'Mission 1').

The high count of smaller particles (from 0 to 4 µm) near the ground is most likely produced by the rotor wash during takeoff over the snow-covered surface. While other effects could yield similar increases in small particle count, the likelihood of rotor wash effects is substantiated by the similar pattern observed during 'Mission 4' following a drizzle event.

Additionally, this pattern is notably absent in 'Mission 2' and 'Mission 3' after periods without precipitation and during the ground-based comparison experiments (Fig. 3.14), which were conducted during a snowfall event with the rotors turned off. The high count

of larger particles (from 8 to 13 µm) from 80 to 110 m shows agreement with the ceilometer's reported cloud base, which had a median altitude of 95.5 m, interquartile range (IQR) of 18 m (between [91 109]), and 82 to 118 m minimum and maximum values. This result demonstrates the system's ability to detect cloud-sized particles and characterize the cloud layer's depth.

Furthermore, upon comparing the four particle size distribution profiles with the ceilometer reports, the WxUAS's high sensitivity to cloud-sized particles becomes evident. During the interval between 'Mission 1' and 'Mission 3,' as the reported cloud base ascended from 95 to 400 m and subsequently descended in 'Mission 4' and beyond, the distribution mode profiles identified by the WxUAS began to manifest the size variation with altitude consistent with the ceilometer reports, albeit earlier. For instance, during 'Mission 3', the reported cloud base exhibits a median altitude of 411 m with an IQR of 305 m. Concurrently, the size distribution profile reveals an increase in particle sizes above 80 m.

During 'Mission 4', the reported cloud base, characterized by a median altitude of 384 m and an IQR of 37 m, corresponds to an increase in particle sizes above 60 m, with particles reaching 11 µm at 120 m. Approximately 40 minutes after 'Mission 4', the ceilometer reports the cloud base at 137 m with an IQR of 91 m. Subsequently, one hour later, the ceilometer records the cloud base at 82 m with a 27 m IQR, between 73 and 100 m.

The abovementioned results indicate the system promptly shielded its sensing elements from precipitation while accurately describing low-altitude atmospheric conditions with enhanced sensitivity in an operational environment. Therefore, this validates the proposed WxUAS in-situ measurement system design. The remaining chapters will revisit the abovementioned field campaigns and provide further details into the role of the proposed WxUAS as a tool to provide novel insight into the low-altitude wintry precipitation environment. However, before the full system can be discussed, Chapter 4 presents the design details and results for an innovative WxUAS vertically pointing weather radar.

Chapter 4

Remote Measurement Design

"Kick some @ss, show some good sh!t, and hit the road!"

Robert D. Palmer

Within wintry precipitation, FZFG, FZDZ, and FZRA remain among the most challenging phenomena to accurately detect via automated systems. Within radar data, FZDZ and FZRA can present overlapping ranges of reflectivity distributions across light, moderate, and heavy intensities compared to other freezing and non-freezing precipitation forms [3]. This ambiguity requires using atmospheric thermodynamic profiles to enable hydrometeor classification and hazard assessments [14, 21]. Additionally, drizzle droplet sizes are below the detection limits of many radar systems [12], and fog is too close to the ground, putting it outside of radar operational limits [3].

In ASOS-based detection and classification, a multi-modal data fusion technique is employed to identify freezing precipitation. Nevertheless, this method may occasionally misclassify light-intensity freezing precipitation as "clear" or categorize mixed-phase precipitation cases as "unknown" [7]. These issues arise because the sensors involved in ASOS's multi-modal fusion each have specific detection thresholds that must be individually met for the

system to reliably classify these complex wintry precipitation events [7, 45]. When the conditions are marginal, where some thresholds are met while others are not, the likelihood of misclassification increases [45].

The in-situ measurement design presented in Chapter 3 addresses the thermodynamic and particle profiling needs associated with the observational limitations mentioned above and detailed in Chapters 1 and 2. However, it does not address the need for high-resolution, low-altitude, precipitation, and obscuration measurements, particularly for FZDZ and FZFG. This chapter presents novel algorithms and integration techniques to enable the detection of drizzle and other weak precipitation types with a low-cost, commercial, off-the-shelf mmWave phased array radar onboard this dissertation's unmanned aerial weather measurement system.

4.1 Radar System

Historically, mmWave radars have only been employed as cloud radars due to their shorter wavelength, which is appropriate for smaller cloud-sized particles. However, leveraging the mobility of UAVs, a mmWave radar can be transported through the lower atmosphere closer to these larger particles, making consecutive, short-range, high-resolution measurements. By combining these measurements during post-processing, it is possible to generate precipitation reflectivity and Doppler velocity profiles with centimeter-scale range resolution. As a result, a WxUAS equipped with thermodynamic and high-resolution reflectivity and Doppler velocity profiling capabilities may offer valuable insights into low-altitude FZFG, FZDZ, and FZRA events.

The Texas Instrument's (TI) AWR2243 is an automotive second-generation high-performance monolithic mmWave integrated circuit coupled with two antennas (transmit and receive) to comprise a highly configurable Frequency-Modulated Continuous Wave (FMCW) phased array radar. The TI AWR2243 operates between 76 to 81 GHz, which makes its transmit

and receive patch antennas small and easy to conform within a UAV design. In addition to its small antenna, the TI AWR2243 consumes less than 12 W and weighs less than 0.4 kg in its evaluation board form factor. These characteristics make it a suitable candidate for UAV-based deployment.

The TI AWR2243's configuration allows users to design sequences of chirps with varying configurations (i.e., active TX and RX antennas, start and stop frequencies) and program repetition of these sequences in loops. Additionally, the TI AWR2243 leverages its phased array antenna to produce a data cube that, theoretically, covers a 180° field of view. This feature, in a more realistic 60° field of view, is crucial for the aircraft motion compensation detailed in Section 4.3. For more details on the TI AWR2243's configuration for this dissertation, see Appendix C.

Although previous studies have demonstrated how this specific radar and others were leveraged for UAV-based deployment, these studies have focused on imaging and collision avoidance applications [70, 71, 72]. These applications better align with the TI AWR2243's design purpose, automotive collision avoidance, and have targets with high reflectivity (e.g., other UAVs, buildings, and plants). The literature survey for this dissertation did not produce any UAV-based active weather radar studies using the TI AWR2243 or other radars. Therefore, before working on its integration, a few chamber experiments were performed to ensure the TI AWR2243 could detect and distinguish between falling water, ice, and mist.

4.2 Initial Experiments

To evaluate the TI AWR2243's ability to detect and distinguish between the characteristics of falling water, ice, and mist, six experiments were designed and later performed at the University of Oklahoma's (OU) Advanced Radar Research Center (ARRC). In these experiments, large water drops, ice shavings, and water mist were used to emulate the target precipitation. The water drops were produced by drips from melting ice and a showerhead.

The ice shavings were created using a hand-cracked ice-shaving machine which uses three steel blades to produce fine shavings from ice cubes. The mist was produced by multiple water vaporizers and a handheld spray bottle. During these experiments, the radar and a camera were placed perpendicularly or parallel to the precipitation. Figure 4.1 provides an illustration and details for this experimental setup.

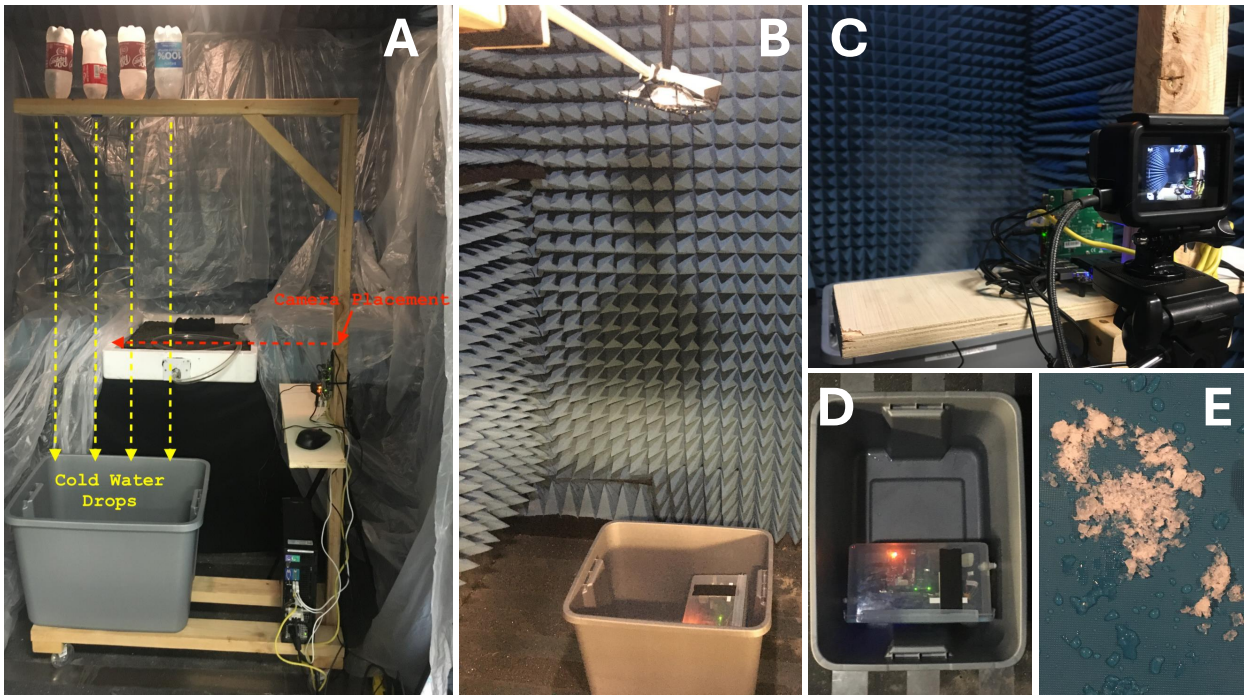


Figure 4.1: Experimental setup for initial evaluation of the TI AWR2243: (A) the setup for precipitation perpendicular to the radar beam, (B) the parallel setup. (C) The perpendicular "Mist" experiment. (D) The improvised radome to emulate a vertically pointing radar in parallel experiments. (E) The ice shavings used to mimic frozen precipitation.

The parallel and perpendicular setups were designed to emulate two modalities of potential deployment conditions. The perpendicular setup emulates the expected operational conditions of a forward-facing airborne weather radar. In this setup, the falling precipitation crosses the radar beam (as indicated by the yellow and red dotted lines in Fig. 4.1-"A"). The parallel setup emulates the expected operational conditions of a vertically pointing radar, similar to a ground-based micro-rain radar. In this setup, the precipitation falls continuously through the radar beam toward the radar. At this point in the research, both modalities

were still under consideration for the final WxUAS integration and deployment, given that both provide different but valuable information regarding the precipitation environment.

Although all experiments were performed inside an anechoic chamber to reduce external interference, the equipament necessary to produce the emulated precipitation conditions was expected to introduce considerable interference in the experimental data. To mitigate this issue and isolate the effects of the precipitation, six complementary experiments were performed without any mock precipitation. Therefore, for each setup (i.e., combinations of parallel and perpendicular with the three types of "precipitation"), data were collected before and during the "precipitation event", generating twelve datasets.

Three of the twelve experimental results illustrate the overall conclusions well. They are presented here in Figs. 4.2 and 4.3. All three resulting plots present the data as a range-Doppler map, a tool for synthesizing the collected data and providing a visual aid for this discussion. In this map, the y-axis represents the range or distance of a detection bin from the radar. In the parallel experiment setups, the range can be interpreted as the height or altitude above the radar. The x-axis represents the Doppler velocities, where negative velocities indicate particles moving toward the radar. In the parallel experiment setups, Doppler velocity can be interpreted as hydrometeor fall velocity.

As expected, the results in Figs. 4.2 and 4.3 show strong reflections at zero Doppler velocity caused by the experimental apparatus. The reflections were confirmed to be caused by the experimental apparatus via comparison with the results without "precipitation" (not shown). The setup interference is even more pronounced in the top map shown in Fig. 4.2, which indicates a high power band of positive and negative velocities caused by the circular motion of the handheld ice shaver. Nonetheless, these three results were promising and indicative of the ensuing developmental challenges.

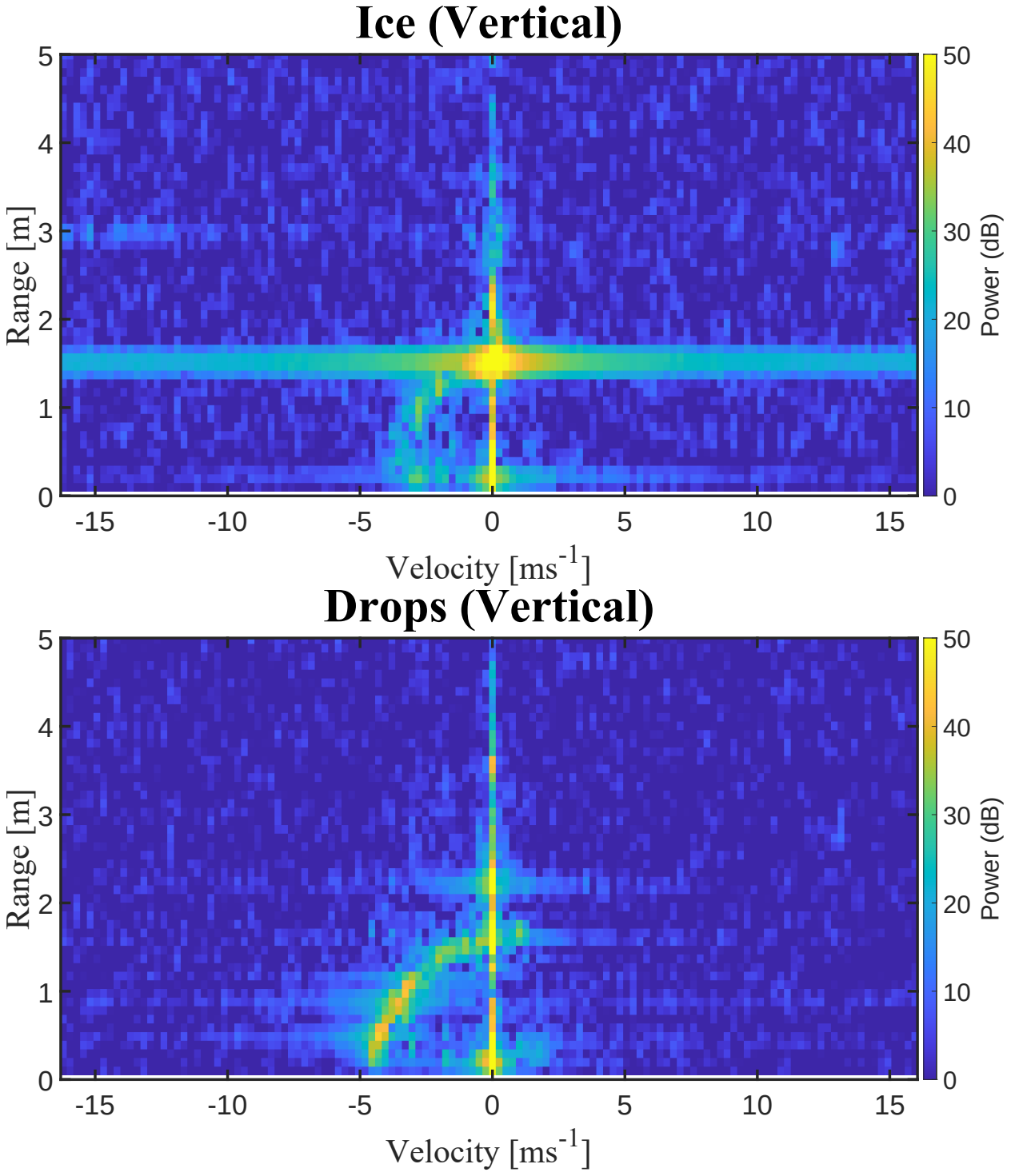


Figure 4.2: range-Doppler map for the large water drops and ice shavings falling vertically toward the radar (i.e., parallel setup).

Comparing the two maps in Fig. 4.2, it is possible to note the distinctive velocity arcs caused by the falling hydrometeors. For the ice shavings experiment, the velocities are slightly slower (under $5\,\mathrm{m\,s^{-1}}$) and show both acceleration and deceleration. These effects are potentially caused by the instabilities introduced by the handheld shaver and the under-developed fall speed caused by this short test section. For the large water drops experiment, the acceleration arc is slightly broader and more pronounced, with a terminal fall velocity at $5\,\mathrm{m\,s^{-1}}$. These results indicate that this low SWaP radar can detect water and ice hydrometeors and the nuances in their fall characteristics.

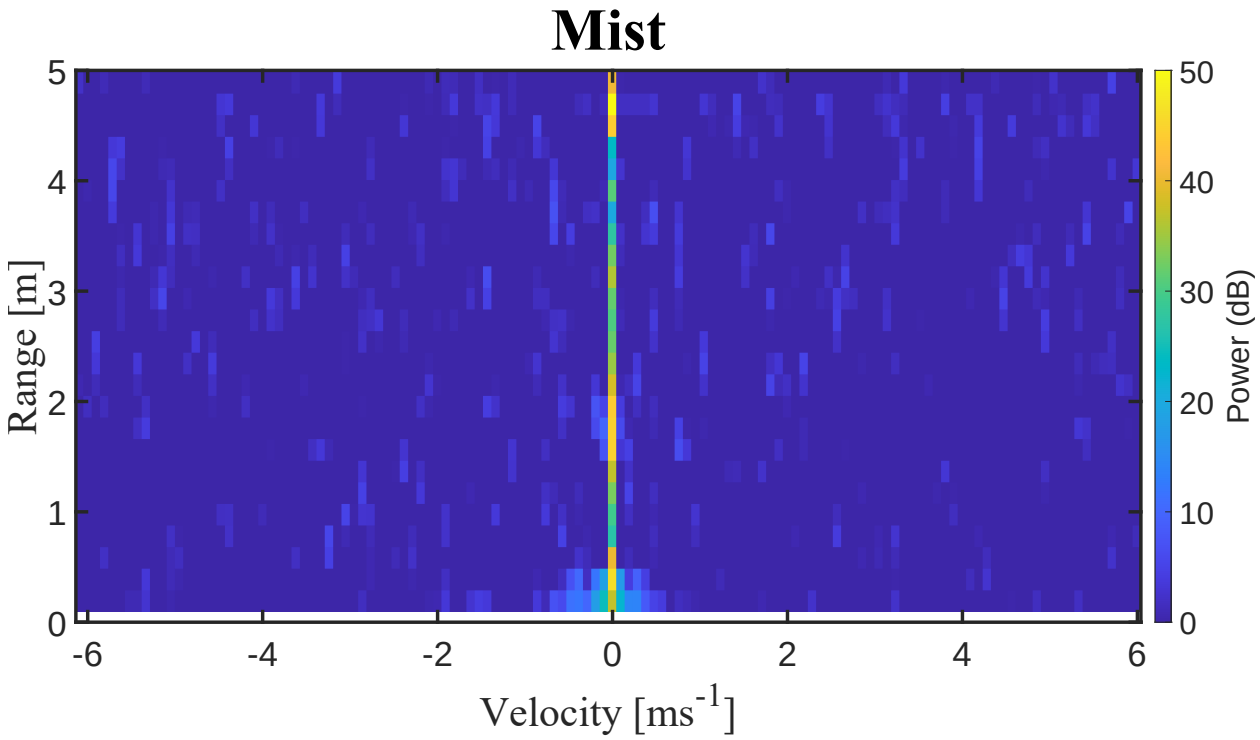


Figure 4.3: range-Doppler map for the mist generated by the handheld spray floating in front of the radar (i.e., perpendicular setup).

The results for the mist experiment (show in Fig. 4.3), where the mist "hovered" in front of the radar in a pseudo perpendicular setup, produced a faint signal nearly indistinguishable from the radar's noise. Given the low output of our mist generators, it is possible that they may not have produced enough mist for a valid experiment. Therefore, even though this result exhibited a minor power increase from the control experiment without the emulated

mist, it still needs to be considered inconclusive. Nonetheless, this result indicates that data from this radar will likely require considerable post-processing for relevant use in field deployment, which is expected to be a noisier environment. These and other post-processing details are presented in Section 4.4.

4.3 Integration and Deployment Strategy

To address the abovementioned need for high-resolution precipitation and obscuration measurements in low-altitude wintry precipitation environments, this dissertation endeavors to develop a WxUAS remote measurement system based on the TI AWR2243. Given the in-situ characteristics of the other sensors integrated into this dissertation's WxUAS and the limited range of the TI AWR2243, the design proposed in this chapter deploys the TI AWR2243 as a vertically pointing radar. This strategy enables the radar to generate localy meaningful measurements that can be correlated with the in-situ measurements to produce insight into the low-altitude wintry precipitation environment.

For example, the vertical radar beam can be used to create a proxy relationship between the detected hydrometeors' Doppler velocity and their fall velocity. In low wind cases, where the hydrometeors fall in a primarily vertical trajectory, their Doppler velocity toward the radar is mostly attributed to their fall velocity. By fusing the hydrometeors' velocity spectrum with wind speed and temperature, it is possible to infer the hydrometeors' phase (i.e., precipitation type). More details on these multi-modal data fusing techniques will be given in Chapter 6.

Furthermore, employing a vertically pointing Phased Array Radar (PAR) removes the necessity for an active gimbal to compensate for aircraft motion. This is achievable because only the aircraft's pitch and roll influence its measurements. By utilizing the WxUAS's ability to detect wind direction, the system can align with the wind (i.e., function as a wind vane), thereby minimizing any wind-induced roll during the multirotor's profiling flight.

Wind-induced pitch variations can be addressed through the TI AWR2243's scanning strategy, which encompasses multiple angles (see Fig. 4.4), and by applying digital beamforming techniques during post-processing (more details are available in Section 4.4.1).

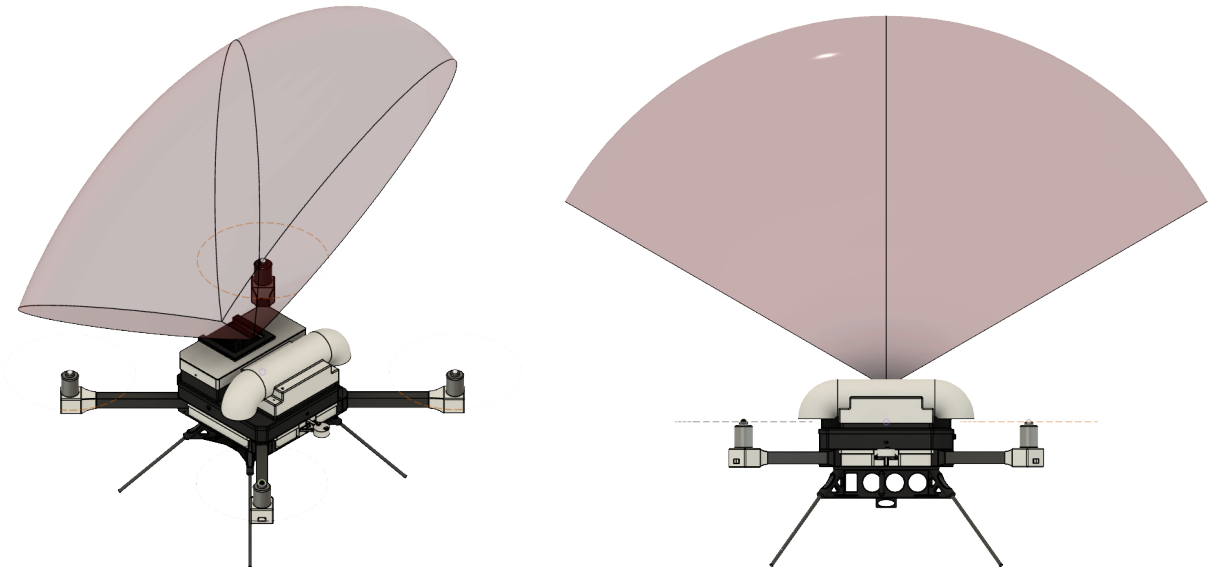


Figure 4.4: Illustration of the multiple angles scanned by the TI AWR2243 PAR, which can be leveraged to compensate aircraft motion in pitch.

Configuring the TI AWR2243's frequency, chirp characteristics, ADC, and other operational parameters, the radar operated with a theoretical range of 225 m and an approximate 0.5 m range resolution. In this configuration, the TI AWR2243 also measured unambiguous maximum velocities up to $26\,\mathrm{m\,s^{-1}}$ with $0.2\,\mathrm{m\,s^{-1}}$ resolution. To reduce the amount of data produced by the system, scans were performed every 9 s during atmospheric profiles with an approximately $3\,\mathrm{m\,s^{-1}}$ ascent rate. This sampling strategy produced a new scan every 27 m, which can be concatenated in post-processing to produce a 0.5 m range resolution reflectivity and Doppler velocity profile from the ground to 225 m above the WxUAS's flight ceiling.

While the vehicle depicted in Fig. 4.4 is the StormTrooper, which is this dissertation's platform design, optimized for data collection in the harsh conditions of the low-altitude wintry precipitation environment (detailed in Chapter 5), it is important to emphasize that the concepts proposed in this chapter's remote measurement system design are applicable

across different platforms. This cross-platform feature is illustrated in Fig. 4.5, which shows this chapter's remote measurement system design partially integrated into Oklahoma State University's multi-rotor testbed (i.e., the Skateboard). Although not fully implemented within this dissertation's scope, this technology is also available for deployment in fixed-wing UAVs with minor aerodynamic modifications. A fixed-wing deployment illustration is also offered in Fig. 4.5. It represents one of this dissertation's early vehicle design considerations.



Figure 4.5: Illustration of cross-platform application of this chapter's proposed remote measurement solution. Images on the top detail the integration into Oklahoma State University's Skateboard, and the bottom image depicts a conceptual design for fixed-wing deployment.

Given the significant storage requirements for the data generated by the TI AWR2243, along with its API's reliance on an MS Windows Dynamic Link Library (DLL), it was not possible to implement a direct flight controller integration as done for the in-situ measurement sensors. Instead, the chosen software integration strategy involved utilizing an external

computer to manage the TI AWR2243. For more details on the advantages and disadvantages of each integration method, please revisit Section 3.3.

The physical integration of the TI AWR2243 into both multi-rotor aircraft presented considerable challenges because the weight of the TI AWR2243, its companion single-board computer, and wires did not allow for extra weight to be used to safeguard these sensitive electronic components from precipitation. To solve this challenge, a 50 g, 3D-printed enclosure was designed using a low-density biodegradable thermoplastic and a 0.25 mm thick Teflon PTFE radome. This material is simple to use, lightweight, and well-characterized in the literature [73, 74]. Therefore, it is not recharacterized in this dissertation.

The radome design, placed at three wavelengths above the radar's antenna, follows an 80 by 80 mm, flat, rectangular pattern in accordance with Texas Instruments' recommendations [75]. However, a flat radome will accumulate water over time in a precipitation environment. To eliminate this accumulation, the enclosure's lid was manufactured in three parts: the base, the Teflon PTFE film, and a radome frame, as shown in Fig. 4.6. The frame was given a 2° tilt angle to create a slope towards the lid's edge, while the frame curves over the lid's edge, attaching to the base's edge below the Teflon PTFE film. This slopped, edgeless design allows water to drip over the radome's top edge as soon as its accumulation achieves the critical level necessary to break the surface friction with the Teflon PTFE film.

Figure 4.7 illustrates this principle well, with an example taken from one of the deployments at Storrs (CT) during the MAI^{2}S field campaign (detailed in Chapter 7). In this illustration, it is possible to note the accumulation of much larger water drops in the flat portion of the enclosure's lid than in the slopped, edgeless radome. As mentioned, small drops will persist due to the friction caused by the Teflon PTFE film's roughness. Once the drops accumulate and become larger, they slide over the edge.

Another relevant physical integration design aspect worth highlighting was the use of a 3D-printed support to mechanically attach the TI AWR2243 to the aircraft. This support was manufactured using a variable-density polyurethane-based thermoplastic (TPU). This

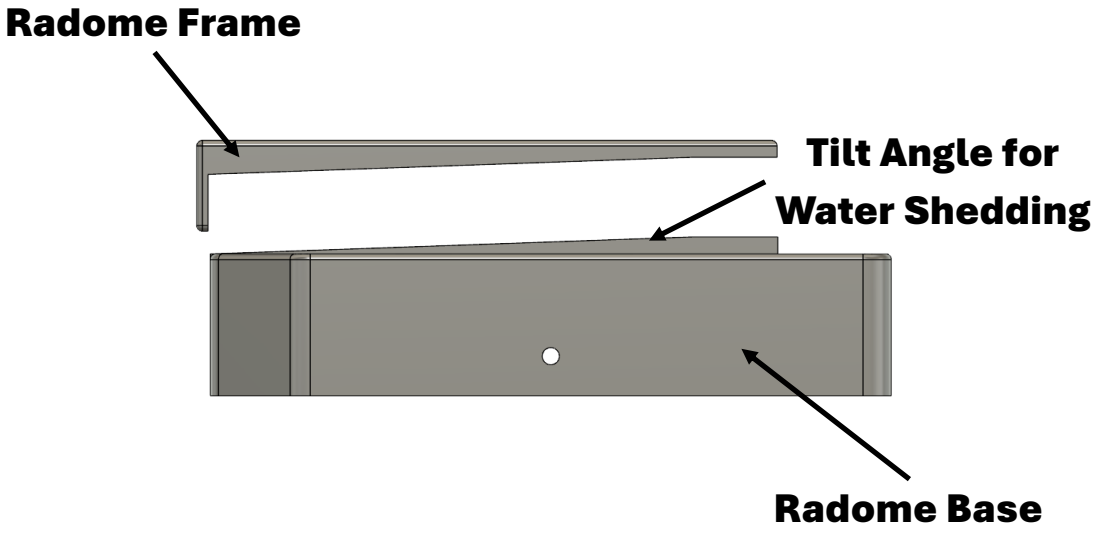


Figure 4.6: Illustration of the 3D-printed radar enclosure lid with a slope to remove precipitation accumulation from the radome.

variable density characteristic enables the manufacturing of complex shapes with varying stiffness properties across them. Figure 4.8 depicts how this material was used to manufacture a partially flexible, floating raft to support the TI AWR2243. This suspended and partially flexible raft creates a vibration-dampening effect that decouples the TI AWR2243 from the motor-induced vibrations commonly found in multi-rotor UAVs.

4.4 WxUAS Radar Post-Processing Algorithm

The TI AWR2243's versatility and low size, weight, and power make it a suitable radar for deployment as part of a multi-sensor WxUAS. Additionally, the encouraging chamber experiment results (shown in Section 4.2) indicate it has the potential to provide important insight into hydrometeor reflectivity and fall velocity in the mixed-phased low-altitude precipitation environment. Nonetheless, these results also indicate that its successful WxUAS integration requires considerable additional development. After all, the TI AWR2243 was

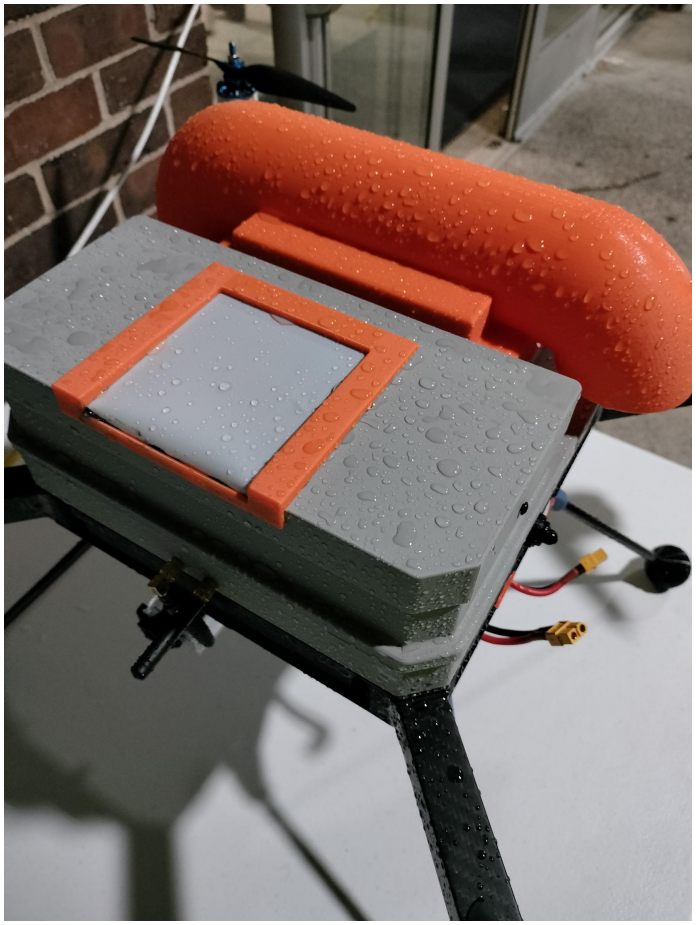


Figure 4.7: Illustration of the effectiveness of the slopped, edgeless design used in the lightweight radar enclosure.

originally developed as an anti-collision automotive radar, making its use as a weather radar and as part of a WxUAS remote measurement solution a considerable deviation from its intended application.

Consequently, the algorithm necessary to process its raw data into meaningful weather data involves several steps. Some of these steps follow conventional radar post-processing techniques (e.g., pulse compression and thresholding), while others are necessary due to the specific design choices in this Texas Instruments product. In addition to these steps, the unique challenges created by deploying the TI AWR2243 as a vertically-pointing mmWave PAR on a WxUAS require a set of sub-algorithms specifically developed for this dissertation. The following subsections highlight three of these sub-algorithms and detail their impact on

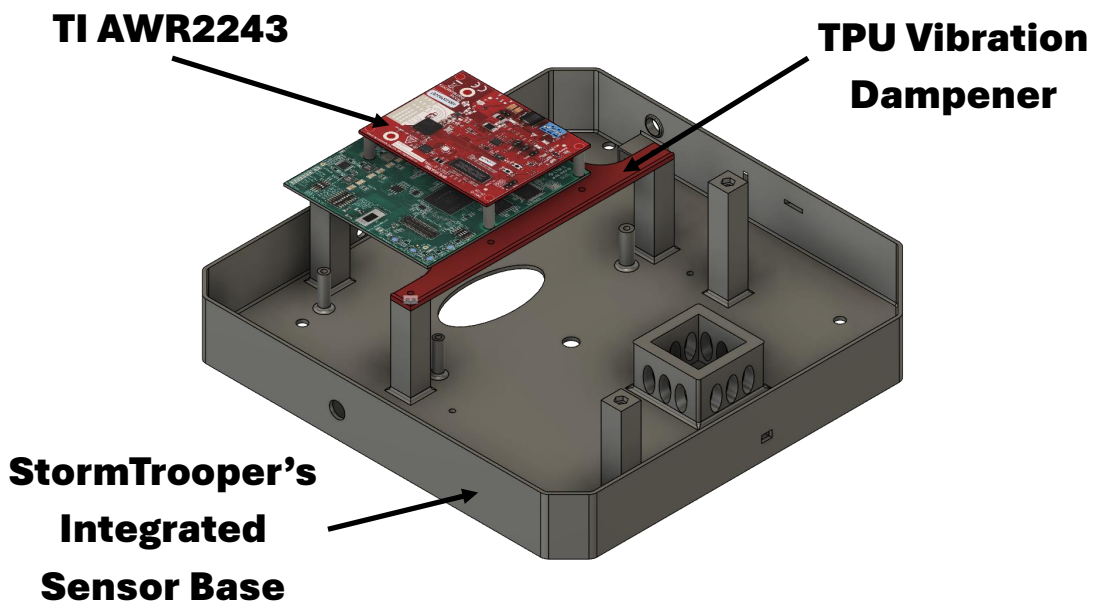


Figure 4.8: Illustration of the TPU-based suspended raft used to decouple the TI AWR2243 from motor-induced vibrations commonly found in multi-rotor UAVs.

producing meaningful weather radar data.

4.4.1 Aircraft Motion Compensation

The first step in processing field-collected data from airborne operations in a vertically pointing configuration is compensating for the aircraft's motion. This dissertation's motion compensation strategy is divided into three components: the physical integration of the TI AWR2243 into the WxUAS, the flight pattern used during data collection, and the post-processing software. Due to the thoughtful design of the first two strategies, the post-processing algorithm discussed in this subsection can rely on a few assumptions, allowing for a considerable simplification of its implementation.

As detailed in Section 4.3, the TI AWR2243 mounted on an elevated variable-density polyurethane-based thermoplastic raft to dampen vibrations from the aircraft's motors and minor flight corrections. Additionally, the aircraft always faces the incoming wind, thereby eliminating wind-induced roll. Combined, these two strategies limit external flight distur-

bances to the aircraft's motion to its pitch axis (see Section 4.3 for more details). Moreover, all field deployment data in this dissertation's scope was collected using multi-rotor profiles with constant ascent rates over a fixed point on the surface and the radar in a vertically pointing configuration.

Under these integration and operational conditions, it is reasonably assumed that the Doppler velocity correction may be simplified to subtracting the aircraft's instantaneous vertical velocity (i.e., velocity in the Z axis on the earth's reference frame) from the reported Doppler velocities. It is also reasonable to assume that digitally formed beams can be produced at zenith to ensure the beam remains perpendicular to the surface (i.e., parallel to the Z axis on the earth's reference frame) based solely on the aircraft's pitch angle.

The aircraft pitch correction is applied when the radar's data cube is being constructed. Since the TI AWR2243 has four receive antennas separated by $\lambda/2$ (i.e., half of a wavelength), the phase compensation term

$$e^{j2\pi \frac{dsin(\theta)}{\lambda}},$$

where d is each antenna's subsequent distance from the first receiver antenna and θ is the aircraft's pitch angle, becomes

$$1,\ e^{j\pi sin(\theta)},\ e^{j2\pi sin(\theta)},\ \text{and}\ e^{j3\pi sin(\theta)},$$

for each of the four receive channels. After this phase correction in each channel, the cube is compressed into a pulse-range matrix by adding all Rx channel data into a single dimension. Since this step occurs during the data cube's construction, all data shown in this section already has this correction applied. This pitch angle assumption and correction algorithm were validated with a small set of experiments in which a metal pole was placed broadside to the radar (i.e., head-on) and at a 60-degree angle, both at a distance of approximately 10 m from the radar. Details of the experimental setup and results are provided in Appendix D.

4.4.2 Synthetic Long Exposure

During the chamber experiments, detailed in Section 4.2, initial data post-processing indicated that small-diameter precipitation would be challenging to discern from the radar's noise. Given this dissertation's interest in freezing drizzle, adopting a strategy to increase the signal-to-noise ratio (SNR) became paramount. This dissertation's strategy to address this issue comprises a data collection and post-processing technique to increase signal strength and a post-processing technique for reducing noise. This subsection details the former.

To enhance the detection of small-diameter precipitation droplets, this dissertation's WxUAS remote measurement design leverages a few characteristics of the TI AWR2243. As an FMCW radar, the TI AWR2243 provides the user with the flexibility to configure several parameters within a chirp (i.e., a frequency-modulated pulse). Additionally, its API allows the user to pre-program chirps with different configurations and string them in a predetermined sequence. These sequences can then be repeated a predetermined number of times to form a frame. Furthermore, frames can be repeated a set number of times with adjustable periodicity for each data capture command. Each frame produces a radar data cube with range, pulse, and Rx antenna dimensions.

Within the scope of this dissertation's remote measurement design, the TI AWR2243 was deployed with a single chirp configuration, 255 pulses, capturing four frames per command, with a 40 µs interval between frames. In this configuration, the TI AWR2243 operated with a theoretical range of 225 m and an approximate 0.5 m range resolution. Its unambiguous maximum velocity was $26\,\mathrm{m\,s^{-1}}$ with $0.2\,\mathrm{m\,s^{-1}}$ resolution. A new capture command was issued every 9 s, generating four new frames every 27 m. More details on the radar's configuration and an illustration of the chirp parameters can be found in Appendix C.

This configuration provides enough resolution in range and velocity to capture the nuances in the fall dynamics of different precipitation types and intensities. Given the expected homogeneity of winter precipitation within time and space scales of a few hundred meters and seconds, this configuration also produces a considerable amount of data overlap that

enables post-processing techniques to enhance the targeted nuances. This overlap occurs in two dimensions. The first is in range, where sequential 27 m data captures with a 225 m range produce a 198 m range overlap. The second is within the four frames in each capture command because under the homogeneity assumption, the 160 µs between the four frames can be considered instantaneous.

Unfortunately, field deployment data indicated that the TI AWR2243's effective range for rain was under 50 m, and its range for smaller precipitation was below 20 m. This limited effective range is understandable considering the TI AWR2243 was designed to be a small, lower power, cost-effective tool to detect large objects (e.g., cars and walls). Nonetheless, this limited range eliminates the possible exploitation of the range data overlap. Additionally, timing and synching stability issues associated with the same radar's characteristics and the potential minor errors from the motion compensation strategies create a small level of incoherence between frames. This incoherence prevents SNR improvements through a simple frame-averaging operation. For this reason, the Synthetic Long Exposure (SLE) algorithm is proposed here as an alternate solution to enhance the power received from small precipitation droplets.

The SLE draws inspiration from the integrative measurement approach used in rain gauges, as well as the commonalities between radar data collection and photography, which have also inspired other radar data collection techniques (e.g., synthetic aperture radar). In low-light photography, a camera's shutter speed can be reduced to expose its film (or charged-couple device) to more light, revealing previously uncaptured targets. This technique is known as Long Exposure. Within the algorithm proposed here, the four frames in each data capture are combined to artificially mimic a long exposure, consequently enhancing the detection of small droplets. Hence the name Synthetic Long Exposure.

SLE is implemented by retrieving the highest power received by each range gate and velocity pair (i.e., pixel) in each frame to produce a new frame representing the cumulative effect of a particular capture command. That is, for each range and velocity pair in the

synthetic fifth frame's range-Doppler map, the same range and velocity pair is then evaluated in all four frames. The maximum power value found in all four frames for that particular range-velocity index is then copied to the synthetic frame.

Although a detailed study regarding the impact of the SLE on the precipitation signal properties was not conducted within this dissertation, impacts in range, velocity, and spectrum width are not expected. They are not expected because considering the low inter-frame coherence issue usually only affects a small number of individual pixels in each frame, all frames maintain the precipitation properties of range and velocity. Consequently, the synthetic frame should maintain these characteristics. However, even in cases where a particular frame does not hold these properties, the values in the other three will still produce a synthetic frame that is representative of the precipitation conditions, making the algorithm robust for operational deployment.

To aid this discussion and illustrate the working principles of this concept, let us consider an example taken from an atmospheric profile performed by this dissertation's WxUAS during the MAI^{2}S field campaign (see Chapter 7 for more details). In this example, the WxUAS was profiling a drizzle event from the surface to 250 m AGL. Figure 4.9 presents the four range-Doppler maps for each frame of a particular capture command during the profile. As expected, all four frames present similar minimum, mean, and maximum velocities, as well as overall range and average power. However, each frame presents a slightly different shape for its detection cluster.

Although each frame maintains the desired precipitation characteristics, these minor detection variations prevent the use of a simple averaging technique to improve SNR. This occurs because, between frames, the power for a range-velocity pair (i.e., pixel) can move to a neighboring pixel, making the power of the original pixel lower, or even zero, for that particular frame. Consequently, averaging a low-power pixel can greatly reduce the average power for that pixel in the synthetic frame. To counter this effect, the SLE algorithm takes the maximum power for a given pixel across all frames. The result of this operation can

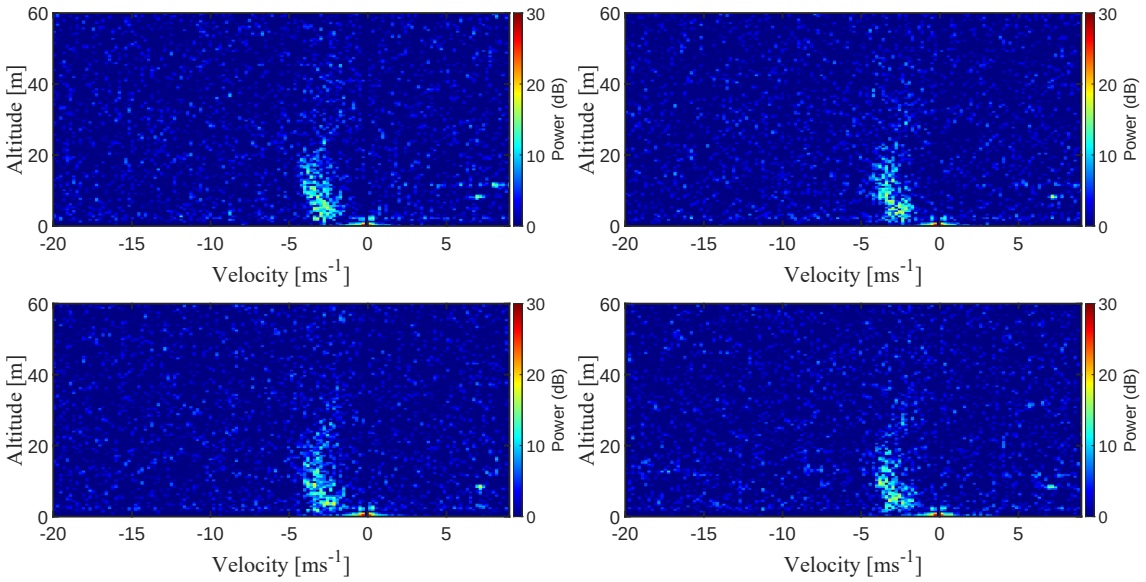


Figure 4.9: Range-Doppler map for the four frames of an atmospheric profile during a drizzle event at the MAI^{2}S field campaign. The data presented here includes the aircraft compensation algorithm.

be seen in Fig. 4.10, where the drizzle signal is much more pronounced than in each of the previous frames.

Comparing each frame in Fig. 4.9 with the partial synthetic frame in Fig. 4.10, it is possible to note that this technique potentially worsens the already elevated noise floor in each frame. This occurs because the technique is applied to all pixels indiscriminately. Applying a noise floor threshold to the partial SLE frame produces the range-Doppler map shown in Fig. 4.11, in which the characteristics of the initially faint drizzle detections are much more pronounced. However, even after the threshold, the remaining noise presents higher values than potential drizzle detections. This is exemplified by the two highlighted pixels in Fig. 4.11, where the potential drizzle that is clustered with all higher power detections produced a 7.55 dB return and the noise on the upper right corner presented an 8.83 dB return.

Although this high noise level is scattered and has a diminished impact on human (i.e., visual and qualitative) evaluation of the collected data, it presents a considerable challenge

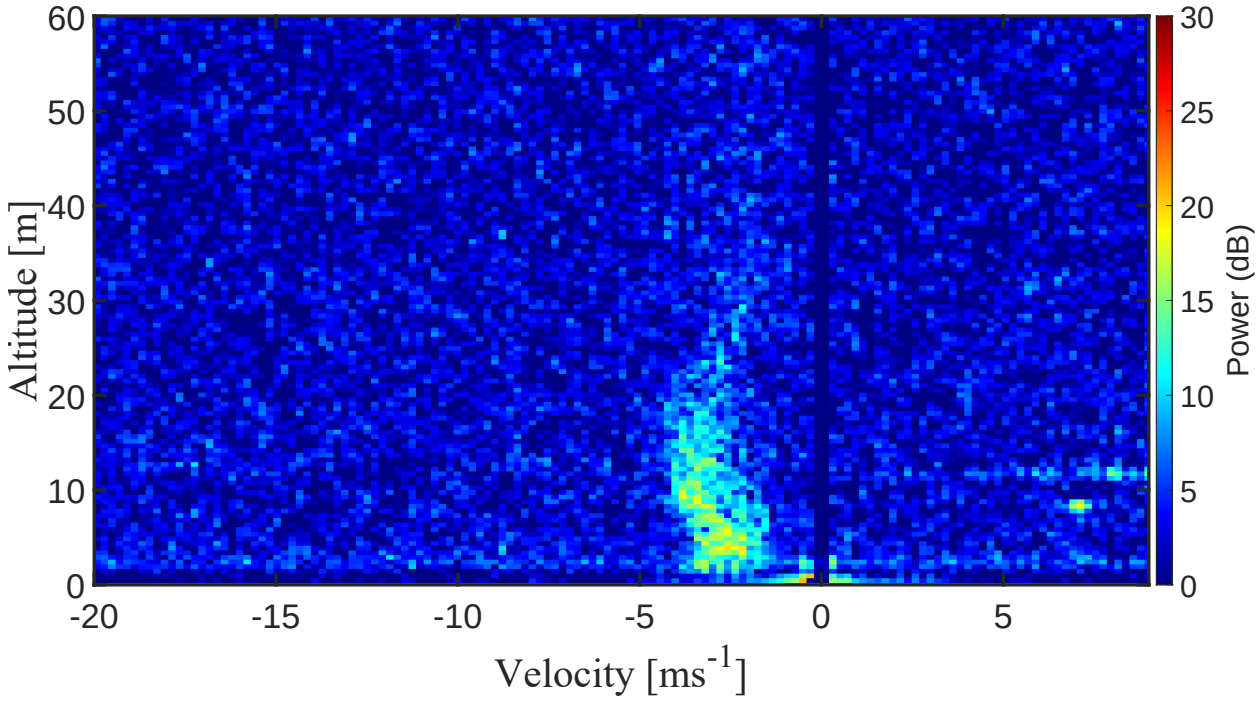


Figure 4.10: Range-Doppler map for an atmospheric profile during a drizzle event at the MAI²S field campaign. The data presented here includes the aircraft compensation and the SLE partial algorithms.

for automated calculations of relevant statistics (e.g., power, velocity, and spectrum width), as illustrated in Fig. 4.12. Comparing the results in Figs. 4.11 and 4.12, which hold the same information, the quantitative evaluation issues become evident. The perceived range (i.e., altitude above the radar) of precipitation seems to be reduced from 30 to 20 m, and the velocity and its spectrum width become undescriptive above 25 and 18 m.

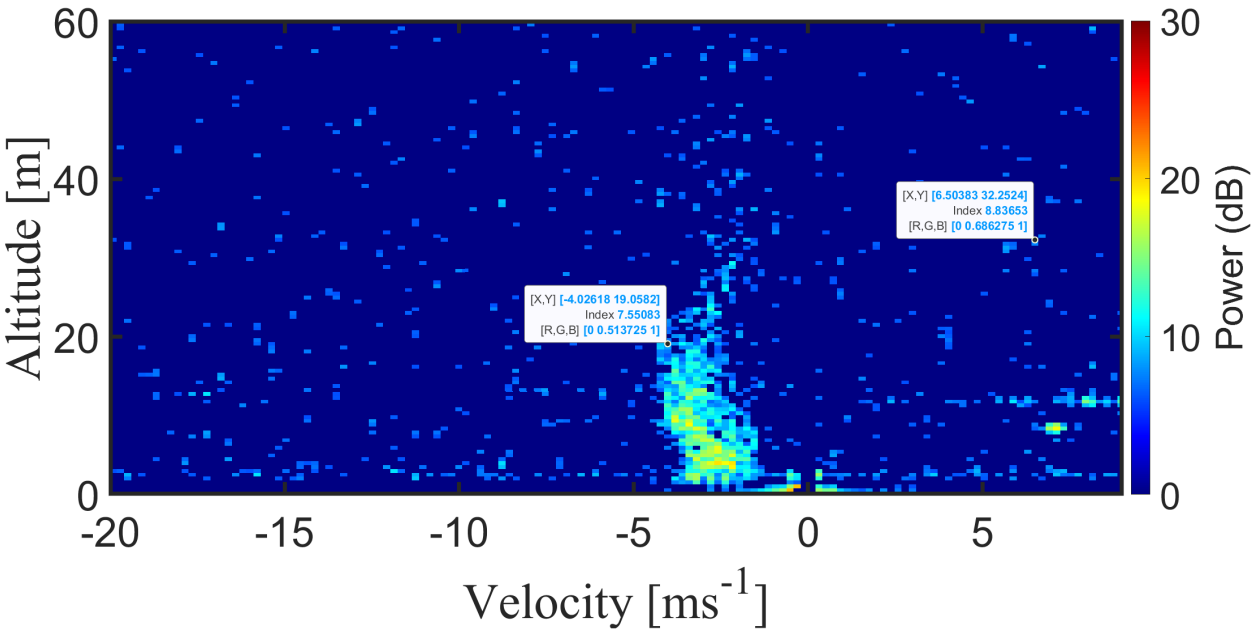


Figure 4.11: Range-Doppler map for the same drizzle event presented in Fig. 4.10 after the use of the motion correction, partial SLE, and a 5 dB threshold.

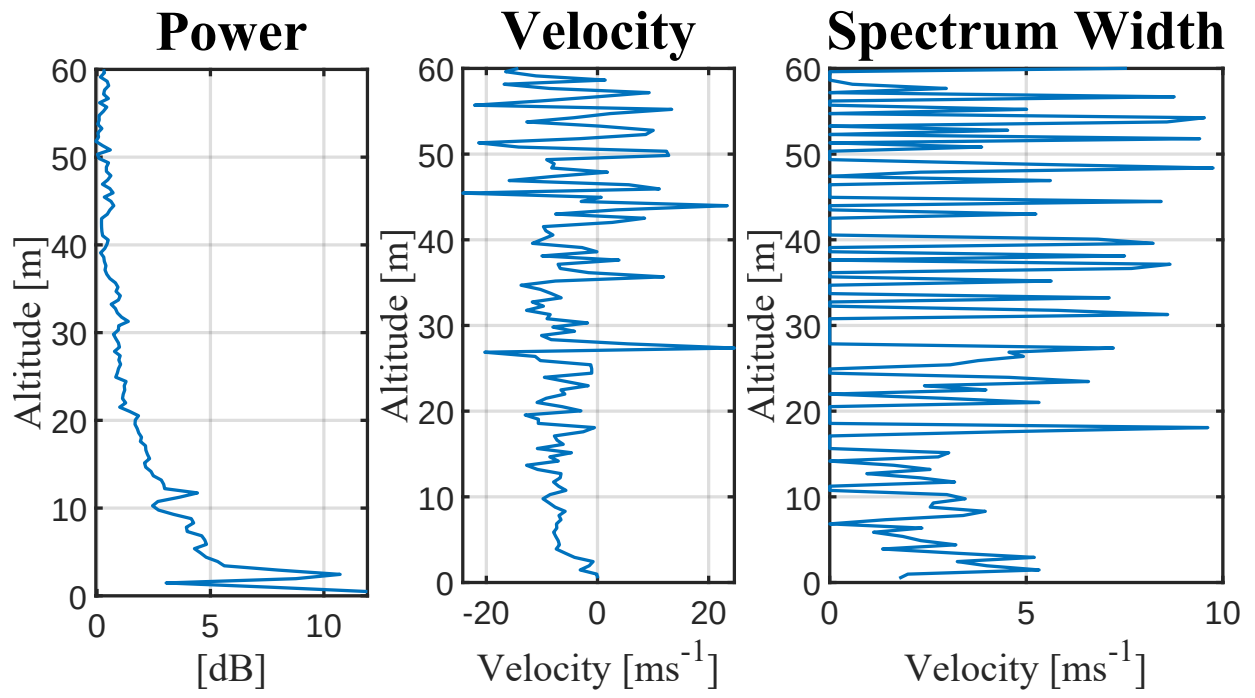


Figure 4.12: Example of the noise-induced challenge for programmatic calculations of relevant statistics, using the data displayed in Fig. 4.11.

However, a closer analysis of the original frames (Fig. 4.9) indicates that this issue was already present in the raw data. This is particularly evident when examining the potentially aircraft-induced noise on the pixels near 10 m and positive 7.5 $\mathrm{m\,s^{-1}}$ (which would indicate a hydrometeor falling upwards). This particular noise feature is present in all four frames and, consequently, in the synthetic frame. In addition to preventing the effective use of a threshold technique, these higher-power noise signals also prevent the use of power-weighted velocity calculations. For these reasons, besides the SLE technique, the use of the TI AWR2243 for weather applications also requires an algorithm capable of discerning these characteristics and selectively removing noise. Hence, this dissertation also proposes the Context-Dependent Noise Reduction algorithm, which is detailed in the following subsection.

4.4.3 Context-Dependent Noise Reduction

As discussed in the previous subsection, the TI AWR2243 produces considerable noise that hinder its ability to detect smaller-diameter precipitation, such as drizzle. Nonetheless, applying the SLE algorithm to the TI AWR2243 data produces a result in which, through context, the targeted precipitation is human discernable. For example, given the radar's vertically pointing beam, all precipitation is expected to present negative Doppler velocities (i.e., toward the radar). Considering the precipitation homogeneity assumptions in the time and space scales sampled (see Section 4.4.2 for more details), it is also reasonable to expect that precipitation will be clustered around a mean velocity characteristic of the sampled precipitation type. Even in mixed-phase precipitation events, it is reasonable to expect the velocity distribution to be continuous, without large jumps in value.

In addition to these contextual cues, the example given in Fig. 4.11 indicates that the TI AWR2243's relatively high-powered noise is scattered. At the same time, the faintest possible drizzle detections are clustered around high-powered precipitation detections near a characteristic mean velocity in the range bins near the radar. In this example, there are a considerable number of 5 to 10 dB potential detections clustered around the 15 to 20 dB

drizzle detections at approximately $-2.5\,\mathrm{m\,s^{-1}}$, 2 to 10 m above the radar.

In light of these contextual and clustering characteristics, one potential solution could involve limiting data processing to the range bins closest to the radar for a certain range of negative velocities. However, considering the variability of range, velocity, and spectrum width within different precipitation types, hard coding such rules becomes challenging. Given the contextual cohesiveness of the data, which leads the low-power-level data to cluster around the high-power-level detections that are representative of the mean Doppler velocities of detected hydrometeors, the solution lies in developing a context-dependent method to identify precipitation detection clusters that can dynamically adapt to each precipitation scenario. Such identification enables the elimination of wanted noise and, consequently, the correct calculation of the desired precipitation metrics.

Leveraging the range and velocity context of the range-Doppler map, the radar data can be interpreted as an image, where range bins and velocities represent a matrix of pixels. Converting thresholded power into a simple "yes or no" indication of data creates a binary (i.e., black and white image) that retains only the original data's contextual cohesiveness. Traversing the binary image pixel by pixel and evaluating each pixel's connectedness to the surrounding pixels, clusters of pixels can be identified. For the TI AWR2243's data, the best connectedness results were obtained using an 8-connect mask.

Once the clusters are identified and their size can be calculated, context-dependent decisions can be applied to the data (e.g., keeping only the largest cluster). Additional examples within the vertically pointing radar data context include, but are not limited to, removing clusters that represent velocities of hydrometeor falling upwards and removing zero velocity clusters in range bins near the radar (i.e., clutter). After applying these or other sets of rules to the binary cluster map, the "pixel positions" of each member of the remaining clusters can be used as a mask to filter the original data, thereby restoring its initial information. In the case of a TI AWR2243's range-Doppler map, restoring power, velocity, and altitude above the radar (i.e., range).

To illustrate the algorithm's robustness and its working principles, Fig. 4.13 presents an example of Context-Dependent Noise Reduction in a simple context. This example presents the data of a binary 20 by 20-pixel matrix. Although simplified, this example presents a more challenging algorithmic case because the noise and data are both represented by the binary digit "1". Therefore precluding the application of a threshold or other traditional noise reduction algorithms.

In this example, the meaningful information, the word "HELLO", does not have a precise mathematical description, yet it has a very explicit contextual meaning. By evaluating pixel clustering or connectedness with the same 8-connect mask, it is possible to identify the largest cluster, the one that composes the word, and eliminate all other clusters. Recovering the original information with the resulting cluster map yields a clean word except for one additional noise pixel connected to the top of the second letter "L"(identified by the red circle).

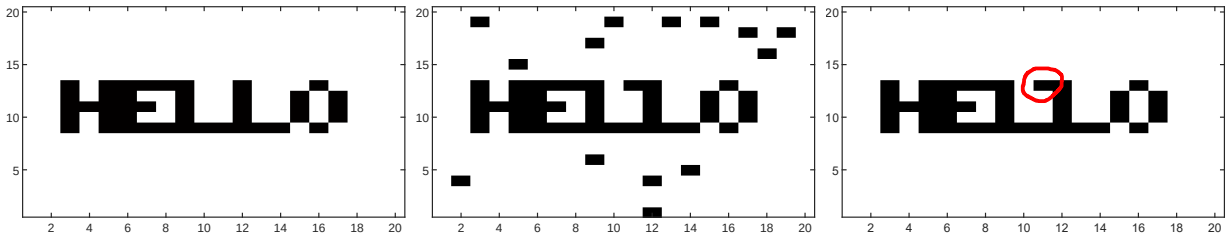


Figure 4.13: Example of Context-Dependent Noise Reduction Algorithm in a simplified context. The left panel presents the binary 20 by 20-pixel matrix with the word "HELLO", and the center panel presents the original and added noise. The right panel presents the noise-reduced recovery results. The red circle indicates a noise pixel that was not cleaned.

Besides indicating the algorithm can remove over 90% of the noise, these results also suggest that any leftover noise will be connected to the desired feature, producing only minor deviations. Within the context of precipitation data for the WxUAS, these minor deviations are not expected to impact the mean hydrometeor fall velocities, potentially manifesting themselves only as minor errors in the spectrum width. To verify these assumptions, the SLE and Context-Dependent Noise Reduction algorithms are applied to the same drizzle case

used as an example throughout this discussion (see Figs. 4.10 and 4.11) and to an additional rain case from the same day. Figure 4.14 presents the final range-Doppler map, mean velocity profile, and velocity distribution profile for the discussed drizzle event. Figure 4.15 presents the range-Doppler map, mean velocity profile, and velocity distribution profile for the new rain event.

The differences between the two cases align with the expected theoretical distinctions between rain and drizzle. For instance, the denser grouping between drizzle hydrometeors resulted in greater attenuation, limiting the radar's range to less than 25 m. In contrast, the more sparsely distributed and larger raindrops caused less attenuation and produced stronger returns, extending the range to nearly 50 m range. The velocity results further support this distinction. The rain case produced faster fall velocities (exceeding $-6\,\mathrm{m\,s^{-1}}$) over a broader range (-9 to $-4\,\mathrm{m\,s^{-1}}$), while the drizzle produced more uniform and slower fall velocities (with a mean around $-3\,\mathrm{m\,s^{-1}}$, ranging from -4 to $-1\,\mathrm{m\,s^{-1}}$).

Beyond demonstrating the robustness of the three post-processing algorithms proposed in this dissertation to produce meaningful data and enable the calculation of key metrics, the results shown in Figs. 4.14 and 4.15 also highlight the attainment of the overarching goal to development of WxUAS remote measurement design for the winter precipitation environment, which is to detect and distinguish different precipitation types. Additional supporting cases are presented in Chapter 7 along with a comparison to other colocated observation systems, including micro-rain radars. Nonetheless, before the discussion on the field deployment results, Chapter 5 offers a detailed discussion on the aircraft design that enables these measurements.

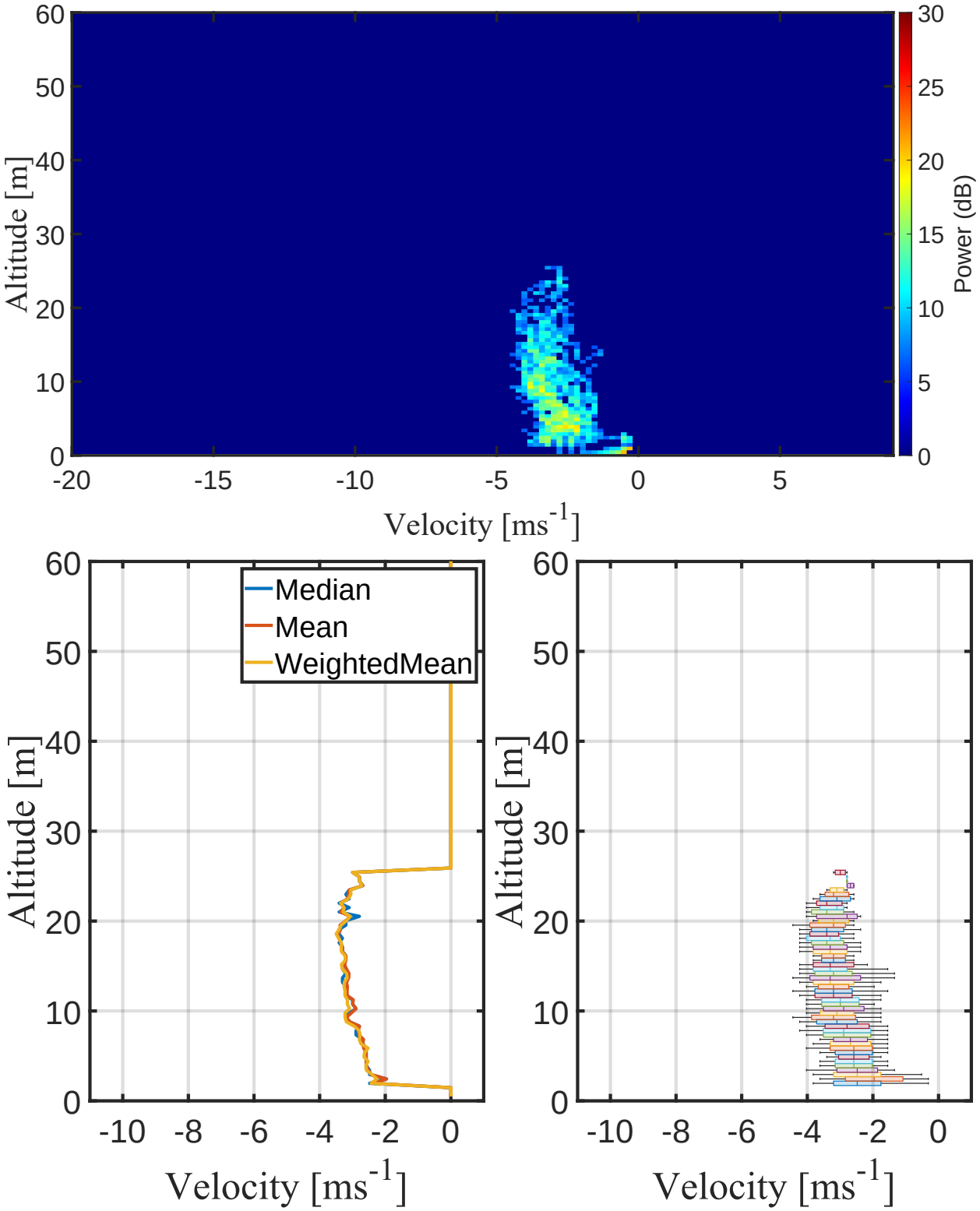


Figure 4.14: Illustration of the final range-Doppler map and velocity and distribution profiles using the motion compensation, SLE, and Context-Dependent Noise Reduction algorithms for the same drizzle event presented in Figs. 4.10 and 4.11.

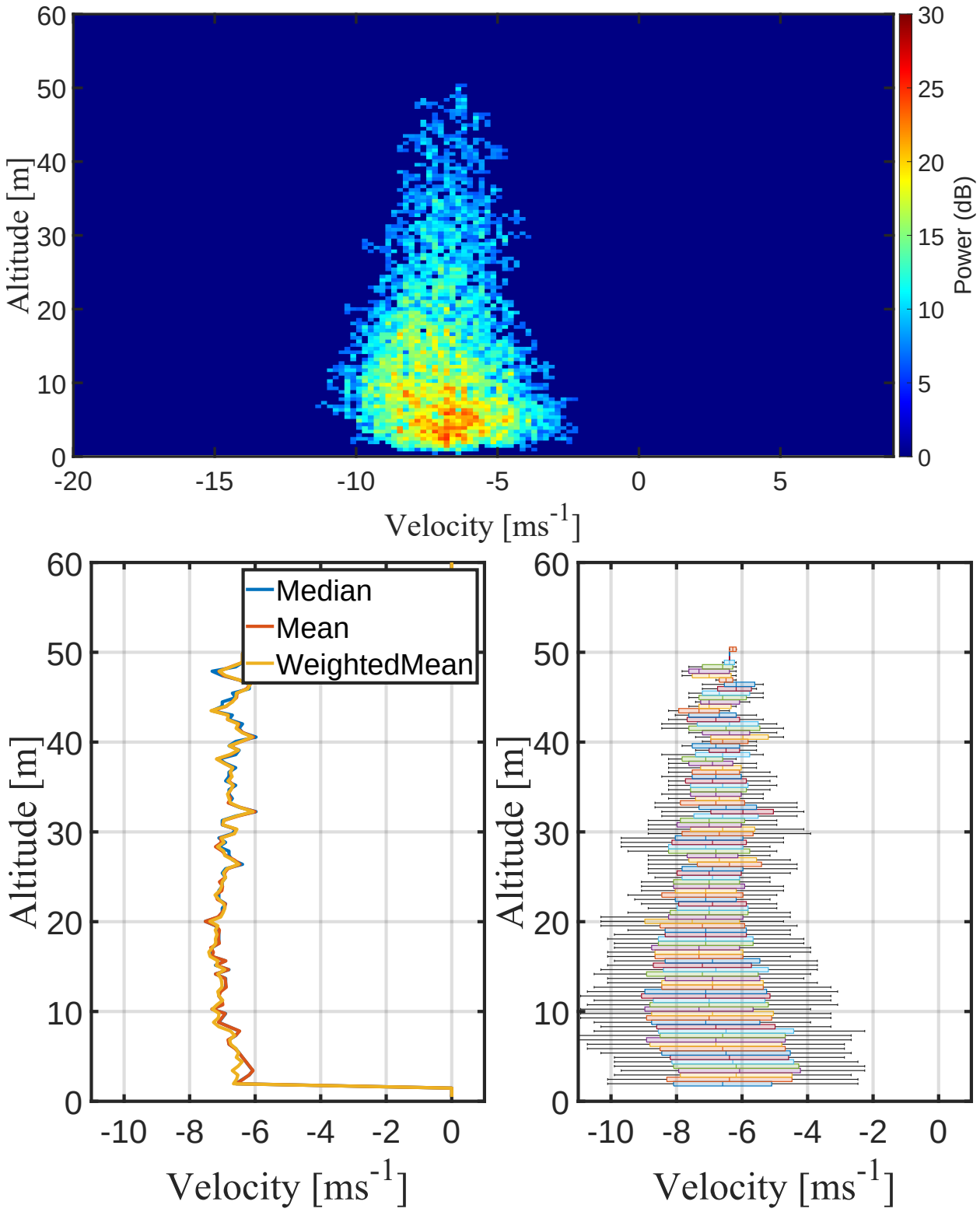


Figure 4.15: Illustration of the range-Doppler map and velocity and distribution profiles using the motion compensation, SLE, and Context-Dependent Noise Reduction algorithms for a new rain event.

Chapter 5

Unmanned Aerial Vehicle Design

"Innovation is not born from mere ideas but from the ability to turn those ideas into reality"

Attributed to Clarence "Kelly" Johnson

The concept of airborne weather observations is not new. In fact, circa 1945, the U.S. Congress mandated a multi-agency meteorological study to investigate the causes and characteristics of thunderstorms. To implement these observations, the Weather Bureau, the Army Air Force, the Navy, and the National Advisory Committee for Aeronautics leveraged the Northrop P-61 Black Widow, the first U.S. military aircraft designed specifically to carry a radar. Besides the radar, the research Black Widow carried instruments for temperature, icing, and precipitation measurements. Additionally, it had provisions to record its position and altitude, making it a pioneer as an airborne multi-sensor atmospheric observation platform [28].

Over the years, the demonstrated value of airborne measurements stimulated the creation of new airborne research groups and research aircraft. For instance, the National Science Foundation (NSF) established the Research Aviation Facility, which operates the HIAPER

GV, a Gulfstream V, and a Lockheed C130. Both platforms carry various scientific payloads as part of the NSF's Lower Atmosphere Observing Facility. In winter weather and aircraft icing research, the Canadian National Research Council instituted a multi-purpose flying laboratory based on a twin-engine Convair 580 aircraft. This aircraft supports a multitude of atmospheric studies, including cloud physics, cloud chemistry, and aircraft icing. In the past five years, this aircraft supported the In-Cloud Icing and Large-drop Experiment and the Investigation of Microphysics and Precipitation for Atlantic Coast-Threatening Snowstorms field campaigns.

Two common traits found in these examples are the systems' ability to carry all the necessary instrumentation and, most importantly, their ability to do so safely through hazardous environments. Although these systems do not operate in the atmosphere's lowest few kilometers due to crew safety reasons, particularly when aircraft icing risks are present, their general approach to tackling the airborne measurement challenge can still inform and inspire WxUAS observations. In this dissertation, this is particularly true because the proposed WxUAS for low-altitude wintry precipitation observations also adopts an integrated multi-sensor approach, combining novel remote and in-situ measurements, much like the P-61 Black Widow in project Thunderstorm.

While the design solutions discussed in Chapters 3 and 4 are intentionally cross-platform to encourage broader adoption by other WxUAS researchers and commercial operators, this chapter presents an aircraft design that integrates them into a cohesive multi-sensor observation system for data collection in the challenging conditions of low-altitude wintry precipitation environments. Therefore, serving as a practical demonstration of the combined potential of the measurement design concepts and the novel data generated through their implementation. Furthermore, since the design process followed a top-down approach, where measurement quality, safety, and operational requirements guided each decision, the resulting vehicle offers modularity, flexibility, and scalability. As such, the proposed aircraft can also be viewed as a generalized WxUAS technology demonstration platform.

5.1 Platform-base Selection

Although the aforementioned manned systems are adaptations of commercial and military aircraft used as a measurement platform, the lower cost and design complexity of UAVs allow for custom aircraft designs that prioritize sensor integration for improved measurement quality while enduring the harsh conditions of the low-altitude wintry precipitation environment. Given the diverse locations and conditions of field deployments in this type of research, design decisions are heavily influenced by operational constraints and flight patterns.

The variability in field deployment conditions for this research requires an aircraft that is small and can be easily loaded and unloaded for travel or redeployment. To accommodate the sensor integration requirements for this research and its weight, a fixed-wing UAV would require a 1.8 to 2.5 m (6 to 8 ft) wing span. To support the same payload, a multirotor could have propeller discs as small as 0.25 m for an equivalent wing span of 0.75 m (approximately 2.5 feet). Besides increasing storage and transportation convenience, a smaller aircraft can be kept fully assembled and flight-ready, eliminating the risks of human errors during field assembly, whereas a larger aircraft often needs to be disassembled for transportation and reassembled before flight.

Additionally, these locations may often be unfavorable for flight operations, with nearby power lines, tall trees, or structures (e.g., water towers, buildings, antennas). Consequently, a small operational footprint is desired. A small UAV that can vertically take off and land requires a small surface area and a small unimpeded volume near the surface to clear nearby obstructions, allowing it to operate in more locations. Although some fixed-wing UAVs have Vertical Take Off and Land (VTOL) capability, they require larger unimpeded volumes near the surface due to higher position-drift potential in windy conditions (common in winter weather storms). Due to their smaller size, multirotors are often more proficient at holding a surface relative position, making their operation safer in obstructed environments.

Considering the measurement design choices discussed in Chapters 3 and 4, particularly the choice to deploy the radar pointing upwards (toward the falling precipitation), the ideal

flight pattern for these measurements is a profile (see Chapter 2 for definition). Although both fixed- and rotary-wing UAVs can perform profiles, fixed-wing profiles require either a spiral or stepped ascent. These two flight paths require a circular motion around a center point. Given that a fixed-wing UAV always faces its flight direction, this leads the aircraft to alternate between facing and not facing the incoming wind. Additionally, given the strength of the incoming wind, the times spent on the upwind and downwind legs of the circular path are not equal. Even though spirals and stepped ascents can be post-processed into profiles, the mentioned flight characteristics often have reduced their sampling uniformity compared to multirotor profiles.

In addition to the sampling uniformity issue, spiral and stepped ascents also require a larger footprint for airspace geofencing. This larger footprint can make the FAA altitude waiver requests more challenging, particularly because in high wind conditions, fixed-wing UAVs present a higher risk of drifting from the profile's center point. Another concern of fixed-wing UAV operations in high winds is the increased surface and aerial footprints in the event of a critical malfunction. As they are aerodynamic systems, they may be kept aloft by the wind and be carried over longer distances on the surface.

Winter precipitation events can occur at any time and location; hence, team availability becomes a critical component of operational readiness. Therefore, a critical vehicle operational constraint is its pilot skill level requirements. The easier an aircraft is to pilot, the more people can be trained on it, more team composition flexibility is achieved, and more operational readiness is attained. Because multirotors do not have moving control surfaces, their flight control hardware and software are more advanced, leading to a more automated aircraft that requires a less skilled pilot.

Considering all the points presented in this section, a multirotor concept was selected as the base platform for the final aircraft design developed to support and demonstrate the WxUAS proposed in this dissertation. Although multirotor platforms better accommodate this research's requirements, the operational and flight characteristics that make it advan-

tageous can also represent challenges for airborne atmospheric measurements. For instance, multirotors cause more mixing and disturbances of the sampled atmosphere (as discussed in Section 2.3), and their reduced aerodynamic stability makes them more susceptible to icing-induced malfunctions and provides reduced flight endurance. However, these issues have well-known mitigation strategies in the aircraft and integration design, which will be addressed in the following sections.

5.2 Winter Weather Requirements

The low-altitude winter precipitation environment presents considerable hazards for small autonomous aircraft. These hazards include but are not limited to, water incursion from precipitation, aircraft icing, high winds with even higher gusts, cold temperatures, and reduced visibility. Therefore, an aircraft designed to support atmospheric sampling in this environment must account for these conditions while minimizing the platform-induced measurement interferences discussed in Chapter 2.

Besides the obvious threat to electronic components, water incursion from precipitation can accumulate inside the vehicle, changing its overall weight. This in-flight weight change can hamper the flight controller's ability to interpret the aircraft response, leading to a catastrophic system failure. This can occur because the Proportional–Integral–Derivative (PID) control algorithm requires a set of pre-determined tuning parameters, which take into account the aircraft's mass, to correctly give inputs to the motors to react to environmental disturbances (e.g., wind gusts) while performing the desired maneuvers (e.g., move from point-A to point-B).

In liquid form, accumulated precipitation can shift inside the aircraft, creating a delayed center of mass shift that further hinders the efficacy of the PID controller. Additionally, because the aircraft will ascend through the atmosphere, it can transport this ingress precipitation to below-freezing temperatures. Aside from potentially affecting electronic components

with above-freezing operational temperature requirements, the expansion in ice formation can internally weaken or damage the airframe. Consequently, a small autonomous aircraft designed for this environment must be waterproof. However, as a research craft, it cannot be permanently sealed, and it must also allow easy access to its main components.

In the mixed-phased wintry precipitation environment, aircraft icing can also take place when SLW or SLD come in contact with the airframe. In the case of multirotors, this is more problematic when this contact occurs with the propellers. Ice formation on the propellers can increase drag and reduce lift, consequently reducing thrust. It can also produce vibrations that induce errors in the aircraft's PID controller. Although flight control algorithms have been progressively improved to recognize and mitigate PID degradation caused by ice accretion, non-uniform ice shedding from the propellers continues to pose a significant challenge. In such cases, the mass of large accretions causes them to be suddenly ejected from the propeller due to its rotation.

When this ejection takes place on only one (or two) of the multirotor's propellers, the now ice-free propeller spins much faster than the others, creating errors in the PID calculations. From an aircraft design perspective, there are limited options for mitigating this issue. For instance, an increased thrust-to-weight ratio and redundant motors and electronic speed controllers may delay performance diminishment, allowing the pilot to maneuver out of the condition. Special anti-icing coating and heated propellers may reduce ice accretion. However, given these strategies' limitations and potential impact on the weather measurement, the most effective approach to managing this challenge remains operational practices that minimize exposure time to such conditions.

Albeit wintry precipitation can happen under a variety of conditions, the mixed-phased scenarios that are of most interest for this research are often associated with winter storms and the temperature and pressure gradients seen on their leading and trailing edges. Also associated with this environment are strong winds with even stronger wind gusts. Within this environment, the winds created by the Low Level Jet (LLJ) are often the most hazardous.

For a WxUAS performing an atmospheric profile, the LLJ represents a sudden increase in mean and gust wind speeds found only a portion of the flight path. Therefore, the pilot can be surprised by these conditions that can overwhelm the aircraft's ability to hold its position.

Regarding aircraft design, an airframe with low drag and a motor-propeller combination for high revolutions per minute is a well-known solution to counter high winds and strong gusts. However, such a design is antagonistic to a WxUAS that favors clean airflow over the sensors and has to carry multiple heavy sensors while ascending slowly to mitigate sensor time-response issues and increase sampling resolution. Therefore, a compromise must be determined considering the desired profile height (1.500 m, approximately 5,000 ft), ascent velocity ($2\,\mathrm{m\,s^{-1}}$, see Chapter 2 for justification), maximum wind speed ($30\,\mathrm{m\,s^{-1}}$, approximately 60 mph), sensor payload capacity (2 kg).

The cold temperatures experienced in the wintry precipitation environment can impact the performance of the flight controller and other electronic components. It also has a well-known negative impact on Lithium-Polymer (LiPo) batteries. To mitigate these temperatures, the aircraft design must provide some form of insulation to the components, which allows them to self-heat. The battery selection must have a total capacity that considers a potential voltage drop and still allows the pilot to perform an emergency landing. Additionally, operational practices should keep the aircraft in a heated environment between flights to avoid unnecessary exposure to the elements.

Finally, the presence of low-altitude clouds, mist, drizzle, or fog can severely hinder the pilot's ability to visualize the aircraft, particularly considering its desired small size for transport and reduced operational footprint, as discussed in the previous section. To mitigate this issue, the proposed aircraft design should leverage illumination patterns adopted by manned aircraft and color schemes that favor aircraft orientation from the remote pilot's perspective on the ground.

Although this is a research prototype, the design should be robust and resilient, support-

ing serviceability and many deployments with the same unit. This is important due to the time-intensive system characterization procedures necessary for meaningful measurements (see Chapter 2 for details) and the comparability of results across deployments.

5.3 Aircraft Design

To meet the requirements outlined in the previous sections, the aircraft design process followed a top-down approach, where measurement quality, safety, and operational needs guided the airframe design. Balancing these three, at times conflicting, requirements, this section details the design decisions and critical features necessary to produce a multirotor WxUAS for atmospheric sampling in the winter weather environment and others.

As discussed in Chapters 2 and 3, minimizing rotor-induced mixing and heating is paramount for higher-quality in-situ WxUAS measurements. However, for a multirotor design concept, a higher number of rotors generally increases flight stability, which is much needed to counter the harsh operational conditions of the wintry precipitation environment. Considering both requirements, the proposed multirotor design was based on an X-frame quadcopter concept because it presents the minimum number of rotors needed for inherent omnidirectional stability. Due to its symmetric thrust vectors relative to the aircraft's center of mass, an X-frame quadcopter is equally resilient to wind gust disturbances in the roll and pitch axes.

Additionally, by increasing the ratio between an X-frame quadcopter's motor arm length and propeller size, a considerable gap between the rotors can be created. This gap allows minimally disturbed airflow over the airframe's center during vertical ascents, particularly when facing the incoming wind, enabling the weather sensors to sample the atmospheric condition with minimal or undetectable interference.

As detailed in Chapter 4, the proposed WxUAS remote sensing design already requires the WxUAS to perform its atmospheric profiles in windvane mode (i.e., facing the incoming

wind). This requirement is based on the mmWave phased array radar's aircraft motion compensation algorithm, which uses digital beamforming to maintain the necessary assumptions to operate as a vertically pointing precipitation observer (see Fig. 4.4). For this reason, its radome needs to have a field of view unimpeded by other aircraft components. Additionally, the radar's antenna must correctly align with the aircraft's pitch axis (see Fig. 5.3).

Based on these radar integration requirements, the aircraft's overall symmetry was maintained by integrating the remote and in-situ sensor enclosures as the topmost elements of this design in a side-by-side configuration. In this configuration, the airframe body's length was determined by the length of the remote measurement's radome base, and its width was given by the sum of the widths of the radome base and the in-situ sensors' outer shield. The proximity of these measurements resulted in a nearly squared airframe body, maintaining the design's overall symmetry. These and other design decisions, further detailed in the following subsections, resulted in the 3-dimensional computer-aided aircraft design illustrated by Fig. 5.1 (additional views are available in Appendix E).

Given the uncertainty inherent in designing a novel airborne atmospheric observation system, modularity, flexibility, and scalability were also key considerations to ensure the design could accommodate future modifications based on insights gained from field deployments. As a result, manufacturing techniques were intentionally limited to 3D printing, basic carbon-cutting methods, and the use of commercially available fasteners and sealants.

Within the rapidly prototyped 3D printed parts, Lightweight Polylactic Acid (LW-PLA), Thermoplastic Polyurethane (TPU), and Carbon-fiber reinforced Polylactic Acid (PLA-CF) filaments were used to accommodate the different material property needs for this design. In the case of load-bearing PLA-CF components (e.g., battery holder, motor mount, and motor arm attachment), the mechanical failure risk was mitigated by printing their layers parallel to their prominent stress.

The airframe construction followed a straightforward carbon fiber sandwich-structured composite technique, where two carbon fiber plates secure the four carbon fiber motor arms.

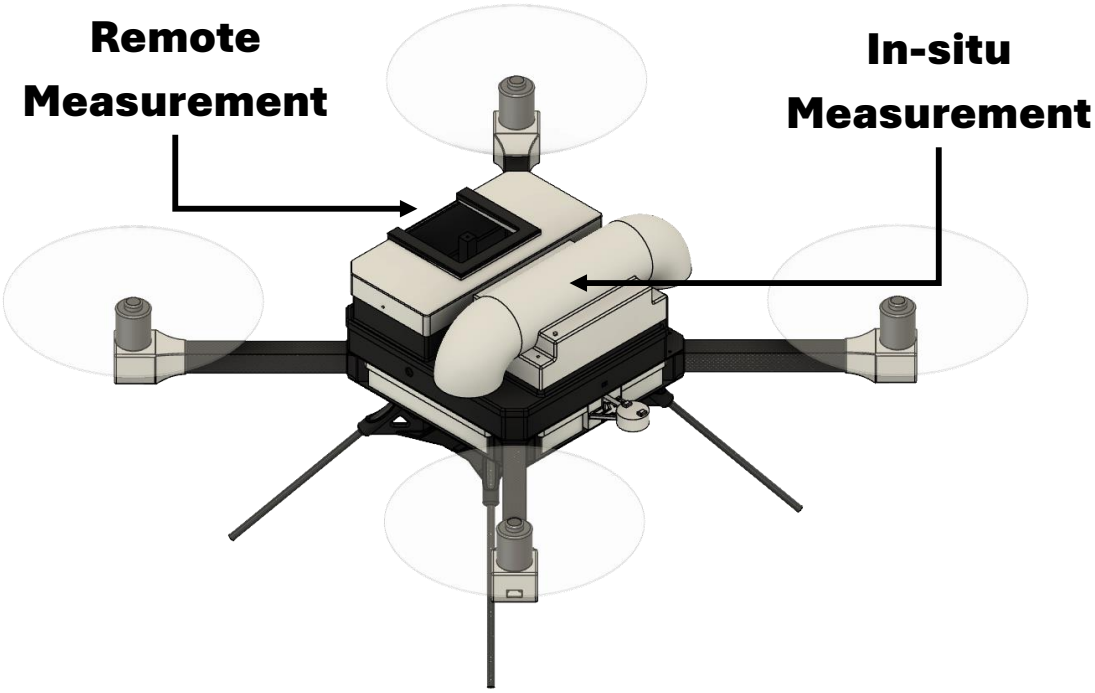


Figure 5.1: Isometric view of the 3-dimensional computer-aided design for this dissertation's WxUAS technology demonstration platform with the remote (left) and in-situ (right) measurement solutions integrated as its topmost component.

To address the need to shield the flight components from water, the usually hollow space between the two carbon fiber plates was replaced by a water-resistant custom LW-PLA flight electronics bay. The stiffness and strength of this carbon-fiber and LW-PLA composite sandwich structure allowed for the use of lighter and more workable 1 mm carbon plates in place of the traditional 2.5 to 3 mm plates. This and other features of this layered composite structure are illustrated by Fig. 5.2.

Another beneficial feature of designing a WxUAS aircraft in which all flight components (except for the flight controller) are below the top plate of the composite sandwich structure is that it naturally accommodates a variety of sensor payloads, making it inherently multi-purpose. This feature is highlighted in Fig. 5.2, which shows the sensor integration bay as a replaceable module above the flight electronics bay and the top plate of the airframe's composite sandwich structure.

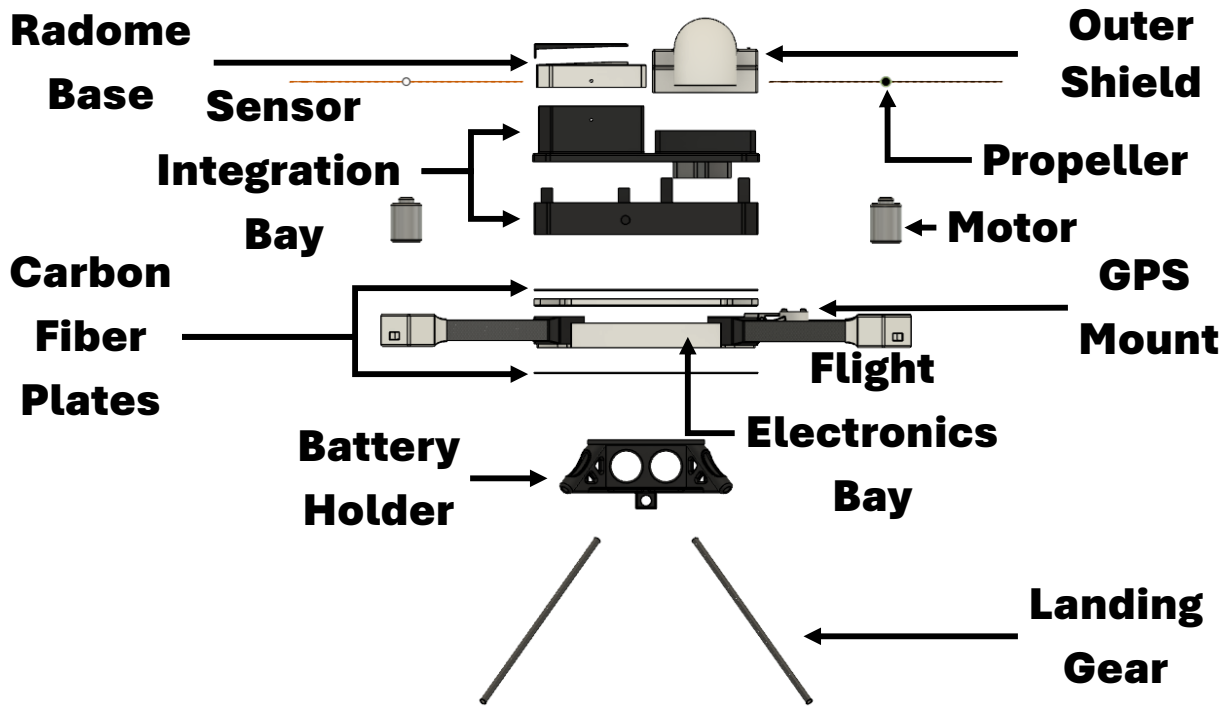


Figure 5.2: Exploded orthographic front view of the main components in the 3-dimensional computer-aided design for this dissertation's WxUAS technology demonstration platform.

Besides promoting modularity, flexibility, and scalability, the simplified and low-cost construction techniques adopted also enable the widespread adoption of this aircraft design within the WxUAS research community. Using this dissertation's Stereolithography Computer-Aided Design (STL) files, researchers in the community can replicate and utilize this aircraft design in their research with this dissertation's atmospheric measurement solutions or their own. Given the potential for aircraft interference in airborne measurements, the broader adoption of this aircraft design as a base platform for WxUAS capability development and demonstration could lead to its further characterization and increased comparability between systems, as well as overall WxUAS data.

Therefore, aside from serving as a practical demonstration of the combined potential of this dissertation's atmospheric measurement design concepts and the novel data generated through their implementation, this chapter's aircraft design hopes to also serve as a generalized WxUAS technology demonstration platform. The critical design features that support

these statements are further detailed in the following three sub-sections, which detail how its design features enable enhanced measurement quality, safety, and operational flexibility.

5.3.1 Measurement Quality Features

As previously discussed, to accurately characterize the low-level wintry precipitation environment, this dissertation's remote and in-situ measurement solutions require an unimpeded path to the incoming air and precipitation that will be sampled. While in a vertical ascent to perform an atmospheric profile, this unimpeded path is defined as a straight line between the air above and in front[1] of the aircraft and the WxUAS's sensor integration bay.

For the mmWave radar, an unimpeded path is necessary to eliminate beam blockage, as well as Doppler noise and clutter effects in the range gates nearest to the radar. Because the remote measurement design uses digital beamforming to mitigate wind-induced pitch changes while maintaining the radar beam perpendicular to the surface, its unimpeded path assumes an elliptical shape above the aircraft along its pitch axis. For the temperature, relative humidity, and particle size measurements, the unimpeded path is a smaller line leading to the in-situ sensor outer shield, in which moisture and cloud-sized particles can travel unaffected to be sampled. Fig. 5.3 illustrates this dissertation's in-situ and remote measurement designs with the critical obstruction zones for each measurement properly highlighted.

While the design choice to position the sensor integration bay at the top of the aircraft helps provide an unimpeded path from above, it does not fully eliminate the potential for aircraft-induced measurement errors. As noted in the literature, proximity to the motors or propeller tips can introduce up to a 1 °C bias in temperature measurements [46]. Furthermore, research on optimal placement of sonic anemometers on WxUAS demonstrates that airflow in this region is accelerated [76], potentially biasing hydrometeor fall velocities near the radar. Therefore, the propeller distance from the sensor integration bay in the horizontal

[1]This frontal path assumes the aircraft is capable of detecting the predominant horizontal wind direction and orienting its nose toward it (i.e., wind vaning, as detailed in Chapter 4)

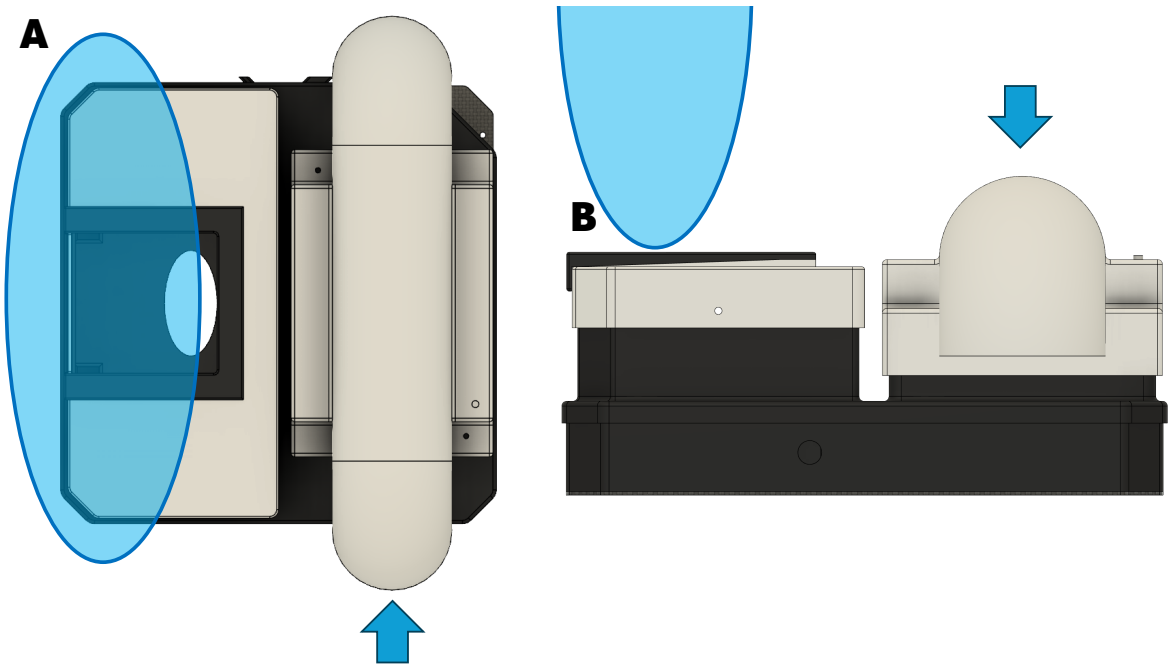


Figure 5.3: 3-Dimensional computer-aided design for this dissertation's in-situ and remote measurement solutions with the critical obstruction zones for each measurement. (A) Orthographic top view, with elliptical shading over the radar's field of view and arrow indicating the predominant direction for the incoming wind for in-situ samples. (B) Orthographic front view with the same obstruction regions.

and vertical planes is critical for accurate measurements.

Although previously published research for WxUAS measurements in convective weather has shown that accurate temperature and relative humidity samples can be obtained directly below the propellers—at one-third of the distance between the propeller tip and the motor shaft[46]—or through an unimpeded path behind the propellers with a gap smaller than half the propeller's diameter [59], the high sensitivity of precipitation phase to temperature changes in the near freezing environment may require a more restrictive approach.

For this reason, the modular and flexible precepts in this aircraft design allow the cut-to-length carbon-fiber motor arms to be replaced to accommodate each application's prescribed distance between the sensor integration bay and the propeller tips. To illustrate this concept, Fig. 5.4 shows the aircraft's orthographic top and front views with red shaded areas representing the propeller discs and the blue shaded area representing the unimpeded path

to the sensor integration bay.

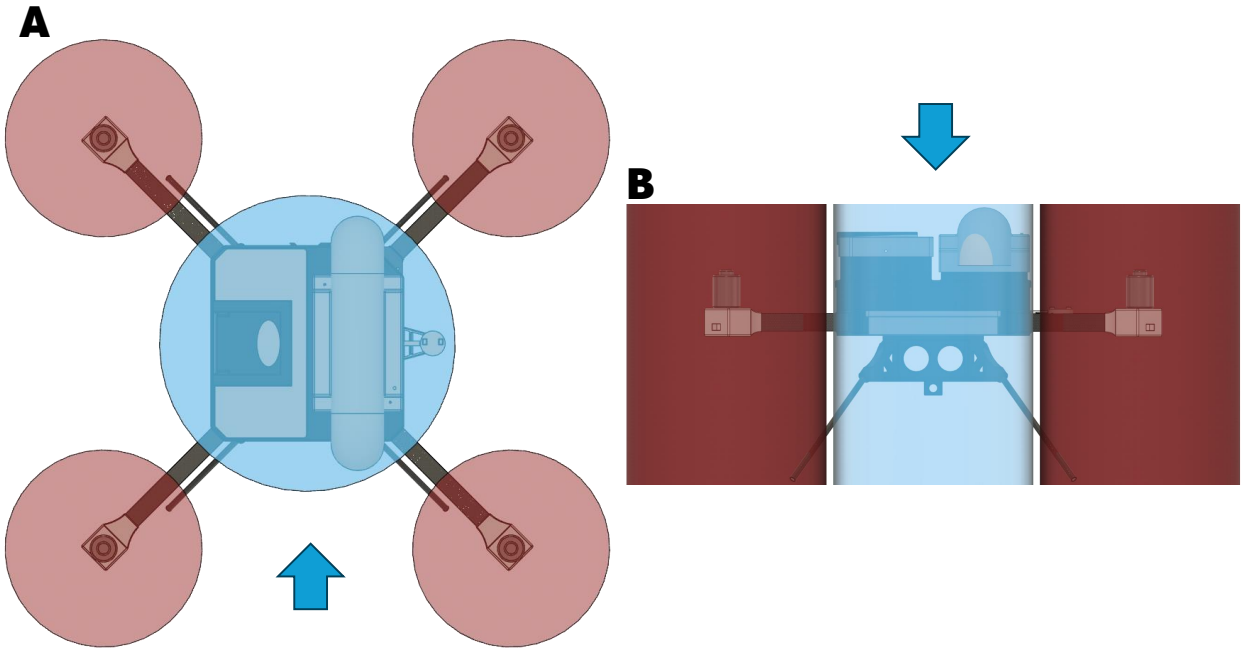


Figure 5.4: 3-Dimensional computer-aided design illustrating how the aircraft arm length can be defined based on propeller size to allow an unimpeded path to the sensors. (A) The aircraft's orthographic top view with the red shaded areas representing the propeller discs and the blue shaded area representing the 1.5-propeller diameter clearance from above. (B) Orthographic front view with the same highlighted regions.

For this dissertation's wintry precipitation application, the prescribed distances were estimated by doubling the successful results presented by Greene et. al [46] and were empirically verified via field experiments. For the unobstructed pathway towards the aircraft's top, the recommended clearance is at least a 1.5-propeller diameter distance between the four propeller tips and the center of the sensor integration bay (Fig. 5.4–A). For the front of the aircraft, at least a 1-propeller diameter clearance between the tips of the two frontal propeller discs (Fig. 5.4–B).

Finally, in cases such as those encountered in this dissertation's research, where the aircraft may need to take off at varying pressure altitudes and temperatures (e.g., in Norman, OK, or Boulder, CO) within a short span of time, it may be advantageous to accommodate

different propeller sizes without altering the motor arm length. In such instances, the motor arm length should based on the largest propeller size. Nonetheless, for increased safety and transportation convenience, motor arm length minimization should always be attempted.

5.3.2 Safety and Operational Features

As discussed in Section 5.2, water ingress into the aircraft presents a considerable risk to its electronic components, the airframe, and the flight controller's PID algorithm. Consequently, a small autonomous aircraft designed for operations in the wintry precipitation environment must be water resistant. However, as a research craft, it cannot be permanently sealed, and it must also allow easy access to its main components. To address these requirements, the proposed aircraft leveraged LW-PLA compartments, temporarily sealed by overlapping layers and the abovementioned composite-sandwich structure.

For instance, the LW-PLA flight electronics bay placed between the two carbon-fiber plates (see Fig. 5.2) was manufactured in two parts: a base and a lid. The lid for the flight electronics bay was manufactured with two overextending "lips" that superpose the base outside and inside of it. The practical effect of these overextending "lips" is to create a 2 mm recess on the lid to close the flight electronics bay. The seal in this system is given by the screws in the composite-sandwich structure and its carbon-fiber plates which clamp the flight electronics bay's lid and base tower. The clamped overlapping layers from the flight electronics bay's lid and base create a water path in which the falling precipitation would have to travel upwards and back down to enter it, rendering it effectively water-resistant without sealants.

This same technique was applied to the sensor integration bay's base, lid, radome, and in-situ sensor outer shield. These overlapping layers and their sealing effect are illustrated in Fig. 5.5, which presents a diagonal cross-section cut of the 3-dimensional computer-aided design highlighting locations where layers and materials are joined.

In addition to this sealant-less water-resistance technique, a method to address the need

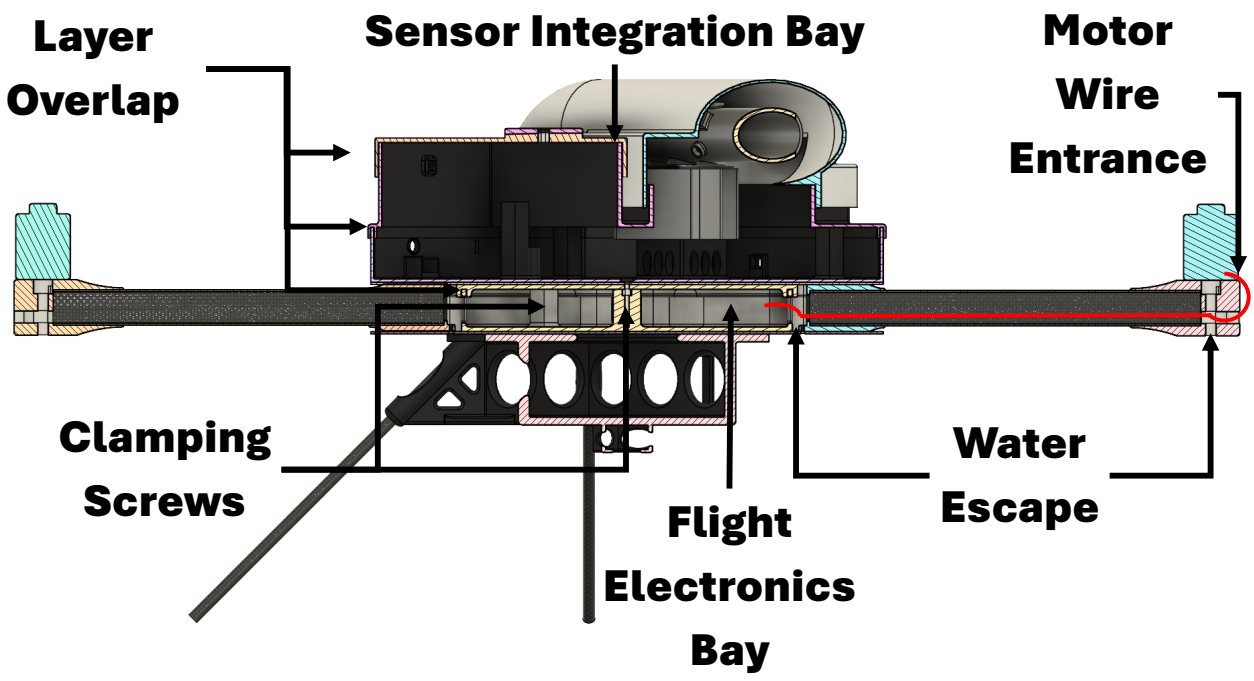


Figure 5.5: Diagonal cross-section view of the aircraft's 3-dimensional computer-aided design illustrating the seal-less water resistance design techniques.

to connect the electronic speed controllers (inside the flight electronics bay) to the motors (outside the airframe) was also implemented in this airframe design. In this method, the motor wires enter the frame through the PLA-CF motor mount with an "C" shaped bend, allowing the drip at the bottom bend of this shape. Before entering the carbon-fiber motor arm, the wire passes a water escape port, which allows any non-dripped water to be caught in the motor mount and exit it through this downward-facing port (see Fig. 5.5). In the unlikely event that water droplets remain attached to the wires and enter the carbon-fiber motor arm, a gap between the motor arm and the flight electronics bay with a secondary water escape orifice offers another method to eliminate accumulated precipitation.

Figure 5.6 presents a horizontal cross-section of the aircraft's orthographic top view highlighting the two water escaping points within the motor arm. It also presents the LiPo battery connector entrances cut through the bottom of the flight electronics bay and the bottom carbon-fiber plate in the composite-sandwich structure. Having the batteries'

male XT-60 connectors enter the female XT-60 connectors on the aircraft from the bottom eliminates the remaining point for potential water ingress.

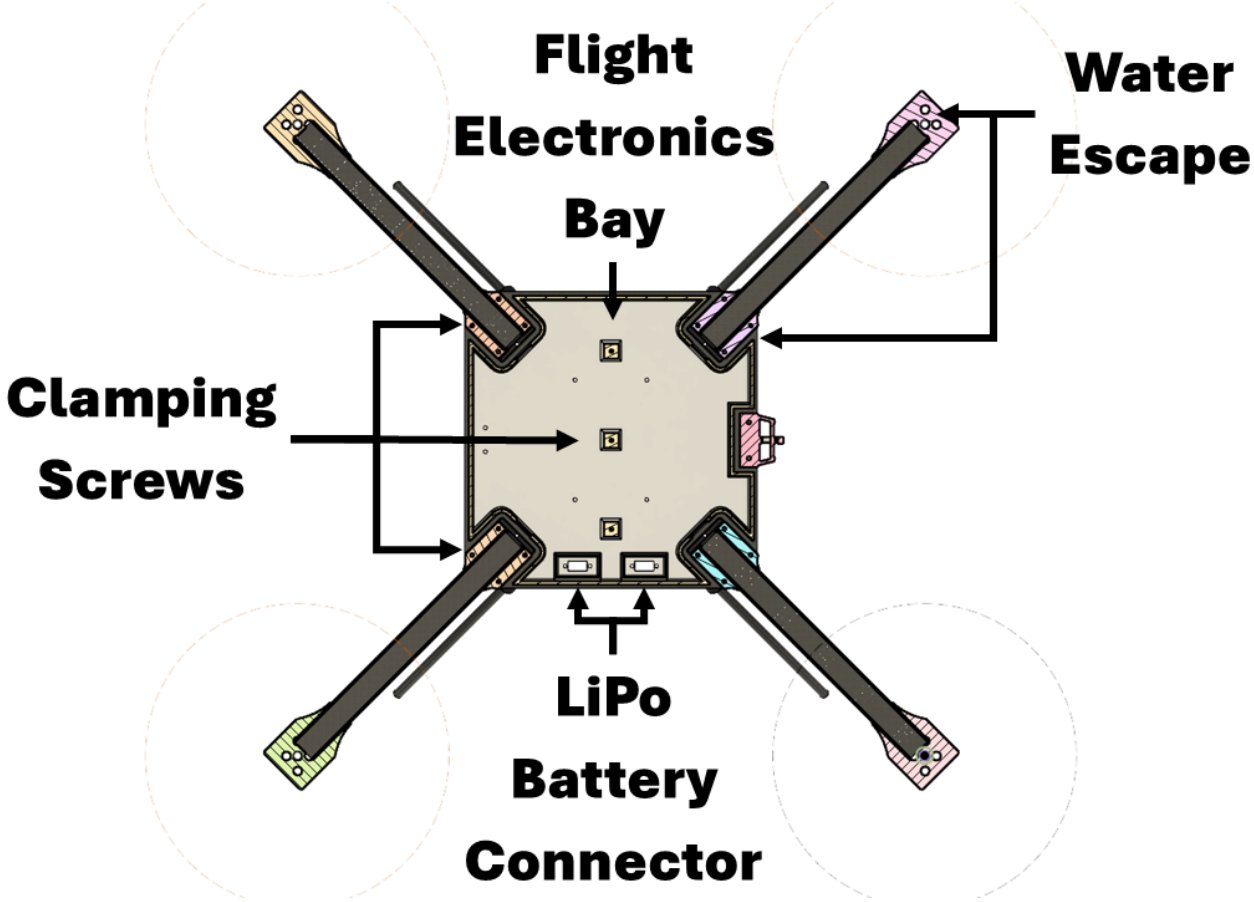


Figure 5.6: Horizontal cross-section of the aircraft's orthographic top view highlighting the two water escaping points within the motor arm.

Besides water ingress, another considerable risk encountered in the low-altitude wintry precipitation environment is the risk of aircraft icing. As discussed in Section 5.2, there are only a few aircraft design strategies to mitigate this risk. Amongst these strategies, an increased thrust-to-weight ratio, as well as redundant motors and electronic speed controllers, can be applied with a smaller risk of interference with the measurement or a considerable increase in design complexity. Given the desired scientific payload (defined in Section 5.2 as 2 kg), an increase in the thrust-to-weight ratio can only be attained by reducing airframe weight or increasing thrust. Considering the airframe was already designed with weight re-

duction techniques (e.g., composite sandwich structure), the remaining strategy is an increase in thrust.

To increase the aircraft's thrust, either a more powerful propeller-motor combination must be employed or the number of rotors must be increased. Employing a powerful propeller-motor combination could require an adjustment of the aircraft's motor arm length and overall dimensions to maintain the measurement quality features detailed in Section 5.3.1. Nonetheless, adjusting these measurements could impact the aircraft's operational characteristics.

Increasing the number of rotors implies changing the aircraft's base concept from a quadcopter to a hexa- or octacopter. However, the X-frame quadcopter concept selected in Section 5.1 combined with the modularity of the 3D printed motor mounts, as well as the integrated landing gear and battery holder feature in this design, enables the implementation of an X-Frame co-axial quadcopter concept without any changes to the airframe. Figure 5.7 illustrates this concept with a partial build of one of this dissertation design's early prototypes. In this illustration, the color-coded tapes indicate the spinning direction of each motor, which is used to confirm the wiring and configuration of the electronic speed controllers.

Each of the four motor arms is equipped with two motors aligned on the same propeller axis. Although this configuration does not double the total thrust due to inefficiencies from the wake of the top motors, it significantly increases the aircraft's thrust while maintaining the same footprint as a traditional quadcopter. Consequently, this design avoids introducing additional heating or mixing regions. In addition to improving the aircraft's thrust-to-weight ratio, this approach, when combined with independent electronic speed controllers, creates an additional layer of safety through redundancy. For example, if the selected propeller-motor combination in the quadcopter configuration achieves a 2:1 thrust-to-weight ratio, the co-axial configuration—with its higher thrust-to-weight ratio—would allow the aircraft to continue flying safely, even if one or two motors fail, enabling it to return to its takeoff point.



Figure 5.7: X-Frame co-axial quadcopter implementation of a partial version of this design for increased resiliency against icing.

5.4 Performance Metrics

As presented in the previous sections, the proposed WxUAS aircraft design is modular and enables many configurations. Within the scope of this dissertation, three iterations of this WxUAS aircraft design were built, tested, and evaluated. Each iteration rendered important lessons that led to all the features presented in this chapter. Figure E.3 in Appendix E presents all three iterations, including the first, which utilized a rudimentary water shield resembling a Storm Trooper's helmet, hence unofficially naming the design from then onwards.

Nonetheless, to give the reader an estimate of the proposed WxUAS aircraft's performance, this section presents the performance metrics for the design in its configuration

used for the MAI^{2}S field campaign (detailed in Chapter 7). In this configuration (shown in Figs. 5.1, 5.2, 5.4 to 5.6 and 5.8), the aircraft uses four 1250 KV motors on 10-inch propellers (25.4 mm). It uses two 4-cell, 8500 mA h LiPo batteries. It has wing span (i.e., a propeller-tip-to-propeller-tip diagonal length) of 1 m and all-up-weight of 5.1 kg. The 25 mm motor arm length produces a 27 mm unobstructed path for incoming airflow in the front and 50 mm unobstructed path for incoming airflow from above.



Figure 5.8: Two units of the StormTrooper winter precipitation WxUAS built for the MAI^{2}S field campaign. This configuration represents the baseline for this dissertation's proposed WxUAS aircraft design.

As shown in Fig. 5.9, which summarizes the aircraft's estimated performance, the StormTrooper has a 2.8:1 thrust-to-weight ratio in this baseline configuration. Although the reduction in thrust due to propeller ice accretion is not linear, this thrust-to-weight ratio provides the aircraft with the ability to tolerate some ice buildup before experiencing a loss of lift. This allows the pilot to perform an emergency landing and recover the system before a critical failure occurs. Additionally, this configuration also produces a 32 m s^{-1} (71 mph) top speed, offering the autopilot a substantial throttle margin to handle the wind conditions within the human pilot's operational limitations (25 m s^{-1} sustained winds). Finally, the

nearly 17 minutes flight endurance enables it to perform atmospheric profiles up to 1500 m (approximately 5000 ft) with a 3 $m\,s^{-1}$ ascent rate and still land with 40% of battery life remaining.

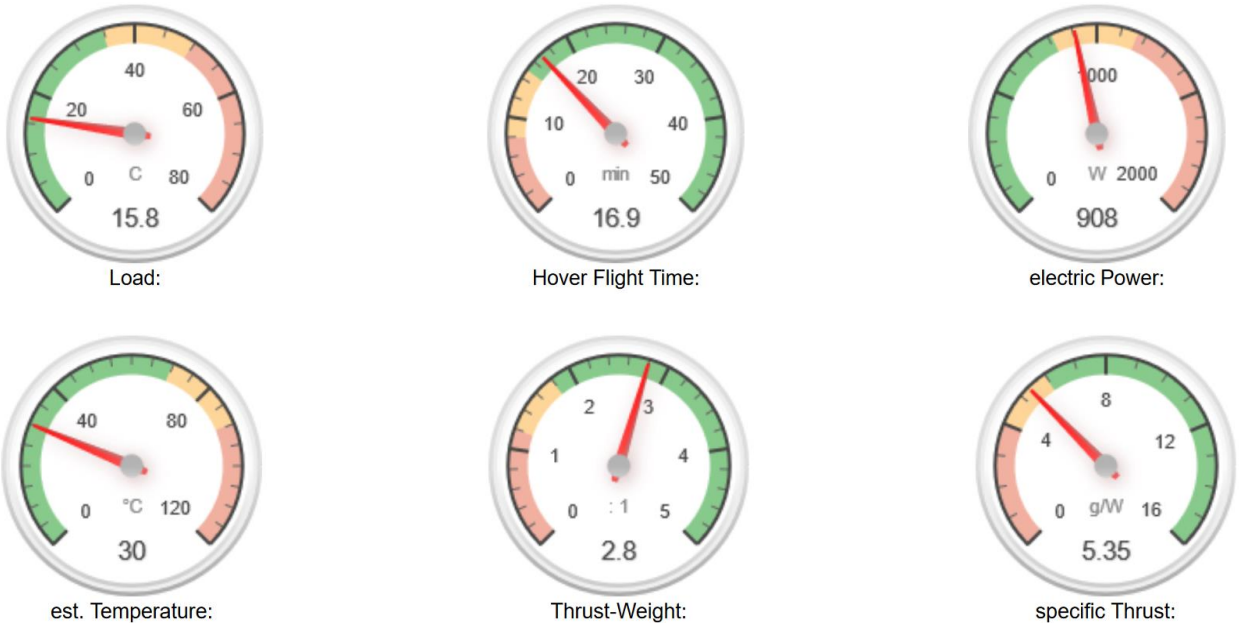


Figure 5.9: Performance metrics for the StormTrooper winter precipitation WxUAS in its baseline configuration.

Besides these flight performance metrics, it is worth noting that all the measurement characterization and performance discussed in Chapters 3 and 4 are based on this configuration. Furthermore, the field deployment results presented in the following chapter are also derived from this same setup.

Chapter 6

Data Processing and Fusion

"Coming together is a beginning; keeping together is progress; working together is success."

Edward Everett Hale

This dissertation endeavors to develop and validate an innovative unmanned aerial weather measurement system for the low-altitude wintry precipitation environment to provide insight into the atmospheric mechanisms that govern it. However, given the large number of atmospheric parameters that influence events in this environment, such an observation system naturally requires a multi-sensor approach leveraging multiple sensing methods (i.e., a multi-modal sensing approach). Additionally, the harshness of this environment and the sensitivity of the governing atmospheric parameters also require a supporting platform that minimizes the known atmospheric observation issues discussed in Chapter 2.

Considering the complexity of this challenge, this dissertation's proposed solutions for the in-situ (Chapter 3) and remote (Chapter 4) measurement, as well as the proposed aircraft design (Chapter 5), have been presented as separate modules. Besides enabling the reader to comprehend the intricate details of each module better, they were intentionally presented

separately as a way to highlight this dissertation's body of work as a low-cost wintry precipitation observation framework in which its modules can be modified, replaced, deployed individually, or in conjunction.

Nonetheless, as mentioned above, relevant insight into the complex low-altitude wintry precipitation environment requires a multi-modal sensing approach and a coherent fusion of raw sensor data into relevant scientific information. To address this requirement, this chapter presents the integration of these modules into a complete atmospheric observation system. Particularly, this chapter focuses on the WxUAS data processing techniques that leverage design, construction, and operation to create weather data products that support human analysis and inferences, leading to a better understanding of low-altitude winter weather phenomena. Additionally, this chapter presents a proof-of-concept for a WxUAS-based automated present weather inference algorithm.

6.1 Measurement, Information, and Insight

As shown in Chapters 3 and 4, the proposed in-situ and remote solutions employ redundant sensors with sampling rates as high as 15 Hz. Therefore, each sensor produces thousands of atmospheric observations per profile. Additionally, sensor data can have a 1-to-1 or 1-to-N (i.e., one-to-many) relationship with atmospheric information. For example, a temperature sensor only produces direct information about air temperature (i.e., a 1-to-1 relationship). However, the mmWave radar has a 1-to-N relationship with precipitation. For one precipitation sample (i.e., one radar data cube), it produces four information variables: reflectivity, maximum detected range, mean Doppler velocity (interpreted as approximated hydrometeor fall velocity), and spectrum width (i.e., width of the fall velocities distributions). This considerably increases the amount of radar-based information in a profile.

Although rich, this large dataset is not particularly useful, and it may even become overwhelming [28]. Fortunately, sensor data fusion techniques provide a practical method

for converting this dataset into insightful information [77, 78]. Sensor data fusion can be adopted at many informational levels. At the raw-data level, samples from similar sensors can be averaged for increased accuracy (as described in Chapter 3). Additionally, samples from different sensing modalities can be combined to produce new data. For example, pressure, temperature, and relative humidity data can be combined to produce wet bulb temperature data.

At the information level, sensor data can be combined to produce new or contextualized information. For instance, pressure and temperature, or even the newly calculated wet bulb temperature, can be combined to create a vertical temperature distribution. In this information-level multi-modal data fusion, quality-controlled data is compressed in space, producing a single value for an atmospheric parameter for that point in space. This considerably reduced data can easily be represented graphically and already enables humans to analyze it and derive additional contextualized information that leads to inferences about the broader atmospheric conditions. Atmospheric soundings are a good example of this graphical representation of information-level multi-modal data fusion.

Within the scope of this dissertation's unmanned aerial weather measurement system for the low-altitude wintry precipitation environment, this graphical representation of spatially compressed information results in the profiles illustrated in Fig. 6.1. In this illustration, panels (A) through (D) show the complete profile summary from in-situ sensors, while panels (E) through (G) illustrate one of the many summaries produced by the radar for a single profile. Even though these graphical summaries help convey a large volume of information, which can help researchers and forecasters investigate the atmospheric conditions at a particular time, it can still be overwhelming to use a collection of these summaries to understand the behavior of a winter event spanning several hours.

Additionally, it is underlined in these graphical summaries that not all data collected by the proposed wintry precipitation WxUAS naturally conforms to this format. For instance, the particle size distribution data requires a fusion step to compress its information into

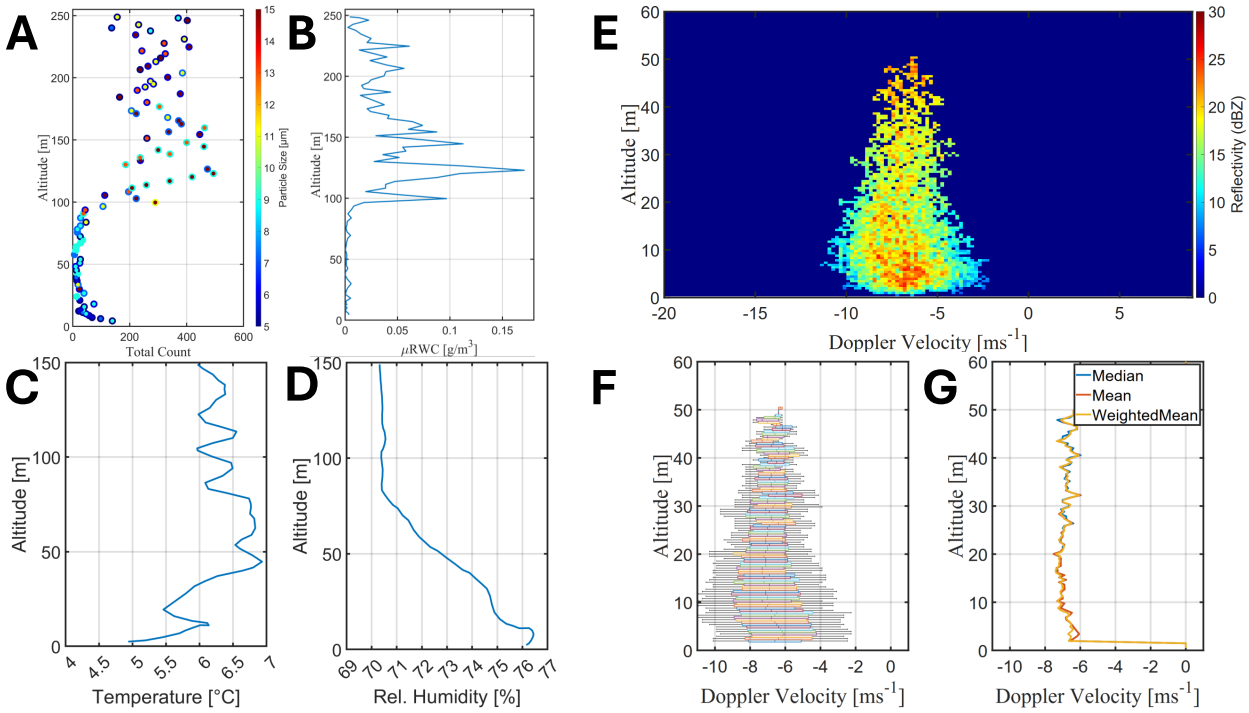


Figure 6.1: Illustration of the graphical summaries for a profile gathered by this dissertation's WxUAS. Variations with height for: (A) particle size distribution, (B) micro-range Water content, (C) temperature, and (D) relative humidity. Along with one of the many similar snapshots produced by the radar during a profile with (E) Doppler-range map, (F) Doppler velocity distributions, and (G) mean velocity.

three altitude-varying variables (i.e., total particle count, distribution mode, and largest size detected) and a secondary step to compress it into a single variable (i.e., the micron-range water content). In the case of the mmWave radar data, a measurement taken at one altitude provides data for several other relative altitudes. Consequently, each measurement can generate a graphical summary, resulting in a collection of summaries for each profile. Therefore, another form of summarizing a large volume of WxUAS data is needed.

6.1.1 Spatiotemporal Maps

As illustrated in Fig. 6.1, the mobility of WxUAS enables it to characterize the spatial distribution of atmospheric parameters. Leveraging the short time it takes a WxUAS to produce these high-resolution spatial profiles, an operational scheme can be set up to repeat

them at regular intervals (e.g., 10 or 15 minutes). In this setup, a single WxUAS can collect a spatiotemporal dataset, which can be graphically summarized to allow researchers to easily track atmospheric changes caused by passing weather systems.

For instance, during the final deployment for the MAI^{2}S field campaign (see Chapter 7 for details), six temperature profiles were collected over 90 minutes, resulting in a profile nearly every 15 minutes. Figure 6.2–A shows the last four spatial profiles in the format discussed in the previous section. Although visualizing the profiles together enables researchers to identify and track temporal changes in structural atmospheric features (e.g., altitude, depth, and intensity of a temperature inversion) over a short period, performing this activity for longer periods may prove challenging. Additionally, in naturally complex environments such as low-altitude wintry precipitation, tracking such changes in multiple variables over long periods becomes nearly impossible.

Leveraging the information contextualization and condensation capabilities of the previously discussed sensor data fusion techniques, the altitude-binned profile data can be converted into color maps (Fig. 6.2–B). In this preliminary stage, it is already notable how general warming and cooling patterns are easier to identify. Nonetheless, the transitions from the atmospheric state in one profile to the next are not as easily distinguishable. Redistributing the altitude-binned color maps into evenly spaced time bins produces a time-height map (Fig. 6.2–C).

Although the time-height map has gaps between profiles, the few minutes between them allow for the reasonable assumption that changes in atmospheric conditions would be gradual. This permits interpolating the data in time for measurements taken at the same altitude. After this interpolation, the final time-height map makes the atmospheric evolution easily identifiable (Fig. 6.2–D). Another example of this time-height map presentation, now for relative humidity, is illustrated by Fig. 6.3. For cases where this simplifying assumption is not valid, similar results can be achieved with a shorter interval between profiles or more robust non-linear interpolation techniques.

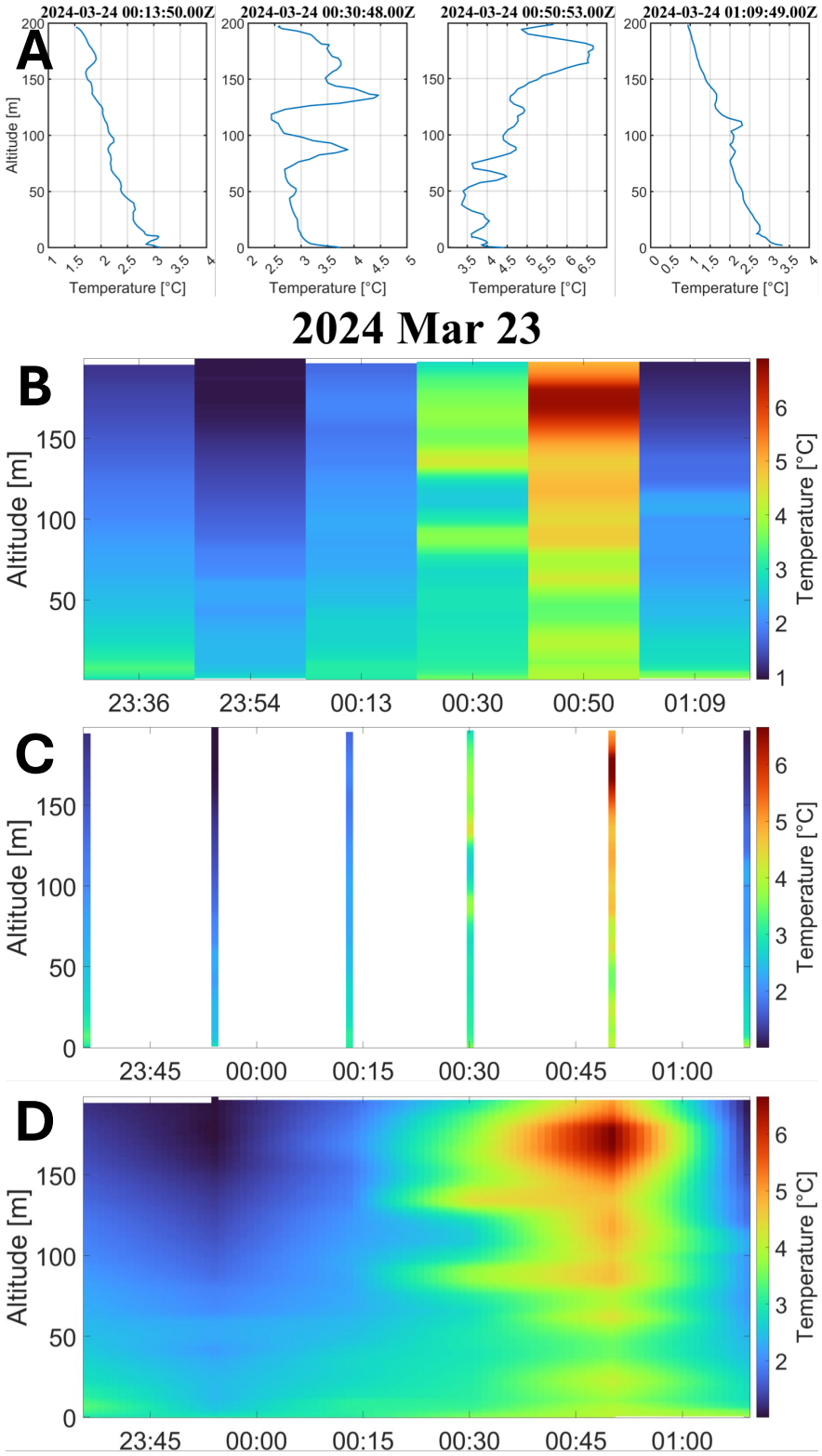


Figure 6.2: Illustration of the steps to produce the time-height maps that graphically summarize the WxUAS spatiotemporal datasets.

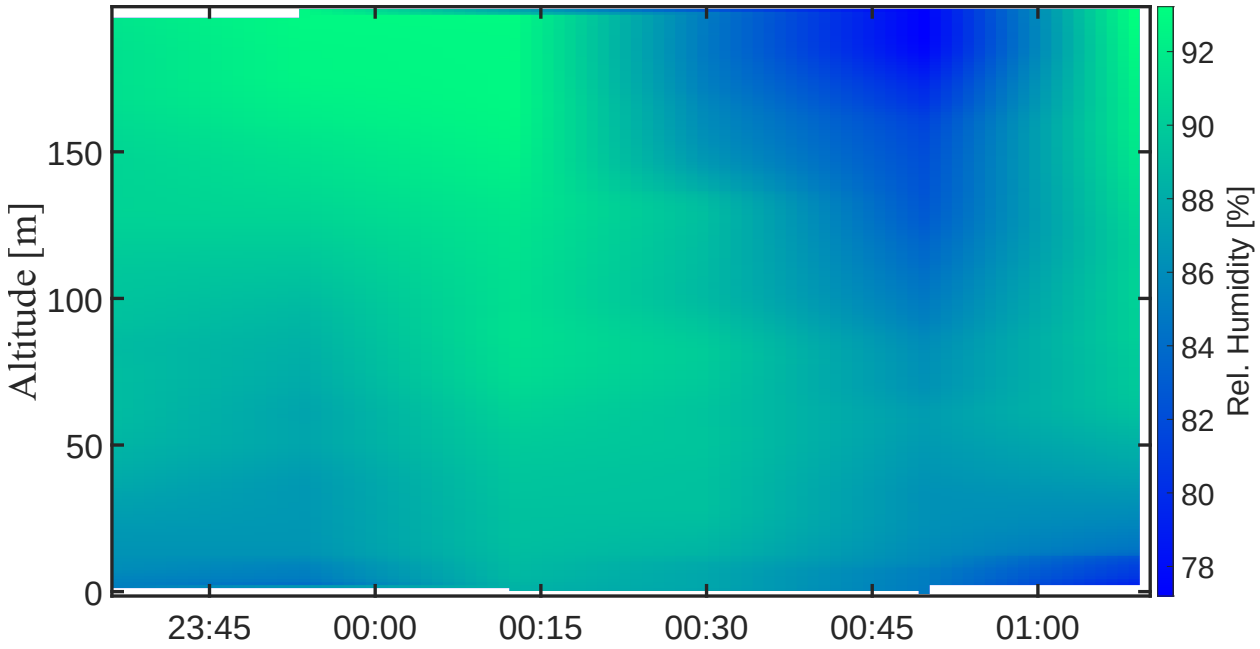


Figure 6.3: Relative humidity time-height map for the last WxUAS data collection in the MAI^{2}S field campaign.

Besides aiding researchers in identifying and tracking temporal changes in structural atmospheric features, these maps also enable comparisons of how these passing weather systems affect each atmospheric parameter. These comparisons can reveal if the relationships between these atmospheric parameters present any time dependency, among other observations. In this particular example from the MAI^{2}S field campaign, it is interesting to note the joint variation in temperature and relative humidity caused by a brief break in the precipitation, which allowed the drier and warmer air from aloft to reach the surface. More details on this and other deployment data will be discussed in Chapter 7.

6.1.2 Time Series

Although this map format also accommodates the radar data generated by the proposed WxUAS well, the FAA-imposed flight ceiling limitations encountered in this dissertation's data collection deployments diminished vertical variability in the weather radar data. Consequently, a time-height map of the weather radar data would produce only variations in

time. For this reason, the WxUAS radar data presented in this dissertation is spatially compressed and presented as four time-series. The four variables represented in each series are approximate hydrometeor fall velocity, spectrum width, maximum detection range, and reflectivity. As an example, Fig. 6.4 presents the time series for the radar-based approximate hydrometeor fall velocity for the 16 profiles collected during the MAI^{2}S field campaign's first field deployment.

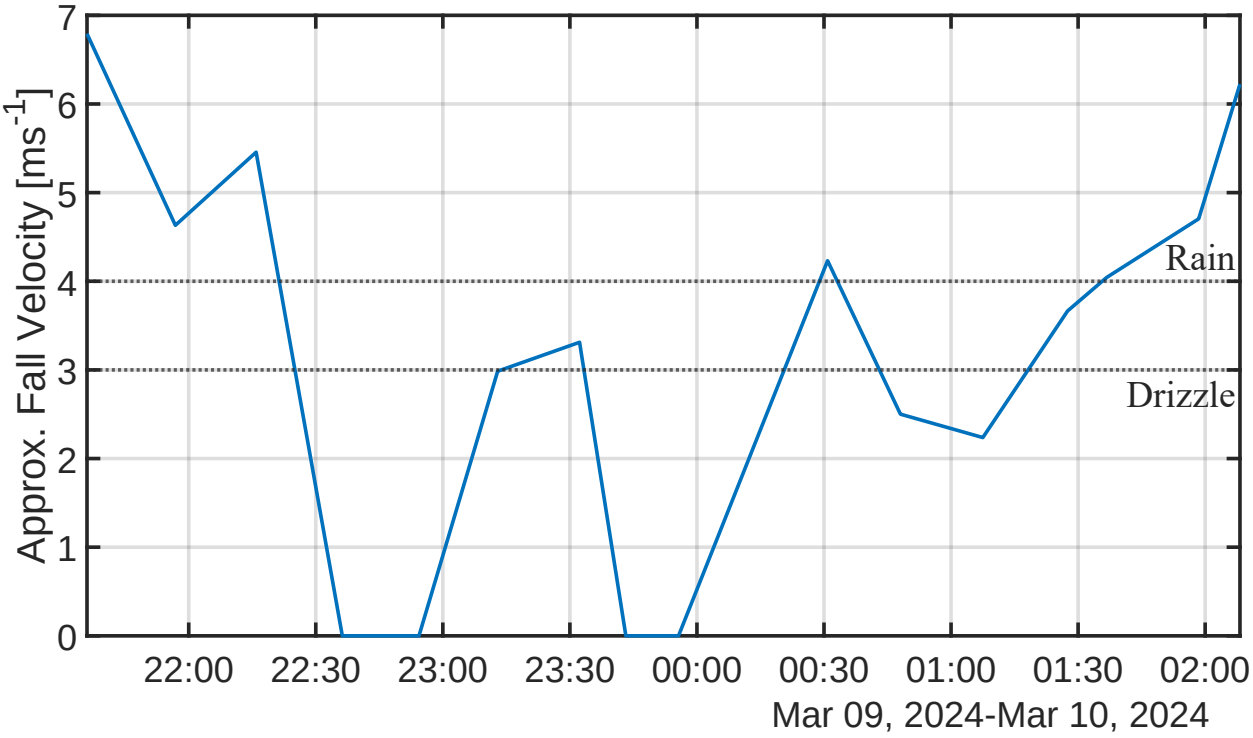


Figure 6.4: Temporal evolution of approximate hydrometeor fall velocity during a rain/drizzle event.

As a stand-alone variable, the time series for approximate hydrometeor fall velocity already enables researchers to identify periods with and without active precipitation, as well as evaluate the length of the transition intervals. Coupled with the thresholds for the WxUAS-based automated present weather inference algorithm (detailed in Section 6.2), it even enables the evaluation of possible precipitation types.

6.1.3 Considerations on Data Use

This dissertation's primary goal is to design an unmanned aerial weather measurement system that provides insight into the low-altitude wintry precipitation environment. To achieve this goal, considerations regarding the system's design, build, and operation are leveraged in a multi-modal sensor data fusion approach to produce spatiotemporal weather information for researchers and forecasters. This work is done in hopes that the new information will enable atmospheric scientists to better understand the mechanisms that govern this environment.

Considering that every observation system has limitations, the processed weather information products from the proposed WxUAS focus on the detection, location, and tracking of the freezing, melting, cloud transition, and cloud layers, as well as the presence of precipitation, its type, and intensity. This choice is based on the current observational challenges that impact the detection and forecasting of hazardous winter weather (see Chapter 1 for more details).

WxUAS are uniquely positioned to detect and characterize the low-altitude freezing and melting layers because, unlike temporal precipitation phase changes, melting and freezing layers induce phase changes while the hydrometeor falls through them. In other words, the layer-induced phase change is interpreted as spatial. Therefore, low-altitude freezing and melting layers can create ambiguity between in-situ surface observations and in-situ or remote observations aloft. The spatiotemporal maps produced by the proposed WxUAS in these regions allow researchers to understand these ambiguities with information about the depth and intensity of these layers, as well as their temporal evolutions.

Similarly, low-altitude cloud layers present visibility and ceiling limitations, as well as other hazards to low-flying aircraft. Low-altitude clouds can also conceal precipitation not detectable by the WSR-88D network [6]. Additionally, the characteristics of the cloud transition layer can present indications of processes that can enhance or stifle precipitation (e.g., dry air mixing or moisture inflow). The WxUAS proposed in this dissertation can pro-

vide meaningful information about these two layers (e.g., dissipation, intensification, and lowering), more flexibly and at a much lower cost than a ceilometer.

This low cost and flexibility also make the system well-suited for deployment in areas with limited weather data availability. Such is the case for the location of the MAI^{2}S field campaign, detailed in Chapter 7, which presents four use cases demonstrating how the proposed WxUAS data provided valuable insights into mixed-phase precipitation events. Particularly the case in Section 7.1.3, which presented dry snow on the surface with temperatures well above freezing.

Besides being well-suited for deployment in areas with limited weather data availability, the proposed WxUAS is also ideal for supporting the hyperlocal weather needs for sUAS and AAM operations. Nonetheless, for this application, the weather condition inferences need to be partially automated. This is the topic of this chapter's next section.

6.2 Multi-modal Fusion and Algorithmic Weather Inference

While the primary motivation for developing the WxUAS in this dissertation is to support researchers and forecasters, the multi-modal sensor data fusion technique used to generate weather information products for human insight and interpretation also enables the development of an automated present-weather inference algorithm. This section presents a proof-of-concept for such an algorithm in hopes of seeding the future work that will eventually produce operational algorithms and models that enable WxUAS complex adaptive sampling, WxUAS-based hyperlocal data for unmanned traffic management, and sUAS and AAM weather detection, awareness, and avoidance.

Algorithms and models for classification and inference based on multi-modal data fusion can vary in complexity. For instance, implementations may range from advanced models incorporating multiple sensor types and their interrelationships (e.g., covariance) in their

outputs, such as random forests and neural networks, to simpler algorithms that apply a logical combination of data using predefined rules and thresholds. Nonetheless, even in its simpler implementation method, it is implicit the assumption that weather sensors are integrated into the flight controller (as described in Chapter 3) and that adequate onboard computational resources are available.

Considering the current restriction on integration levels and computational resource availability, the algorithm proposed in this dissertation leverages the previously detailed spatial distribution of WxUAS data to algorithmically define the target atmospheric features via a smaller number of thresholds. Logical propositions using these thresholds generate states which jointly define the resulting inference. In addition to its low computational effort and implementation simplicity, this approach allows the algorithm to grow in complexity because the thresholds can be determined based on atmospheric-science theory, empirical observations, or mined from large and well-characterized datasets.

For this initial implementation attempt, precipitation type and the freezing, melting, cloud transition, and cloud layers are defined by the previously discussed information-level variables and empirically defined thresholds as follows:

- **Melting and freezing layers** – The melting layer is defined as at least 30 contiguous altitude levels where the wet bulb temperature exceeds 0.3 °C and is either preceded or followed by sub-freezing temperatures. Freezing layers are analogously defined for temperatures below negative 0.3 °C. This ±0.3 °C buffer around 0 °C accounts for the WxUAS's potential sensing errors, its time response, and the complex behavior of water near freezing temperatures. It also creates a more realistic gradual transition between layers, not binary transitions at 0 °C.

- **Cloud transition and cloud layers** – The start of a cloud transition layer is defined as the barometric altitude at which the particle size distribution sensor begins to report a particle size distribution with a mode equal to or larger than 7.5 µm in diameter, the size of the largest detected particle as 10 µm or greater, and total particles counted

is equal to or greater than 150. The WxUAS is considered to be in a cloud at the first reported distribution mode equal to or larger than 9 µm in diameter, the size of the largest detected particles is 13 µm or greater, and total particles counted is equal to or greater than 200. Note that the relative humidity measurements are not included in this criteria because, in mixed-phased precipitation, where cloud layers are lowering and rising, it is possible to be on the edge of a cloud in unsaturated air. Therefore, empirically defining a relative humidity threshold is not possible within this dissertation's scope.

- **Precipitation** – Given the proposed WxUAS's 1500 m altitude range, precipitation phase, and consequently type, can change along the profile. Therefore, precipitation-type inferences depend on melting and freezing layer inferences, their depths, and the distance from the layer transition. Analogously, due to ambiguous signals within the source data, precipitation intensity inference is dependent on the precipitation type inference. Considering the FAA-imposed flight ceiling limitation in this dissertation's field deployments, its dataset does not present vertical temperature layer transitions. Consequently, for this proof of concept, algorithmic precipitation-type inference assumes one type per profile. Its definition follows the criteria in Table 6.1 where all conditions need to be met for classification within a type.

Variable	**Rain**	**Drizzle**	**Snow**	**Ice Pellets**
Approx. Fall Velocity [$\mathrm{m\,s^{-1}}$]	≥ 4	≤ 3	< 3	> 3
Spectrum width [$\mathrm{m\,s^{-1}}$]	≥ 6	≤ 5	< 4	> 5
Max. Detection Range [m]	> 30	≤ 30	–	–
Reflectivity [dBZ]	≥ 15	< 15	–	–
Wet Bulb Temperature [°C]	≥ 0.3	≥ 0.3	≤ -0.3	≤ -0.3

Table 6.1: Thresholds for precipitation type.

As an initial implementation attempt, the above criteria for precipitation type do not present categories for mixed-phased precipitation, as its classification remains one of the biggest challenges in the field. Nonetheless, the implied mutual exclusivity between the defined categories also does not present a definition for mixed rain-drizzle events. Since the official FAA definition for rain and drizzle is based solely on drop size, mixed-sized events can produce overlapping results that meet neither the rain nor the drizzle criteria. To account for these cases, a new rule based solely on the fall velocity and its distribution was implemented using terminal velocity as a proxy for particle diameter. The pseudo-code for the rule is presented below.

```
if(fallVelocity < 4 AND fallVelocity > 3) OR
  (spectrumWidth < 6 AND spectrumWidth > 5) then
  pType == ‘‘RNDZ’’; %Rain-Drizzle mix;
end
```

Additionally, in cases where only rain or drizzle was detected, a basic precipitation intensity algorithm using the maximum detection range was implemented and applied following the type classification. Using data from a rain-drizzle event during the MAI^{2}S field campaign's first deployment, a small simulation of the automated present weather report was tested. In this event, illustrated in Fig. 6.4, sixteen WxUAS profiles were collected in either rain, drizzle, or no precipitation. This case also presented low-altitude clouds to test the cloud layer detection algorithm. However, due to the flight ceiling limitations, none of the MAI^{2}S cases presented freezing or melting layers.

To evaluate the cloud and cloud transition layers detection algorithm, two profiles were selected from within the period in which the cloud layer was lowering, as reported by the ceilometer. For the first profile, at 23:43, the algorithm reported only a cloud transition layer starting at 107 m AGL but never reported a cloud layer. At the same time, the ceilometer

reports for the lowest cloud base varied between 130 and 150 m AGL. This variation in the ceilometer reports indicates the absence of a well-defined cloud base, which is expected as the cloud was still descending at this moment. Careful inspection of the particle size distribution profile yielded similar results.

The second profile selected was taken during the period when the ceilometer reported the cloud base at 100 m AGL without variation for several minutes. Applying the cloud layer algorithm in this WxUAS particle size distribution profile yielded a cloud transition layer at 96 m AGL and a cloud layer at 99 m. Besides the agreement between the ceilometer and the algorithm's reported start for the cloud layer, the 3 m difference between the reported cloud transition and cloud layers also indicates the sharp transition into cloud, as reported by the ceilometer. To illustrate these results, the outputs for the cloud layer detection algorithm were overlayed on the graphical representation for the particle size distribution profiles (see Fig. 6.5). An illustration for the boxplot for the ceilometer's reported lowest cloud bases is shown in Fig. 6.6.

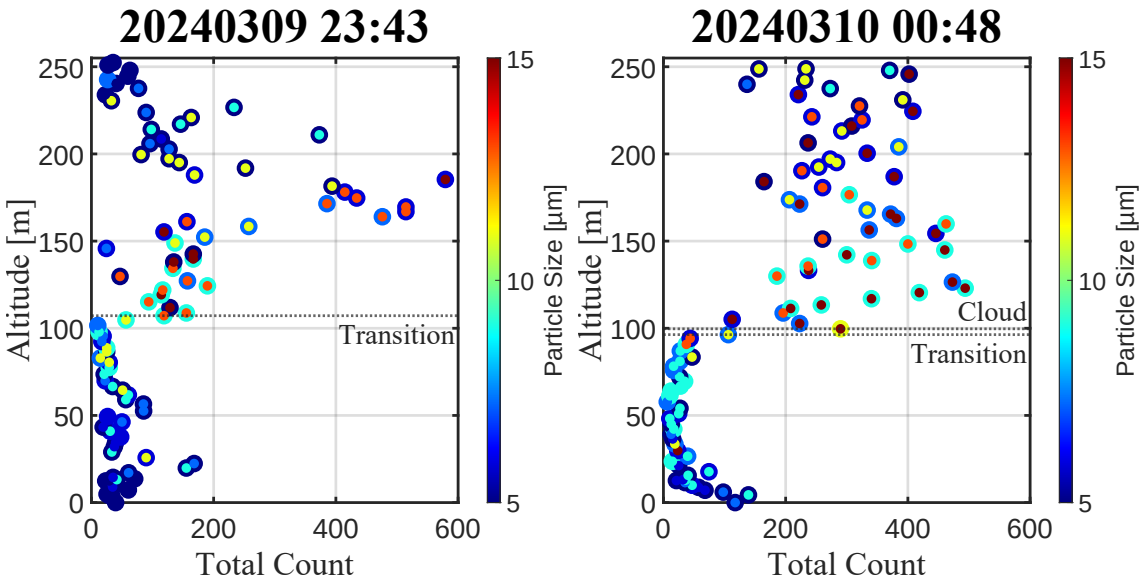


Figure 6.5: Overlay of the results for the automated cloud detection algorithm.

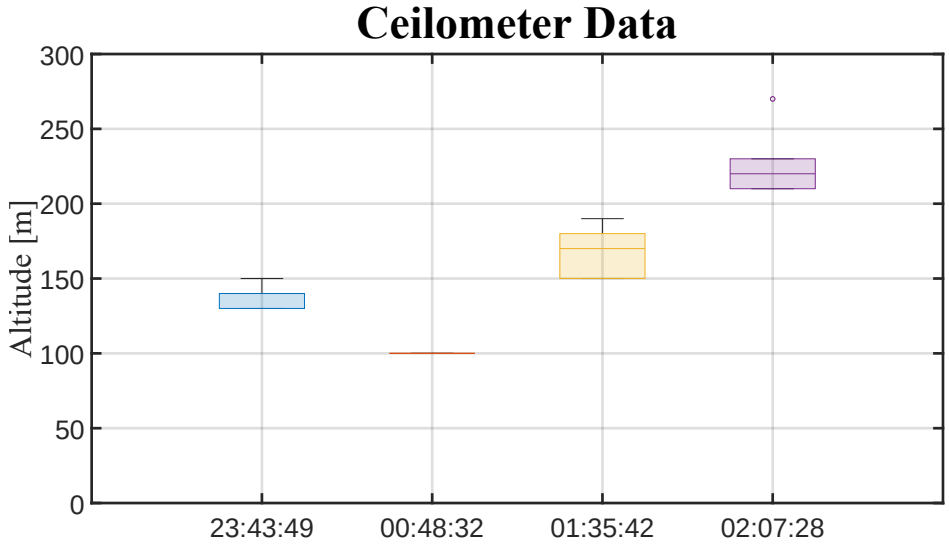


Figure 6.6: Distribution of the reported lowest cloud bases by a colocated ceilometer.

To evaluate the results for the precipitation type and intensity algorithms, all sixteen profiles were used. The results of the algorithms were compared to the field notes made by the MAI^{2}S team field atmospheric scientist (Brian Filipiak). In this initial implementation, the algorithm agreed with the field notes 10 out of 16, that is 62% of the time. Results for this test are available on Table 6.3, in the columns labeled Human and Exclusive Algorithm. The noteworthy divergences were the two reports of unknown precipitation during moderate drizzle events. These reports result from adopting an algorithm where precipitation types are mutually exclusive, meaning one classification requires all criteria to meet its thresholds.

In the case of mix-sized precipitation events (i.e., rain-drizzle for liquid precipitation), the wide variety of particle diameters creates partially ambiguous results for each evaluated variable. These types of errors are very common in other multi-sensor automated weather classification algorithms [7, 45]. To mitigate this issue, in recent years, aviation weather products have migrated to reporting precipitation and its related hazards on a continuum or via probabilities [14, 16].

To mimic this strategy in this dissertation's algorithmic precipitation type and intensity classification, the radar variable criteria can be redefined to express a continuum within each

variable (see Table 6.2). Each criterion can be evaluated independently, generating an output for the precipitation type met within it. After evaluating all criteria, the algorithm reports the proportion associated with each precipitation type. For example, if all four criteria were met for Rain, the algorithm reports Rain. However, if one criterion is met for Rain, one for Drizzle, and two for RNDZ, the algorithm reports:

```
Rain: 0.25, RNDZ: 0.50, Drizzle: 0.25.
```

Columns Human and Proportional Algorithm in Table 6.3 present the results for this new algorithm.

Variable	**Rain**	**RNDZ**	**Drizzle**
Approx. Fall Velocity [$\mathrm{m\,s^{-1}}$]	≥ 4	< 4 AND > 3	≤ 3
Spectrum width [$\mathrm{m\,s^{-1}}$]	≥ 6	< 6 AND > 5	≤ 5
Max. Detection Range [m]	≥ 30	< 30 AND > 25	≤ 25
Reflectivity [dBZ]	≥ 15	< 15 AND > 14	≤ 14

Table 6.2: Thresholds continuum for precipitation type classification.

Again, the results produce a 62% match to the human-reported type and intensity. However, in this new algorithm, the unknown precipitation is eliminated, and the six divergences reported indicate disagreement only in intensity. Upon careful inspection and comparison with the reports from the colocated MRRs (see Fig. 7.6), the six divergent cases seem to be correct. In the first two cases, at 23:12 and 23:32, the divergence in intensity is underlined by a general trend match. The human report indicates a transition from no precipitation to light drizzle to moderate drizzle. The algorithm reported a transition from no precipitation to RNDZ–0.25 and Drizzle–0.75 to RNDZ–0.50 and Drizzle–0.50. This increase in the matches for the RNDZ criterion can be interpreted as an increase in the presence of larger drops, which can lead to the perceived intensity increase.

The most noteworthy mixed-sized precipitation cases are the last three (starting at 01:07), which capture the transition from drizzle to rain. In these cases, moderate drizzle transitions

to a mix of RNDZ and drizzle that gradually meets fewer criteria for drizzle and more criteria for RNDZ and rain until it is reported as moderate rain (at 01:58). For the same period, the human reports presented a direct transition from moderate drizzle to moderate rain in one time-step.

Time	Human	Exclusive Algorithm	Proportional Algorithm
21:35:59	Moderate Rain	Moderate Rain	Moderate Rain
21:56:51	Moderate Rain	Moderate Rain	Moderate Rain
22:15:55	Moderate Rain	Moderate Rain	Moderate Rain
22:36:16	No precipitation	No precipitation	No precipitation
22:54:22	No precipitation	No precipitation	No precipitation
23:12:57	Light Drizzle	Moderate Drizzle	RNDZ: 0.25 Drizzle: 0.75
23:32:17	Moderate Drizzle	RNDZ	RNDZ: 0.50 Drizzle: 0.50
23:43:13	No precipitation	No precipitation	No precipitation
23:55:39	No precipitation	No precipitation	No precipitation
00:30:51	Moderate Drizzle	Unknown	Rain: 0.25 Drizzle: 0.75
00:48:03	Moderate Drizzle	Moderate Drizzle	Moderate Drizzle
01:07:30	Heavy Drizzle	Moderate Drizzle	RNDZ: 0.25 Drizzle: 0.75
01:27:31	Moderate Drizzle	RNDZ	RNDZ: 0.50 Drizzle: 0.50
01:36:45	Moderate Drizzle	Unknown	Rain: 0.75 Drizzle: 0.25
01:58:28	Moderate Rain	Moderate Rain	Moderate Rain
02:08:13	Moderate Rain	Moderate Rain	Moderate Rain

Table 6.3: Precipitation type and intensity for the first MAI^{2}S deployment. The first column is observations from the atmospheric scientist on site, the second column presents the result for the first inference algorithm, and the third column presents the results for the adjusted algorithm.

While acknowledging the limitations of the small simulated sample size, this algorithm meets the precipitation-type reporting quality requirements set forth in the newly approved ASTM standard for third-party weather data providers. Furthermore, examples such as this nuanced transition event involving mixed-size precipitation types illustrate how the development of a proof-of-concept WxUAS-based automated present-weather inference algorithm can serve as a valuable tool to support human analysis of WxUAS weather products.

Chapter 7

Field Deployment

"God thunders wondrously his voice; he does great things that we cannot comprehend. For to the snow he says, 'Fall on the earth', likewise to the downpour, his mighty downpour ..."

Job 37:5-6

As detailed in Chapter 2, the development of new atmospheric observation systems should start with initial feasibility studies and field testing. These initial tests are commonly followed by exploratory research in small-scale investigative field campaigns alongside well-established systems. Within this roadmap, the previous chapters served to justify and validate the modules and technologies that compose this dissertation's proposed WxUAS. To do so, several laboratory and field experiments were conducted.

Amongst these experiments, the controlled chamber experiments at the Oklahoma Mesonet's calibration laboratory (Section 3.4 and Appendix A) and the Radar Innovations Laboratory (Section 4.2), as well as the intercomparison experiments at the Oklahoma Mesonet's Washington tower (Section 3.4.2 and Appendix B) and National Center for Atmospheric Research's Marshall field station (Section 3.4.3) are noteworthy.

Nonetheless, as discussed in Chapter 2, new atmospheric observation technologies must be matured as complete systems in their intended operational environment. Therefore, after successful results in these initial validation studies, the complete system was deployed in an investigative field campaign alongside well-established instruments for further validation. This chapter presents the WxUAS measurements in contrast to some ground validation instruments from NASA's Global Precipitation Measurements mission. It also discusses how the WxUAS data provided insight into particular low-altitude mix-phased precipitation events.

7.1 Multi Atmospheric Instrument Intercomparison Study

MAI^{2}S was a wintry precipitation study organized by Oklahoma State University, the University of Connecticut, the University of Oklahoma, and the NASA GPM ground validation program. It leveraged the ground-based instruments and location from the 2021-2023 Investigation of Microphysics and Precipitation for Atlantic Coast-Threatening Snowstorms (IMPACTS) field campaign. In 2024, the instruments previously geographically distributed through three locations across Connecticut were collocated at the University of Connecticut's campus (red dot in Fig. 7.1) for evaluation of potential deviations found in the previous years. In addition to this wide array of ground-based remote and in-situ sensors, the MAI^{2}S scientific dataset was augmented by the StormTrooper (the WxUAS proposed in this dissertation). It performed 46 atmospheric profiles in drizzle, rain, and snow, producing valuable insight into low-altitude wintry precipitation events, some of which were not detected by the weather service's current observation systems.

The selected location for the study presents a high potential for mixed-phased precipitation events. A common pattern of winter storms in the region is for low-pressure systems to descend from Manitoba or Ontario (CA) toward the Atlantic Ocean through New York, Penn-

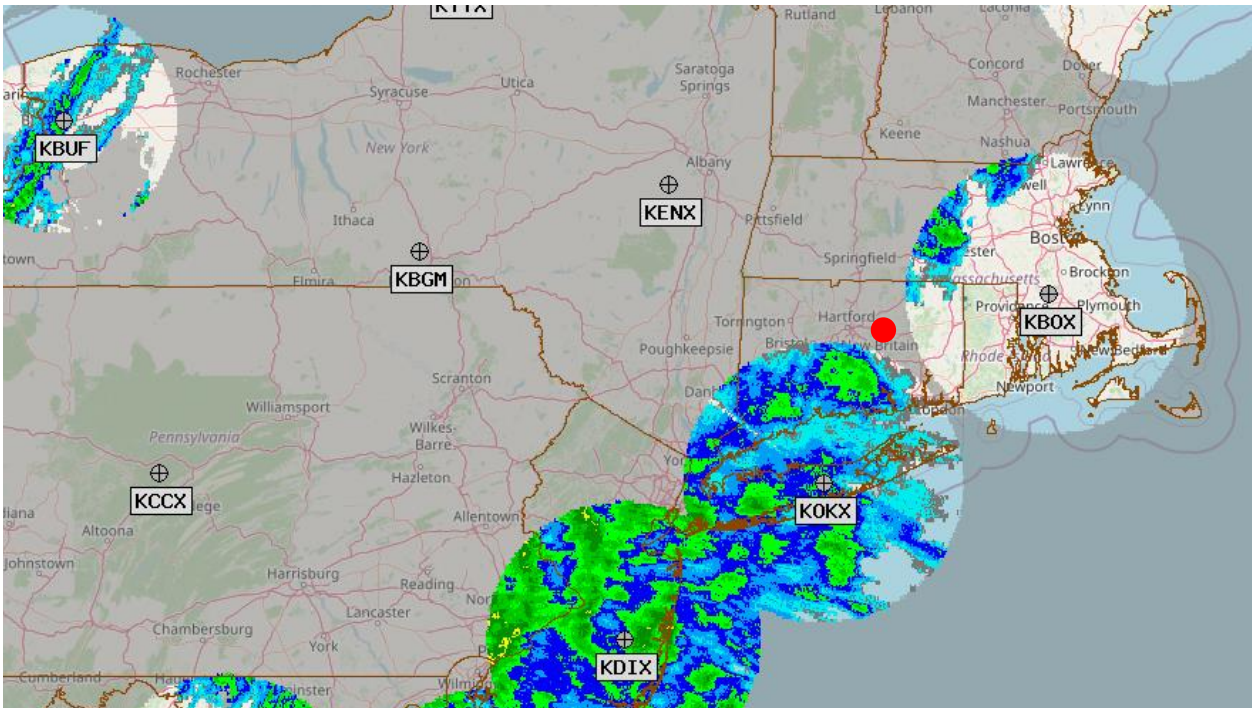


Figure 7.1: MAI^{2}S location at the University of Connecticut's Campus (red dot) shown here with an MRMS reflectivity overlay for the 500 m level.

sylvania, and Connecticut. After reaching the coast, these storms return north to Canada through Massachusetts and Maine in a quasi-circular pattern. These storms generally present a predominant west-to-east pattern coupled with a north-to-south and back-north motion. A larger scale version of this weather pattern is often referred to as an Alberta Clipper [79, 80]. Either in its smaller or full-scale variation, these storms are characterized by their fast progression and strong winds.

Due to its location in this pattern, Connecticut can be affected by these storms on their way south or back north. Sometimes, the same storm will affect the state twice in a few days. Besides encountering the temperature changes, expected due to its northwest-south-northeast pattern, storms in this region also encounter transition zones due to terrain elevation changes (high to low) as well as the transition from continental to oceanic. For these reasons, precipitation events in the region can present a wide variety of phases and hydrometeor size distribution within a few hours [81].

Although Connecticut is a critical location for understanding the behavior of winter weather storms in the northeastern portion of the United States, it has little weather data coverage, particularly at low altitudes. The state is located between the KOKX (New York), KOBX (Boston), and KENX (Albany) WSR-88D radars. However, due to regional topographic characteristics, the state has partial coverage below 750 m and no coverage in the Hartford-Mansfield region at the 500 m level, as illustrated by Fig. 7.1. Additionally, Connecticut does not have a weather service office or a station for the Rawinsond network.

Besides these characteristics, which make this location ideal for evaluating the impact of enhanced weather observations, the actual field used for sensor deployment within the University of Connecticut campus offers the necessary logistical conditions to support setting up the ground-base sensors for several months and protect the WxUAS crew in case the storm conditions become severe. Figure 7.2 presents an illustration of the sensor distribution and the WxUAS landing pad.

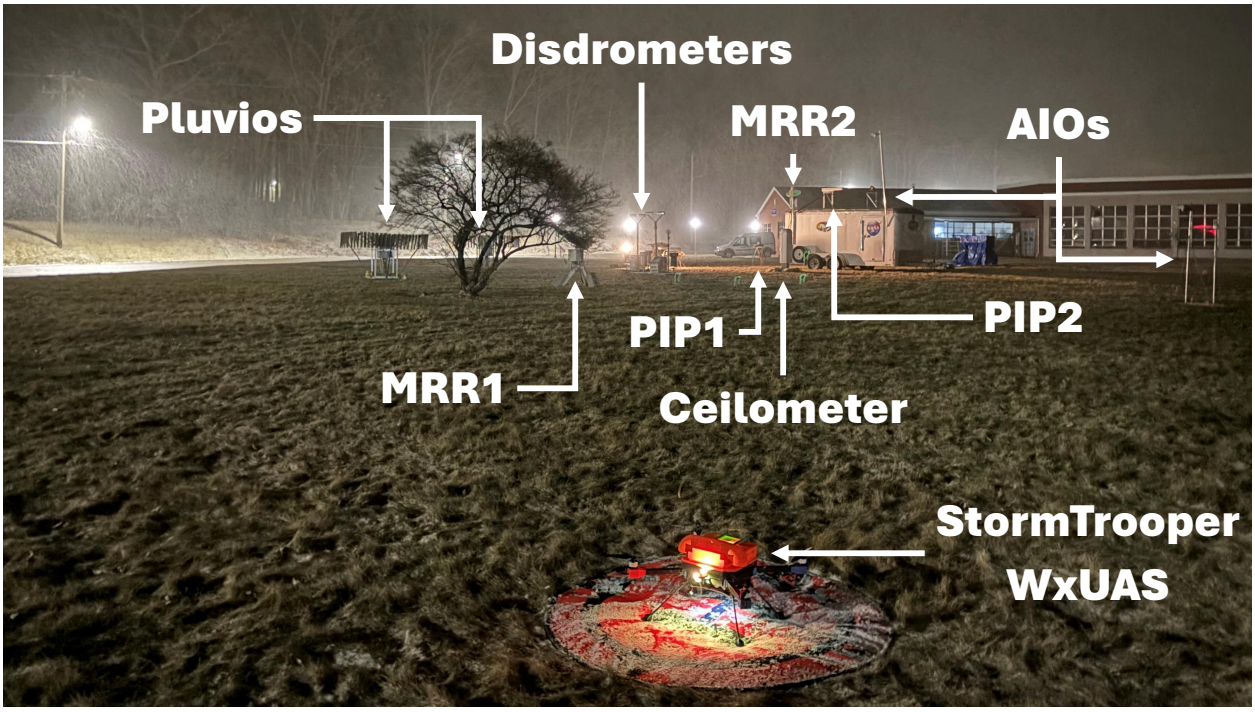


Figure 7.2: MAI^{2}S instruments.

The ground-based sensors for MAI^{2}S were two MRRs, two Pluvio weighing bucket gauges, two PARSIVEL disdrometers, two Precipitation Imaging Packages (PIPs), two all-in-one weather stations (AIO), and one ceilometer, amongst other instruments supported by the NASA GPM Atmospheric Instrumentation Laboratory (GAIL). In this chapter, the ground-based sensor data will only be presented in support of the WxUAS findings. For a complete description of the ground-based instrument portion of MAI^{2}S, the reader should refer to the following references [82, 83].

7.1.1 WxUAS Data and Sampling Strategy

Although the ground-based sensors were deployed from December 2023 until April 2024 at the study site, the StormTrooper was only deployed in March 2024 due to logistical constraints. In these deployments, the WxUAS sampled two storms targeting mixed-phased precipitation often seen in the temperature and pressure gradients caused by the leading and trailing edges of these storms. To capture the vertical structure of the low-altitude atmosphere, the targeted altitude for the StormTrooper profiles was 900 m (approximately 3000 ft.).

Given the FAA's 120 m flight ceiling for commercial UAV flights, an altitude restriction waiver request was submitted. Even though the study site is in uncontrolled airspace with low traffic, particularly when hazardous winter storms are present, and the surrounding surface near the campus is sparsely populated, the FAA rejected the request without much justification. Nonetheless, leveraging nearby terrain elevation change and structures, the FAA Part 107 rules allowed the aircraft to reach up to 200 m (650 ft.) AGL.

To increase the chances of capturing the low-altitude phase transition periods while accommodating the limited flight crew size and the FAA crew resource management practices, the WxUAS deployment plan was based on an 8-hour window. The intention was to start sampling one to two hours before the target storm effects were forecasted to occur and end it another one to two hours after. For the approaching storm cases, the targeted deployment

would characterize the local conditions before the storm front's arrival, its arrival, and its transition to active storm conditions. For departing storms, this same strategy would characterize the local conditions during the storm, its departure, and the conditions behind its trailing edge.

Considering the timescale in which precipitation phase changes had been reported by the surface observations in the past three winters and the time necessary to perform the pre and post-flight safety procedures, the 8-hour WxUAS data collection window was broken down into flights every 15 minutes. For these profiles, the WxUAS maintained a 3 m/s ascent rate while countering the winds to hold latitude and longitude over its take-off spot near the surface instruments.

As discussed in Chapter 6, the StormTrooper collects thousands of samples per variable, per profile. These samples produce high-resolution snapshots of the atmosphere, allowing researchers to tease out minor details in each variable for each flight. Nonetheless, presenting each variable through individual profiles may become overwhelming, making understanding a passing weather system's temporal evolution and general patterns more challenging. For this reason, the data presented in this chapter will follow the spatiotemporal map format presented in Chapter 6 with occasional profiles presented when a specific time requires detailed analysis. Additionally, all the data presented in the following subsections is shown in UTC in the 24-hour format.

7.1.2 Deployment 1

The first WxUAS deployment for the MAI^{2}S field campaign took place on March 9, 2024. For this event, the team aimed to sample a variety of conditions in front of an approaching cold front from the low-pressure system coming from Ontario (CA) over the Great Lakes (for an evolutionary pictogram of MRMS reflectivity, see Fig. F.1). Although rain was the forecasted precipitation type, the team anticipated observing some phase-change variations during the system's onset due to temperature gradients commonly associated with these

boundaries. The WxUAS profiles started at around 21:00 and continued until 02:00 on March 10, 2024, in an approximate 15-minute cadence. This cadence produced 17 profiles, enabling the characterization of the system's impact in the lowest atmospheric layers.

For these 17 profiles, the temperature spatiotemporal map (shown in Fig. 7.3) revealed considerable temperature oscillations between 4 and 7 °C varying in time and height. This intense variation indicated considerable mixing occurring during the sampled period. This mixing of above-freezing temperatures in the atmosphere's lowest altitudes resulted in only liquid precipitation being observed within 250 m AGL. Through these profiles, the StormTrooper's radar indicated rain, drizzle, and rain-drizzle mixes, with some precipitation breaks in between.

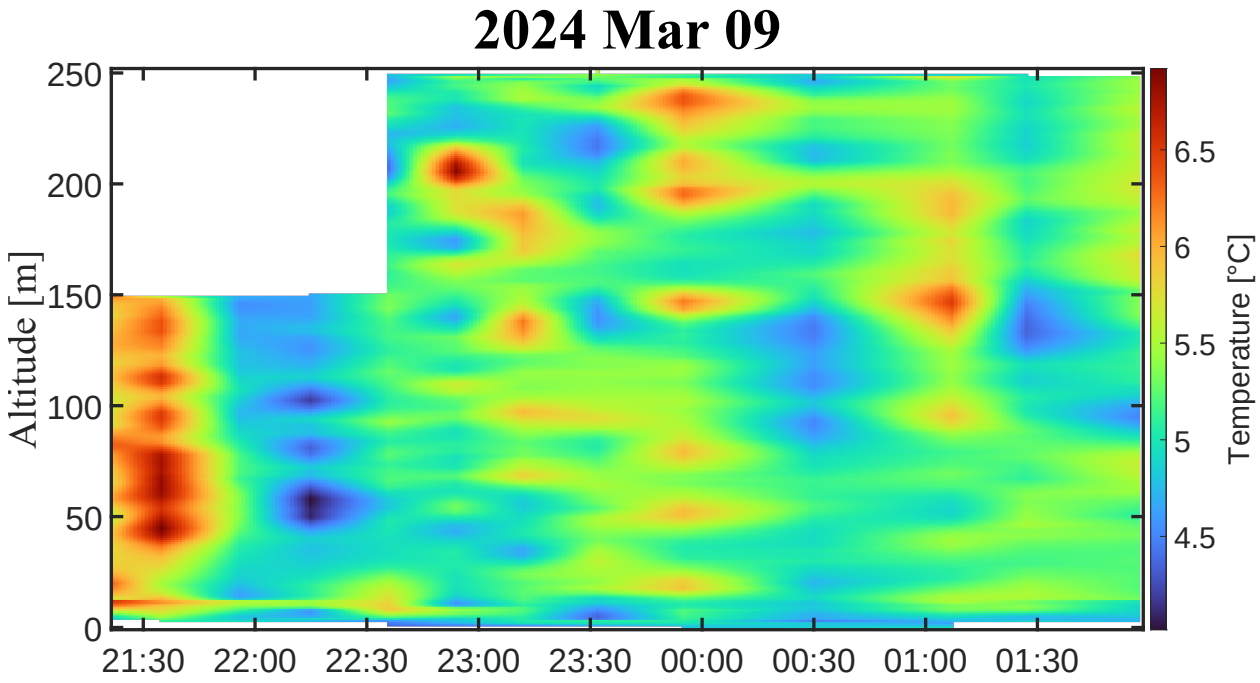


Figure 7.3: Spatiotemporal temperature map for the WxUAS profiles on March 9, 2024.

Figure 7.4 shows the time series for the radar-derived precipitation variables with the above-freezing thresholds used for the automated present weather inference algorithm (detailed in Chapter 6). Analyzing these variables in conjunction reveals the nuance and variability of this precipitation event, particularly between 23:00 and 01:30. During this sub-

interval, the human observer classified the precipitation mostly as drizzle. However, the evaluation of the radar-derived precipitation variables indicates distinctions in these types of drizzle that would produce different levels of low-altitude hazards under freezing conditions.

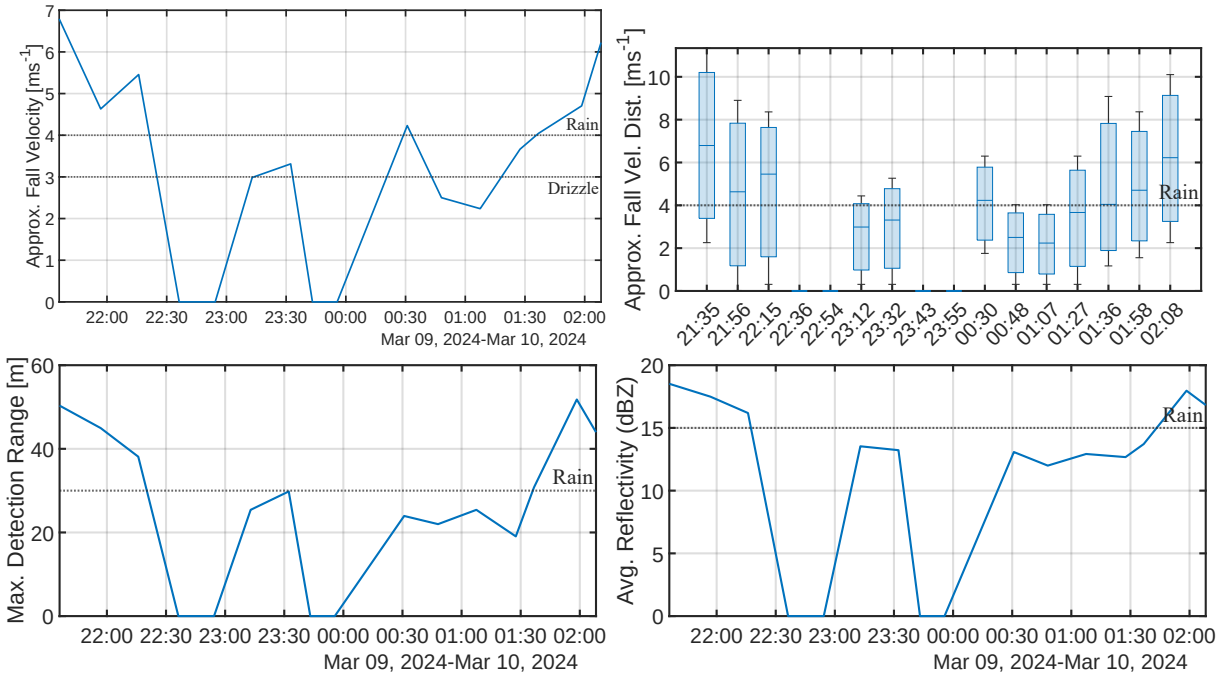


Figure 7.4: Radar-derived precipitation variables used for type and intensity classification. The dynamic classification thresholds for liquid precipitation are shown as a reference.

For instance, a comparison of data collected at 23:12 and 00:30 shows that both cases exhibited relatively narrow velocity distributions (below a $4\,\mathrm{m\,s^{-1}}$ width), reflectivities under 15 dBZ, and maximum detection ranges below 30 m, characteristics generally indicative of drizzle (as detailed in Section 6.2). However, the 23:12 case presents approximate fall velocities around $3\,\mathrm{m\,s^{-1}}$, consistent with drizzle, while the 00:30 case shows velocities exceeding $4\,\mathrm{m\,s^{-1}}$, which suggests rain. Although both cases were classified as mixed rain-drizzle, the 00:30 data likely reflects larger-diameter hydrometeors, as inferred from the higher fall velocities. In freezing conditions, such larger hydrometeors would lead to more rapid icing upon contact with aircraft or power lines.

It should be mentioned that the proportional classification algorithm captured this nuance well (see Section 6.2), classifying the first case as 0.25 rain-drizzle mix and 0.75 drizzle, and

the second case as 0.25 rain and 0.75 drizzle. The shift from the 0.25 contribution from rain-drizzle to rain, while maintaining an overall classification of mixed-size precipitation, indicates the potential presence of larger hydrometeors and, consequently, an increased risk.

In addition to the mixing indicated by the temperature map and the rain-drizzle precipitation classifications, the StormTrooper cloud-sized particle profiles revealed considerable changes in the lowest cloud layers. Although a system error reduced the number of valid cloud-sized particle profiles, the four valid profiles (shown in Fig. 7.5) still captured the above-mentioned variations in the cloud base. The first two profiles indicated that a 125 m deep cloud transition layer, starting at 100 m AGL, was compressed into a 3 m deep transition layer followed by a cloud layer starting at 99 m AGL in nearly one hour. The last two profiles indicated that within another hour, a few cloud-sized particles were still detectable in low clouds, but in this case, with total counts too small to indicate a cloud or cloud-transition layer. This pointed to the potential low-altitude cloud's departure from the sampled region (up to 250 m AGL).

Evaluating the results from these four cloud-sized particle profiles together with the radar-derived precipitation variables, it is possible to note that the compression of the low-altitude cloud-transition layer into a low cloud base occurred during the precipitation break and that the departure of this low cloud base occurred as precipitation resumed and intensified from rain-drizzle into rain. The results from the colocated MRRs and ceilometer (shown in Fig. 7.5-A and Fig. 7.6) corroborate these findings.

Comparing the abovementioned results with the distributions of the ceilometer's cloud-base-1 reports during the highlighted cloud-sized particle profiles further corroborates this conclusion. This comparison also highlights the StormTrooper's potential for capturing nuance in this environment. During the first two profiles, the ceilometer's reported cloud-base-1 distribution widths changed from 20 m to zero, while during the last two profiles, they increased to 40 and 60 m (see Fig. 7.5-C).

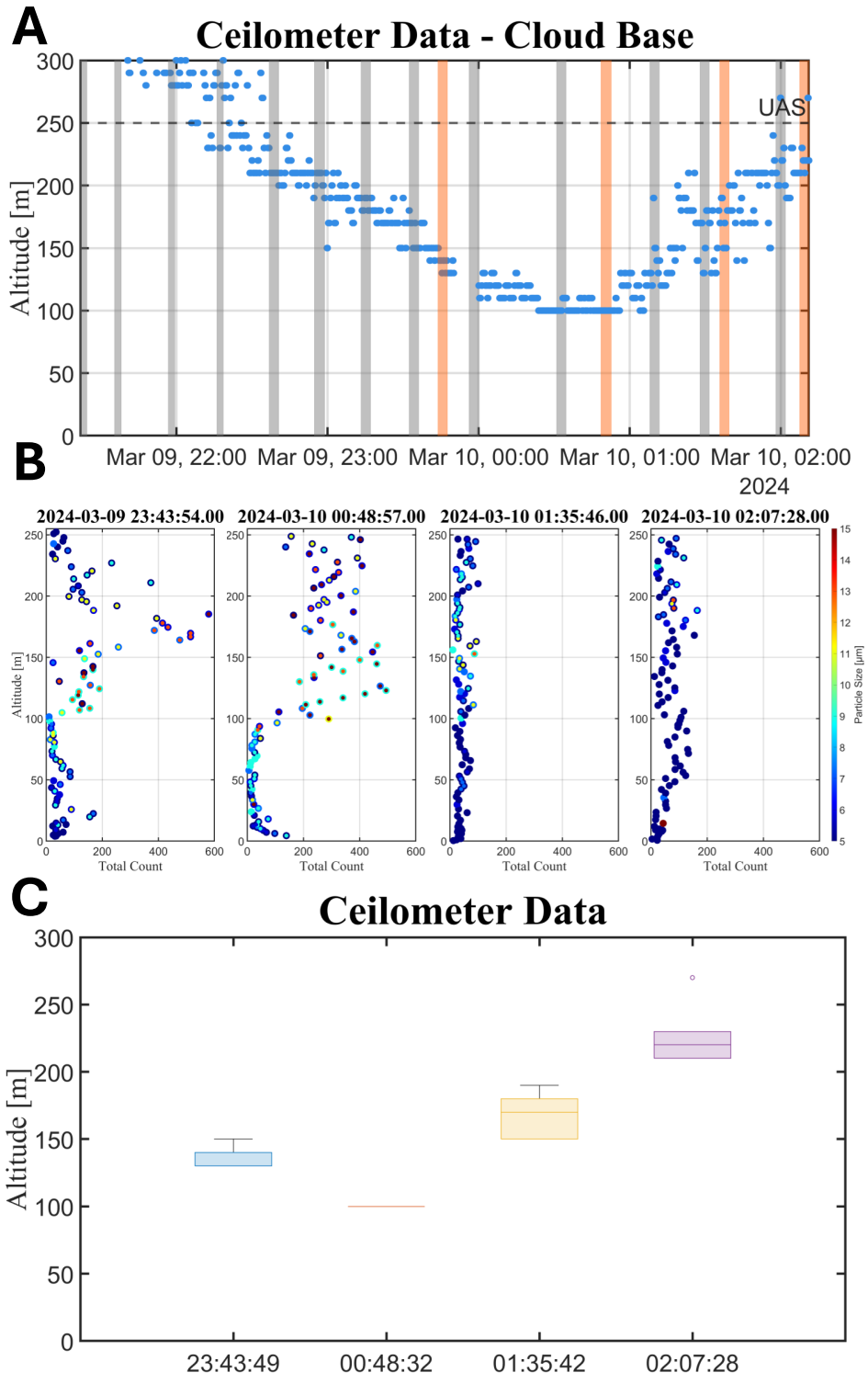


Figure 7.5: WxUAS cloud-sized particle distribution profiles compared to the colocated ceilometer. (A) ceilometer reports for the lowest cloud base. (B) WxUAS cloud-sized particle distribution profiles. (C) Box and whisker plot for the ceilometer lowest cloud base for the interval of the four WxUAS profiles.

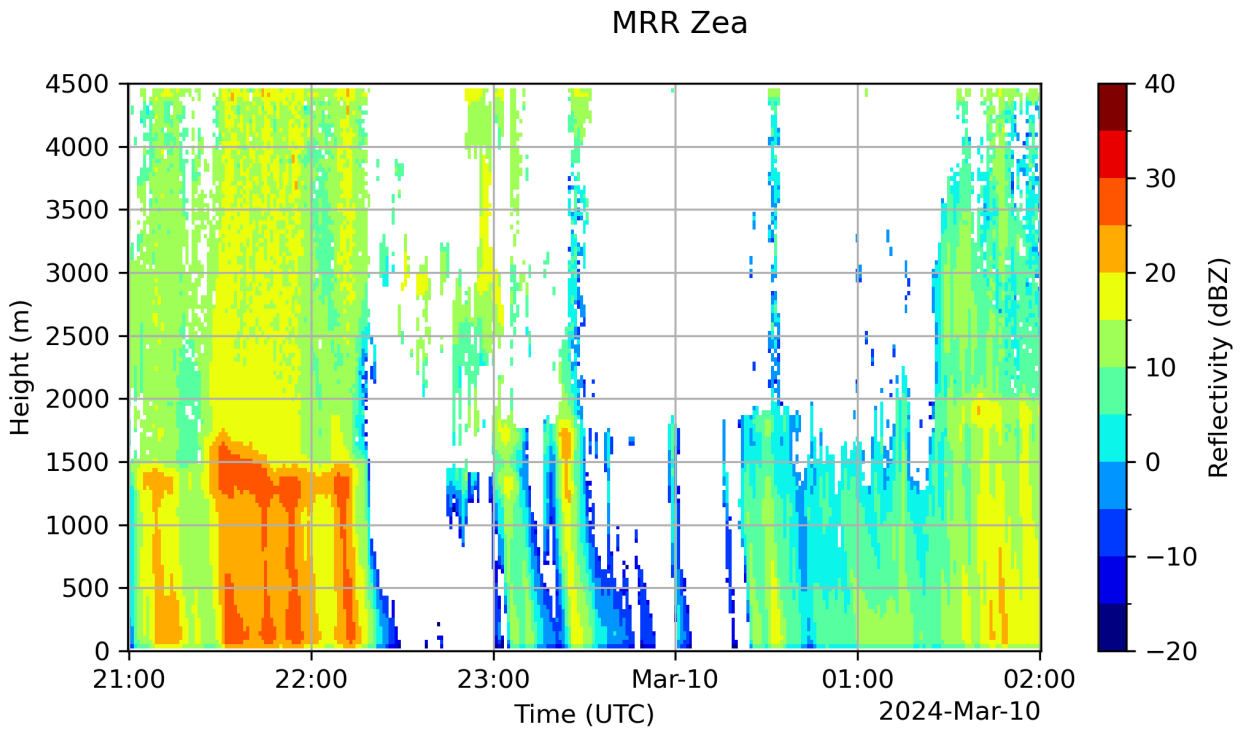


Figure 7.6: Height-time map for precipitation reflectivity from the colocated MRRs.

Finally, the StormTrooper's spatiotemporal map for relative humidity (Fig. 7.7) reveals the sampling period began within a predominantly dry environment (below 72%RH) from the surface to the flight ceiling, gradually transitioning to a more humid state. At the conclusion of the sampling period, relative humidity had increased to approximately 86 %RH at the surface and remained above 80 %RH up to 200 m AGL. Although this map presents a spatiotemporal evolution that generally agrees with remaining WxUAS weather products, the reported values for the relative humidity appear low in contrast to the precipitation and low-altitude cloud layers also detected by the WxUAS. To address this unexpected result, Section 7.1.2.1 offers a deeper discussion of the system's performance relative to the broader atmospheric conditions.

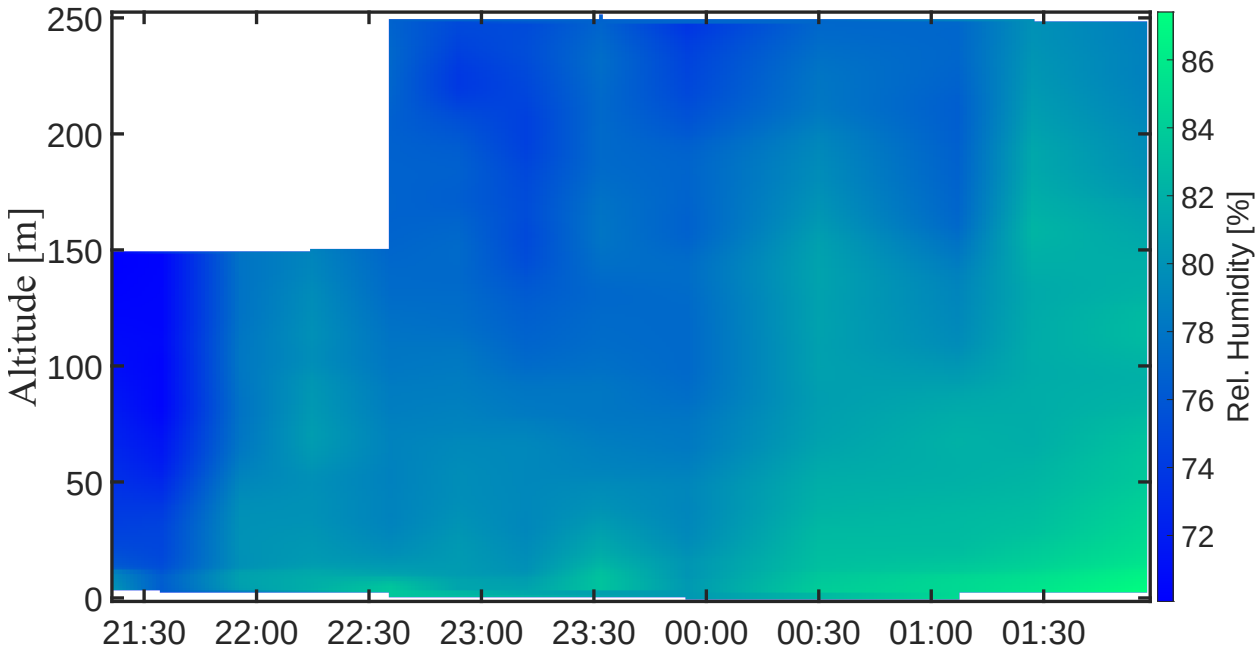


Figure 7.7: Relative humidity map for the WxUAS profiles on March 9, 2024.

7.1.2.1 Discussion

Before this analysis starts, it is worth mentioning that the StormTrooper's relative humidity measurements were quality-controlled using the neighboring sensor analysis detailed in Chapter 3, which did not indicate any bias or deterioration from the sensor's laboratory calibration. Its measurements were also compared to the ground-based sensors from NASA's GAIL trailer, which showed consistency in the general trends in temporal changes. More information regarding the limitations of this comparison will be presented later in this chapter. Finally, it is also worth mentioning that after this field campaign, the StormTrooper was compared to the Washington station in the Oklahoma Mesonet, producing acceptable errors and indicating overall measurement health.

In the preceding discussion, the StormTrooper's weather products highlighted precipitation periods and the presence of low-altitude clouds that were expected to have yielded saturated or at least near-saturated relative humidity profiles. However, the relative humidity data presented in Fig. 7.7 revealed profiles well below saturation, following a decreasing

relative humidity with height pattern. Leveraging the StormTrooper's onboard camera and external measurements from mesoscale observation networks, this discussion brings additional insight into this unexpected result.

The StormTrooper's onboard camera has not been presented in this dissertation because it is not a sensor yet. Nonetheless, even as a proof of concept, its images still serve for disambiguation and validation. For this discussion, Fig. 7.8 presents four frames taken during the 22:55 profile at 160, 185, 210, and 240 m AGL. This profile was selected for this analysis because it is the last profile in daylight, allowing direct observation of the cloud-base features. Although earlier than the previously discussed cloud-sized particle profiles, this 22:55 profile serves as an in-situ verification of the ceilometer's cloud base height.

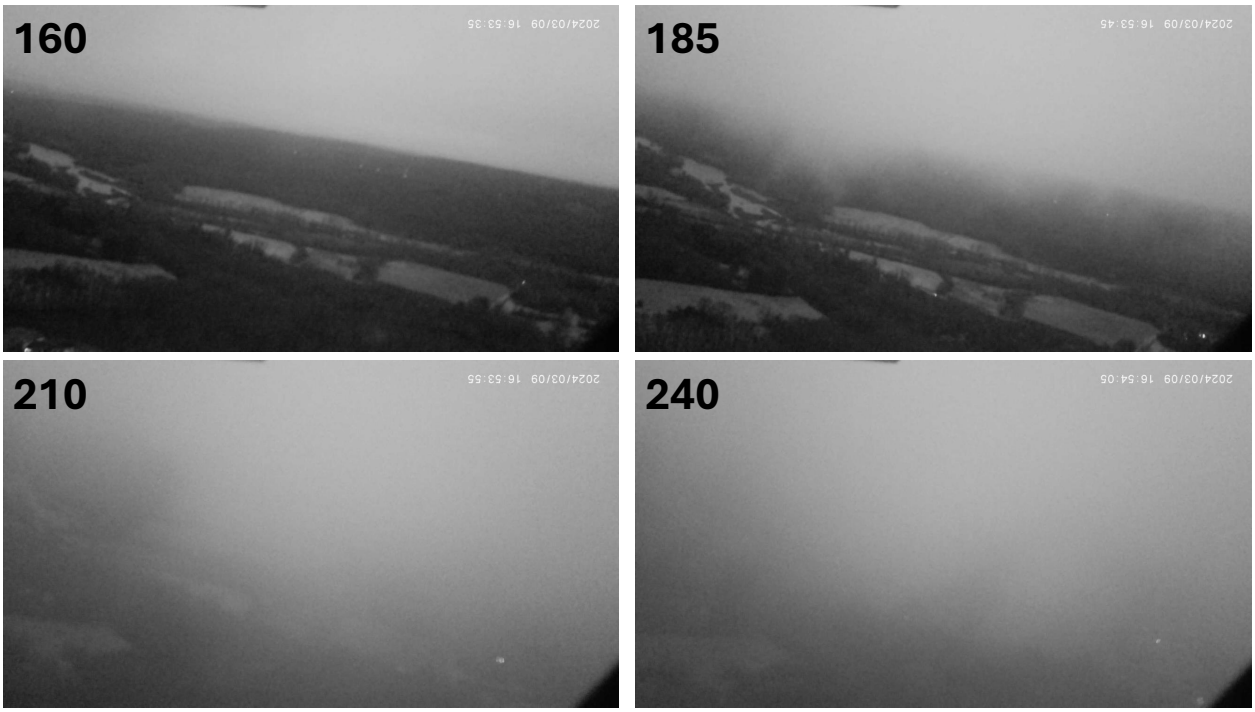


Figure 7.8: Frames from the WxUAS's onboard camera at 160, 185, 210, and 240 m indicating the start of the cloud transition layer and base of the cloud layer during the profile at 22:55.

In these images, it is possible to note the first hints of the cloud-transition layer blurring the horizon at 160 m AGL, as well as some downward cloud protuberances in the 185 m frame. Although the field of view is almost dominated by the cloud at the 210 and 240 m AGL

frames, the surface is still visible at the bottom of both frames. This indicates the WxUAS did not reach the cloud layer in this profile, which could explain the lack of saturation in the corresponding relative humidity profile.

Comparing the ceilometer's lowest cloud base with the images reveals a potential discrepancy. During the 22:55 profile, the ceilometer reported its lowest cloud base at altitudes varying between 190 to 210 m AGL, while the images indicate the WxUAS did not reach the cloud layer. Given the ceilometer's 20 m cloud base height variation within a few minutes, followed by an even more intense variation from 150 to 190 m in the subsequent two minutes, it is reasonable to infer that the ceilometer is identifying as the cloud base the atmospheric layer defined in this dissertation as the cloud transition layer. That is the atmospheric region marked by cloud-sized particles in smaller quantities, which do not entirely hinder visibility. For the formal definition, please revisit Chapter 6.

Interpreting cases where the ceilometer's reported cloud base distributions present a 20 m or larger width as a cloud-transition layer yields the expected coherence between the different observation technologies. For instance, the image-indicated cloud-transition layer from 160 to 210 m in the 22:55 profile agrees with the ceilometer's reported cloud-transition layer from 150 to 210 m AGL. This interpretation also produces agreement with the 23:43 cloud-sized particle profile, which indicated the presence of a cloud-transition layer starting at 100 m and intensifying at 150 m AGL, while the ceilometer reported cloud-transition layer from 130 to 150 m.

In both cases, the aircraft did not reach the cloud layer, which would explain the non-saturated relative humidity profiles. However, the 00:48 profile presented ceilometer-reported cloud bases at 100 m, with zero report variation, while the cloud-sized particle profile indicated a cloud layer starting at 99 m AGL. Although the 00:48 relative humidity profile presented an overall higher humidity than the 22:55 and 23:43 profiles, it still did not present saturated relative humidity measurements. On the contrary, the 00:48 profile followed the same

rate of change in relative humidity[1] seen in the 22:55 and 23:43 profiles, -0.028 $\%RHm^{-1}$.

Considering the lack of indication of any relative humidity measurement issues and the coherence between the multiple indications of the atmospheric conditions, the presence of a low-altitude dry-air mass deserves consideration. Upon preliminary examination, the presence of low-altitude warm and dry-air mass at our sampling location ahead of the incoming low-pressure system coming from Ontario (CA) would help explain the intense mixing indicated by the temperature spatiotemporal map, the varying altitude of the cloud's downward protuberances seen in the onboard camera and ceilometer data, the intermittence of the precipitation event, and the strong winds experienced by the WxUAS.

Examining the Weather Prediction Center's surface observation maps for the NE U.S. (shown in Fig. F.2) indicates that six hours before the WxUAS's deployment, a stationary boundary extending from the Great Lakes to Virginia was overtaken by a fast-moving warm front coming from the SE coast, with the potential to stifle the impact of the targeted cold front. The following time steps in the referred pictogram indicate that warm and dry air was being advected from the SE/ESE, reaching Connecticut before the cold front.

To complement the surface observations, the relative humidity sounding data from the closest stations in the Rawingsonde network, Long Island (KOKX) and Albany (KALB), are presented in Fig. 7.9 as an indication of conditions aloft. Although distant, the KOKX and KALB are strategically positioned to understand the conditions approaching the Connecticut sampling location. KOKX is located south of the WxUAS site, near the coast, while KALB is located northwest of the WxUAS in the direction of the mountains in NW Connecticut. Examining the relative humidity profiles before, during, and after the WxUAS period reveals an intensely dry air mass at both stations before the WxUAS sampling period. As the precipitation advanced from the west, the surface became saturated, but KALB still presented the same decreasing humidity-with-height trend observed by the WxUAS. The same trend can be observed in both stations after the WxUAS sampling period.

[1]This rate of change is calculated using the measurement value at the surface and the top of the profile.

Finally, data for the MRMS composite reflectivity is also shown in Fig. 7.9 in the same time steps as the soundings. This data shows that even as the incoming low-pressure system moved through Connecticut, the dry-air mass present in the region produced a no-precipitation notch extending from the coast towards the KALB station at 0Z. A more detailed view of the MRMS data is available in an evolutionary pictogram in Fig. F.1.

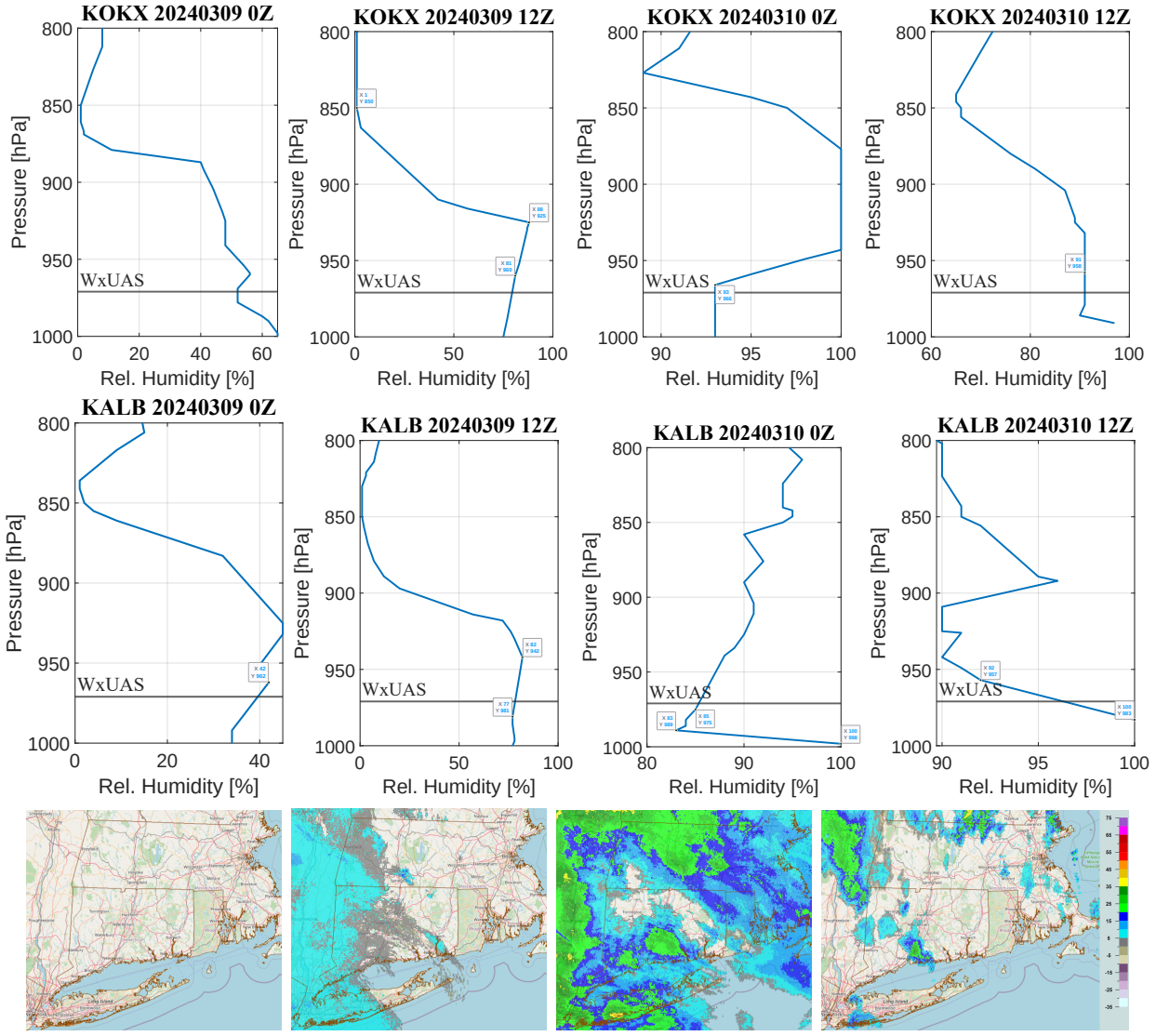


Figure 7.9: Complementary weather data from mesoscale networks. The top two rows present the relative humidity profiles from the KOKX and KALB sounding stations, and the bottom row presents the MRMS composite reflectivity at the same time steps.

Together, the multiple WxUAS measurements, the collocated ground-based sensors, and the data from the mesoscale networks produced a detailed description of this precipitation event, confirmed the validity of the WxUAS measurements, and highlighted the potential insights revealed by the WxUAS's low-altitude wintry precipitation products.

7.1.3 Deployment 2

Less than 24 hours after concluding the first deployment, the MAI^{2}S team returned to the study site, targeting the potential snow bands on the backside of the departing low-pressure system from the March 9$^{\text{th}}$ rain event. Models for this period indicated freezing temperatures could be present at altitudes lower than the WxUAS's flight ceiling. Based on this forecast, the WxUAS profiles started around 01:30 under strong N and NW winds, no precipitation, dry conditions, and temperatures near 4 °C.

After six profiles in an approximate 15-minute cadence, the temperature profiles indicated a cooling trend aloft, with temperatures below 1 °C, as shown in Fig. 7.10. However, the lack of precipitation indicated the predicted snow bands would occur later than expected. Considering the strong wind and its potential hazard to the WxUAS operations, the team temporarily interrupted the sampling operation at 03:00 until the bands approached our location. This sampling gap is notable in both spatiotemporal maps.

The WxUAS profiles resumed at 04:50 based on the radar indication of a precipitation band approaching from the north. At this time, the winds were still strong and intensifying, reaching approximately 16 m s^{-1}. By 05:01, the first snowflakes were observed at the study site. As noted and photographed by the team's meteorologist, the initial snowflakes were small, with estimated diameters at 5 mm and smaller, only increasing to nearly 30 mm in diameter around 05:51. As predicted, the snow bands were short. In this case, by 06:29, the snow intensity had lessened, and the strong wind gusts experienced during the event, particularly as the snow band approached, had subsided.

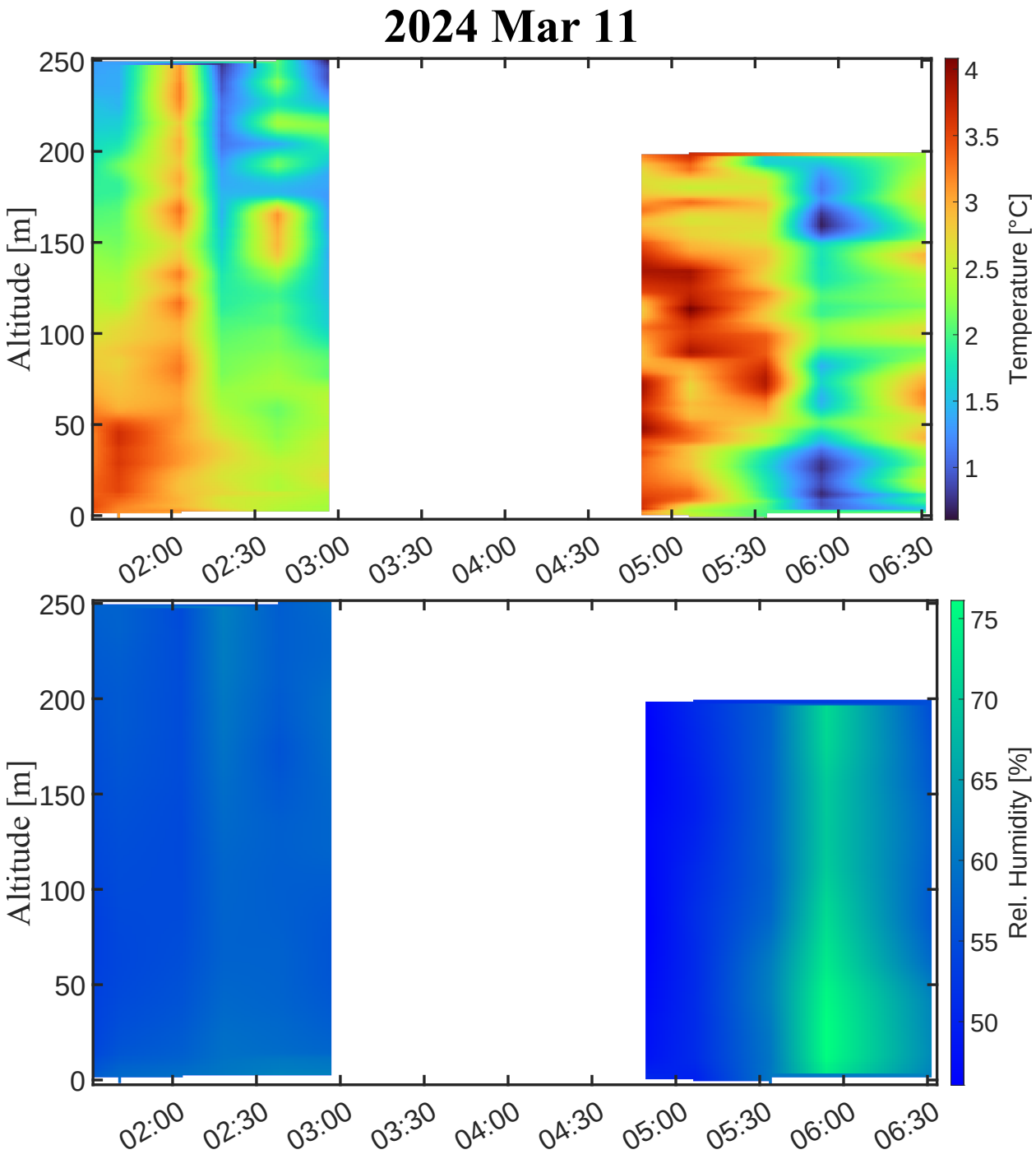


Figure 7.10: Temperature and relative humidity maps for the WxUAS profiles on March 11$^{\text{th}}$, 2024.

The WxUAS measurements describe a similar timeline for this event. The temperature and relative humidity spatiotemporal maps indicate the atmosphere's first 200 m was still well above freezing and dry until 05:50, when a sharp drop in temperature and increase in relative humidity occurred. By 06:30, the maps show the atmosphere's first 200 m returned to a warmer and dryer condition. The WxUAS's radar observations also agree with this timeline. The time series for the radar-derived precipitation variables, shown in Fig. 7.11, indicate a decrease in approximate hydrometeor fall velocity, as well as an increase in reflectivity and maximum detection range at 05:50. In conjunction, these changes are indicative of larger snowflakes and agree with the human observations. During the sampling period, the cloud-sized particle profiles did not indicate the presence of a low-altitude cloud or cloud-transition layer.

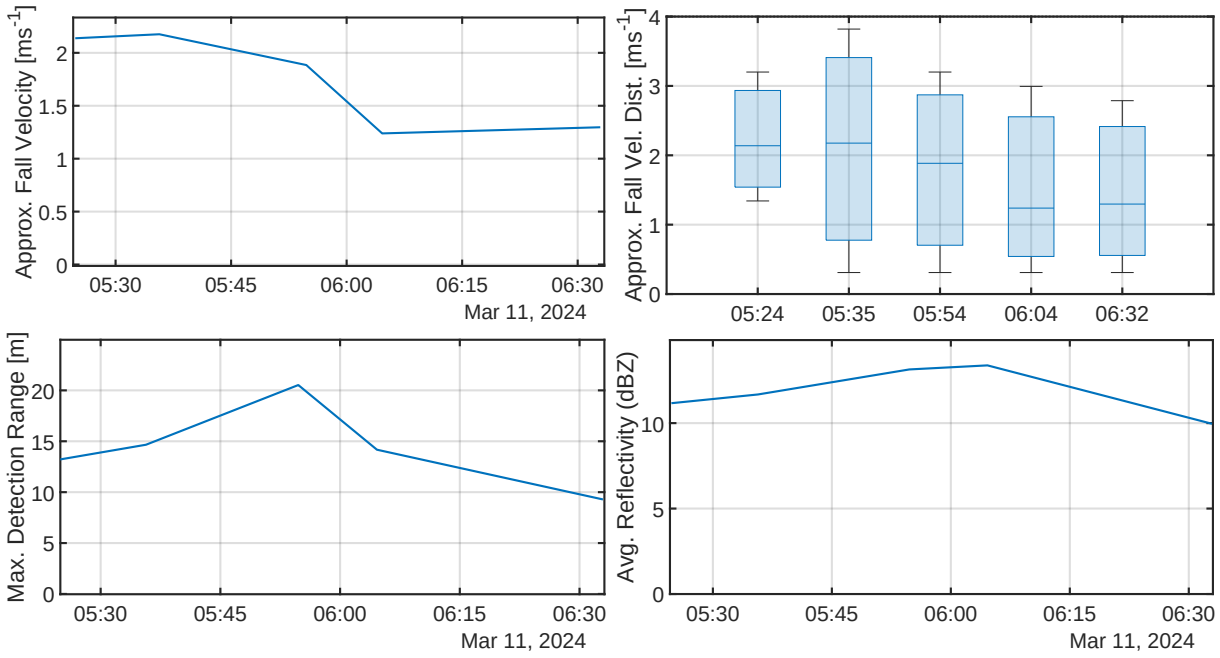


Figure 7.11: Radar-derived precipitation variables used for type and intensity classification for March 11$^{\text{th}}$, 2024.

Besides the agreement with the human observations, the WxUAS measurements also agree with the event timeline seen on the MRMS's composite reflectivity product. As shown in Fig. 7.12, at 05:30, the snow band had almost fully crossed the state's northern border,

moving toward its southern coastline following the path of the Connecticut River valley. At 06:00, the edge of the 30 to 35 dB shaded region reached the study site's approximate latitude, however, about 35 km west of the site's longitude. At 06:30, the snow band had passed the study site. Although brief, this event was full of nuances that produced minor variations in the multiple collocated instruments. Section 7.1.3.1 presents a small discussion on these nuances.

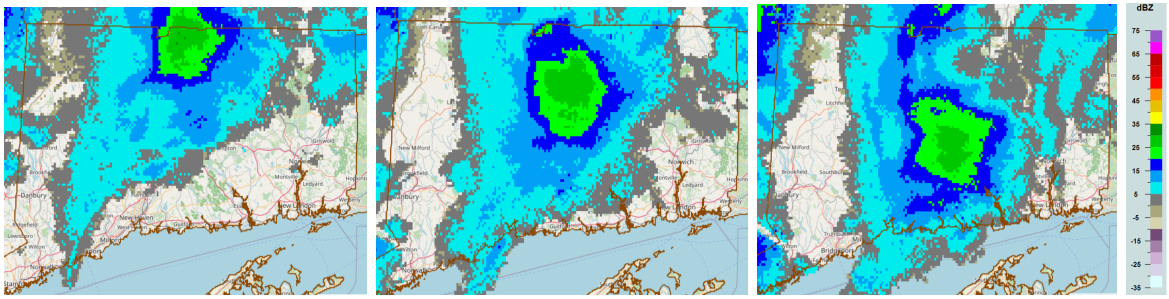


Figure 7.12: MRMS composite reflectivity for the snow band sampled on March 11th, 2024: (left) 05:30, (center) 06:00, and (right) 06:30.

7.1.3.1 Discussion

As previously detailed, the period between 05:00 and 05:50 produced small-diameter snowflakes with light intensity. In this same period, the WxUAS profiles revealed that the atmosphere's first 200 m was still well above freezing. Initially, this result was surprising due to the dryness of the snowflakes observed at the surface, which did not exhibit any sign of melting as they fell. However, leveraging the WxUAS's pressure, temperature, and relative humidity measurements to produce a wet bulb temperature spatiotemporal map (shown in Fig. 7.13) reveals the conditions were well suited for the observed dry snow.

Given that, at 05:30, the snow band was mostly north of the MAI^{2}S study site, the dry and small-diameter snow detected at the site was likely blown in by the strong northerly winds. These marginal conditions yielded differing reports by the human observer and the colocated instruments. For instance, at 05:00, the MRRs indicated precipitation at 1000 m AGL. At

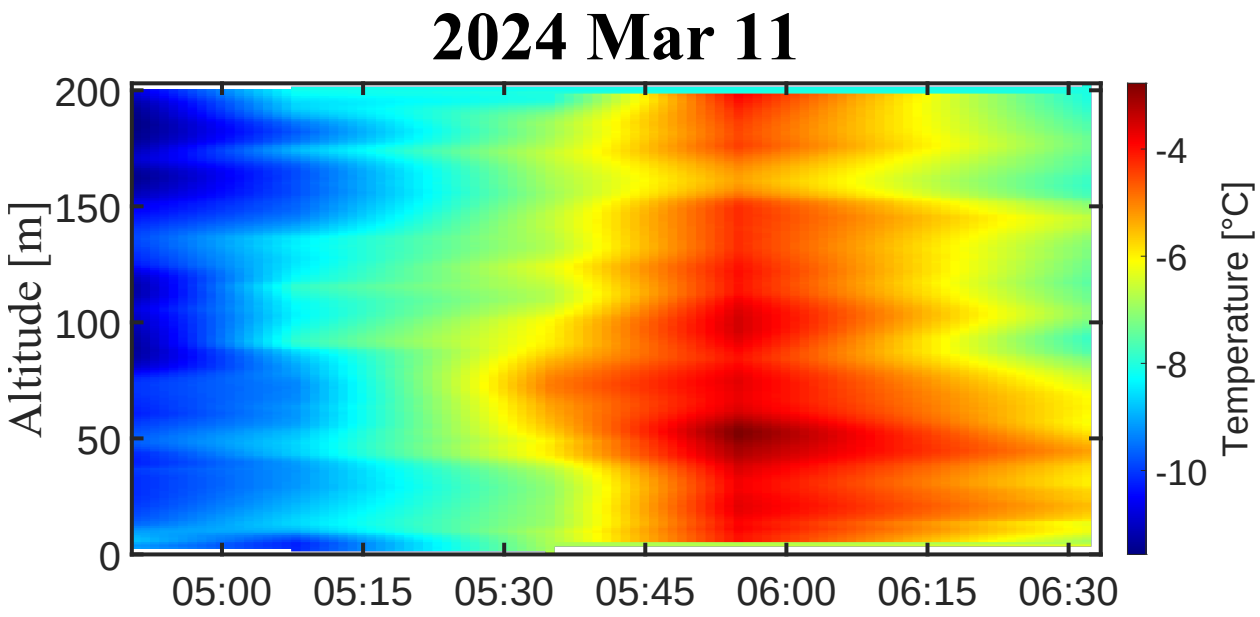


Figure 7.13: Wet bulb Temperature spatiotemporal map from the WxUAS profiles for March 11th, 2024.

05:01, small and dry snowflakes were seen by the team and detected by the PIP at the surface. At 05:07, the disdrometer detected the first precipitation particles. However, these particles only met its snow classification criteria at 05:13. Finally, at 05:24, the WxUAS's radar detected its first snowflakes.

Besides being considerably late, the WxUAS-based radar detections for this event were relatively weak. Compared to the snow event sampled during the experiment at Marshall Field (shown in Fig. 3.14), the data in this event produced considerably smaller values for reflectivity and maximum detection range (shown in Fig. 7.11). The detection challenges experienced in this event are likely explained by the joint impact of the event's light intensity, small-diameter snowflakes, and the dryness of the snow, as reflectivity is directly proportional to the total number of hydrometeors in the sampled volume, as well as their diameters and backscatter cross-sections. The hydrometeor phase impacts its backscatter cross-section through the complex refraction index, which is usually much higher for water than ice.

The results from this event are important in the StormTrooper's maturing process as they suggest a potential system limitation. This limitation is particularly evident when con-

sidering the system's automated present weather inference algorithm, which would not have been able to solve the ambiguity in the weakly detected frozen precipitation. Nonetheless, it is worth highlighting that some of this ambiguity is also present in the MRR data (shown in Fig. 7.14) and that the confirmation of the precipitation condition is provided by the WxUAS's wet bulb temperature profiles.

Finally, it is noteworthy that this peculiar snow event also presented detection challenges to the colocated ground-based instruments. As previously mentioned, the disdrometers also took several minutes to detect the snow, and the ceilometer erroneously reported these very dry snowflakes as cloud bases, as seen in Fig. 7.15. The indication the ceilometer reported precipitation as a cloud base stems from the discussion presented in Section 7.1.2.1 and the data from the WxUAS's cloud-sized particle profile at 05:50, which did not indicate the presence of a low-altitude cloud or cloud-transition layer when the ceilometer reported the cloud base altitudes varying from 80 to 140 m AGL.

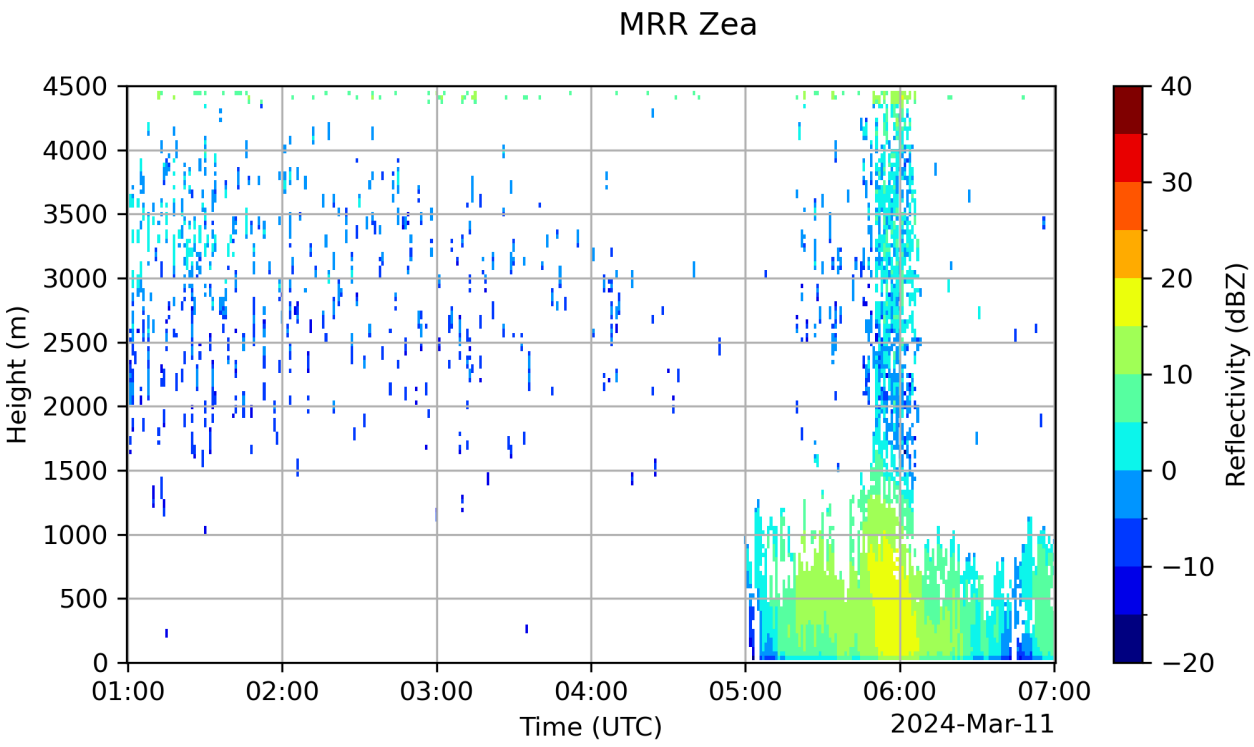


Figure 7.14: Height-time map for precipitation reflectivity from the colocated MRRs.

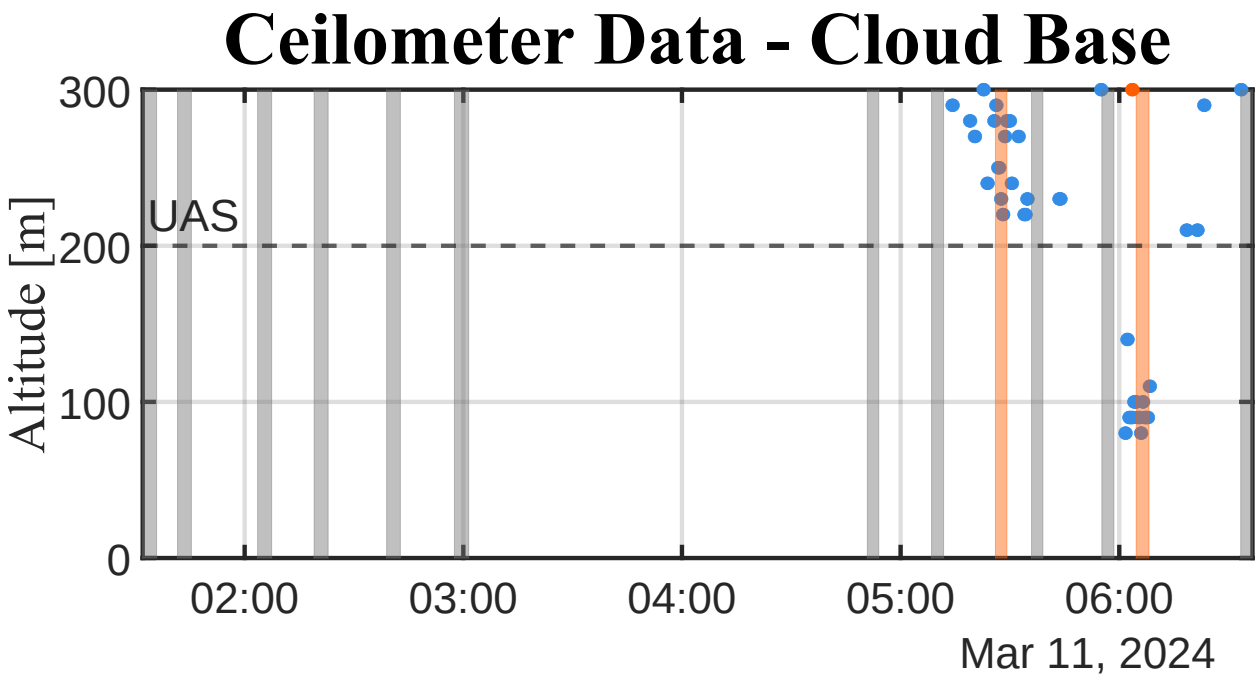


Figure 7.15: Height-time map for the Ceilometer's cloud-based reports during the passage of the snow band on the backside of the low-pressure system.

7.1.4 Deployments 3 and 4

The last two WxUAS deployments in the MAI^{2}S field campaign followed a similar format to the first two. Based on the forecast from the UCONN team, the Oklahoma WxUAS team was deployed to target the onset and departure of a low-pressure system from the Great Lakes. The forecast for deployment 3, on March 23$^{\text{th}}$, 2024, was a mix of snow and rain with the possibility for a transition to freezing rain or ice pellets. Sampling for the onset event started at 03:45 with winds out of the south-southeast and no precipitation.

Although Meteorological Phenomena Identification Near the Ground (mPING) app reported freezing rain during the WxUAS sampling period, these reports were limited to locations north of the study site and at higher elevations. At the study site, the nine WxUAS profiles within the 5-hour sampling interval did not detect temperatures below freezing within the atmosphere's first 200 m. On the contrary, the temperature spatiotemporal map

shown in Fig. 7.16 reveals a low-altitude temperature inversion from 04:15 to 05:15.

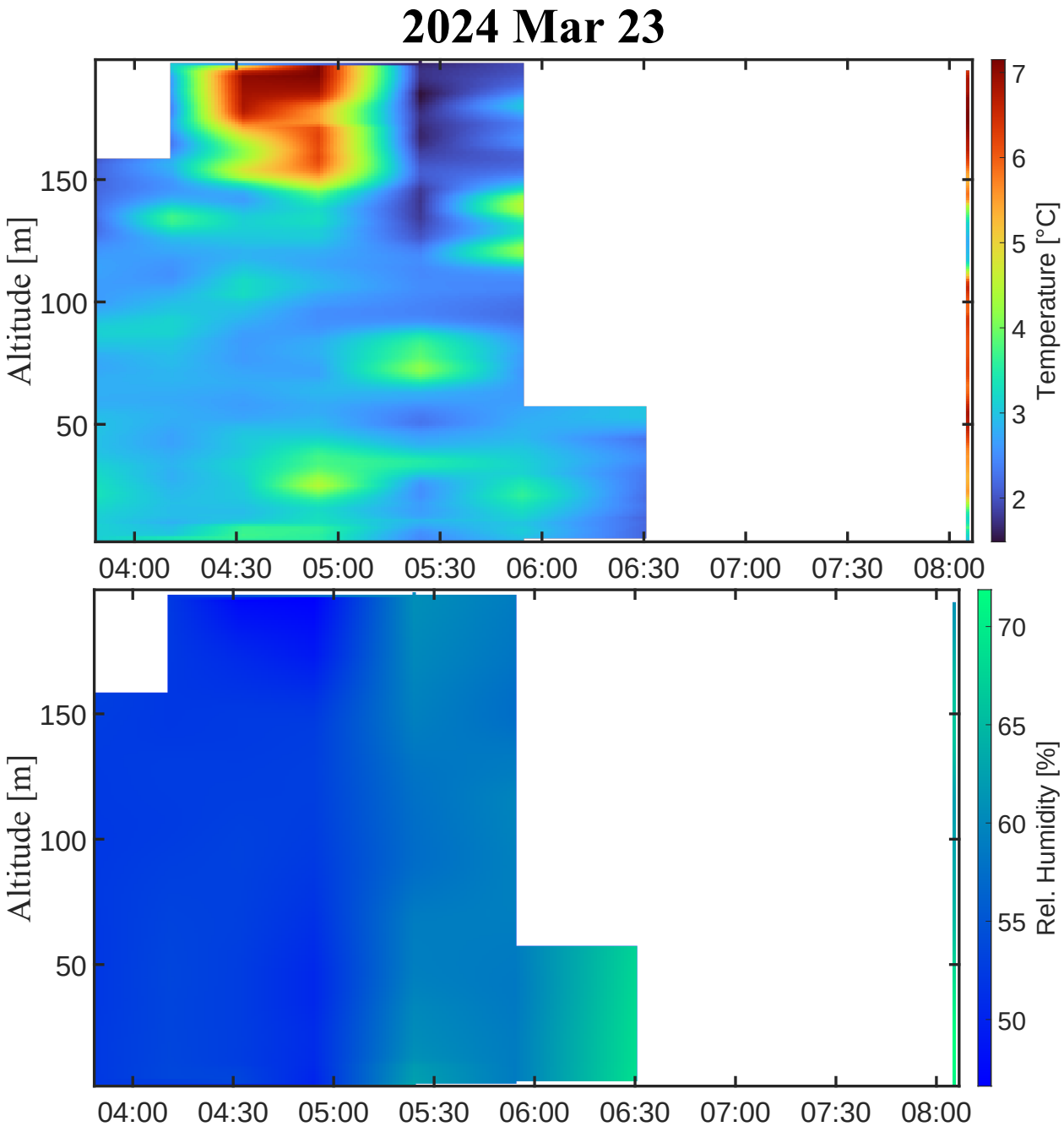


Figure 7.16: Temperature and relative humidity spatiotemporal maps for the WxUAS profiles on March 23rd, 2024.

These warmer temperatures were likely caused by an approaching warm front that hin-

dered the potential for freezing precipitation at the study site. Consequently, the forecast did not materialize, and the sampling period was dominated by sporadic precipitation in the form of light and moderate drizzle. This pattern showed some similarities to the events in the first deployment, including the dry air and the spatiotemporal mixing indicated by the temperature oscillations between 2 and 7 °C, which have been discussed in Sections 7.1.2 and 7.1.2.1.

During the sampling period, the WxUAS did not detect any cloud or cloud-transition layers within the atmosphere's first 200 m, and the ceilometer indicated the lowest cloud base reports at altitudes above 500 m. After the second profile, the first one in active precipitation, the auxiliary data conversion board on the WxUAS's mmWave radar presented an error that prevented the radar from saving its data. Unfortunately, this error could not be fixed in the field, disabling the StormTrooper's remote measurements for the remainder of the profiles in deployment 3 and all profiles in deployment 4.

At 06:30, the team opted to pause the WxUAS profiles in hopes of sampling mixed-phased precipitation later as the colder air from the low-pressure system descended the mountains west and northwest of the study site. However, by 07:00, surface temperatures and humidity started to increase, and the precipitation event was dominated by well-above-freezing rain. A little after 08:00, a WxUAS profile was taken to confirm the surface observations. This profile indicated even warmer temperatures aloft, concluding the deployment.

7.1.4.1 Deployment 4

As with the first two deployments, the MAI^{2}S team also sampled the departing low-pressure system initially targeted for its onset event. For this deployment, the model runs predicted rain with vertical profiles near freezing temperatures aloft. The model also predicted the system's departure from the study site's region between 03:00 and 04:00. Although the forecasted surface temperatures were above freezing, the team hoped the predicted low clouds would lower the freezing layer below the WxUAS's FAA-imposed flight ceiling.

Based on this forecast, the WxUAS profiling started at 23:30 on March 23rd under moderate rain and winds from the southeast. Although the first two profiles indicated temperatures as low as 0.98 °C above 150 m AGL, by 00:00, the precipitation started to dwindle without ever reaching freezing temperatures. By 00:45, the precipitation had stopped, and the WSR-88D radar products indicated the system had left the study's region entirely, which is much earlier than the forecasted timeline. Given the system's early departure, the sampling interval concluded at 01:15, and this outing only produced six profiles following the previously explained 15-minute cadence.

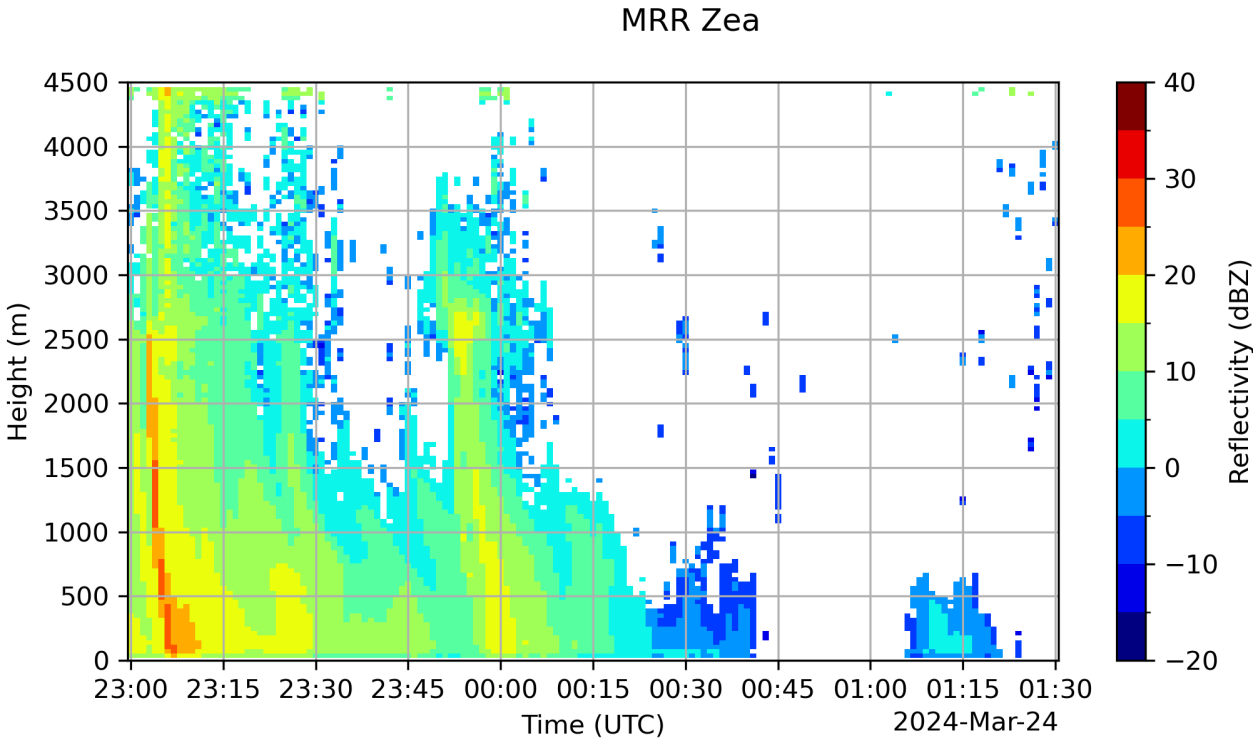


Figure 7.17: Height-time map for precipitation reflectivity from the colocated MRRs.

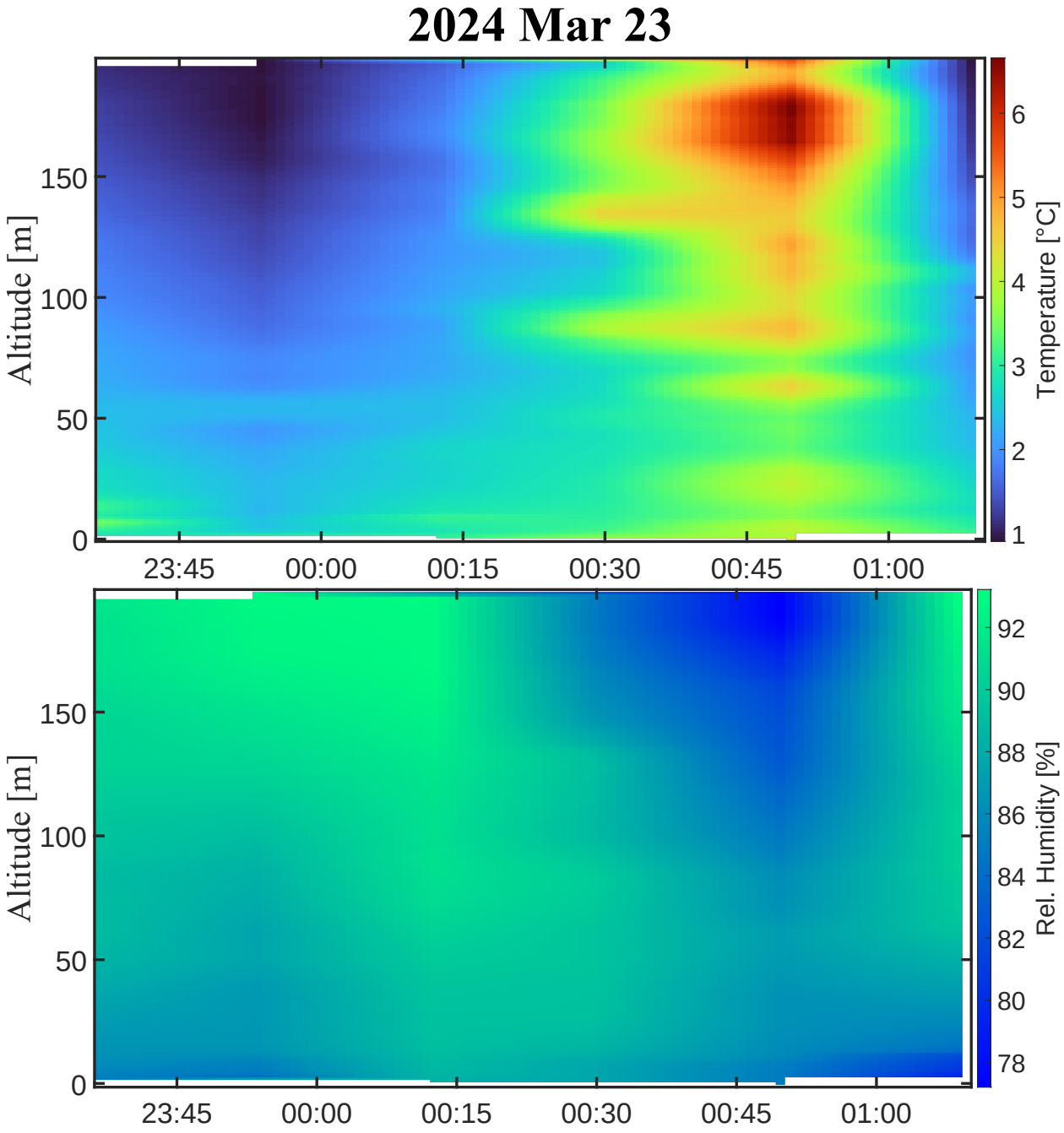


Figure 7.18: Temperature and relative humidity spatiotemporal maps for the WxUAS profiles on March 23rd, 2024.

7.1.4.2 Discussion

Although brief, this deployment produced profiles that present interesting features, particularly when contrasted with the previous three deployments. As can be noted on the WxUAS spatiotemporal maps, shown in Fig. 7.18, temperatures were near freezing, and relative humidity was approaching saturation with gradual spatial transitions instead of the large oscillations seen on the previous deployments. Also different than the earlier deployments was the pattern of moister air aloft. Combined, these results indicate that the previously detected warm fronts that brought dry air from the south-southeast were absent.

Another interesting feature in the spatiotemporal maps is the transition from cold and humid air to warm and dryer when the precipitation stopped, followed by a transition back to cold and humid when the precipitation resumed. Comparing this transition's timing with the precipitation indication from the MRRs (see Fig. 7.17), it is possible to note how the WxUAS's high-resolution measurements captured the nuances of the precipitation intensity changes. This high-resolution spatiotemporal view of this precipitation break also provides insight into conditions above the FAA-imposed flight ceiling.

For instance, within 1-hour, the conditions above 150 m AGL transitioned from 0.98 °C and 93 %RH to nearly 7 °C and 78 %RH. Evaluating the atmospheric conditions above the FAA-imposed flight ceiling through data from the closest sounding stations, KOKX and KALB, reveals a temperature inversion in both cases (shown in Fig. F.4). Considering the timing of this transition and its seeming top-to-bottom pattern, the strong low-altitude inversion at 00:50 was likely caused by subsidence induced by the departing system. Evaluating the MRMS composite reflectivity, shown in Fig. F.3, confirms the system was departing the study region at this time. The fast return to cold and humid air, as captured by the WxUAS, also corroborates this conclusion.

Finally, it is worth noting that the return to cold and humid air aloft, detected by the WxUAS after 01:00, matches with the brief drizzle event detected by the colocated MRRs. However, the MRMS composite reflectivity product for 01:00 (shown in Fig. 7.19) does

not show this event. Considering the lack of low-altitude coverage in the region (shown in Fig. 7.1) and the colocated ceilometer's report of cloud transition layers as low as 250 m AGL, this final drizzle was likely produced by a cloud below the radar coverage. Such an event demonstrates this dissertation's motivation for a low-altitude winter weather precipitation measurement system to complement the current observation systems.

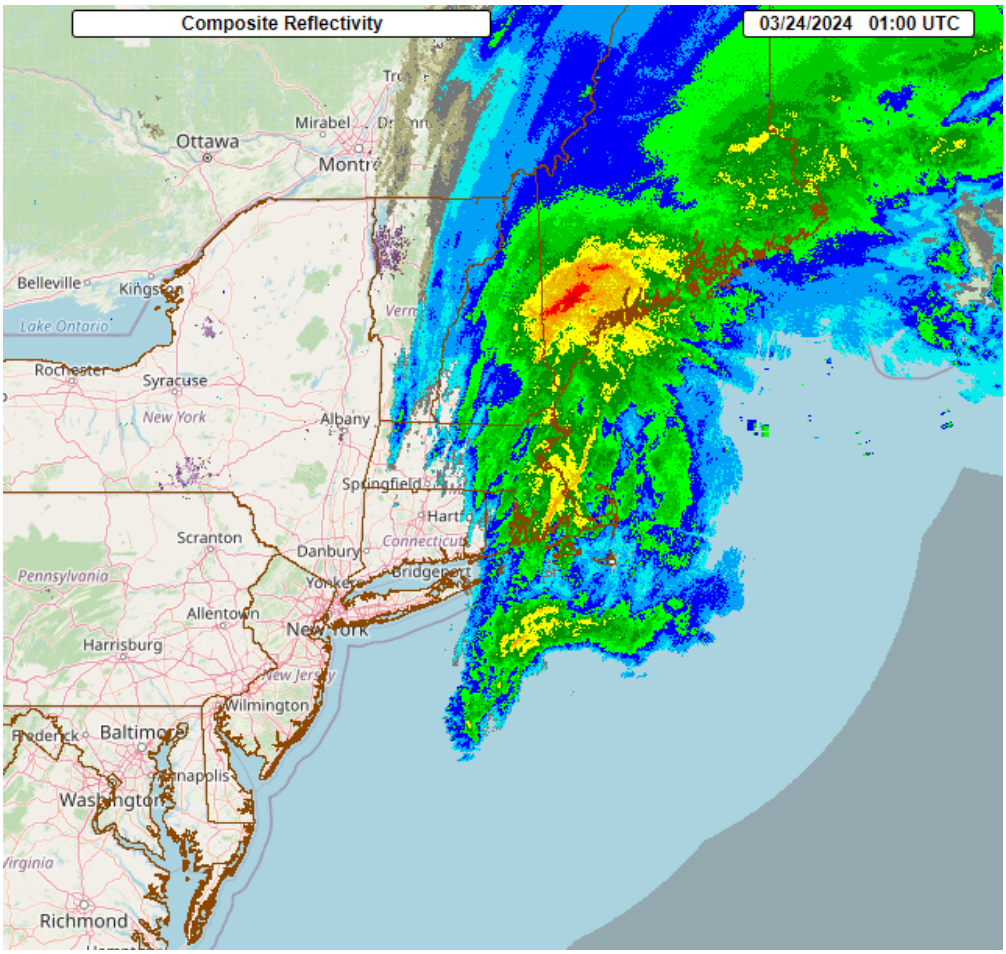


Figure 7.19: MRMS composite reflectivity for March 24th, 2024 at 01:00.

7.2 Final MAI^{2}S Considerations

While the StormTrooper's measurement performance metrics were validated in the experiments described in Chapters 3 and 4, the storms in the Storrs (CT) region present an

exceptionally complex environment, providing a valuable opportunity to assess the proposed WxUAS performance alongside well-established instruments for winter precipitation. Despite differences in measurement technology among the colocated systems, which preclude direct comparison, and the FAA-imposed flight ceiling, which limited exposure to freezing conditions, the cases presented in this chapter offer insights into the StormTrooper's ability to detect and characterize complex features, such as cloud and cloud-transition layers, precipitation type and intensity, and melting and freezing layers.

Through these 46 low-altitude profiles, the StormTrooper's multi-modal sensing approach complemented the colocated surface observations and the region's mesoscale observations networks, providing insight into the complex encounters between warm and cold fronts. Besides the expected insights from the high-resolution hyper-local information in each profile, the repetition of these profiles in regular intervals also enabled the capture of the extent and timing of passing features. Finally, comparing the atmospheric conditions in each deployment provides a broader insight into these storm setups and their expected impact.

For instance, leveraging the data from all four deployments indicates that the greater strength of the warm front that stifled the onset of the first storm target still impacted the expected features in its departures. In contrast, the weaker warm front associated with the second storm had a reduced impact on these expected features during its departure. Analysis such as this indicates the potential impact of this novel type of observation will only be fully appreciated with its wider adoption and the development of an accompanying novel data ingestion workflow. Chapter 8 offers additional commentary and points regarding the future of this research.

Chapter 8

Conclusion

"Most often, innovation is not the result of a sudden moment of realization, anyway, but the incremental steps toward improvement. Even groundbreaking paradigm shifts are most often the consequence of many small moves in the right direction instead of one big idea."

Sönke Ahrens

This dissertation endeavored to develop a novel atmospheric observation system to complement the currently available observation systems (e.g., radiosondes, ground and space-based radars, and automated surface observations) and provide insight into the mechanisms that govern low-altitude wintry precipitation. In addition to this goal, this research aimed to contribute to the emerging need for low-altitude weather observations to support the safe introduction of sUAS and AAM aircraft into the NAS. Given the growing interest in leveraging UAVs for atmospheric observations, this dissertation also expounded upon the generalized critical concepts regarding designing novel unmanned aerial weather measurement systems and the necessary considerations regarding platform selection, sensor integration, and system characterization.

To address such a broad and complex set of goals, the technological solutions developed for this dissertation were naturally divided into modules. Besides enabling the reader to better comprehend the intricate details of each module, they were intentionally presented separately as a way to highlight this dissertation's body of work as a low-cost atmospheric observation framework in which its modules can be modified, replaced, deployed individually, or in conjunction.

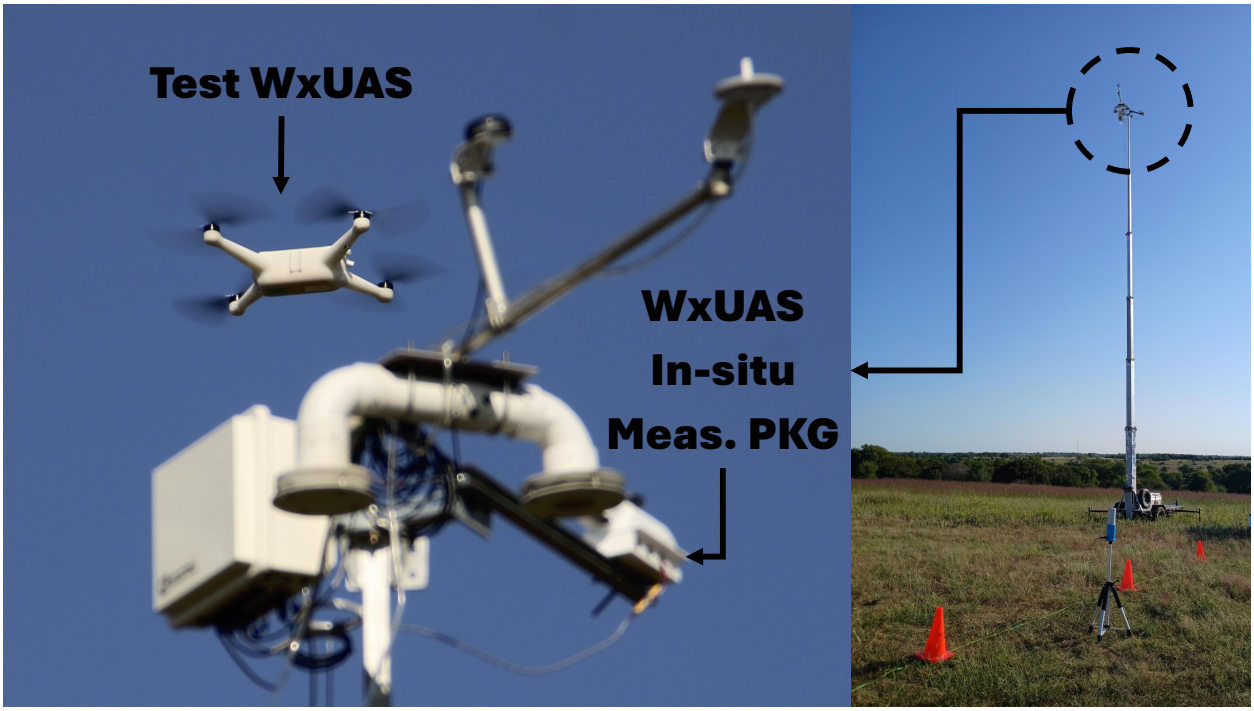


Figure 8.1: This dissertation's in-situ measurements solution deployed as a calibration reference for 36 WxUAS from various manufacturers and research groups.

Besides the cross-platform (i.e., between fixed- and rotary-wing WxUAS) technology use examples shown in Chapter 3, the advantages of this modular design and its flexibility are highlighted by its current and future unintended uses. As of the time of this writing, one such example occurred when this dissertation's in-situ measurement module was deployed as the reference measurement for calibrating all 36 WxUAS deployed in the Small-UAS Coordination for Atmospheric Low-Level Environmental Sampling (SCALES) field campaign, organized by the International Society for Atmospheric Research using Remotely-piloted

Aircraft (ISARRA), in September of 2024.

In this unintended use case, the in-situ measurement module was installed at a 20 m tower to serve as a low-altitude, fast-response reference for WxUAS calibration (illustrated in Fig. 8.1). This calibration process enabled their coordinated deployment targeting meso- and micro-scale weather phenomena across Oklahoma in the subsequent days. While this case demonstrates the technology's application outside of a UAS and beyond the scope of this dissertation's research on winter precipitation, it also represents an endorsement from the scientific community regarding the quality of measurements produced by this technology.

Although the extent to which this dissertation's technologies will be employed in additional applications is yet to be determined, each module has a well-defined contribution to the broader WxUAS research field and this dissertation's low-cost wintry precipitation observation framework. These contributions are:

- **A multi-rotor UAV design for reduced impact on weather measurements.** Leveraging a composite sandwich structure, the vehicle design isolated the primary vehicle components, prioritized sensor integration capability, and minimized rotor-induced bias on the sensors. Besides promoting modularity, flexibility, and scalability, the simplified and low-cost construction techniques employed also enable the widespread adoption of this aircraft design within the WxUAS research community. For winter weather research, the design delivers a field-serviceable, weather-resistant aircraft that can withstand the harsh storm environment.

- **A new measurement technique for in-situ temperature, relative humidity, and particle size sampling for airborne instruments in active precipitation environments.** This technique reduces bias from contact with supercooled liquid water and other error sources (e.g., sunlight). This design efficacy is underscored by temperature measurements exhibiting a mean absolute error of 0.051 °C and a maximum absolute error of 0.17 °C. These design attributes enable the accurate capture of atmospheric gradients of $0.22\,^{\circ}\mathrm{C\,m^{-1}}$. These results hold particular importance

in mixed-phase wintry precipitation environments, where even minor disturbances of 0.5 °C can have notable implications on hydrometeor phase.

- **UAV-based mmWave radar precipitation measurements.** As one of the initial studies in this domain, this dissertation provides insights into the complexities associated with integrating a weather radar system into the SWaP constrained environment of UAV platforms. Moreover, this dissertation presents novel algorithms and integration techniques to enable the detection of drizzle and other weak precipitation types with a low-cost, commercial off-the-shelf mmWave radar.

- **Multi-modal sensor data fusion method for autonomous present weather reporting.** This dissertation demonstrates a method for combining temperature, relative humidity, and micron-range particle size measurements with hydrometeor reflectivity and Doppler velocity to develop an automated present-weather inference algorithm. This algorithm focuses on the detection and location of freezing, melting, cloud transition, and cloud layers, as well as the presence of precipitation, its type, and intensity. Although still in the early stages, the demonstrated algorithm produced results that meet the acceptance criteria outlined in the new ASTM standard for third-party weather data providers for aviation.

While these modules can be modified, replaced, or deployed individually, their development was guided by and contributed to achieving this dissertation's goals. Therefore, it is in their integrated format that they can be evaluated as a new tool for atmospheric observations. The StormTrooper WxUAS integrates these modules, demonstrating how this framework can be applied to produce novel atmospheric observation systems. As such, it illustrates the implementation of this dissertation's considerations on the design of unmanned aerial weather measurement systems for wintry precipitation observations.

To further illustrate this point, Fig. 8.2 presents a diagram showing how each technology composes each module, how each module composes the framework, and how the

StormTrooper is this dissertations implementation of this framework that leads to novel low-altitude wintry precipitation information.

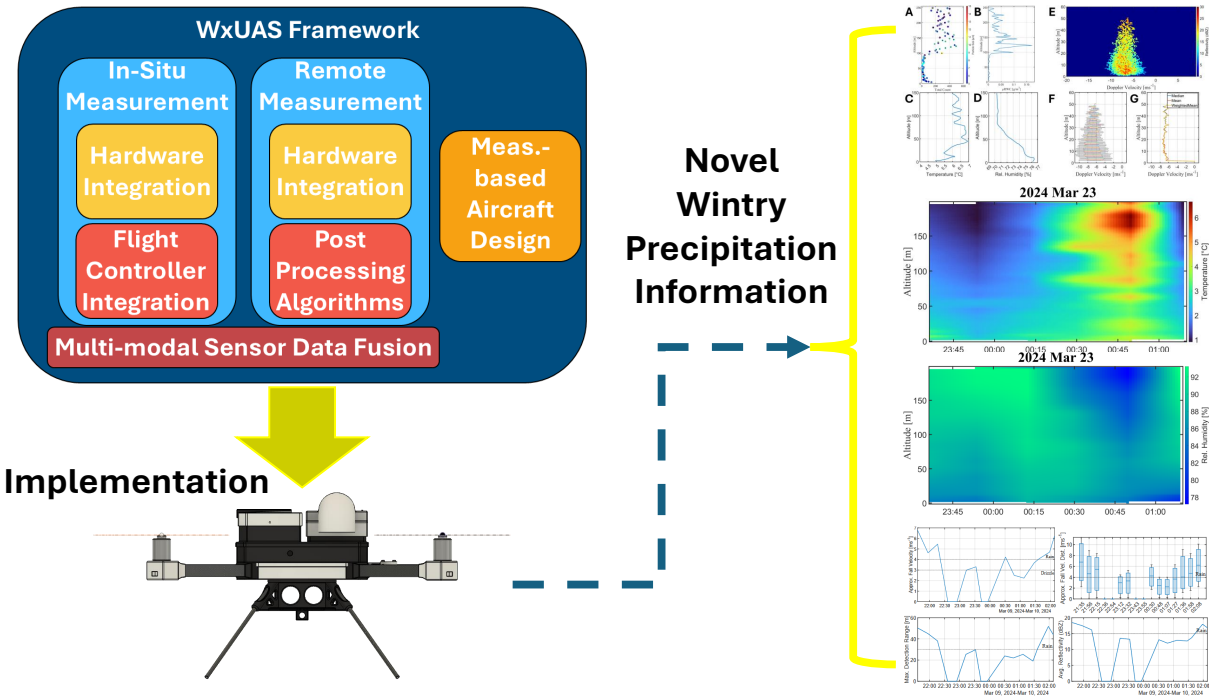


Figure 8.2: Diagram illustrating the framework, its modules, and how its implementation leads to novel atmospheric information.

Besides the essential results from laboratory and field experiments conducted during each module's development, results from the integrated system's deployment alongside well-established measurement systems demonstrated its potential to characterize complex atmospheric environments and offer valuable insights to researchers. Over 46 low-altitude profiles, the StormTrooper's multi-modal sensing approach complemented colocated surface observations and the regional mesoscale observation networks, shedding light on the intricate interactions between warm and cold fronts.

In addition to the expected insights from the high-resolution hyper-local information in each profile, the repetition of these profiles in regular intervals also enabled the capture of the extent and timing of passing features. Finally, comparing the atmospheric conditions in each deployment provides a broader insight into these storm setups and their expected

impact.

Aside from these tangible contributions, the work necessary to produce these outcomes also led to numerous intangible lessons regarding the design of atmospheric measurement systems, their validation, and field deployment. The following section presents small comments on these intangible lessons as a way to document them and promote future discussion.

8.1 Discussion

The MAI^{2}S field campaign was designed as a system performance evaluation study with ground- and WxUAS-based measurements. Although this was its main scientific objective, there was an additional operational objective for the ground-based sensors in MAI^{2}S. The MAI^{2}S ground-based sensors were deployed as part of the IMPACTS field campaign in the four previous years. During IMPACTS, these sensors were geographically distributed to sense the spatiotemporal behavior of storms in the region. Initial post-processing and analysis for the IMPACTS dataset revealed potential discrepancies between its sensors. To evaluate if these discrepancies were caused by spatial differing atmospheric phenomena or measurement errors, these sensors were colocated for direct intercomparison during the MAI^{2}S field campaign. The sensing challenges encountered during IMPACTS that partially motivated MAI^{2}S are not unique to this field campaign and reveal a few broader aspects of winter and general weather observations worth highlighting.

The first aspect worth highlighting is the harshness of the targeted environment and its impacts on sensing technologies. During the StormTrooper's development, the deployments at Marshall (CO) and Storrs (CT) were marked by partial systems failures, which hindered the system's ability to fully characterize the atmospheric conditions. Superficially, these failures could have been attributed to the low-cost and manual construction of the StormTrooper prototypes. However, similar failures on well-established, commercially supported systems during IMPACTS and MAI^{2}S denote a bigger association with the environment than with

a particular system's build quality.

Systems operating in this environment must be expected to fail, and deployments that require uninterrupted observations must employ contingency plans. To address this issue, two units of the StormTrooper WxUAS were built and deployed in the MAI^{2}S field campaign. Having two units enables quick replacement, diminishing the need for field maintenance, which is error-prone and presents an operational hazard. This redundancy is only possible due to the low cost of these systems. However, for two units of a WxUAS to be "hot swappable", their characterization implies an additional system definition layer.

As discussed in Chapters 1 and 2, the WxUAS is a system composed of a vehicle, sensors, and the integration techniques, and due to the interactions of these elements, it must have its characterization performed as a complete system. Analogously, if two units of a WxUAS can be swapped during a sampling period, seamless post-processing of this dataset implies the two units have comparable errors and bias. Consequently, these units must be characterized together under the same conditions, making the two units one system. Such was the case for the two StormTrooper units used in this dissertation.

The second aspect worth highlighting is associated with this characterization need. As discussed, systems should be characterized in their operation environment and conditions. The limitations in the size and range of environmental chambers imply that part of this characterization must be performed outdoors via intercomparison with other systems. This implication presents a number of issues, particularly for novel observation systems.

The first set of these issues is created by differing measurement technology. This issue was illustrated in Chapter 7 by comparing the ceilometer's reported cloud-base height with the WxUAS cloud-sized particle profiles and onboard camera. In this case, the differences between the measurement technologies prevent a direct performance comparison. This issue still arises even when two systems measure the same atmospheric parameters instead of features.

For example, the StormTrooper WxUAS and NASA's surface weather stations measure

temperature and relative humidity. However, because the surface station's sensors are slow-response, deployed with micro-porous filters in an unaspirated shield, while the WxUAS measurements are fast-response, unfiltered, and actively aspirated, the comparison between their data is limited to general trends (e.g., increasing and decreasing temperatures).

In this case, to account for the slow time response on the surface observations, WxUAS data were taken from the lowest altitudes in the spatiotemporal maps to create a time series for the WxUAS surface-level observations during the deployment period. The WxUAS surface level was then compared with the time series for the ground-based weather stations. Besides delay issues created by the filter and aspiration use discussed in the literature review (see Section 2.2.1, particularly [38]), this comparison method is also limited because the WxUAS data is taken during its takeoff phase, a flight stage in which measurements may be affected by ground effects and rotor wash recirculation. To account for these limitations, one can evaluate both systems using general trends with the proper time delay compensations (e.g., $\Delta RH/\Delta t$ and $\Delta T/\Delta t$).

These characterization limitations, coupled with the atmospheric unknowns, can lead to a lack of trust in atmospheric observations. This lack of trust is the final aspect from MAI^{2}S highlighted in this discussion. Given resource limitations, atmospheric measurement systems often have to be distributed to increase coverage. Although this distribution enables sensing the spatiotemporal behavior of storms in the region, it creates single observation points that can present unexpected or ambiguous results. In these cases, it is often hard to determine if the unexpected or ambiguous results are caused by an unexpected atmospheric behavior or sensor error.

WxUAS data is considerably more likely to encounter such issues. This occurs because a WxUAS moves through the atmosphere while atmospheric features move through its profiling path. For instance, consider the example illustrated in Fig. 8.3. In this case, a cloud protuberance encountered the WxUAS at T_1 and departed at T_2. Considering the fast response of StormTrooper's sensors, this type of encounter would likely produce a sharp change in

temperature, relative humidity, and cloud-sized particle counts. Because the StormTrooper is designed with sensor redundancy and its multi-modal sensing approach provides the means for partial self-validation, this high-resolution feature would likely be correctly interpreted.

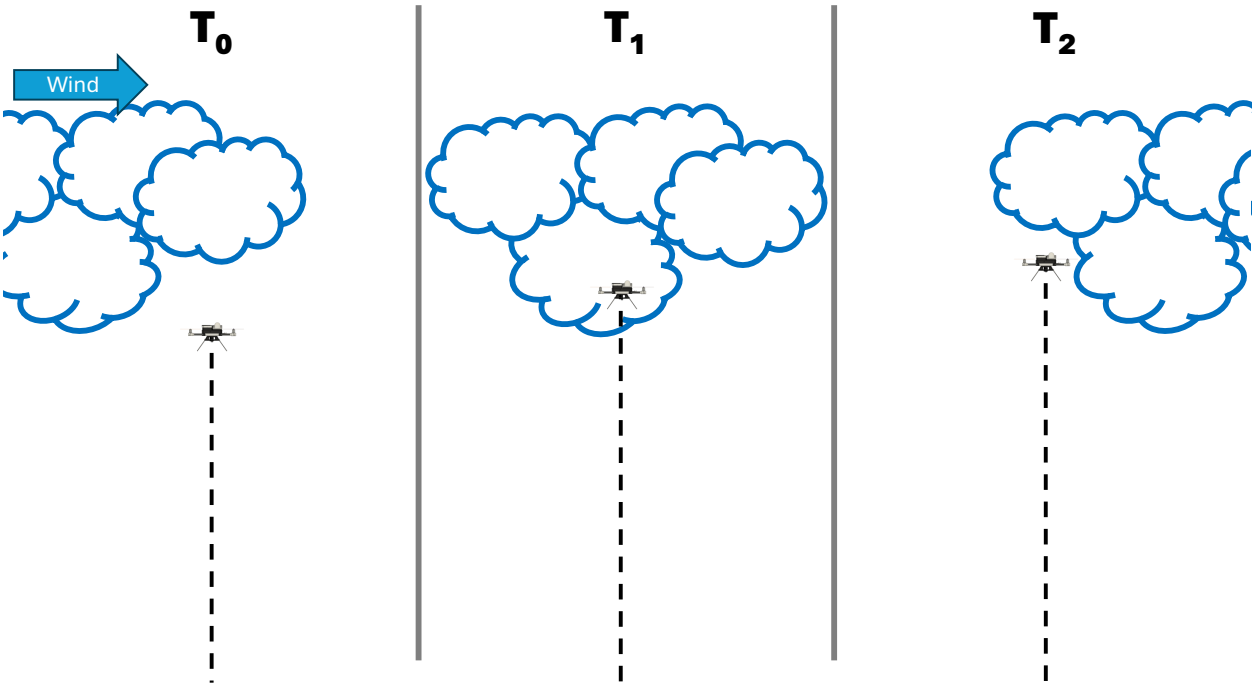


Figure 8.3: Illustration of weather passing through the WxUAS profile path and inducing unexpected measurement values (e.g., sharp increase and decrease in relative humidity).

Nonetheless, in a WxUAS with just temperature and relative humidity, particularly those with slower time response sensors for relative humidity, this result would likely be misinterpreted due to research bias. If this event happened in only one of the many profiles taken during a sampling interval, researcher bias would likely classify these accurate measurements as a sensor error due to a lack of trust in observation systems and a biased expectation of gradual behaviors. Without any other means of verification, this profile would likely be quality-controlled, and the sharp changes would either be discarded or filtered out of the profile.

This example underscores the need for a paradigm shift in interpreting WxUAS data. The high-resolution nature of WxUAS data increases the likelihood of detecting subtle fluc-

tuations associated with transient atmospheric conditions. As WxUAS research continues to advance, so too must the methods for data interpretation and assimilation, which will, in turn, guide future improvements in WxUAS technology. The insights gained in this dissertation have revealed areas for potential enhancement, which are discussed in the following section.

8.2 Future Work

The StormTrooper demonstrated the feasibility and value of WxUAS atmospheric sampling in the low-altitude wintry precipitation environment. Nonetheless, as a novel system, it presents considerable room for improvement. Additionally, this nascent field of WxUAS-based low-altitude wintry precipitation sampling should continue to grow based on the lessons learned in this research. Below are three recommendations for continued work in this field.

- **Dedicated WxUAS-based weather radar** – In this research, a commercial off-the-shelf mmWave radar, originally developed for collision avoidance applications in the automotive industry, was converted into a WxUAS-based vertically pointing precipitation radar. Although successful in providing a low-cost assessment of precipitation type and intensity, this conversion also encountered several limitations. Given the value of the information demonstrated in this dissertation, this research field would greatly benefit from the development of a dedicated WxUAS-based weather radar. Particularly one with the separation between the antenna and the radar's backend, which will increase flexibility in physical integration. Another desired feature is better software integration options, which will reduce weight and system complexity.

- **Hydrometeor trajectory-based sampling** – Cases such as the one presented in the second MAI^{2}S deployment (see Section 7.1.3) illustrate how the precipitation experienced at the surface can travel considerable horizontal distances relative to its generation layer. The winds that cause this travel also cause considerable drift on

radiosondes. The WxUAS's ability to counter the wind minimizes this drift. However, the temperature gradients that induce phase change as the hydrometeors falls may be underrepresented in both cases. Leveraging the flight controller and sensor integration described in Chapter 3, a multi-modal sensor data fusion algorithm should be developed to enable real-time hydrometeor-trajectory-based sampling via autonomous adaptive behavior. Utilizing an autonomous adaptive sampling algorithm designed for the environmental characteristics of the mix-phased wintry precipitation environment, the StormTrooper will compensate for atmospheric conditions and trace an atmospheric profiling trajectory mirroring the hydrometeors' path from the generation layer to the surface.

- **WxUAS image-based sensing** – Considering the complexity of the low-altitude wintry precipitation environment, the actual observation of the weather is still the norm in the field for disambiguation and validation. For this reason, some researchers limit their studies to use only human-augmented present weather reports, and a growing amount of effort has been made toward image-based sensing. In this dissertation, the WxUAS's conceptual onboard camera played a pivotal role in disambiguating the discrepancies between the ceilometer and WxUAS data. Therefore, WxUAS-base wintry precipitation research field would greatly benefit from the development of a low SWaP image-based sensing. Particularly one that could be automated to detect atmospheric changes with height.

8.3 Final Considerations

The considerations on the design of unmanned aerial weather measurement systems for wintry precipitation observations presented in this dissertation represent a practical contribution to this research field exemplified by the StormTrooper WxUAS. Additionally, the abstraction of these concepts and considerations presents a broader impact on the general field of

WxUAS research and atmospheric observations, particularly towards the emerging need for high-resolution, low-altitude weather data. Consequently, this work hopes to inspire and inform subsequent research that leads to more atmospheric insight, better forecasting, and the safe introduction of the next generation of aircraft into the NAS.

Appendix A

OK Mesonet Chamber Experiment

Initial calibrations of the Sensor Inner-Shield for the In-situ Measurement Design (see Chapter 3 at the Oklahoma Mesonet's Calibration Laboratory. This procedure used the Thunder Scientific 2500 benchtop humidity generator (left panel in Fig. 3.11). This chamber produces controlled temperature and relative humidity conditions following NIST's Two-pressure method. Within this controlled environment, the design's inner shield was taken through three 3-hour ramps where temperatures varied from 5 to 15 °C and relative humidity ranged from 65 through 95 %RH, jointly. As seen, dwell and step periods for each variable were mismatched to produce several test conditions.

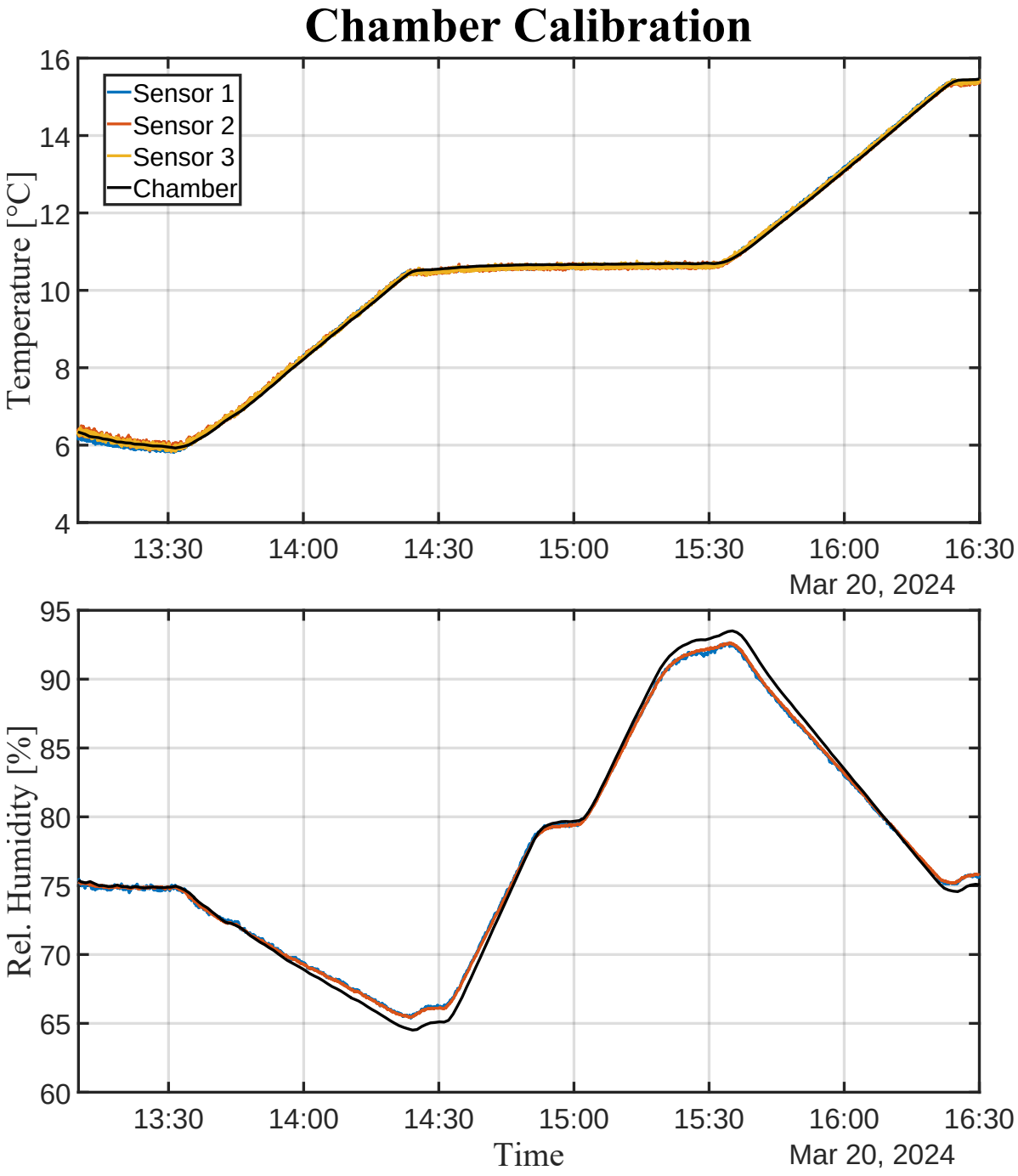


Figure A.1: Time series for the temperature and relative humidity experiment at the Oklahoma Mesonet's Calibration Laboratory. The black series represents the chamber reference values, and the colored series represents the calibrated individual sensors.

Appendix B

OK Mesonet Flight Comparison Experiment

To evaluate performance under operational conditions, the system was deployed near an Oklahoma Mesonet tower for collocated measurements. Each Mesonet station has a collection of instruments placed at heights that range from 60 cm below to 10 m above the surface. This experiment leveraged the temperature sensors at 1.5 and 9 m and the relative humidity sensor at 1.5 m. Figure 3.12 offers an illustration of the tower's sensor placements along with a depiction of the experimental setup.

In this comparison experiment, two identical rotary-wing WxUAS, with the proposed in-situ measurement design solution, were placed on the ground next to the tower (one on each side). After a period of baseline measurements without any effects introduced by the aircraft's flight characteristics, both aircraft took off and hovered next to the tower at 9 m above the ground (height of the temperature sensor). This hover height was selected to eliminate any potential recirculation produced by aircraft ground effects, which could bias the experiment and interfere with the time series of this operational Mesonet station. For similar reasons, each aircraft flanked the tower on opposing sides, facing the mild incoming breeze.

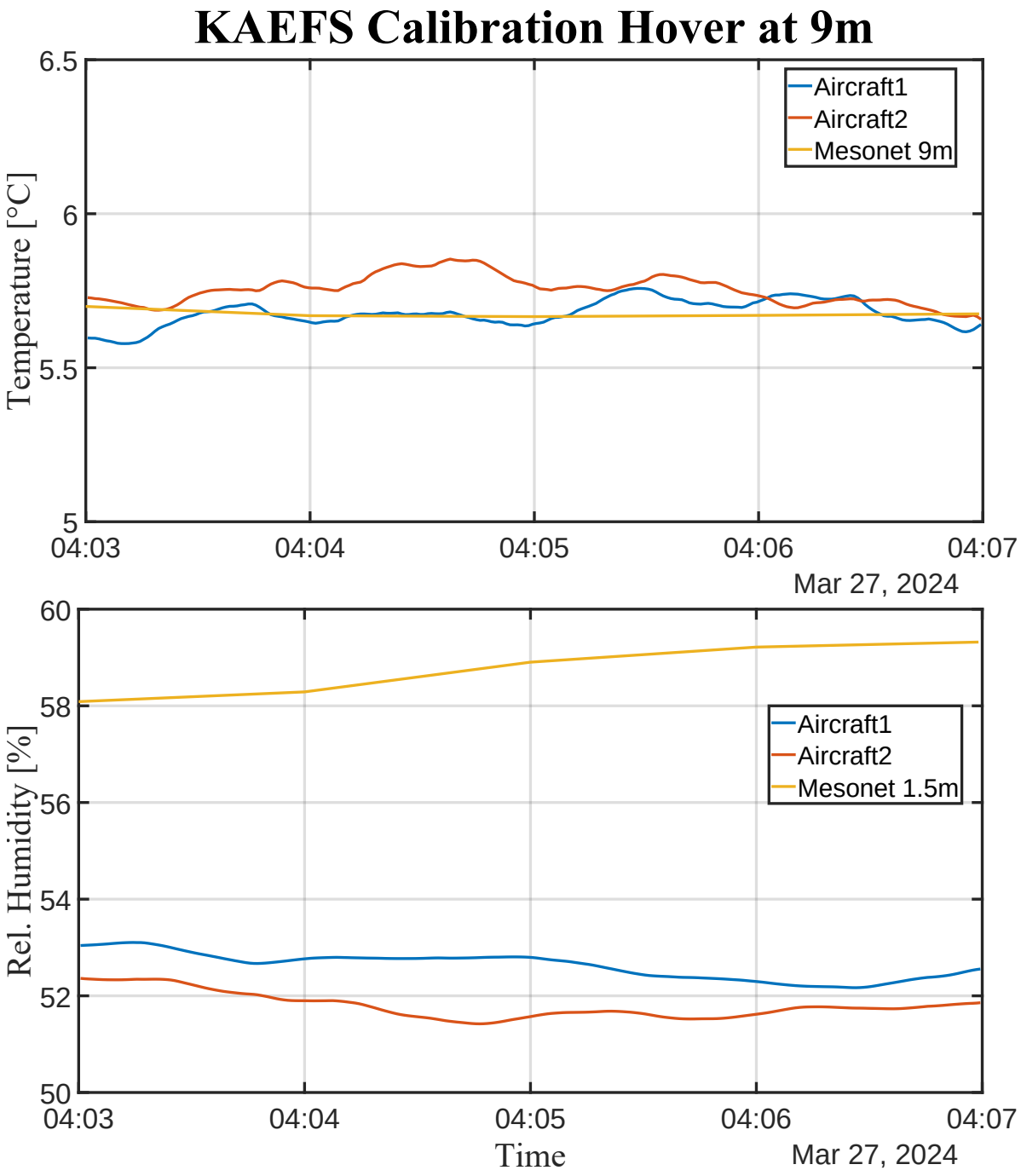


Figure B.1: Time series for the tower and two aircraft data highlighting the comparison interval. Mean and maximum absolut errors are found in Table 3.4.

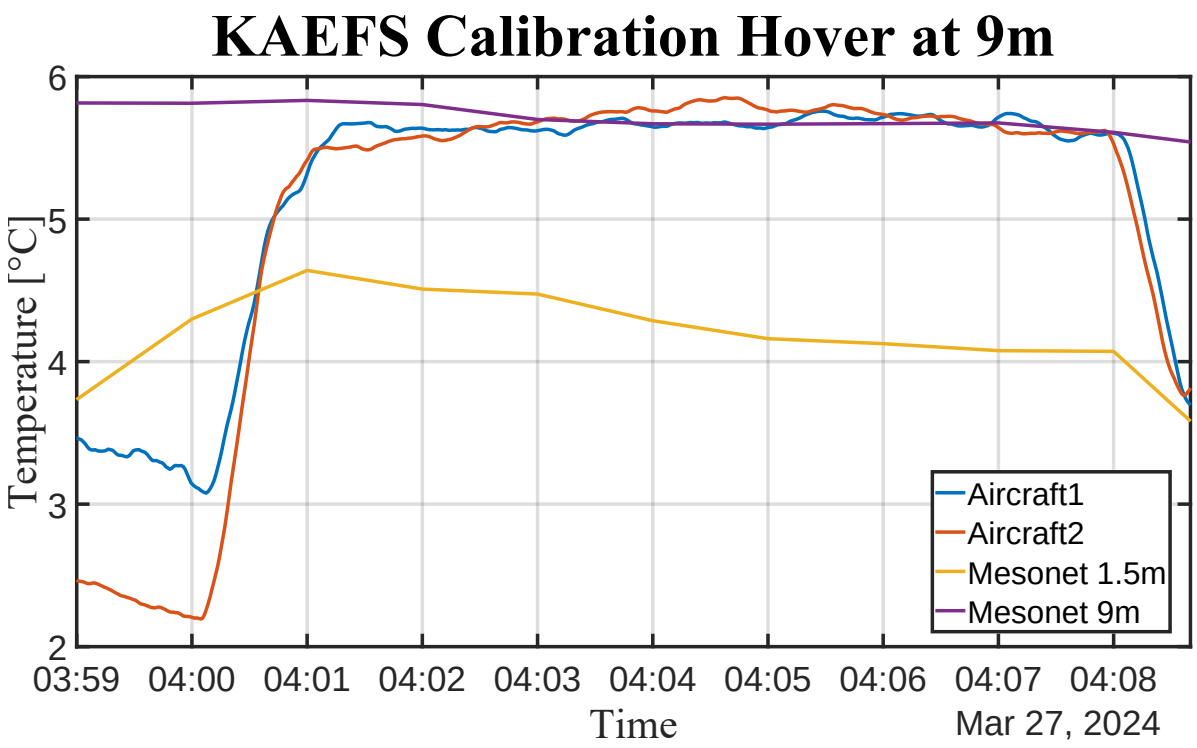


Figure B.2: Temperature time series for the tower data (1.5 and 9 m) with both aircraft data, including data before and after take-off.

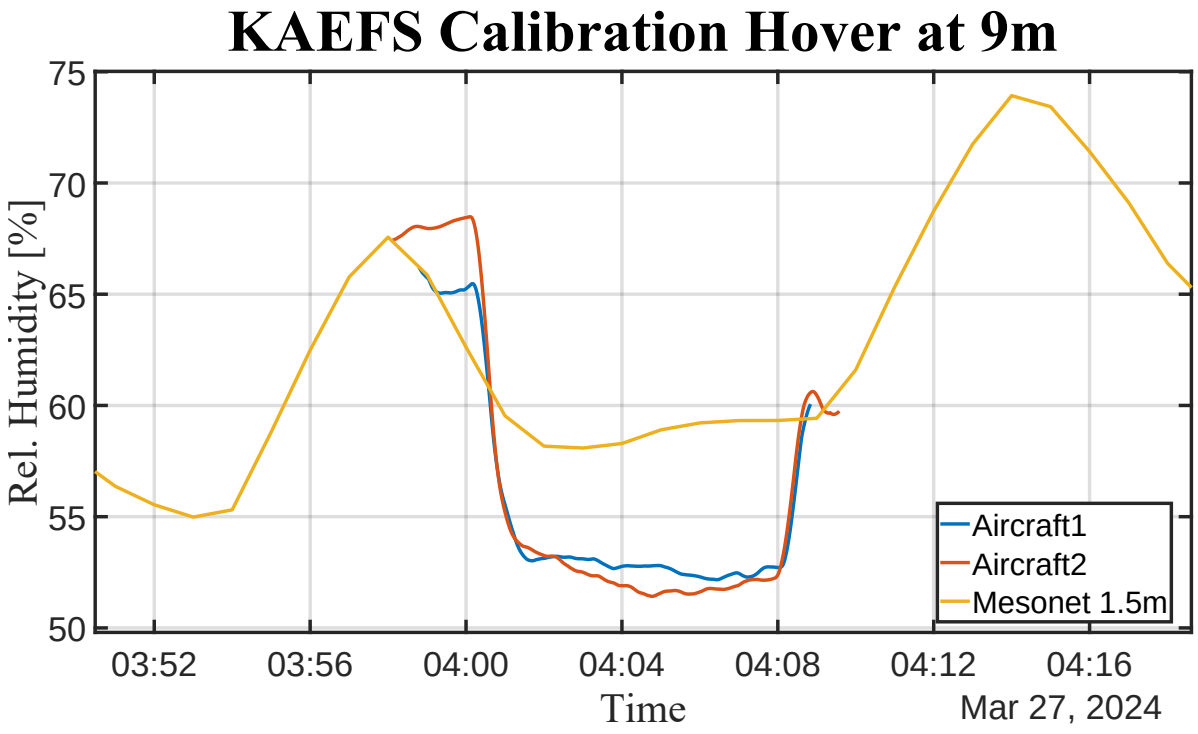


Figure B.3: Relative humidity time series for the tower data (1.5 m) with both aircraft data, including data before and after take-off.

Appendix C

Radar Configuration Parameters

Table C.1 presents the parameters used to configure the TI AWR2243 for all data collected within this dissertation's scope. Figure C.1 presents an illustration of the radar's chirp and how the variables on Table C.1 influence it.

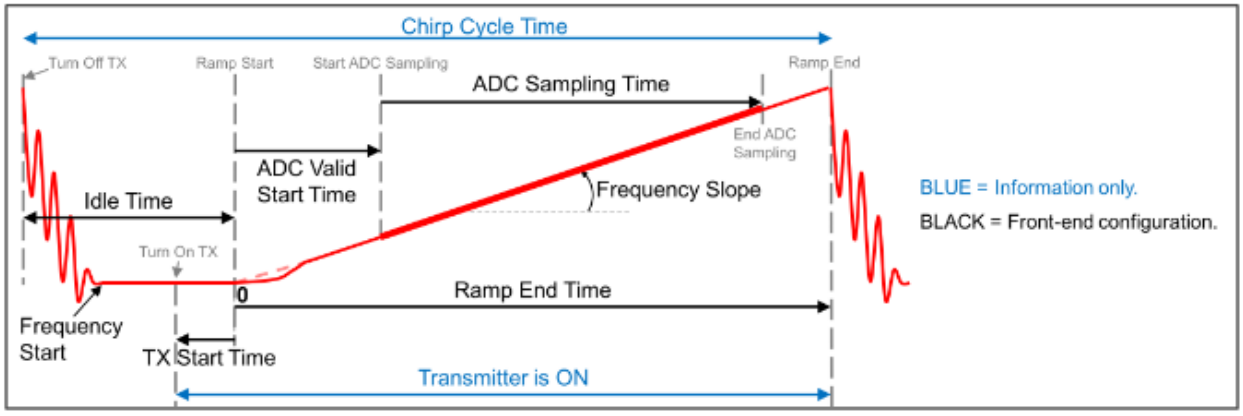


Figure C.1: Chirp illustration from Texas Instrument's user guide showing each chirp parameter. Source: TI mmwaveSDKUserGuide.

Parameter	Value
Active TX Antennas	3
Active RX Antennas	4
Starting Frequency	77 GHz
Bandwidth	349.79 MHz
Wavelength (Lambda)	3.9 mm
Frequency Slope	$9.994\,\mathrm{MHz\,\mu s^{-1}}$
ADC Sample Rate	16 670 kbps
Number of Range Bins	512
Idle Time	2 µs
Ramp End Time	35 µs
Pulse Repetition Frequency	27.027 kHz
Loops per Frame	255
Chirps per Loop	1
Pulses	255
Number of Frames	4
Interframe Interval	40 µs
Range (Max)	250 m
Range (Resolution)	0.4887 m
Doppler Velocity (Max)	$26.32\,\mathrm{m\,s^{-1}}$
Doppler Velocity (Res)	$0.2065\,\mathrm{m\,s^{-1}}$

Table C.1: Radar configuration parameters.

Appendix D

Pitch Angle Compensation Experiment

Experiment to validate the TI AWR2243's capability to collect data at different angles and the post-processing algorithm's capability to correct the detection angle used to compensate aircraft pitch via beamforming in post-processing. In these experiments, a metal pole was placed broadside to the radar (i.e., head-on) and at 60 degrees, both at approximately 10 m from the radar. Figure D.1 presents the experimental setup and Fig. D.2the power per angle results for both experiments, broadside on the left and 60 degrees on the right.



Figure D.1: Experiment setup, a metal pole at broadside and a 60-degree angle. Both at approximately 10 m.

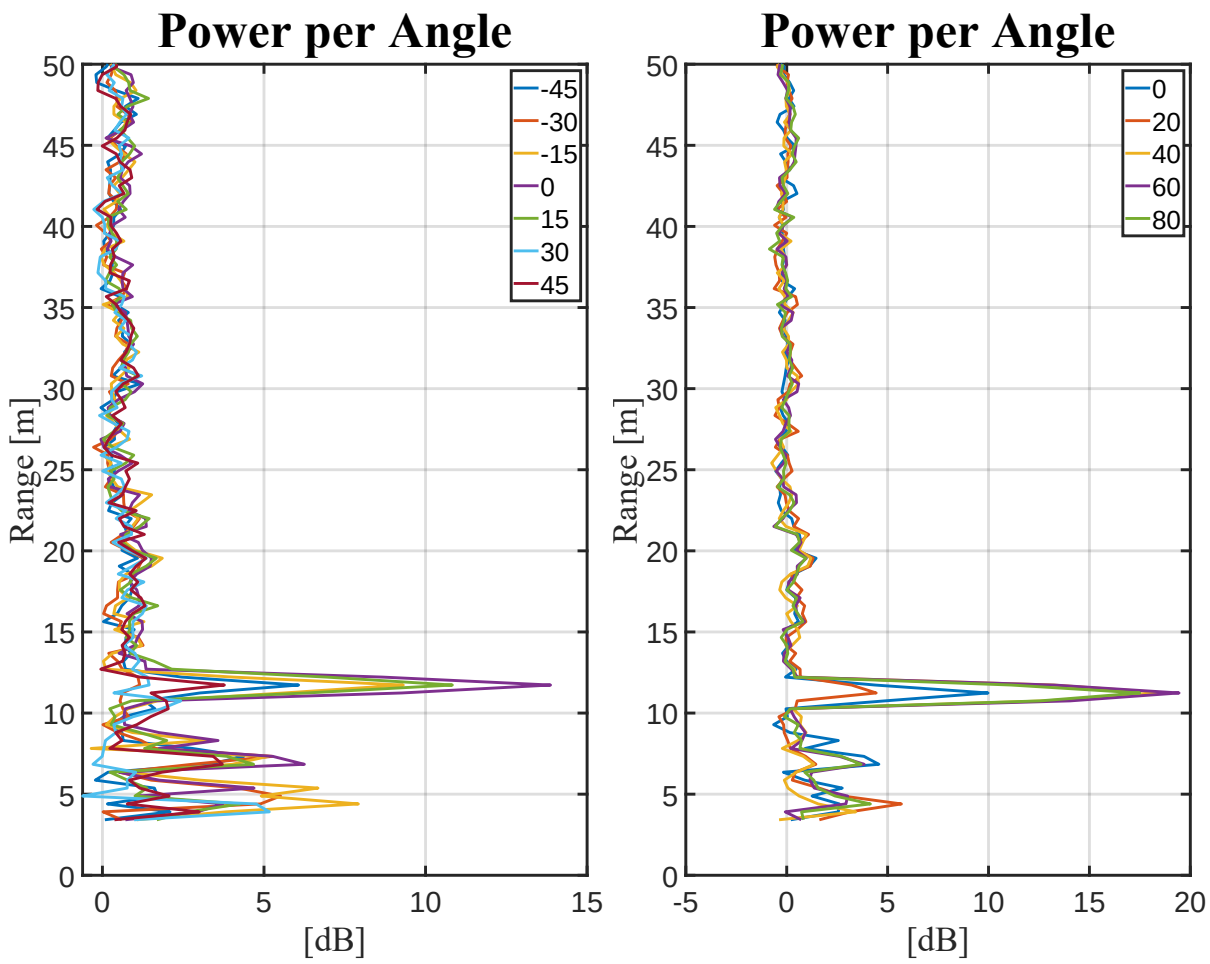


Figure D.2: Experiment results for the pitch angle compensation via beamforming in post-processing. Metal pole at broadside on the left and 60 degrees on the right.

Appendix E

Aircraft CAD

Illustration of the 3-dimensional computer-aided design for this dissertation's WxUAS aircraft designs, highlighting its symmetry, modularity, and flexibility. Figure E.1 shows the orthographic top and front views, while Fig. E.2 shows a cut of its orthographic back view revealing its internal modules. Figure E.3 shows the three iterations that express the modularity of the design. Finally, Fig. E.4 shows two units built for the MAI^{2}S field campaign.

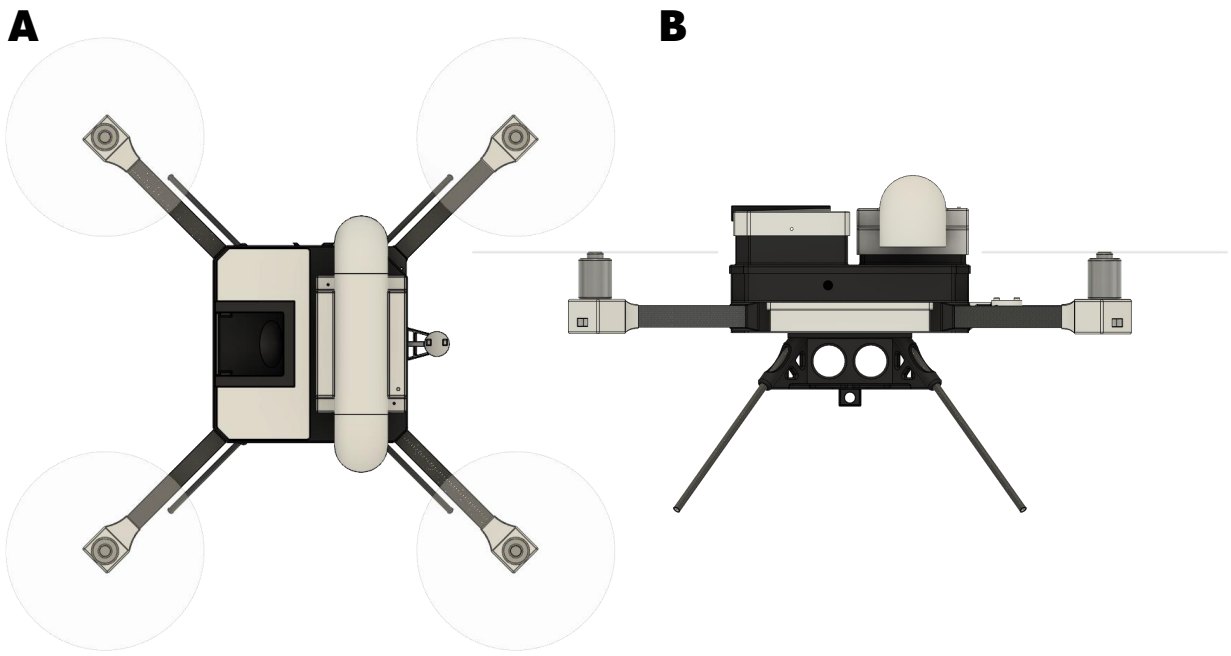


Figure E.1: 3-dimensional computer-aided design for this dissertation's WxUAS aircraft designs. (A) Orthographic top view and (B) orthographic front view.

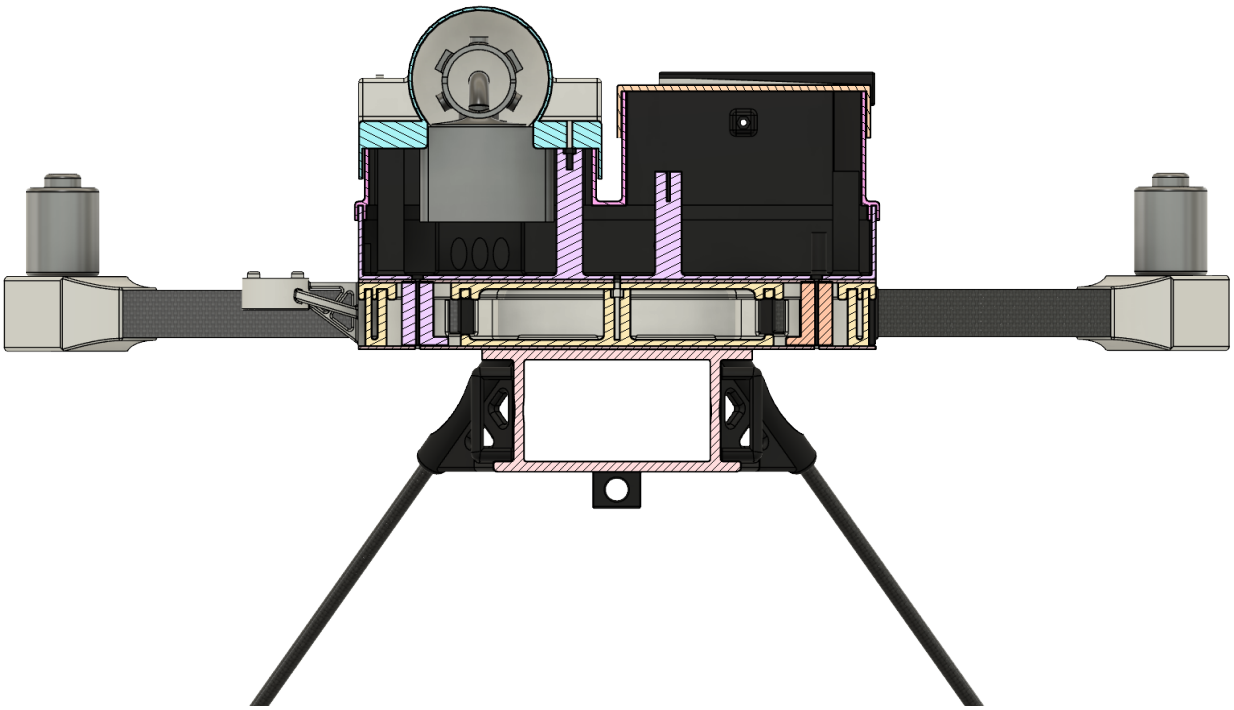


Figure E.2: 3-dimensional computer-aided design for this dissertation's WxUAS aircraft designs in a vertical cross-section cut of the orthographic back view illustrating the internal components and the overlapping layer technique for seal-less water-resistance.



AircraftStormTrooper

Figure E.3: Evolutionary desing steps that led to the StormTrooper's final design. The top left corner shows the initial waterproofing test. The top right corner shows the initial test of the landing gear integration for modular co-axial design. The bottom image shows the final baseline configuration as used in the MAI^{2}S field campaign.



Figure E.4: Two units of this dissertation's WxUAS aircraft design in the baseline configuration. These two units were purpose-built for the MAI^{2}S field campaign.

Appendix F

Field Campaign Supporting Weather Data

This appendix presents weather data publicly available weather products by federal agencies, which provide context to and temporal evolution of the general weather patterns seen during the WxUAS deployments in the MAI^{2}S field campaign.

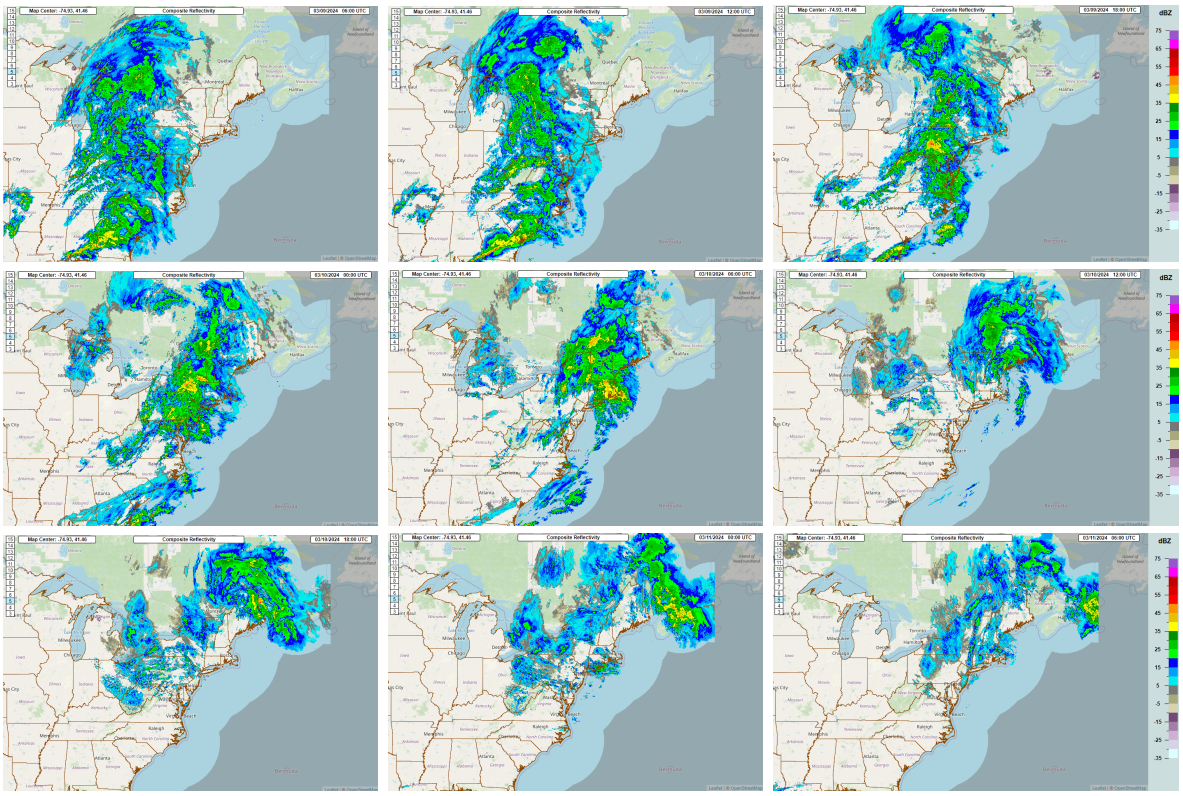


Figure F.1: MRMS composite reflectivity product for the northeastern United States from March 9$^{\text{th}}$, 06Z (top left) until the 11$^{\text{th}}$ at 06Z (bottom right).

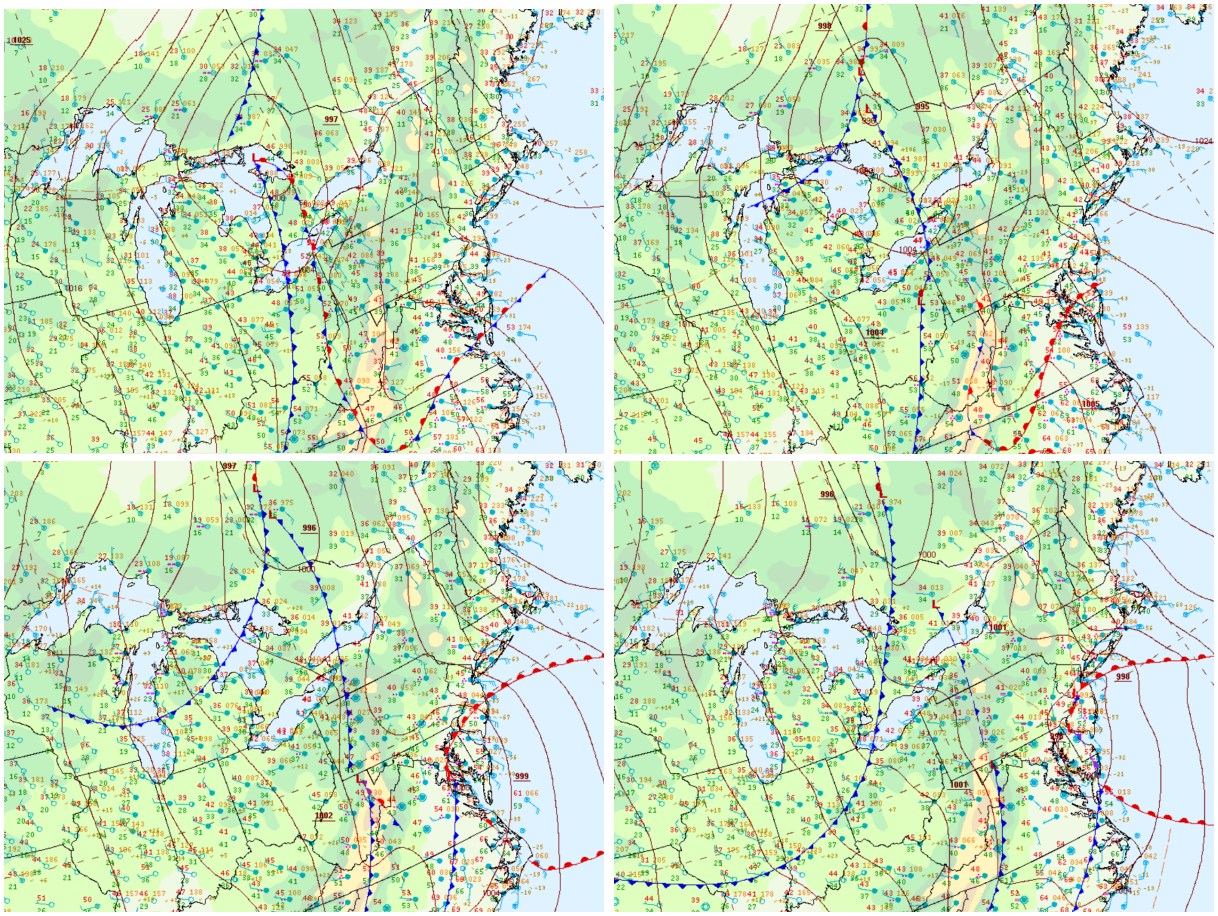


Figure F.2: Weather Prediction Center's surface observation maps for the NE U.S. The time stamps for the data are (top left) March 9$^{\text{th}}$ 15Z, (top right) 18Z, (bottom left) March 10$^{\text{th}}$ 0Z, and (bottom right) 3Z.

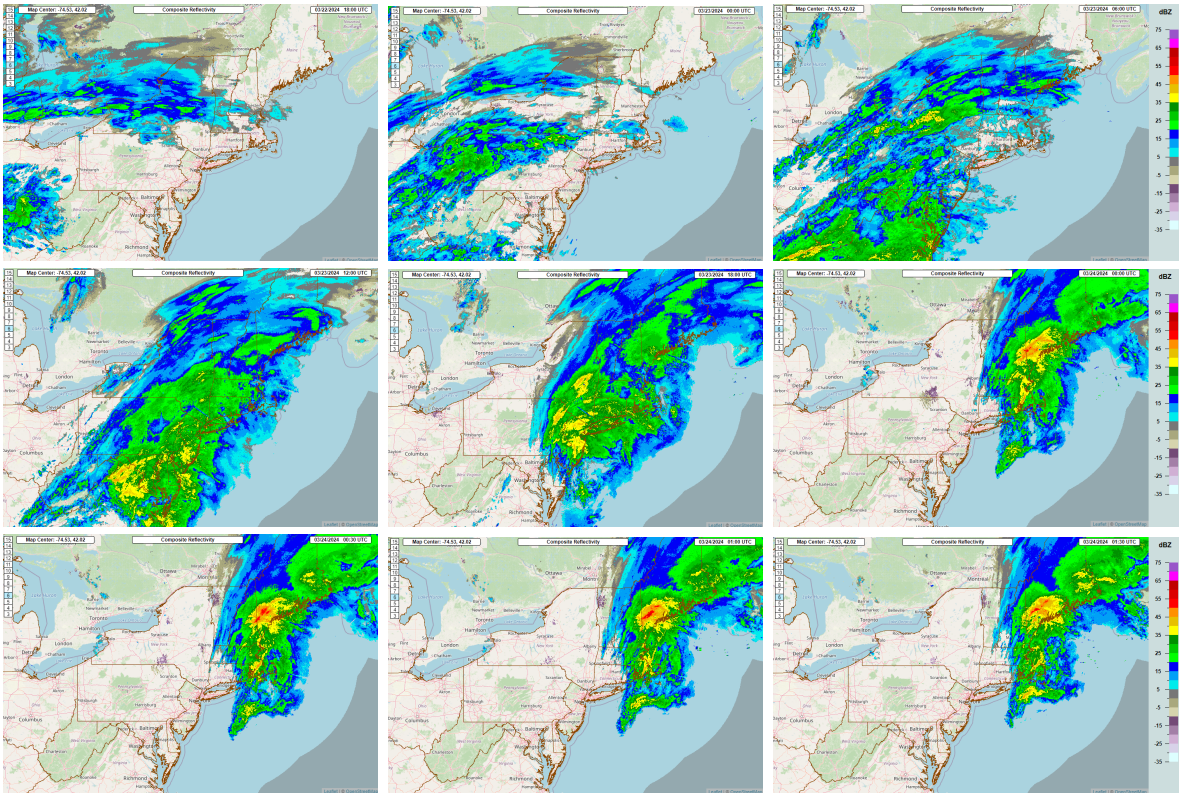


Figure F.3: MRMS composite reflectivity product for the northeastern United States from March 22$^{\text{th}}$, 18Z (top left) until the 24$^{\text{th}}$ at 0130Z (bottom right). The initial two rows advance in a 6-hour step, while the final row advances in a 30-minute step to highlight the missed rain event at Storrs (CT).

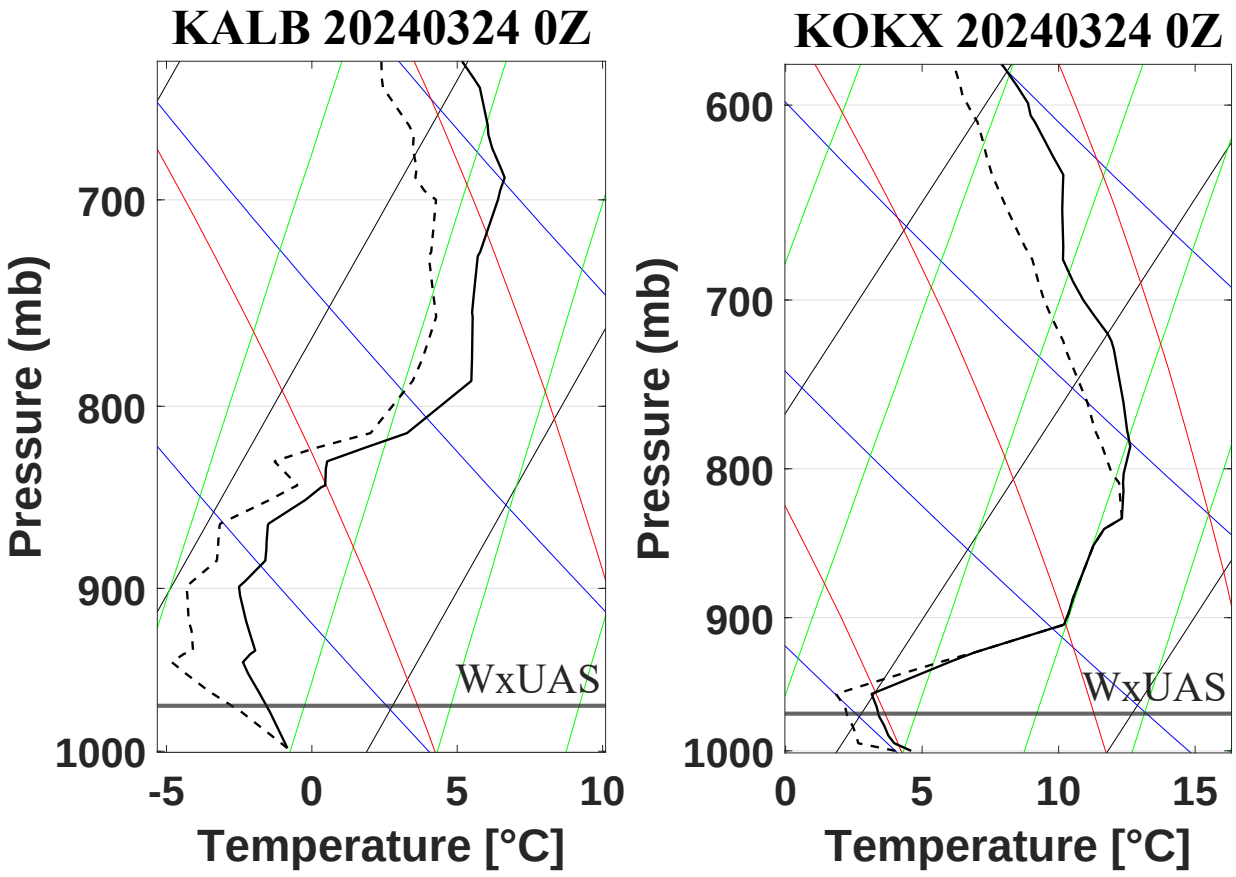


Figure F.4: Soundings from Albany (left), and Long Island (right) for March 24$^{\text{th}}$ 0Z.

Bibliography

[1] D. D. Tripp, E. R. Martin, and H. D. Reeves, "Applications of uncrewed aerial vehicles (UAVs) in winter precipitation-type forecasts," *Journal of Applied Meteorology and Climatology*, vol. 60, no. 3, pp. 361 – 375, 2021. [Online]. Available: https://journals.ametsoc.org/view/journals/apme/60/3/JAMC-D-20-0047.1.xml

[2] T. M. Bell, B. R. Greene, P. M. Klein, M. B. Carney, and P. B. Chilson, "Confronting the boundary layer data gap: Evaluating new and existing methodologies of probing the lower atmosphere," *Atmospheric Measurement Techniques Discussions*, vol. 2019, pp. 1–23, 2019. [Online]. Available: https://www.atmos-meas-tech-discuss.net/amt-2019-453/

[3] H. D. Reeves, N. Lis, G. Zhang, and A. A. Rosenow, "Development and testing of an advanced hydrometeor-phase algorithm to meet emerging needs in the aviation sector," *Journal of Applied Meteorology and Climatology*, vol. 61, no. 5, pp. 521 – 536, 2022. [Online]. Available: https://journals.ametsoc.org/view/journals/apme/61/5/JAMC-D-21-0151.1.xml

[4] FAA, "Airplane and engine certification requirements in supercooled large drop, mixed phase, and ice crystal icing conditions; final rule," *Parts 25 and 33, Aeronautics and Space, U.S. Code of Federal Regulations*, p. 34, 2015.

[5] S. G. Cober and G. A. Isaac, "Characterization of aircraft icing environments with supercooled large drops for application to commercial aircraft certification," *Journal of Applied Meteorology and Climatology*, vol. 51, no. 2, pp. 265 – 284, 2012. [Online]. Available: https://journals.ametsoc.org/view/journals/apme/51/2/jamc-d-11-022.1.xml

[6] H. D. Reeves and J. Waters, "Dual-polarized radar coverage in terminal airspaces and its effect on interpretation of winter weather signatures: Current capabilities and future recommendations," *Journal of Applied Meteorology and Climatology*, vol. 58, no. 1, pp. 165 – 183, 2019. [Online]. Available: https://journals.ametsoc.org/view/journals/apme/58/1/jamc-d-18-0123.1.xml

[7] S. D. Landolt, J. S. Lave, D. Jacobson, A. Gaydos, S. DiVito, and D. Porter, "The impacts of automation on present weather–type observing capabilities across the conterminous united states," *Journal of Applied Meteorology and Climatology*, vol. 58, no. 12, pp. 2699 – 2715, 2019. [Online]. Available: https://journals.ametsoc.org/view/journals/apme/58/12/jamc-d-19-0170.1.xml

[8] G. Britto Hupsel de Azevedo, "Spatially-temporally resolved sampling system for carbon dioxide concentration in the atmospheric boundary layer: a low-cost UAS approach," Master's thesis, University of Oklahoma, 2020. [Online]. Available: https://shareok.org/handle/11244/324315

[9] R. Stull, *An Introduction to Boundary Layer Meteorology*, ser. Atmospheric and Oceanographic Sciences Library. Springer Netherlands, 2012. [Online]. Available: https://books.google.com/books?id=2PjrCAAAQBAJ

[10] J. M. Kurdzo, E. F. Joback, P.-E. Kirstetter, and J. Y. N. Cho, "Geospatial QPE accuracy dependence on weather radar network configurations," *Journal of Applied Meteorology and Climatology*, vol. 59, no. 11, pp. 1773 – 1792, 2020. [Online]. Available: https://journals.ametsoc.org/view/journals/apme/59/11/JAMC-D-19-0164.1.xml

[11] FAA, "Aeronautical information manual," *Air Traffic Plans and Publications, U.S. Code of Federal Regulations*, 2023. [Online]. Available: https://www.faa.gov/air_traffic/publications/media/aim_basic_dtd_4-20-23.pdf

[12] R. G. Hallowell, M. F. Donovan, D. J. Smalley, and B. J. Bennett, "Icing hazard detection with NEXRAD IHL," in *36th Conference on Radar Meteorology*, 2013.

[13] N. T. S. Board, "In-flight icing encounter and loss of controll: Simmons airlines, d.b.a. american eagle 4184," *Aircraft Accident Reports*, 1994. [Online]. Available: https://www.ntsb.gov/investigations/AccidentReports/Reports/AAR9601.pdf

[14] S. DiVito, J. Riley, S. D. Landolt, B. Bernstein, S. Green, and J. Bracken, "An update of the federal aviation administration terminal area icing weather information for nextgen (TAIWIN) project," in *101st American Meteorological Society Annual Meeting*. AMS, 2021. [Online]. Available: https://ams.confex.com/ams/101ANNUAL/meetingapp.cgi/Paper/384097

[15] FAA, "Pilot guide: Flight in icing conditions," *Advisory Circular 91-74B*, 2015. [Online]. Available: https://www.faa.gov/regulations_policies/advisory_circulars/index.cfm/go/document.information/documentID/1028388

[16] B. Bernstein, S. DiVito, S. D. Landolt, A. Gaydos, J. Lave, D. Jacobson, M. Xu, A. Jensen, S. M. Ellis, and S. Faber, "An introduction to the terminal area icing weather information for nextgen (TAIWIN) capability," in *103rd AMS Annual Meeting*. AMS, 2023.

[17] A. Tokay, L. P. D'Adderio, D. B. Wolff, and W. A. Petersen, "Development and evaluation of the raindrop size distribution parameters for the NASA global precipitation measurement mission ground validation program," *Journal of Atmospheric and Oceanic Technology*, vol. 37, no. 1, pp. 115 – 128, 2020. [Online]. Available: https://journals.ametsoc.org/view/journals/atot/37/1/jtech-d-18-0071.1.xml

[18] R. Rasmussen, B. Baker, J. Kochendorfer, T. Meyers, S. Landolt, A. P. Fischer, J. Black, J. M. Thériault, P. Kucera, D. Gochis, C. Smith, R. Nitu,

M. Hall, K. Ikeda, and E. Gutmann, "How well are we measuring snow: The NOAA/FAA/NCAR winter precipitation test bed," *Bulletin of the American Meteorological Society*, vol. 93, no. 6, pp. 811 – 829, 2012. [Online]. Available: https://journals.ametsoc.org/view/journals/bams/93/6/bams-d-11-00052.1.xml

[19] H. S. Park, A. V. Ryzhkov, D. S. Zrnic, and K.-E. Kim, "The hydrometeor classification algorithm for the polarimetric WSR-88D: Description and application to an MCS," *Weather and Forecasting*, vol. 24, no. 3, pp. 730 – 748, 2009. [Online]. Available: https://journals.ametsoc.org/view/journals/wefo/24/3/2008waf2222205_1.xml

[20] T. M. Smith, V. Lakshmanan, G. J. Stumpf, K. L. Ortega, K. Hondl, K. Cooper, K. M. Calhoun, D. M. Kingfield, K. L. Manross, R. Toomey, and J. Brogden, "Multi-radar multi-sensor (MRMS) severe weather and aviation products: Initial operating capabilities," *Bulletin of the American Meteorological Society*, vol. 97, no. 9, pp. 1617 – 1630, 2016. [Online]. Available: https://journals.ametsoc.org/view/journals/bams/97/9/bams-d-14-00173.1.xml

[21] H. D. Reeves, "The uncertainty of precipitation-type observations and its effect on the validation of forecast precipitation type," *Weather and Forecasting*, vol. 31, no. 6, pp. 1961 – 1971, 2016. [Online]. Available: https://journals.ametsoc.org/view/journals/wefo/31/6/waf-d-16-0068_1.xml

[22] D. D. Tripp, "An assessment of oklahoma winter weather through the high-resolution lens of unmanned aerial vehicles," Master's thesis, University of Oklahoma, 2019. [Online]. Available: https://shareok.org/handle/11244/322848

[23] B. Bernstein, S. DiVito, J. T. Riley, S. Landolt, J. Haggerty, G. Thompson, D. Adriaansen, D. Serke, C. Kessinger, S. Tessendorf, M. Wolde, A. Korolev, A. Brown, L. Nichman, D. Sims, and C. Dumont, "The in-cloud icing and large-drop experiment science and operations plan," *DOT/FAA/TC-21/29*, 2021. [Online]. Available: https://rosap.ntl.bts.gov/view/dot/59922

[24] I. Strangeways, *Measuring the Natural Environment*. Cambridge University Press, 2000.

[25] F. V. Brock and S. J. Richardson, *Meteorological measurement systems.*, ser. Oxford scholarship online. New York: Oxford University Press, 2001.

[26] S. Emeis, *Measurement methods in atmospheric sciences: in situ and remote*. Stuttgart [Germany]: Gebr. Borntraeger Science Publishers, 2010.

[27] S. Burt, *The Weather Observer's Handbook*, 1st ed. New York, NY: Cambridge University Press, 2012.

[28] J. L. Stith, D. Baumgardner, J. Haggerty, R. M. Hardesty, W.-C. Lee, D. Lenschow, P. Pilewskie, P. L. Smith, M. Steiner, and H. Vömel, "100 years of progress in atmospheric observing systems," *Meteorological Monographs*, vol. 59, pp. 2.1 – 2.55, 2018. [Online]. Available: https://journals.ametsoc.org/view/journals/amsm/59/1/amsmonographs-d-18-0006.1.xml

[29] E. Le Roy Ladurie, *Times of feast, times of famine: a history of climate since the year 1000 / translated by Barbara Bray.* Garden City, N.Y.: Doubleday, 1971.

[30] J. R. Ziolkowska, C. A. Fiebrich, J. D. Carlson, A. D. Melvin, A. J. Sutherland, K. A. Kloesel, G. D. McManus, B. G. Illston, J. E. Hocker, and R. Reyes, "Benefits and beneficiaries of the oklahoma mesonet: A multisectoral ripple effect analysis," *Weather, Climate, and Society*, vol. 9, no. 3, pp. 499 – 519, 2017. [Online]. Available: https://journals.ametsoc.org/view/journals/wcas/9/3/wcas-d-16-0139_1.xml

[31] M. Smith, *Warnings: the true story of how science tamed the weather.*, 1st ed. Austin, Tex.: Greenleaf Book Group Press, 2010.

[32] G. Britto Hupsel de Azevedo, A. Avery, and D. Schvartzman, "UAS-based low-altitude freezing precipitation observation system: development updates and initial field deployment results." in *104th AMS Annual Meeting.* AMS, 2024. [Online]. Available: https://ams.confex.com/ams/104ANNUAL/mediafile/Manuscript/Paper435706/J10.5Azevedo435706.pdf

[33] Committee on Developing Mesoscale Meteorological Observational Capabilities to Meet Multiple National Needs, Board on Atmospheric Sciences and Climate, Division on Earth and Life Studies, National Research Council of the National Academies, *Observing weather and climate from the ground up : a nationwide network of networks.* Washington, D.C.: National Academies Press, 2009.

[34] G. Britto Hupsel de Azevedo, B. Doyle, C. A. Fiebrich, and D. Schvartzman, "Low-complexity methods to mitigate the impact of environmental variables on low-cost UAS-based atmospheric carbon dioxide measurements," *Atmospheric Measurement Techniques*, vol. 15, no. 19, pp. 5599–5618, 2022. [Online]. Available: https://amt.copernicus.org/articles/15/5599/2022/

[35] *Guide to Instruments and Methods of Observation*, 8th ed. Geneva, Switzerland: Secretariat of the World Meteorological Organization, 2021, vol. I-V.

[36] S. Waugh and T. J. Schuur, "On the use of radiosondes in freezing precipitation," *Journal of Atmospheric and Oceanic Technology*, vol. 35, no. 3, pp. 459 – 472, 2018. [Online]. Available: https://journals.ametsoc.org/view/journals/atot/35/3/jtech-d-17-0074.1.xml

[37] B. R. Greene, A. R. Segales, T. M. Bell, E. A. Pillar-Little, and P. B. Chilson, "Environmental and sensor integration influences on temperature measurements by rotary-wing unmanned aircraft systems," *Sensors*, vol. 19, no. 6, 2019. [Online]. Available: https://www.mdpi.com/1424-8220/19/6/1470

[38] S. J. Richardson, S. E. Frederickson, F. V. Brock, and J. A. Brotzge, "Combination temperature and relative humidity probes: Avoiding large air temperature errors and associated relative humidity errors," in *Preprints, 10th Symposium on Meteorological Observations and Instrumentation, Phoenix, AZ, American Meteorological Society*, vol. 278, 1998, p. 283.

[39] R. Rew and G. Davis, "NetCDF: an interface for scientific data access," *IEEE Computer Graphics and Applications*, vol. 10, no. 4, pp. 76–82, 1990.

[40] R. Black and K. Kretschmann, "EarthCube: A community-driven organization for geoscience cyber infrastructure," *Limnology & Oceanography Bulletin*, vol. 23, no. 4, 2014.

[41] G. Giuliani, B. Chatenoux, A. De Bono, D. Rodila, J.-P. Richard, K. Allenbach, H. Dao, and P. Peduzzi, "Building an earth observations data cube: lessons learned from the swiss data cube (SDC) on generating analysis ready data (ARD)," *Big Earth Data*, vol. 1, no. 1-2, pp. 100–117, 2017. [Online]. Available: https://doi.org/10.1080/20964471.2017.1398903

[42] B. Killough, "Overview of the open data cube initiative," in *IGARSS 2018 - 2018 IEEE International Geoscience and Remote Sensing Symposium*, 2018, pp. 8629–8632.

[43] J. Garratt, "Review: the atmospheric boundary layer," *Earth-Science Reviews*, vol. 37, pp. 89–134, 1994.

[44] E. Fedorovich, R. J. Conzemius, I. Esau, F. K. Chow, D. C. Lewellen, C. Moeng, P. P. Sullivan, D. Pino, and J. V.-G. de Arellano, "Entrainment into sheared convective boundary layers as predicted by different large eddy simulation codes," in *Proceedings of the 16th Symposium On Boundary Layers and Turbulence*. Portland, ME: American Meteorological Society, August 2004. [Online]. Available: https://ams.confex.com/ams/pdfpapers/78656.pdf

[45] S. D. Landolt, D. Jacobson, S. Faber, S. DiVito, A. Gaydos, W. Underwood, C. Enders, and A. Pierce, "The impacts of erroneous freezing fog observations on aircraft ground icing operations," in *104th American Meteorological Society Annual Meeting*. AMS, 2024. [Online]. Available: https://ams.confex.com/ams/104ANNUAL/meetingapp.cgi/Paper/439622

[46] B. R. Greene, A. R. Segales, S. Waugh, S. Duthoit, and P. B. Chilson, "Considerations for temperature sensor placement on rotary-wing unmanned aircraft systems," *Atmospheric Measurement Techniques*, vol. 11, no. 10, pp. 5519–5530, 2018. [Online]. Available: https://amt.copernicus.org/articles/11/5519/2018/

[47] G. M. McFarquhar, E. Smith, E. A. Pillar-Little, K. Brewster, P. B. Chilson, T. R. Lee, S. Waugh, N. Yussouf, X. Wang, M. Xue, G. de Boer, J. A. Gibbs, C. Fiebrich, B. Baker, J. Brotzge, F. Carr, H. Christophersen, M. Fengler, P. Hall, T. Hock, A. Houston, R. Huck, J. Jacob, R. Palmer, P. K. Quinn, M. Wagner, Y. R. Zhang, and D. Hawk, "Current and future uses of UAS for improved forecasts/warnings and scientific studies," *Bulletin of the American Meteorological Society*, vol. 101, no. 8, pp. E1322 – E1328, 2020. [Online]. Available: https://journals.ametsoc.org/view/journals/bams/101/8/bamsD200015.xml

[48] J. O. Pinto, D. O'Sullivan, S. Taylor, J. Elston, C. B. Baker, D. Hotz, C. Marshall, J. Jacob, K. Barfuss, B. Piguet, G. Roberts, N. Omanovic, M. Fengler, A. A. Jensen, M. Steiner, and A. L. Houston, "The status and future of small uncrewed

aircraft systems (UAS) in operational meteorology," *Bulletin of the American Meteorological Society*, vol. 102, no. 11, pp. E2121 – E2136, 2021. [Online]. Available: https://journals.ametsoc.org/view/journals/bams/102/11/BAMS-D-20-0138.1.xml

[49] P. B. Chilson, A. R. S. Espinosa, W. J. Doyle, T. M. Bell, B. R. Greene, J. J. Martin, E. A. Pillar-Little, and G. B. H. de Azevedo, "Unmanned aerial system for sampling atmospheric data," *U.S. Patent number 266793 (pending)*, 2021. [Online]. Available: https://patents.google.com/patent/US20210214079A1/en

[50] A. A. Jensen, J. O. Pinto, S. C. C. Bailey, R. A. Sobash, G. Romine, G. de Boer, A. L. Houston, S. W. Smith, D. A. Lawrence, C. Dixon, J. K. Lundquist, J. D. Jacob, J. Elston, S. Waugh, D. Brus, and M. Steiner, "Assimilation of a coordinated fleet of uncrewed aircraft system observations in complex terrain: Observing system experiments," *Monthly Weather Review*, vol. 150, no. 10, pp. 2737 – 2763, 2022. [Online]. Available: https://journals.ametsoc.org/view/journals/mwre/150/10/MWR-D-22-0090.1.xml

[51] L. Barbieri, S. T. Kral, S. C. C. Bailey, A. E. Frazier, J. D. Jacob, J. Reuder, D. Brus, P. B. Chilson, C. Crick, C. Detweiler, A. Doddi, J. Elston, H. Foroutan, J. González-Rocha, B. R. Greene, M. I. Guzman, A. L. Houston, A. Islam, O. Kemppinen, D. Lawrence, E. A. Pillar-Little, S. D. Ross, M. P. Sama, D. G. Schmale, T. J. Schuyler, A. Shankar, S. W. Smith, S. Waugh, C. Dixon, S. Borenstein, and G. de Boer, "Intercomparison of small unmanned aircraft system (sUAS) measurements for atmospheric science during the LAPSE-RATE campaign," *Sensors*, vol. 19, no. 9, 2019. [Online]. Available: https://www.mdpi.com/1424-8220/19/9/2179

[52] J. D. Jacob, P. B. Chilson, A. L. Houston, and S. W. Smith, "Considerations for atmospheric measurements with small unmanned aircraft systems," *Atmosphere*, vol. 9, no. 7, 2018. [Online]. Available: https://www.mdpi.com/2073-4433/9/7/252

[53] A. L. Houston and J. M. Keeler, "The impact of sensor response and airspeed on the representation of the convective boundary layer and airmass boundaries by small unmanned aircraft systems," *Journal of Atmospheric and Oceanic Technology*, vol. 35, no. 8, pp. 1687 – 1699, 2018. [Online]. Available: https://journals.ametsoc.org/view/journals/atot/35/8/jtech-d-18-0019.1.xml

[54] A. Islam, A. L. Houston, A. Shankar, and C. Detweiler, "Design and evaluation of sensor housing for boundary layer profiling using multirotors," *Sensors*, vol. 19, no. 11, 2019. [Online]. Available: https://www.mdpi.com/1424-8220/19/11/2481

[55] B. L. Hemingway, A. E. Frazier, B. R. Elbing, and J. D. Jacob, "Vertical sampling scales for atmospheric boundary layer measurements from small unmanned aircraft systems (sUAS)," *Atmosphere*, vol. 8, no. 9, 2017. [Online]. Available: https://www.mdpi.com/2073-4433/8/9/176

[56] S. E. Koch, M. Fengler, P. B. Chilson, K. L. Elmore, B. Argrow, D. L. Andra, and T. Lindley, "On the use of unmanned aircraft for sampling mesoscale

phenomena in the preconvective boundary layer," *Journal of Atmospheric and Oceanic Technology*, vol. 35, no. 11, pp. 2265 – 2288, 2018. [Online]. Available: https://journals.ametsoc.org/view/journals/atot/35/11/jtech-d-18-0101.1.xml

[57] M. O. Jonassen, "The small unmanned meteorological observer (SUMO): characterization and test of a new measurement system for atmospheric boundary layer research," Master's thesis, University of Bergen, Bergen [Norway], 2008.

[58] J. Reuder, P. Brisset, M. Jonassen, M. M ller, and S. Mayer, "Sumo: A small unmanned meteorological observer for atmospheric boundary layer research," *IOP Conference Series: Earth and Environmental Science*, vol. 1, 2008.

[59] A. R. Segales, B. R. Greene, T. M. Bell, W. Doyle, J. J. Martin, E. A. Pillar-Little, and P. B. Chilson, "The CopterSonde: an insight into the development of a smart unmanned aircraft system for atmospheric boundary layer research," *Atmospheric Measurement Techniques*, vol. 13, no. 5, pp. 2833–2848, 2020. [Online]. Available: https://amt.copernicus.org/articles/13/2833/2020/

[60] J. González-Rocha, S. F. J. De Wekker, S. D. Ross, and C. A. Woolsey, "Wind profiling in the lower atmosphere from wind-induced perturbations to multirotor UAS," *Sensors*, vol. 20, no. 5, 2020. [Online]. Available: https://www.mdpi.com/1424-8220/20/5/1341

[61] M. Hill, T. Konrad, J. Meyer, and J. Rowland, "A small, radio-controlled aircraft as a platform for meteorological sensors," *Johns Hopkins APL Technical Digest*, vol. 11, 1970.

[62] J. Elston, B. Argrow, M. Stachura, D. Weibel, D. Lawrence, and D. Pope, "Overview of small fixed-wing unmanned aircraft for meteorological sampling," *Journal of Atmospheric and Oceanic Technology*, vol. 32, no. 1, pp. 97 – 115, 2015. [Online]. Available: https://journals.ametsoc.org/view/journals/atot/32/1/jtech-d-13-00236_1.xml

[63] T. Wetz and N. Wildmann, "Spatially distributed and simultaneous wind measurements with a fleet of small quadrotor UAS," *Journal of Physics: Conference Series*, vol. 2265, no. 2, p. 022086, may 2022. [Online]. Available: https://dx.doi.org/10.1088/1742-6596/2265/2/022086

[64] L. M. Miloshevich, A. Paukkunen, H. Vömel, and S. J. Oltmans, "Development and validation of a time-lag correction for vaisala radiosonde humidity measurements," *Journal of Atmospheric and Oceanic Technology*, vol. 21, no. 9, pp. 1305 – 1327, 2004. [Online]. Available: https://journals.ametsoc.org/view/journals/atot/21/9/1520-0426_2004_021_1305_davoat_2_0_co_2.xml

[65] J. McCarthy, "A method for correcting airborne temperature data for sensor response time," *Journal of Applied Meteorology and Climatology*, vol. 12, no. 1, pp. 211 – 214, 01 Feb. 1973. [Online]. Available: https://journals.ametsoc.org/view/journals/apme/12/1/1520-0450_1973_012_0211_amfcat_2_0_co_2.xml

[66] S. K. Kimball, C. J. Montalvo, and M. S. Mulekar, "Assessing iMET-XQ performance and optimal placement on a small off-the-shelf, rotary-wing UAV, as a function of atmospheric conditions," *Atmosphere*, vol. 11, no. 6, 2020. [Online]. Available: https://www.mdpi.com/2073-4433/11/6/660

[67] J. Roadman, J. Elston, B. Argrow, and E. Frew, "Mission performance of the tempest unmanned aircraft system in supercell storms," *Journal of Aircraft*, vol. 49, no. 6, pp. 1821–1830, 2012. [Online]. Available: https://doi.org/10.2514/1.C031655

[68] G. J. Holland, P. J. Webster, J. A. Curry, G. Tyrell, D. Gauntlett, G. Brett, J. Becker, R. Hoag, and W. Vaglienti, "The aerosonde robotic aircraft: A new paradigm for environmental observations," *Bulletin of the American Meteorological Society*, vol. 82, no. 5, pp. 889 – 902, 2001. [Online]. Available: https://journals.ametsoc.org/view/journals/bams/82/5/1520-0477_2001_082_0889_taraan_2_3_co_2.xml

[69] A. L. Houston and J. M. Keeler, "Sounding characteristics that yield significant convective inhibition errors due to ascent rate and sensor response of in situ profiling systems," *Journal of Atmospheric and Oceanic Technology*, vol. 37, no. 7, pp. 1163 – 1172, 2020. [Online]. Available: https://journals.ametsoc.org/view/journals/atot/37/7/jtechD190191.xml

[70] P. Hugler, F. Roos, M. Schartel, M. Geiger, and C. Waldschmidt, "Radar taking off: New capabilities for UAVs," *IEEE Microwave Magazine*, vol. 19, no. 7, pp. 43–53, 2018.

[71] J. Svedin, A. Bernland, A. Gustafsson, E. Claar, and J. Luong, "Small UAV-based sar system using low-cost radar, position, and attitude sensors with onboard imaging capability," *International Journal of Microwave and Wireless Technologies*, vol. 13, no. 6, p. 602–613, 2021.

[72] F. Abushakra, N. Jeong, D. N. Elluru, A. K. Awasthi, S. Kolpuke, T. Luong, O. Reyhanigalangashi, D. Taylor, and S. P. Gogineni, "A miniaturized ultra-wideband radar for UAV remote sensing applications," *IEEE Microwave and Wireless Components Letters*, vol. 32, no. 3, pp. 198–201, 2022.

[73] J. Diaz, J. Salazar, A. Mancini, and J. Colom, "Radome design and experimental characterization of scattering and propagation properties for atmospheric radarapplications," in *Proceedings of American Meteorological Society*. AMS, 01 2015, pp. 819–823.

[74] A. Mancini, J. L. Salazar, R. M. Lebrón, and B. L. Cheong, "A novel instrument for real-time measurement of attenuation of weather radar radome including its outer surface. part i: The concept," *Journal of Atmospheric and Oceanic Technology*, vol. 35, no. 5, pp. 953 – 973, 2018. [Online]. Available: https://journals.ametsoc.org/view/journals/atot/35/5/jtech-d-17-0083.1.xml

[75] *Application Report: mmWave Radar Radome Design Guide*, Texas Instruments, 8 2021, rev. 1. [Online]. Available: https://www.ti.com/lit/an/swra705/swra705.pdf?ts=1733238954600

[76] T. C. Wilson, J. Brenner, Z. Morrison, J. D. Jacob, and B. R. Elbing, "Wind speed statistics from a small UAS and its sensitivity to sensor location," *Atmosphere*, vol. 13, no. 3, 2022. [Online]. Available: https://www.mdpi.com/2073-4433/13/3/443

[77] D. Hall and J. Llinas, "An introduction to multisensor data fusion," *Proceedings of the IEEE*, vol. 85, no. 1, pp. 6–23, 1997.

[78] L. Klein, *Sensor and Data Fusion: A Tool for Information Assessment and Decision Making*, ser. Press Monographs. Society of Photo Optical, 2004. [Online]. Available: https://books.google.com/books?id=-782bo4u_ogC

[79] R. W. Harms, "Snow forecasting for southeastern wisconsin," *Weatherwise*, vol. 26, no. 6, pp. 250–271, 1973. [Online]. Available: https://doi.org/10.1080/00431672.1973.9931668

[80] T. A. Hutchinson, "An analysis of NMC's nested grid model forecasts of alberta clippers," *Weather and Forecasting*, vol. 10, no. 3, pp. 632 – 641, 1995. [Online]. Available: https://journals.ametsoc.org/view/journals/wefo/10/3/1520-0434_1995_010_0632_aaonng_2_0_co_2.xml

[81] L. A. McMurdie, G. M. Heymsfield, J. E. Yorks, S. A. Braun, G. Skofronick-Jackson, R. M. Rauber, S. Yuter, B. Colle, G. M. McFarquhar, M. Poellot, D. R. Novak, T. J. Lang, R. Kroodsma, M. McLinden, M. Oue, P. Kollias, M. R. Kumjian, S. J. Greybush, A. J. Heymsfield, J. A. Finlon, V. L. McDonald, and S. Nicholls, "Chasing snowstorms: The investigation of microphysics and precipitation for atlantic coast-threatening snowstorms (impacts) campaign," *Bulletin of the American Meteorological Society*, vol. 103, no. 5, pp. E1243 – E1269, 2022. [Online]. Available: https://journals.ametsoc.org/view/journals/bams/103/5/BAMS-D-20-0246.1.xml

[82] D. Cerrai, B. Filipiak, A. Spaulding, D. B. Wolff, A. Tokay, C. N. Helms, A. M. Loftus, A. V. Chibisov, C. Schirtzinger, L. Bliven, C. S. Pabla, M. J. Boulanger, E. Kim, H. Thant, F. Junyent, V. Chandrasekar, B. Notaros, and G. B. H. De Azevedo, "The 2021-2024 winter precipitation ground validation field campaign at The University of Connecticut," in *IGARSS 2024 - 2024 IEEE International Geoscience and Remote Sensing Symposium*, 2024, pp. 717–720.

[83] B. Filipiak, D. B. Wolff, A. Spaulding, A. Tokay, C. N. Helms, A. M. Loftus, A. V. Chibisov, C. Schirtzinger, M. J. Boulanger, C. S. Pabla, L. Bliven, E. Kim, H. Thant, F. Junyent, V. Chandrasekar, B. Notaros, G. B. H. De Azevedo, and D. Cerrai, "In preparation: Winter precipitation measurements in new england: Results from the global precipitation measurement ground validation campaign in connecticut," *Earth System Science Data*, 2025. [Online]. Available: https://essd.copernicus.org/